EQUILIBRIUM AND QUENCH-DYNAMICAL STUDIES OF ULTRACOLD FERMIONS IN RING-SHAPED OPTICAL TRAPS

A Thesis

Submitted to the Faculty

in partial fulfillment of the requirements for the

degree of

Doctor of Philosophy

in

Physics and Astronomy

by

Daniel G. Allman

DARTMOUTH COLLEGE

Hanover, New Hampshire

August 2023

Examining Committee:

Kevin Wright, Chair

Alex Rimberg

James Whitfield

Luigi Amico

F. Jon Kull, Ph.D.
Dean of the Guarini School of Graduate and Advanced Studies

Abstract

The unique capability to precisely tune the few and many-body configurations of ultracold Fermi gases provides a multi-dimensional platform for studying novel, exotic aspects of quantum systems. These aspects include superfluid/superconducting phenomena supported by potentially exotic pairing mechanisms, non-equilibrium and critical dynamics, and proposed quantum sensing or computing applications based on atomtronics.

Ring geometries provide natural arenas for probing transport properties of superfluids. Metastable states of quantized superfluid flow —persistent currents— exhibit remarkable properties, and the manner in which they form is an incredibly rich subject. Studies of quenched superfluids demonstrate that persistent currents can form from fragments of spontaneous symmetry breaking as second-order phase transitions are crossed at finite rates. The extent of these fragments of the higher-symmetry phase can in some limits be predicted by the Kibble-Zurek mechanism (KZM), which is fundamentally tied to the universal properties characterizing the transition. Thus, studies of spontaneous currents in superfluid rings can shed light on universality classes that microscopically distinct systems fall into.

This thesis describes the experimental results of two separate yet complimentary investigations of the physics of ultracold ^{6}Li atoms confined to ring geometries. The subject of the first investigation is the heating of degenerate fermionic rings subject to collisions with background molecules. The most important result of this

study was that the heating due to these ever-present collisions can be substantially reduced by maintaining a reservoir of non-degenerate fermions in contact with the deeply-degenerate atoms in the ring. These findings permit the possibility to perform seconds-long experiments that require maintaining low temperatures. The second part of the thesis describes the first experimental studies of the KZM ever conducted with ultracold fermions in ring-shaped traps. By exploiting long lifetimes offered by the trapping potential utilized in the aforementioned heating studies, we reveal two distinct regimes of quench dynamics. The fast-quench regime agrees with KZM predictions, while the slow-quench regime governed by finite-size effects follows a different trend. Our KZM studies should be readily extendable to scenarios that include current biases, inhomogeneities and disorder, where these controls can be employed to obtain additional information about the phase transition.

Preface

In my years as a graduate student at Dartmouth college, I have had the absolute privilege of working with a small yet incredibly talented and dedicated team of physicists in the Wilder hall basement. I was fortunate enough to be given the chance to contribute to the construction and operation of a unique, carefully planned experimental ecosystem that would eventually conduct my first main contributions to the vast and rapidly growing field of ultracold atoms.

Of course, none of this would have been possible without Kevin's expansive vision, laser-focused attention to detail, and methodically-executed construction of our ultracold lithium machine. Kevin was an invaluable resource to me, not just for his assistance in the lab when we relied on him most, but also for his ever-present enthusiasm for physics and how he welcomed discussion with open arms at a moment's notice. Despite numerous experimental setbacks along this journey, Kevin taught me to meet challenges with an attitude of "if it's broken, I can figure out how to fix it", which is a mindset I plan to carry with me in any of my future endeavors. He has taught be how to be a professional within an incredibly demanding ecosystem, and to lead a battle against entropy. I'm forever grateful for the opportunity you gave to me when you enthusiastically welcomed me into your lab.

The time I have spent in the lab has been made infinitely easier with the help and presence of several incredible labmates. Firstly, Yanping, who pioneered with Kevin the construction of our experimental apparatus, has been someone who I have turned

to on countless occasions for guidance and technical advice. As the one most familiar with the intricacies of the many devices in our lab, he was an invaluable resource to me even after his graduation in 2020. You were always willing to pick up the phone when I had a troubleshooting question or when I couldn't see atoms on the camera. I forgive you for being a bandwagon Warriors fan, plus you know I can't say much because my favorite teams are perpetually bad. Secondly, I have witnessed Parth over the last few years become a talented and confident physicist, who welcomed the opportunity to choreograph the incredibly complex ultracold atoms dance, and whose capabilities have now awarded him a unique opportunity to explore potentially groundbreaking physics. I am excited to see where you lead the lab within the remainder of your time at Dartmouth. I also wanted to say thank you for all the root beers you offered to me when we were working late night shifts in the lab. Finally Pradipta, I can tell from even our limited overlap in the lab that you have the toolkit, passion, and ambition required to be a capable AMO physicist, and I wish you nothing but the best of luck on your Ph.D journey.

There have been a great number of friends and colleagues within Dartmouth who have had a lasting impact of my years in graduate school. Kanav, you never ceased to amaze me with the manner in which you could elevate the stupidity of your "Kanav" jokes. But joking aside, it is inspiring to see where your devotion to and passion for quantum computing has taken you. Max, there's no one I'd rather take an impromptu trip to Switzerland with in my first year of grad school than you. You better come visit us after we move there. Christina, the Nats are the wrong team but I forgive you because so are the Mets. Ben and Mana, I thank you for being all ears to bounce physics and math concepts off of, including the highly controversial reciprocal delta function idea. Jesse, I think you and Yanping convinced me to join the lab after my first year, and I don't know whether to thank you or resent you for that, but I'll

choose to thank you. To the "basement dwellers," I know we didn't get the chance to interact very often, but the times we got to chat were always enlightening to me, and I wish you all success in your future endeavors.

To family, and the friends I have made along this journey, you mean more to me than perhaps I have shown. I do not want to understate just how much your unwavering support and numerous words of encouragement you have provided to me have meant. To my mom, dad and sister, you have been the backbone and pillar of support for my graduate career and I will be forever grateful for this. You have truly been my rock throughout my graduate career. There are certainly a great many others, from aunts and uncles to friends in other Dartmouth departments, who I also say thank you to.

Finally, I would like to say thank you to my wife, travel buddy, best friend and life partner Alejandra. You have been my most constant source of support, someone who motivates me to succeed and picks we up with words of encouragement, support, and love. This journey would have felt a lot less meaningful had I not bumped into you at that grad student mixer almost seven years ago. I can't wait to see where the future takes us. Maybe someday Truffles will even let us get a full night's sleep.

Contents

List of Tables

List of Figures

Chapter 1

Introduction

The incredibly rich and vast subjects of fermionic superfluidity and superconductivity are known to house many unanswered questions regarding, in particular, the role of pairing and many-body correlations in giving rise to macroscopic quantum phenomena observed in real material systems. Unconventional aspects of superconductivity, such as those seen in high-T_c or heavy fermion superconductors and in hypothetical "super" systems supporting exotic pairing mechanisms such as the Fulde-Ferrell-Larkin-Ovchinnikov phases, have either eluded satisfactory theoretical descriptions or have not seen concrete physical realization [1–3]. Furthermore, attempts at a unified theoretical description of even conventional superconducting systems have been mostly fruitless except in several outstanding limits. The success of BCS theory in describing aspects of the Cooper and Meissner effects in superconducting electronic systems is perhaps the most notable example [4], although it is a mean-field description that sweeps the many-body correlations under the vast rug of the many-body quantum system. Nonetheless, the theory is non-perturbative and incredibly manages to capture some of the core pieces of the extraordinarily complex many-body quantum physics, and in particular how a Cooper pair superfluid that supports dissipationless flow can remarkably emerge from the coupling of moving electrons to phononic lattice

excitations.

On the other hand, it is well known that systems supporting a second-order phase transition often carry certain simple, universal descriptions of the otherwise rich physics near the critical point. Due to the diverging correlation length, much of the microscopic details of the interacting sample can be ignored, at least in certain limits, and the resulting theory is said to become universal, depending only a small set of generic properties of the system. In this way, distinct physical systems with vastly different microscopic properties can display remarkably similar behavior near their critical points. The phenomenological Landau-Ginzburg theory and renormalization group techniques, for instance, have seen success in describing the universal properties of strongly correlated systems near a second-order phase transition [5, 6]. Incorporating time-dependence into the physics revolving around second-order phase transitions, the Kibble-Zurek mechanism (KZM) has become a paradigmatic model of non-equilibrium critical dynamics [7, 8]. In its original and most elegant form, it predicts a scaling law for the spatial extent of the fragments of a system's spontaneously-broken symmetry as its second-order phase transition is crossed at variable rates. The laws of thermodynamics allow the system to pick up these fragments, but nature randomly decides the manner in which they are pieced back together. The newly reassembled system will then assume a topological order that reflects the geometry of the underlying confinement. In multiply-connected geometries for instance, spontaneous persistent rotation can emerge following the symmetry-breaking. Due to the universal properties of second-order transitions, the key arguments of the KZM are indeed elegant and encompass a broad range of scenarios, but oftentimes sweep under the rug the complexity experienced in real systems. Yet, the beauty of the Kibble-Zurek argument lies in its ability to predict the outcomes of quenching a system across its critical point, whether that system is the universe experiencing rapid

cool-down moments after the Big Bang [7, 9], or a mesoscopic ring of superconducting material [10]. These examples are certainly not exhaustive, and indeed observations of the KZM have been made in many diverse settings that include superfluid ^{3}He, colloidal monolayers, spinor BECs, and non-linear optical systems [11–18]. Extensions to the quantum regime, where thermal fluctuations are completely frozen out and quantum fluctuations pave the way for the KZM, have also been observed, for instance in programmable atomic Rydberg arrays [19–22]. That there exists a unified theory that can encapsulate the dynamics of systems with such vastly disparate microscopic complexity is at the heart of the KZM. It is the simplicity and elegance of the KZM argument that experiments probing non-equilbrium critical dynamics often hope to preserve, but also to utilize the predictions of the KZM to further connect observables to the critical exponents describing the corresponding phase transition. These critical exponents encode the essential features of the phase transition and their universal properties, and for this reason the measurement of these exponents in various systems is a focus of much experimental effort.

Section 1.1

In This Thesis

Ultracold atoms have emerged over the past few decades as leading candidates for studying superfluid phenomena as well as offering a promising platform for quantum simulation and computing [23, 24]. In particular, the high degree of controllability, cleanness, and versatility offered by ultracold atoms lays out a promising path forward to answering several of the key unanswered questions that have presented themselves in studies of real materials systems. In this work, we exploit this versatility to explore both equilibrium non-equilibrium physics associated to ring-shaped ensembles of ultracold fermionic samples of ^{6}Li, where the metastable states of quantized su-

perfluid flow provide invaluable information on the rich physics associated to various quantum phenomena. Building on the findings of Yanping Cai in his doctoral work, this work places a heavy focus on studying the Kibble-Zurek mechanism (KZM), and more generally spontaneous current formation, in samples of quenched-cooled ultracold fermionic rings. The use of ring-shaped traps provides a natural setting for investigating the stochastic formation of spontaneous currents, which carry a directly observable metric quantifying their flow called the winding number. In fact, a ring-shaped geometry was the setting originally envisaged by W. Zurek in his attempts to bridge predictions by T. Kibble of cosmic string formation on cosmological scales with spontaneous currents in superfluid ^{3}He [7, 8]. Much of the ability to perform these studies in an ultracold atoms setting relies on our unique experimental capabilities, and the great deal of effort spent characterizing the superfluid properties of fermionic ^{6}Li in multiply-connected geometries.

This thesis is organized as follows:

- Chapter 2 gives an overview of the thermodynamics of non-interacting Fermi ensembles. It then discusses the role of interactions and how those interactions are tuned experimentally via Feshbach resonances, and how superfluidity emerges from the two and many-body physics.

- Chapter 3 Gives an overview of the experimental apparatus and some of its key features.

- Chapter 4 discusses the findings of a recent experiment pertaining to hole-induced heating of a sample of degenerate ^{6}Li confined to a ring-shaped trap. In particular, it discusses a means of mitigating this heating via a particular choice of trapping configuration. More than just a technical result, the findings pave the way for future experiments performed on weakly interacting BCS superfluids that require maintaining extremely low temperatures for long periods of time.

- Chapter 5 gives a detailed theoretical description of the Kibble-Zurek mechanism and its mathematical foundations. Furthermore, we investigate theoretically the statistics of spontaneous currents formed in ring-shaped superfluids after quenching a system across its second-order phase transition.

- Chapter 6 discusses the techniques used to detect persistent currents in ring-shaped traps. We put a heavy focus on the interferometric detection technique that was utilized extensively in the experiment discussed in Chapter 6.

- Chapter 7 discusses the findings of an experiment performed on thermally-quenched rings of ^{6}Li. In particular, we discuss the techniques used to measure the statistics of spontaneous current formation, and describe how these observations are and are not in line with predictions from the Kibble-Zurek mechanism.

- Chapter 8 describes two potential future experiments that are essentially extensions of the experiment performed in Chapter 6 to even richer settings. These experiments are certainly within reach of our current experimental capabilities.

- Chapter 9 gives a summary of the work performed in this thesis, and the outlook for the future directions of the lab.

Chapter 2

Ultracold Fermi Gases

This chapter introduces and describes the core elements of ultracold fermionic physics. We will first introduce the fundamentals of the non-interacting (ideal) Fermi gas, applied to both uniform systems and the non-uniform ring-shaped systems relevant to the experiments performed in this work. Next we will discuss interacting Fermi systems in the ultracold regime, and an incredibly useful technical feature particularly well-suited to ^{6}Li studies called a Feshbach resonance. We will then discuss how superfluidity and macroscopic phenomena can emerge from interacting Fermi systems in certain limits, and apply these findings to ring-shaped geometries.

Section 2.1

Thermodynamics of Trapped Fermi Gases

2.1.1. The Non-Interacting Fermi Gas

In this section, we study the equilibrium properties of trapped (non-interacting) Fermi gases. We are particularly interested in deriving key quantities that parameterize the BEC-BCS crossover, such as the Fermi energy, and properties that capture the essential thermodynamics of interacting Fermi systems.

The equilibrium properties of a uniform ensemble of non-interacting fermions are captured by the well-known Fermi-Dirac distribution. Because of the Pauli exclusion principle, at zero temperature fermions will fill up successively higher and higher energy levels, up to the Fermi energy. The Fermi energy is a function of the density of fermions for a uniform system, but the exact form depends on the dimensionality of the system under consideration.

We study explicitly the thermodynamic properties of an ideal trapped Fermi gas confined to some conservative potential $V(\mathbf{r})$. The exact form of $V(\mathbf{r})$ will depend on the details of the experiment. The lasers used to trap our atoms, for instance, generate a piece of such a conservative potential, $V_{\text{optical}}(\mathbf{r})$, that is proportional to the local intensity $I(\mathbf{r})$ of the laser field [25]. Furthermore, the exact form of the potential depends on the implementation of those laser fields. For instance, while the ring-shaped potential generated by an axicon is an approximately Gaussian function with radius R and full-width w, that generated by a ring-shaped, binary digital micromirror device (DMD) pattern has a more box-like structure [26]. Other potentials such as those due to magnetic fields and the ever-present gravitational field will additionally contribute to the total potential. The exact details of implementation will affect the thermodynamics of the ensemble, at the fundamental level modifying the density of ideal fermionic states. Additionally, while many ultracold atoms experiments (both fermionic and bosonic) have typically operated in a regime where a harmonic approximation to the potential can be safely applied, we have found that our trapping potentials have a significantly more complex landscape whose full structure must be maintained for theoretical considerations of the thermodynamics. Thus, we will keep approximations to a minimum and attempt to describe the thermodynamics in as general a framework as possible.

Partition and distribution functions. We begin with a non-interacting system described by the generic single-particle Hamiltonian operator

$$H(\hat{\mathbf{r}}, \hat{p}) = \frac{\hat{p}^2}{2m} + V(\hat{\mathbf{r}}) \tag{2.1}$$

The goal of equilibrium statistical mechanics is to compute the partition function $\mathcal{Z}$ from which the relevant thermodynamic properties of the system can be derived. We will employ a grand canonical ensemble to describe the systems in this work, where explicitly $\mathcal{Z} = \mathcal{Z}(\mu, T, \mathcal{V}, \eta)$ where μ is the chemical potential, T the temperature, and $\mathcal{V}$ and η represent sets of variables containing any additional extensive and intensive quantities used to describe the system, respectively. In a uniform system, i.e., $\mathcal{V}$ could represent the volume, while η could represent the aspect ratios of a rectangular box. The grand canonical partition function is computed as

$$\mathcal{Z}(\mu, T, \mathcal{V}, \eta) = \sum_{N=0}^{\infty} \sum_{J} e^{-[E_J(N,\mathcal{V},\eta) - \mu N]/k_B T} \tag{2.2}$$

where the sum runs over all particle numbers and many-body energy levels J. For concreteness, we have made explicit how the dependence on $\mathcal{V}$ and η enters into the partition function via the energy spectrum. Due to the non-interacting nature of the Hamiltonian, $E_J(N, \mathcal{V}, \eta) = \sum_j \epsilon_j(\mathcal{V}, \eta) n_j$ with $\sum_j n_j = N$, and the partition function factorizes into products of mini-partition functions within each energy level ϵ_j. Additionally, for fermions, the occupancies per level n_j can only be 0 or 1. We therefore have

$$\mathcal{Z}(\mu, T, \mathcal{V}, \eta) = \prod_j \sum_{n_j=0,1} e^{-[\epsilon_j(\mathcal{V},\eta) - \mu] n_j / k_B T} = \prod_j \left\{1 + e^{-[\epsilon_j(\mathcal{V},\eta) - \mu]/k_B T}\right\} \tag{2.3}$$

From the mini-partition functions, we can derive the familiar Fermi-Dirac distribution, given by

$$f(\epsilon_j) \equiv \langle n_j \rangle = -k_B T \frac{\partial \ln \mathcal{Z}}{\partial \epsilon_j} = \frac{1}{e^{(\epsilon_j - \mu)/k_B T} + 1} \tag{2.4}$$

The Fermi-Dirac distribution allows one to compute statistical properties of the full system from knowledge of the single particle properties. Namely if x_j is some dynamical quantity (energy, momentum, etc.) pertaining to a single particle eigenstate, then its ensemble average X can be computed as

$$X = \sum_j f(\epsilon_j) x_j \tag{2.5}$$

Density of States. Even if x_j is a simple function of j, explicitly computing the sum (2.5) is generally difficult even for simple and known energy spectra $\{\epsilon_j\}$. Computing ensemble averages can be simplified using the so-called density of states (DoS), which measures the number of available single-particle energy levels per unit of energy. Its utility arises in replacing discrete sums over the energy levels ϵ_j, such as those in (2.5), with integrals over a continuous energy variable E. If $\mathcal{N}(E) = \sum_j \Theta(E - \epsilon_j)$ is the number of states with energy at or below E (Θ is the step function), then the density of states $g(E)$ is simply given by its derivative

$$g(E) = \frac{d\mathcal{N}}{dE} = \sum_j \delta(E - \epsilon_j) \tag{2.6}$$

from which we may compute

$$X(\mu, T) = \int dE g(E) f(E; \mu, T) x(E) \tag{2.7}$$

where we have made the dependence of this quantity on μ and T now explicit. The expression (2.6) is merely a *definition*, used to recast (2.5) as an integral. To proceed

with analytics, however, we can utilize the semi-classical approximation, where it is assumed that the discrete and potentially complicated energy spectrum of the (non-interacting) Hamiltonian operator can be replaced by a continuous classical Hamiltonian function $H(\mathbf{r}, p) = \frac{p^2}{2m} + V(\mathbf{r})$. This approximation is valid whenever the potential is roughly constant over the average interparticle spacing, and atoms in some small volume of phase space *locally* experience a constant potential [27]. The density of states in D dimensions can then be approximated as

$$g_D(E) = \frac{s}{(2\pi\hbar)^D} \iint \delta[E - H(\mathbf{r}, p)] d^D\mathbf{r} d^D\mathbf{p} \tag{2.8}$$

where E is the energy, and the factor $(2\pi\hbar)^D$ is the discretization unit in D-dimensional phase space. The integral is taken over all phase space, while the factor of s accounts for the spin-s degeneracy. We can use the "delta function of a function" property to write $\delta[E - H(\mathbf{r}, p)] = \frac{m}{p_0(\mathbf{r};E)}\delta[p - p_0(\mathbf{r}; E)]$, where $p_0(\mathbf{r}; E) \equiv \sqrt{2m[E - V(\mathbf{r})]}$ is the classical momentum for a fixed-energy orbit. The density of states simplifies to

$$g_D(E) = \frac{smS_D}{(2\pi\hbar)^D} \int_{V(\mathbf{r})\leq E} d^D\mathbf{r} [p_0(\mathbf{r}; E)]^{D-2} \tag{2.9}$$

where S_D is the surface area of the D-dimensional unit sphere and the integral is taken over the so-called *Thomas-Fermi* region defined by $V(\mathbf{r}) \leq E$.

Fermi Energy. With the density of states, one may compute relevant thermodynamic quantities pertaining to the Fermi ensemble. One important quantity is the Fermi energy E_F, which is the energy of the highest occupied state for a system of N fermions at $T = 0$. The Fermi energy, and similar quantities such as Fermi momentum $p_F \equiv \sqrt{2mE_F}$, set useful scales for normalizing thermodynamic quantities pertaining to the BEC-BCS crossover. Knowledge of the density of states is sufficient

to compute the Fermi energy. At finite temperature T, we may use the density of states to compute the average atom number N (taking $x(E) = 1$ in (2.7))

$$N(\mu, T) = \int_0^\infty dE g_D(E) f(E; \mu, T) \tag{2.10}$$

This equation may be inverted to compute the chemical potential $\mu(N, T)$. At $T = 0$, the Fermi-Dirac distribution becomes a step function with a sharp energy cutoff defining the Fermi energy $E_F(N) \equiv \mu(T = 0, N)$. Evaluating Eq.(2.10) at $T = 0$, we implicitly define the Fermi energy via

$$N = \int_0^{E_F(N)} dE g_D(E) \tag{2.11}$$

Taking $x(E) = E$ gives the definition of the internal energy

$$U(\mu, T) = \int dE g_D(E) f(E; \mu, T) E \tag{2.12}$$

It is interesting to note that the Fermi energy is essentially a *geometric* property of the trap; It is defined by the number, N, of lowest available single-particle energy levels offered to the system of fermions, and is completely agnostic to the other thermomdynamic variables such as temperature and chemical potential, or even interactions (which have been neglected thus far). It is partly for this reason that the Fermi energy is often sought as a convenient energy scale for normalizing other thermodynamic energies with.

Finite Temperature. Inverting equations (2.10) and (2.12) allows one to express the intensive quantities μ and T in terms of the extensive N and U, which can be beneficial in certain cases. As is discussed in chapter 4.4, heating associated to trap losses is governed by a simple dynamic evolution of N and U, and the associated rate

of temperature increase is derived via the above relations.

Local Density Approximation. We may equivalently define (2.10) as

$$N(\mu, T) \equiv \int n(\mathbf{r}) d^D r \tag{2.13}$$

where we associate to the total atom number N the density of atoms $n(\mathbf{r})$ at position $\mathbf{r}$, and the integral is taken over all space. By inserting the density of states integral (2.8) into equation (2.10) and swapping the order of integration, we may write

$$\begin{aligned} N(\mu, T) &= \frac{s}{(2\pi\hbar)^D} \iint d^D r d^D p f[H(\mathbf{r}, p); \mu, T] \\ &= \frac{s}{\lambda_T^D} \int d^D r F_{\frac{D}{2}-1}\left[\frac{\mu - V(\mathbf{r})}{k_B T}\right] \end{aligned} \tag{2.14}$$

where $\lambda_T^2 \equiv 2\pi\hbar^2/(m k_B T)$ is the thermal deBroglie wavelength and F_j is the Fermi-Dirac integral of order j [28]. We used the explicit form of the Fermi-Dirac distribution function to evaluate the momentum integral, and we can now identify

$$n(\mathbf{r}) = \frac{s}{\lambda_T^D} F_{\frac{D}{2}-1}\left[\frac{\mu - V(\mathbf{r})}{k_B T}\right] \tag{2.15}$$

The spatial dependence of the density of fermions is seen to depend only on the variable $\mu(\mathbf{r}) \equiv \mu - V(\mathbf{r})$, i.e. $n(\mathbf{r}; \mu, T) \equiv n_0[\mu - V(\mathbf{r}), T]$. This is the essence of the local density approximation (LDA); The density of particles in potential $V(\mathbf{r})$ with chemical potential μ can be approximated by the density of the corresponding homogeneous system at $V(\mathbf{r}) = 0$ and chemical potential $\mu - V(\mathbf{r})$. This approximation, as stated before, breaks down when the variation in $V(\mathbf{r})$ over the average interparticle spacing becomes large relative to the Fermi energy, and the semiclassical approximation to spectrum of the quantum Hamiltonian breaks down.

Experiments, such as those performed in this work, often probe density profiles

via absorption imaging [29], which provides information on the *column* density

$$n_{\rm col}(\mathbf{r}_\perp) \equiv \int_{-\infty}^{\infty} dx_{\rm probe} n(\mathbf{r}_\perp, x_{\rm probe}) \tag{2.16}$$

where $x_{\rm probe}$ is the so-called probe axis, $\mathbf{r}_\perp$ is a position vector transverse to this axis, and $\mathbf{r} = (\mathbf{r}_\perp, x_{\rm probe})$. In certain cases, the observable column density can be inverted to find the total density by exploiting certain symmetries of the trapping potential via the inverse Abel transform [30]. For the common scenario where the potential is both harmonic along the probe axis and separable along the probe and transverse axes, $V(\mathbf{r}) = V_\perp(\mathbf{r}_\perp) + m\omega^2 x_{\rm probe}^2/2$, equation (2.15) can be directly integrated:

$$\begin{aligned} n_{\rm col}(\mathbf{r}_\perp) &= \frac{s}{\lambda_T^D}\sqrt{\frac{2\pi k_B T}{m\omega^2}} F_{\frac{D-1}{2}}\left[\frac{\mu - V_\perp(\mathbf{r}_\perp)}{k_B T}\right] \\ &\overset{T\to 0}{\sim} \frac{s}{(2\pi)^{\frac{D-1}{2}}\Gamma\left(\frac{D+3}{2}\right)}\frac{1}{a^{D-1}}\left[\frac{E_F - V_\perp(\mathbf{r}_\perp)}{\hbar\omega}\right]^{\frac{D+1}{2}} \end{aligned} \tag{2.17}$$

where $a \equiv \sqrt{\hbar/(m\omega)}$ is the usual harmonic oscillator length and the definition $E_F = \mu(T=0,N)$ was used in the $T \to 0$ limit. This equation can be readily inverted to solve for the local Fermi energy as a function of the column density in the $T \to 0$ limit. We can further utilize this equation by noting that for $x_{\rm probe} = 0$, $V(\mathbf{r}) = V_\perp(\mathbf{r}_\perp)$, and the total density here is given by

$$\begin{aligned} n(\mathbf{r}_\perp, x_{\rm probe}=0) &= \frac{s}{\lambda_T^D} F_{\frac{D}{2}-1}\left[\frac{\mu - V_\perp(\mathbf{r}_\perp)}{k_B T}\right] \\ &\overset{T\to 0}{\sim} \frac{s}{(4\pi)^{\frac{D}{2}}\Gamma\left(\frac{D}{2}+1\right)}\left\{\frac{2m[E_F - V_\perp(\mathbf{r}_\perp)]}{\hbar^2}\right\}^{\frac{D}{2}} \end{aligned} \tag{2.18}$$

Comparing this equation with the column density (2.17), we find that for any transverse position $\mathbf{r}_\perp$, there is a direct relationship between the measurable column density and the total density at $x_{\rm probe} = 0$. At $T = 0$ in particular, we can use the asymptotic

behavior of the Fermi-Dirac integrals to derive an explicit relationship between the two:

$$n(\mathbf{r}_\perp, x_{\text{probe}} = 0) = \frac{s^{\frac{1}{D+1}}}{\Gamma\left(\frac{D}{2}+1\right)} \left[\frac{\Gamma\left(\frac{D+3}{2}\right)}{2\pi}\right]^{\frac{D}{D+1}} \left[\frac{n_{\text{col}}(\mathbf{r}_\perp)}{a^2}\right]^{\frac{D}{D+1}}. \tag{2.19}$$

For a $D = 3$ sample with $s = 2$ spin states, this reduces to

$$n(x, y, z = 0) = \left(\frac{512}{81\pi^5}\right)^{1/4} \left[\frac{n_{\text{col}}(x, y)}{a^2}\right]^{3/4} \tag{2.20}$$

where the probe axis was chosen to be the z-axis.

The LDA is an incredibly powerful tool for studying the local equation of state of trapped Fermi gases, and offers a convenient means of performing thermometry on degenerate Fermi gases. This will be discussed and expanded upon in Sec. 4.4.

2.1.2. Ring-Shaped Traps

Simplified Ring Trap. The density of states integral (2.9) can be readily evaluated for certain potentials. In most of our experiments, we employ potentials with cylindrical symmetry, such that $V(\mathbf{r}) = V(r, z)$ with r and z the distance from the symmetry axis and axial coordinate, respectively. Furthermore, our potentials typically employ a tight vertical confinement, such that the potential is separable in regions of the trap and the axial component is roughly harmonic. While in general our trapping potentials are extended and quite complex, we can gain insight into several general thermodynamic features of our systems by applying our results from the previous subsection to the specific case of a Gaussian ring-shaped trapping potential on top of a harmonic axial confinement.

$$V(\mathbf{r}) = V_0 \left[1 - e^{-2\left(\frac{r-R}{w}\right)^2}\right] + \frac{1}{2} m\omega_z^2 z^2 \equiv V_r(r - R) + V_z(z) \tag{2.21}$$

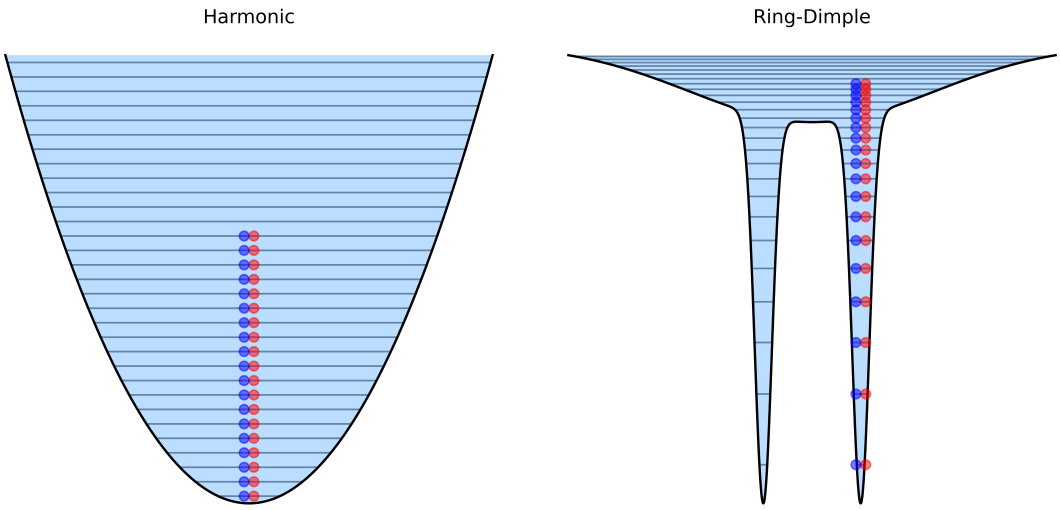

Figure 2.1: Qualitative visual depiction of the discrete energy levels in a harmonic (left) and experimentally-relevant ring-dimple (right) trap. The cylindrically-symmetric potentials are depicted via a 1D slice along trap center. Fermions in two distinct spin states (red/blue circles) populate the energy levels up to the Fermi energy. While the levels are equally spaced in the harmonic trap, anharmonicities and a weakening in the curvature of the ring-dimple potential cause a decrease in the discrete energy level spacings, and thus an increase in the density of states, towards higher energies.

The ring depth V_0 is related to the experimentally-measurable radial trapping frequency ω_r via $V_0 = \frac{1}{4}m\omega_r^2 w^2$, where w is the $1/e^2$ radius of the ring. The axial potential $V_z(z)$ is characterized by its frequency ω_z. In certain limits, it can be safe to approximate the radial potential as a parabola centered a R as $V_r(r-R) = \frac{1}{2}m\omega_r^2(r-R)^2$. This is typically the case for trapped Bose gases that condense into a small region about the potential minimum, and i.e. for wide pancake-shaped dipole traps used routinely to trap both fermions and bosons. However, we will refrain from the harmonic approximation in subsequent analysis as our experiments often operate in a regime where the anharmonic regions of the traps are occupied. Fig. 2.1 shows a qualitative depiction of the distinction between a harmonic trap and the so-called ring-dimple potential landscape typically employed in the studies performed in this thesis and discussed in detail in Sec. 4.4.

The density of states in 3D, given by (2.9) can then be written explicitly for the potential (2.21) as

$$\begin{aligned} g_3(E) &= 2\frac{m}{\pi\hbar^3}\int_{R-r_F}^{R+r_F} dr\ r \int_{-z_F(r)}^{z_F(r)} dz\sqrt{2m[E - V_r(r-R) - V_z(z)]} \\ &= 2\sqrt{\frac{\pi}{2}}\frac{mRwV_0}{\hbar^3\omega_z}K(\beta) \equiv \frac{2\sqrt{2}N_0}{V_0}K(\beta) \end{aligned} \tag{2.22}$$

where the integration (in cylindrical coordinates) is taken over the Fermi volume bounded axially by $z_F(r) \equiv \sqrt{\frac{2}{m\omega_z^2}[E - V_r(r-R)]}$ and radially by $r_F \equiv \frac{w}{\sqrt{2}}\beta$. Here $\beta \equiv \sqrt{\ln\left(\frac{1}{1-E/V_0}\right)} \in [0,\infty]$ is a dimensionless function of the energy that interpolates between the harmonic ($E \ll V_0$) and anharmonic ($E \approx V_0$) regimes. The dimensionless function

$$K(\beta) \equiv \mathrm{Erf}(\beta) - \frac{2}{\sqrt{\pi}}\beta\exp\left(-\beta^2\right) \tag{2.23}$$

lies between 0 and 1. $N_0 \equiv \frac{mRwV_0^2\sqrt{\pi}}{2\hbar^3\omega_z} = \frac{\sqrt{\pi}}{2}\left(\frac{Rw}{a_z^2}\right)\left(\frac{V_0}{\hbar\omega_z}\right)^2$ is the number of available free-fermion states in the ring. It has a simple geometric interpretation: If the average atom extent is given by a_z, we can fit $\sim Rw/a_z^2$ atoms in the ring trap for a given axial energy level, where Rw is the transverse area of the ring. There are $\sim \left(\frac{V_0}{\hbar\omega_z}\right)^2$ axial states, so $N_0 \sim \frac{Rw}{a_z^2}\left(\frac{V_0}{\hbar\omega_z}\right)^2$. For the case of the Gaussian ring, the geometric scaling factor is $\sqrt{\pi}/2$, while the scaling is exact for a box-like ring trap.

We find N by integrating eq. (2.22) up to E_F, which interestingly still admits a closed form solution:

$$\begin{aligned} N &= \frac{mRwV_0^2\sqrt{\pi}}{2\hbar^3\omega_z}\mathcal{K}(\beta|_{E_F}) \\ &\equiv N_0\mathcal{K}(\beta_F) \end{aligned} \tag{2.24}$$

where the dimensionless function

$$\mathcal{K}(\beta) \equiv \mathrm{Erf}(\sqrt{2}\beta) - 2\sqrt{2}\exp\left(-\beta^2\right)\mathrm{Erf}(\beta) + 2\sqrt{\frac{2}{\pi}}\beta\exp\left(-2\beta^2\right) \tag{2.25}$$

is again bounded between 0 and 1. This equation can be inverted numerically to find $E_F(N)$, but admits a simple closed form solution in the harmonic ($\beta_F \approx 0 \rightarrow N \ll N_0$) limit, where $\mathcal{K}(\beta_F) \approx \frac{16}{15}\sqrt{\frac{2}{\pi}}\left(\frac{E_F}{V_0}\right)^{5/2}$. Thus,

$$\frac{E_F}{V_0} \approx \left(\frac{15}{16}\sqrt{\frac{\pi}{2}}\frac{N}{N_0}\right)^{2/5} \quad \text{(Harmonic approximation)} \tag{2.26}$$

We can equivalently express this in terms of trapping frequencies as

$$\frac{E_F}{\hbar\Omega} = \left(\frac{15N}{16}\right)^{2/5}\left(\frac{\bar{\omega}}{\Omega}\right)^{4/5} \tag{2.27}$$

where $\Omega \equiv \hbar/(2mR^2)$ is the angular frequency associated to motion around the ring and $\bar{\omega} \equiv \sqrt{\omega_r\omega_z}$ is the geometric mean trapping potential.

It is interesting to note that, in this simple potential, there is a finite capacity for the ring to hold fermions. For trap parameters typical of our experiment, we find the dimple capacity $N_0 \sim \mathcal{O}(10^3)$. While the actual experimental trapping geometry can be much more complicated, the dimple capacity N_0 sets a scale for the number of atoms confined to the ring-shaped region of highest density. The average dimple (2D) density $n_0 \equiv N_0/(2\pi Rw) \sim V_0^2/\omega_z$. This implies that one can more densely pack fermions into the ring by either increasing the ring depth or decreasing the vertical confinement. The former makes intuitive sense; A deeper ring can hold more atoms. The latter can be understood intuitively by the fact that atoms are "squeezed" out of the ring dimple when the trap is compressed vertically. This axial squeezing leads to a greater spacing between axial energy levels, and thus a decrease in the density

of ring-bound states.

We now discuss the experimentally relevant case where the Fermi energy is larger than the ring dimple depth V_0. This can be the case when, for example, there is a broad radial confinement superimposed upon the ring potential, as was the case in the experiments performed in [31, 32]. We can account for this weak radial confinement by adding a potential of the form $V_s(x,y) = \frac{1}{2}m(\omega_x^2 x^2 + \omega_y^2 y^2)$ to (2.21), where $\omega_x \approx \omega_y$ are the transverse trap frequencies. Because the confinement is weak, we can attempt to modify the ring density of states described previously by adding a term that accounts for any spill-over into the broad sheet-like potential. Namely, we approximate

$$g_3(E) = \frac{2\sqrt{2}N_0}{V_0}K(\beta)\Theta(V_0 - E) + \frac{2(E - \frac{1}{2}m\omega_x\omega_y R^2)^2}{(\hbar\bar{\omega})^3}\Theta(E - V_0) \tag{2.28}$$

where $\bar{\omega}^3 = \omega_z\omega_y\omega_z$ is the sheet geometric mean trap frequency and Θ is the Heaviside function and the second term describes the density of states of the $(3D)$ sheet trap. Because the sheet may be slightly anisotropic, the ring potential minimum may vary azimuthally. We thus take the geometric mean of the sheet transverse frequencies to approximate the slightly elliptical trap by a circular trap with the same integrated power. Then, we set the potential zero at the ring minimum $r = R$ and $z = 0$. This makes $V(r = 0) \approx -\frac{1}{2}m\omega_x\omega_y R^2$ for $w \ll R$. Thus, the full potential can be approximated as

$$V(r,z) \approx V_0\left[1 - e^{-2\left(\frac{r-R}{w}\right)^2}\right] + \frac{1}{2}m\omega_z^2 z^2 + \frac{1}{2}m\omega_x\omega_y(r^2 - R^2) \tag{2.29}$$

We find a closed form solution for the Fermi energy now by integrating the modified $g_3(E)$ up to a Fermi energy $E_F \geq V_0$, making use of the fact that the integral over

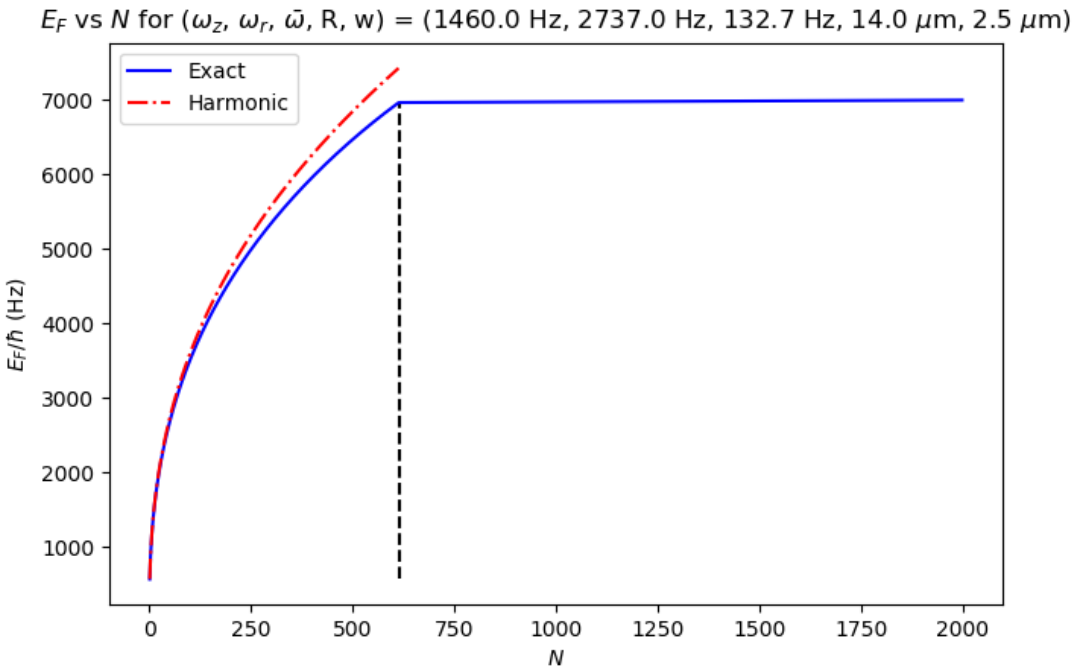

Figure 2.2: Plot of 3D Fermi energy in the combined ring plus sheet trap, where the effect of the weak radial sheet confinement at $\bar{\omega} = 132.7$ Hz, is included. Vertical dashed line is the number N_0 (≈ 613) of available ring bound states.

the first term simply gives N_0:

$$E_F = \frac{1}{2}m\omega_x\omega_y R^2 + \left(V_0 - \frac{1}{2}m\omega_x\omega_y R^2\right)\left[1 + \frac{3}{2}(N - N_0)\left(\frac{\hbar\bar{\omega}}{V_0 - \frac{1}{2}m\omega_x\omega_y R^2}\right)^3\right]^{1/3} \tag{2.30}$$

Figure 2.2 shows the plot of 3D Fermi energy versus atom number for the experimental configuration used. Fermi energies below $V_0 \approx 7$ kHz are computed by numerically inverting (2.24), while above V_0 they are given by (2.30). Clearly, the Fermi energy remains roughly constant at V_0 for $N > N_0$ in this simplified model. This is because the ring depth is typically much greater than the energy scales associated with the broad sheet. This simplified model does not account for the incompressibility of the Fermi sea, and the density of states should be computed from the combined trap.

Numerically-modelled Ring Dimple Trap. The incompressibility of the Fermi sea at $T = 0$ means that the density of states and local Fermi energy for atoms above the ring dimple depth $V_{0,r}$ are affected by the presence of the fermions occupying the dimple. To properly quantify the density of states, one would have to carry out the integral (4.2) over the entire Thomas-Fermi region, which may extend well into the sheet region for energies $E > V_{0,r}$. This integral is typically impossible to carry out analytically for the trapping potentials utilized in the experiment, which are generally non-separable and complicated. However, one may compute the density of states numerically with knowledge of this potential. We will discuss the experimental implementation of the potential and its various components in Chap. 4.4, but for now, we will take it to consist of three main terms: A narrow ring-shaped potential, a broad circular sheet-like potential, and gravity. The inclusion of gravity is important for discussion of evaporative dynamics, and plays an important role in setting the fermion capacity for the entire trap, as we will also see in chapter 4.4.

We assume the sheet-like potential is formed from a flat Gaussian beam propagating along the y-axis, and whose width along the z-axis is small compared to the transverse width. Thus, we write

$$V_{\text{tot}}(r, z) = V_{\text{ring}}(r, z) + V_{\text{sheet}}(r, z) + mgz \tag{2.31}$$

where

$$V_{\text{sheet}}(r, z) = V_{0,s} e^{-2\left(\frac{r^2}{w_s^2} + \frac{z^2}{w_z^2}\right)} \tag{2.32}$$

and $w_s \gg w_z$. Note the difference between this potential and the simplified ring potential (2.21) discussed previously; This one has generally inseparable character. We have assumed that the sheet beam is transversely (x, y) circularly symmetric in the region of interest, despite the fact that it will become asymmetric outside of its

Rayleigh range. The ring potential V_{ring} is slightly more complicated. Since this potential is formed experimentally by projecting a ring-shaped pattern, propagating along the z-axis, onto the broad sheet, we must account for the through-focus diffraction experienced by this propagating beam to fully model its potential. If we assume that at $z = 0$ the ring comes to a sharp, unaberrated focus described by a Gaussian ring-shaped function with radius R

$$V_{\text{ring}}(r, z = 0) = V_{0,r} e^{-2\left(\frac{r-R}{w_r}\right)^2}, \tag{2.33}$$

then we can find the through-focus potential by propagating (2.33) via the angular spectrum method [33]. This method essentially decomposes the light-field, and thus the potential, at $z = 0$ into plane waves whose propagation has a simple analytic form. The resulting field at some distance z away is then obtained by summing these plane waves up, each having been modified by the Fourier-space (k_x, k_y) transfer function $h(k_x, k_y; z) = \exp\left(iz\sqrt{k_0^2 - k_x^2 - k_y^2}\right)$ associated with the monochromatic Helmholtz equation, where k_0 is a constant [34]. With the definition $\tilde{A}(k_x, k_y) = \mathcal{F}[\sqrt{V_{\text{ring}}(r, z = 0)}](k_x, k_y)$, may write

$$\begin{aligned} V_{\text{ring}}(r, z) &= \iint dk_x dk_y \tilde{A}(k_x, k_y) h(k_x, k_y; z) e^{i(k_x x + k_y y)} \\ &= \mathcal{F}^{-1}\left[\tilde{A}(k_x, k_y) h(k_x, k_y; z)\right](x, y) \end{aligned} \tag{2.34}$$

where $\mathcal{F}$ is the Fourier transform operation and the square-root of the potential is taken to properly model the propagation of the *amplitude* of the light field (as opposed to its intensity). This propagation, expressed as a pair of Fourier transforms, can be efficiently carried out numerically via a fast Fourier transform (FFT) operation. We show an example of $V_{\text{ring}}(r, z)$ computed via (2.34) in Fig. 2.3.

With the full 3D trapping potential, given by equation (2.32), one may compute

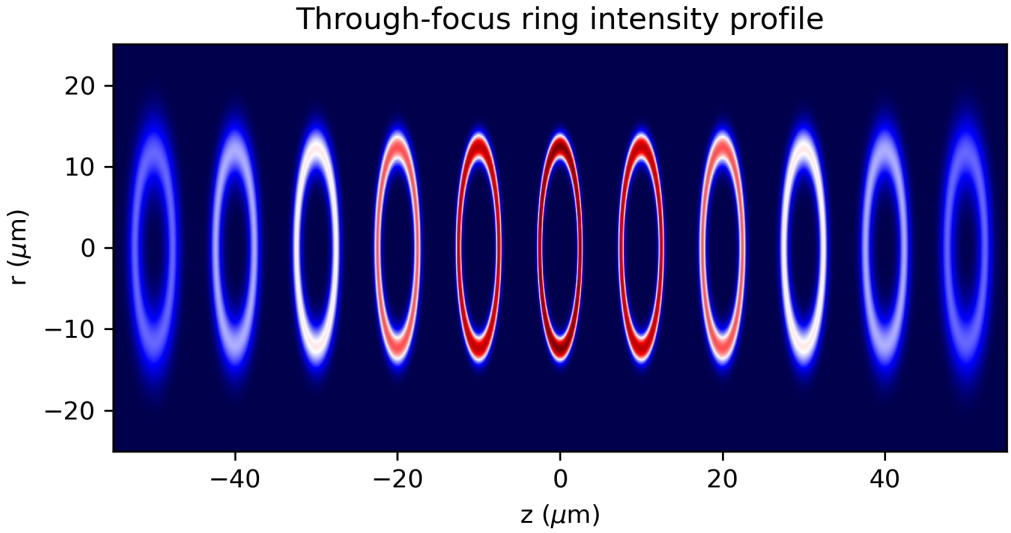

Figure 2.3: A mosaic showing the through-focus propagation of the ring beam. The ring comes into focus at $z = 0$ with a radius of 12 μm and width 2.3 μm. Interestingly, it retains its sharp focus for several tens of microns above and below the focal plane, but blurs considerably outside this range.

the density of states by numerically integrating equation (2.9), using $D = 3$. This integral can be further simplified using the cylindrical symmetry of the potential, and we can write

$$g_3(E) = \frac{(2m)^{3/2}}{\pi\hbar^3} \iint_{V_{\mathrm{tot}}(r,z)\leq E} dr dz \; r\sqrt{E - V_{\mathrm{tot}}(r,z)}. \tag{2.35}$$

We show an example of a cross-section of our model trap in Fig. 2.4, for a ring of radius 12 μm. In addition we plot the Fermi energy for atoms populating this trap, computed from the density of states (2.35) and the definition of the Fermi energy

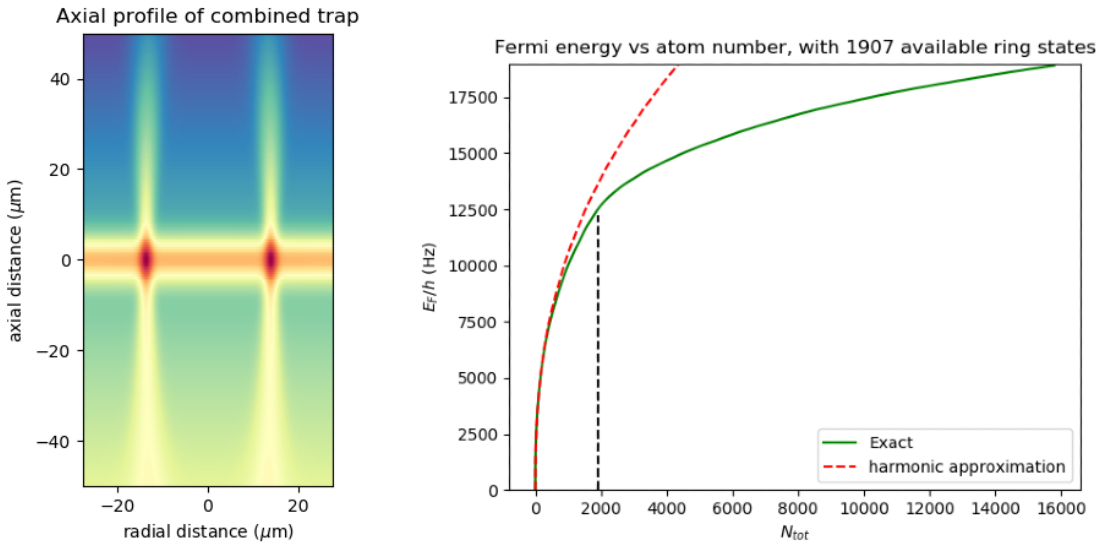

Figure 2.4: (Left) A cross-section of the combined trap including gravity along the plane $y = 0$. The ring is clearly recognized as the two dense regions, whereas gravity is responsible for the asymmetry about $z = 0$. It is notable how the ring dimple has the structure of a vertically elongated cylindrical "can", but away from the dimple the potential is flat and "washer"-like. (Right) The trap Fermi energy as a function of the total atom number (green solid line). We also show the harmonic approximation of the Fermi energy to the ring dimple minimum (red dashed line), and the dimple capacity (black vertical dashed line).

(2.11). The Fermi energy computed from a simple harmonic approximation to the trap minimum is shown for comparison, highlighting the need for a complete trap model as the ring becomes overfilled. We note that the Fermi energy, for $E_F > V_{0,r}$, doesn't plateau as it does in the crude model described by equation (2.30). We certainly notice a weaker dependence of the Fermi energy in this regime on atom number, which is a result of the vastly larger density of states in the broad sheet. However, Pauli blocking is responsible for reducing the density of states at energies $E_F > V_{0,r}$, and the Fermi energy does not plateau as strongly as it does in the crude model.

Section 2.2

BEC-BCS Crossover and Pair Superfluids

This section will discuss how interactions between pairs of ^{6}Li atoms are controlled, and how ultracold samples of fermionic ^{6}Li can be smoothly and reversibly tuned between two distinct limits using this feature. The first is the molecular BEC (mBEC) limit of tightly bound ^{6}Li dimers, which exhibit bosonic charcater due to their large binding energies. The second is the limit of weakly bound Cooper pairs, where signatures of Bardeen-Cooper-Schrieffer (BCS) superfluidity emerge from strong correlations between pairs of fermions in equal and opposite momentum and spin states. The crossover between these two limits is described by a variational wavefunction ansatz that smoothly interpolates between these two limits and provides the means to compute the relevant many-body thermodynamic quantities as the interactions are tuned.

2.2.1. Feshbach Resonances

The Feshbach resonance, first studied by Herman Feshbach in the context of nuclear reactions, is routinely used to modify the scattering properties of ultracold atoms [35–39]. With such modifications, ultracold atoms exhibiting a useful and controllable Feshbach resonance can be made to interact more or less strongly with eachother, and with either attractive or repulsive character. In ^{6}Li, a broad Feshbach resonance exists, which allows interactions to be tuned precisely and controllably over an extremely large range. This is perhaps the most exemplary feature of ^{6}Li as an ideal species for ultracold fermion experiments.

Feshbach resonances occur when the energy of two atoms, scattering in free space, is brought into degeneracy with the energy of a certain bound molecular state. In most cases, the potential energy landscape experienced by two interacting atoms

depends on the internal structure of the atoms. Scattering in the so-called open channel occurs for atoms in a certain internal configuration, which gives rise to a potential energy landscape that is accessible by energy conservation. The potential energy in this channel asymptotically approaches 0 at large inter-atomic separation, and scattering in this channel can occur when the two-atom energy $E > 0$. The so-called closed-channel potential experienced in a different internal state, on the other hand, asymptotically approaches a potential energy $V^{\infty}_{\text{closed}} > E$ at large separations, and is thus inaccessible to the outgoing scattering pair. A non-zero coupling between one or more bound states in the closed-channel and the open channel continuum modifies the scattering properties of the two interacting atoms. By reformulating the scattering problem entirely in the open channel by means of an effective scattering potential, one finds that the scattering length can be affected by changes to the energy difference between the free atoms and molecular bound states. Typically, this energy difference can be tuned by an external magnetic field, as the magnetic moments of the closed and open channel states are different.

Using a simple model which assumes only a single relevant bound molecular state in the closed channel, one can derive an expression for the scattering length as a function of the external magnetic field using an effective potential model [40]. The result is that the s-wave scattering length, with encodes all the relevant scattering properties in the low-energy (ultracold) regime, can be written as

$$a = a_{\text{bg}} \left(1 - \frac{\Delta B}{B - B_0} \right) \tag{2.36}$$

where B is the magnetic field. ΔB is the width of the resonance and a_{bg} is the off-resonance background scattering length, each of which depends on the atomic details. Some important observations of (2.36) are that the scattering length can be tuned from negative (attractive) to positive (repulsive) values, and that the scattering

length diverges at the Feshbach resonance field $B = B_0$. As we will soon discuss, this tunability can allow the investigation of many interesting features of ultracold fermions in a many-body setting.

In the case of ultracold ^{6}Li, scattering occurs between atoms in the lowest-energy hyperfine states $|F, m\rangle = |1/2, 1/2\rangle$ and $|F, m\rangle = |1/2, -1/2\rangle$, referred to as $|1\rangle$ and $|2\rangle$, respectively. The open and closed channel potentials are distinct due to the different interatomic interactions between the triplet $|1\rangle|1\rangle$ and singlet $|1\rangle|2\rangle$ states, respectively, and the hyperfine interaction couples the two channels. The background scattering length and the resonance width are $a_{\rm bg} = -1405a_0$, where a_0 is the Bohr radius and $\Delta B = 300$ G, respectively. More detailed scattering properties of ^{6}Li (and of ^{6}Li in general) can be found in [41]. We note that the s-wave scattering length across the Feshbach resonance can be precisely measured via radio-frequency dissociation spectroscopy [42] .

2.2.2. BEC-BCS Crossover

In an ultracold gas of fermions, pairing can typically occur between atoms within different hyperfine states. The nature of this pairing, however, depends fundamentally on the nature of the interactions, and more specifically the scattering length. Using Feshbach resonances to tune the interparticle scattering properties between the attractive and repulsive limits, both the two-body and many-body physics can be altered in a controllable way. Typically, the strength of interactions is parameterized by $(k_F a)^{-1}$, where k_F is the Fermi wave-vector. On the weakly repulsive (BEC, $(k_F a)^{-1} \gg 0$) side of the Feshbach resonance, one or more bound states in the interatomic potential exist in 3D free space, and two fermions can form a bound molecule at some energy $\epsilon_B \ll 0$. These molecules are tightly bound and exhibit bosonic character, and can thus undergo Bose-Einstein condensation. On the weakly attractive (BCS, $(k_F a)^{-1} \ll 0$) side, pairing is a many-body effect in 3D and happens

most robustly in momentum space; Two fermions with opposite spin and momenta can form Cooper pairs. These pairs can condense due to the presence of off-diagonal long-range order (ODLRO) in the pair correlation function [43]. Furthermore, the existence of the superfluid phase in this limit is a direct consequence of the finite pair energy gap required to break a Cooper pair into its constituent fermions. On the resonance where the scattering length diverges, the system is in the so-called unitarity regime. Here, the only relevant length scale in the (uniform) system is the interparticle spacing $n^{-1/3}$, and thermodynamic properties of the system depend functionally only on the ratio of the system temperature to the Fermi temperature, T/T_F. The BEC and BCS regimes, while seemingly distinct, are actually connected by a smooth crossover [44]. Just beneath the Feshbach resonance, the bound state energy disappears as $\epsilon_B = \hbar^2/(ma^2)$; Pairing is actually quite fragile despite the diverging (positive) scattering length.

Crossover Wavefunction. In mean-field BCS theory, the ground state wavefunction takes the form

$$|\Psi_{\mathrm{BCS}}\rangle = \prod_{\mathbf{k}} (u_{\mathbf{k}} + v_{\mathbf{k}} c^{\dagger}_{\mathbf{k},\uparrow} c_{-\mathbf{k},\downarrow})|\mathrm{vac}\rangle \tag{2.37}$$

in which $u_{\mathbf{k}}$ and $v_{\mathbf{k}}$ are the coefficients of the Bogoliubov transformation, $c^{\dagger}_{\mathbf{k},\sigma}$ and $c_{\mathbf{k},\sigma}$ are the creation and annihilation operators for fermions in momentum state $\mathbf{k}$ and spin state σ ($=\uparrow,\downarrow$), and $|\mathrm{vac}\rangle$ is the vacuum state. This BCS wavefunction is derived from the pair wavefunction product state ansatz which minimizes the mean-field free energy of the interacting system. This pair wavefunction describing two particles at positions $\mathbf{r}_1$ and $\mathbf{r}_2$ in states $\uparrow$ and $\downarrow$ is defined as

$$\phi(\mathbf{r}_1 - \mathbf{r}_2) = \langle \Psi_{\mathrm{BCS}}|\hat{\Psi}^{\dagger}_{\uparrow}(\mathbf{r}_2)\hat{\Psi}^{\dagger}_{\downarrow}(\mathbf{r}_2)|\Psi_{\mathrm{BCS}}\rangle \tag{2.38}$$

where $\hat{\Psi}^{\dagger}_{\sigma}(\mathbf{r})$ is the fermionic field operator for position $\mathbf{r}$. The full coordinate-space respresentation of the many-body wavefunction is then built up from antisymmeterized products of these two-particle functions. The full BCS wavefunction, while mean-field in nature, smoothly connects the thermodynamic properties of the interacting Fermi system throughout the BEC-BCS crossover. Furthermore, by virtue of the variational ansatz itself, a macroscopic number of pairs can occupy the same quantum state with pair wavefunction ϕ. This hints at the possibility of forming a coherent many-body object from these pair states, in line with the notion of a condensate or order parameter, although the nature of this condensate again depends on the interaction regime. Indeed, it can be shown that off-diagonal long range order, the signature of condensation, exists below a certain critical temperature that smoothly varies across the BEC-BCS crossover, and reaches a maximum value near the Feshbach resonance. In this way, condensates of molecules, Cooper pairs, and more exotic pairs that exhibit a qualitative mixing of real and momentum space pairing, exist and can be accessed using the tunable interactions in ^{6}Li.

Section 2.3

The Superfluid Transition

2.3.1. Order Parameter

It was shown in [44] that below some interaction-dependent critical temperature T_c the ODLRO in the pair correlation function that signifies the presence of a condensate is non-zero. In the language of second-order phase transitions, there exists a field - the order parameter- that is zero in the "disordered" phase at $T > T_c$ and grows in magnitude into the ordered phase $T \leq T_c$. The order parameter in particular associated to a superfluid transition of fermionic ^{6}Li is the bosonic field ψ describing a pair condensate. Above the Feshbach resonance, pairing is a many-body effect. In

the weakly attractive (BCS) limit in particular, this pairing typically occurs between states of equal and opposite momenta, and of opposite spin [4]. These so-called Cooper pairs exhibit a strong delocalization of their relative separation, as pairing in this limit predominantly occurs between fermions in a narrow momentum-space shell around the Fermi surface. Cooper pairs may display bosonic character in certain limits and can form a condensate. As mentioned above, the presence of ODLRO which signifies the existence of a condensate shows up in the Cooper pair correlation function. This macroscopically-occupied state described by the wavefunction ψ is directly proportional to the BCS pairing field or gap Δ, which is the energy cost to break a Cooper pair into its constituent fermions.

As the order parameter can be represented by a coherent, macroscopically occupied object $\psi(\mathbf{r})$, certain mathematical restrictions must be placed on the values that $\psi(\mathbf{r})$ can take to ensure it is physically allowable. The order parameter can therefore be represented by some single-valued, analytic and complex-valued function, and can be written in density-phase form as $\psi(\mathbf{r}) = \sqrt{n(\mathbf{r})}\exp[i\phi(\mathbf{r})]$. The flow velocity associated to the order parameter is given by $\mathbf{v}(\mathbf{r}) = \hbar\nabla\phi(\mathbf{r})/m$. Imposing single-valuedness on ψ means that, for some closed contour $\mathcal{C}$, the net phase $\Delta\phi$ accumulated around this contour must be quantized in units of 2π. The average flow speed $\bar{v} = \hbar\Delta\phi/(mL_{\mathcal{C}})$ around this contour is therefore also quantized, in units of $v_0 \equiv 2\pi\hbar/(mL_{\mathcal{C}})$, where $L_{\mathcal{C}}$ is the length of the contour. In particular, we have

$$\Delta\phi = \oint_{\mathcal{C}} \nabla\phi \cdot d\mathbf{s} = 2\pi w \tag{2.39}$$

$$\bar{v} = \frac{\oint_{\mathcal{C}} \mathbf{v} \cdot d\mathbf{s}}{\oint_{\mathcal{C}} |d\mathbf{s}|} = v_0 w \tag{2.40}$$

with $d\mathbf{s}$ the line element of the contour and $w \in \mathcal{Z}$ is the so-called *winding number* of the order parameter. Deforming the closed contour $\mathcal{C}$ does not affect the winding

number except in extraordinary cases; Only when the contour intersects a point $\mathbf{r}_0$ where the superfluid density $n(\mathbf{r}_0)$ becomes zero does the phase $\phi(\mathbf{r}_0)$ become locally undefined and the winding number can change abruptly. In a thermodynamic context, there is a free-energy barrier associated with these states of persistent and metastable superfluid flow with non-zero w. These persistent currents are not only relevant to theoretical studies of quenched ring-shaped superfluids, but are oftentimes the fundamental objects associated to potential neutral atom quantum computing applications such as atomtronics [24, 45].

2.3.2. Winding Numbers on Ring-Shaped Contours

In general, the winding number is a functional of the complex, single-valued order parameter defined on some closed contour in real space. The order parameter represents a complex mapping from this contour onto the complex plane. There exist many equivalent definitions of the winding number. The most visually intuitive definition counts the number of times the order parameter wraps around the origin, and back onto itself, as the contour is traversed. As the focus of much of the work in this thesis is on ring-shaped geometries, we specialize to the case of a ring-shaped contour parameterized by angle θ. We use the polar representation to write

$$\psi(\theta) = \sqrt{n(\theta)}e^{i\phi(\theta)} \tag{2.41}$$

where $n(\theta+2\pi) \equiv n(\theta) \geq 0$ and $\phi(\theta+2\pi) \equiv \phi(\theta)+2\pi w$, defining the integer winding number w. To compute w directly, we may logarithmically differentiate and then integrate (2.41) around the ring, using $\int_0^{2\pi} d\theta\phi'(\theta) = 2\pi w$, to find

$$w = \frac{1}{2\pi i}\int_0^{2\pi} \frac{\psi'(\theta)}{\psi(\theta)}d\theta = \frac{1}{2\pi i}\oint_{\Gamma(\psi)} \frac{d\psi}{\psi} \tag{2.42}$$

where in the second equality $\Gamma(\psi)$ represents the closed curve traced out by ψ in the complex plane as θ is advanced by 2π. In this equation we have assumed that $n(\theta) > 0$, or else the phase (at one or more points) and thus winding number would become undefined. From the residue theorem, (2.42) shows that the winding number is non-zero whenever the closed contour traced by ψ encloses the simple pole at the origin. Additionally, (2.42) shows that the winding number is a *functional* of the complex-valued order parameter and the contour on which it is evaluated. We can recast the definition of the winding number by using the Fourier decomposition of ψ. Namely, we write

$$\psi(\theta) = \sum_{\ell} c_\ell e^{i\ell\theta} = \sum_{\ell} c_\ell z^\ell(\theta) \tag{2.43}$$

where $z \equiv \exp(i\theta)$. By inserting this expansion into (2.42), and using $d/d\theta = izd/dz$, we may write

$$w = \frac{1}{2\pi i} \oint_{|z|=1} dz \frac{d}{dz} \log \psi \tag{2.44}$$

Now, using the argument principle of complex analysis, evaluation of the integral (2.44), which contains a logarithmic derivative of ψ, is obtained by counting the number of roots (with multiplicity) of the complex polynomial

$$\psi(z; \{c_\ell\}) \equiv \sum_{\ell} c_\ell z^\ell \tag{2.45}$$

whose magnitudes are less than 1 and subtracting off the order of the largest pole in the expansion (2.43). For the finite-mode expansion

$$\psi(z; \{c_\ell\}) = \sum_{\ell=-\ell_c}^{\ell_c} c_\ell z^\ell, \tag{2.46}$$

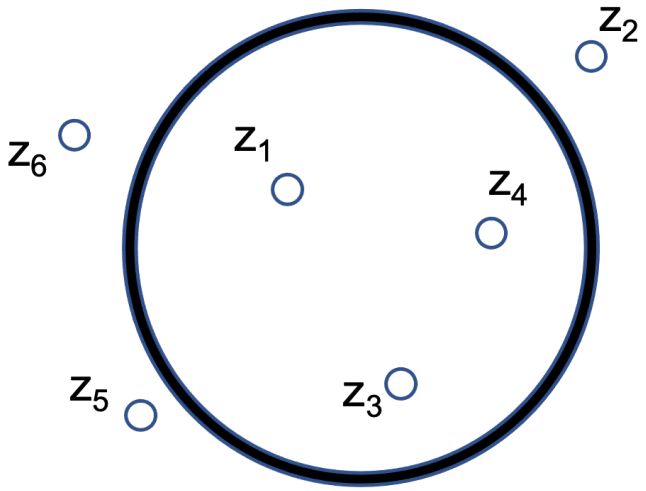

Figure 2.5: An example showing how the winding number is computed in the Fourier space representation. For some single-valued function, the winding number is found as the number of roots of the complex polynomial (2.45) lying within the unit circle, with the order of the largest pole subtracted off.

with $\ell_c \geq 0$ we have an explicit equation

$$w = \sum_{n=1}^{2\ell_c+1} \Theta(1 - |z_n|) - \ell_c \tag{2.47}$$

Here, z_n with $n \in [1, 2l_c + 1]$ denotes a root of (2.45) and Θ is the step function. The simplest example of functions with well-defined winding numbers are the complex exponentials $\psi_\ell^{(1)}(z) \equiv z^\ell$. Taking WLOG $\ell \geq 0$, the roots of these functions occur at $z = 0$ with multiplicity ℓ, and thus $\psi_\ell^{(1)}(z)$ has trivially winding number ℓ.

The simplest non-trivial examples of functions with well defined winding number are those composed of two modes. It suffices to study a function of the form

$$\psi_\ell^{(2)}(z) \equiv c_0 + c_\ell z^\ell \tag{2.48}$$

with $\ell \geq 1$. This function has a root of multiplicity ℓ at $z^\ell = -c_0/c_\ell$. Furthermore, this root lies within the unit circle when $|c_0| < |c_\ell|$. The winding number of the

function (2.48) is therefore determined by the ratio $|c_0/c_\ell|$:

$$w = \begin{cases} \ell, & \left|\frac{c_0}{c_\ell}\right| < 1 \\ 0, & \left|\frac{c_0}{c_\ell}\right| > 1 \end{cases} \tag{2.49}$$

To go beyond simple one or two-mode functions means solving an order $n \geq 2$ polynomial equation and finding conditions on the coefficients c_ℓ that place the roots within the unit circle. This is a very challenging task analytically, but we note that numerically this is very straightforward, as polynomial roots can be efficiently computed using i.e. Newton's method. In general, the winding number of a many-mode expansion will not be given by the dominant Fourier component, as is the case in the two-mode expansion; It will depend in a complicated manner on the magnitudes and phases of each of the Fourier components. Equivalently, a given winding number w may still be observed even if the $c_{\ell=w}$ mode is not the dominant one.

Finally, it is insightful to ask when happens when one or more of the complex roots lies precisely on the unit circle $|z| = 1$. In this case, the argument principle cannot be directly applied to (2.44), and the winding number becomes undefined. In real space, the presence of one or more roots lying on $|z| = 1$ implies that the order parameter vanishes at one or more points around the ring. This in turn creates one or more phase singularities that cause the winding number to become ill-defined. In a dynamical setting where the order parameter varies in time, these "phase slip" events, where the order parameter locally vanishes at one or more points, provide a means for the topologically protected winding number to change its value, even though the probability of observing such an event at any given time is vanishingly small. One should note the analogy between a complex root of the order parameter crossing the unit circle and a vortex migrating across the ring. Simple examples of single-valued functions with ill-defined winding numbers are the elementary trigonometric

functions $\sin(\ell\theta)$ and $\cos(\ell\theta)$, with $|\ell| \geq 1$. Clearly, these functions have zeroes at at least one position on the ring, and their complex Fourier expansion $\psi(z) \sim z^{\ell} \pm z^{-\ell} = z^{\ell}(1 \pm z^{-2\ell})$ gives roots lying on $|z| = 1$, implying that their winding numbers are undefined.

Chapter 3

The Experimental Apparatus for ^{6}Li

This chapter will outline some of the architecture of the experimental apparatus as well as techniques used to conduct experiments on ultracold fermionic ^{6}Li. We point to the Ph.D thesis of Yanping Cai as a thorough and detailed reference to the experimental apparatus. The details of the 2D magneto-optical trap and its performance will be discussed in greater detail in the Ph.D thesis of Parth Sabharwal from our group. We will now expand the discussion of the pair of custom microscope objectives and the digital micromirror device (DMD) and its accompanying software control implementation. Although used in the previous work of Yanping Cai to some extent, we describe these experimental components in greater detail in this section as they played a central role in the outcome of experiments described in this work.

Section 3.1

Custom Microscope Objectives

Imaging objectives for ultracold atoms experiments often require high resolution, multi-element designs that are compatible with the rigid geometric constraints imposed by the experimental apparatus. Additionally, the often strict requirement of a non-conductive, non-magnetic objective housing imposes limitations on the type of materials used. We will now discuss the details of the design, assembly, and installation of the objective pair.

3.1.1. Objective Design

Typically, an ultracold atoms experiment would like to probe features of an atomic ensemble down to micron-sized scales. To achieve the necessary numerical aperture, and thus resolution, a highly curved front lens is usually required to gather light at large angles. This lens may be placed external to the cell, or, in some cases, inside the cell to enhance numerical aperture [46]. Due to potentially large aberrations introduced by this lens and the flat glass cell experiment window, additional compensation lenses are required to achieve sufficient optical performance, however. The appropriate compensation lenses typically depend on the nature of this front lens. While aspheric front lenses perform very well for on-axis field points, the point spread function rapidly degrades for even small departures from the optical axis. The compensation lenses must therefore be chosen to correct for off-axis aberrations, such as coma and astigmatism. A simple plano-convex front lens, on the other hand, will suffer greater symmetric aberrations such as spherical aberration and Petzval curvature, and will therefore benefit from compensation lenses that correct these aberrations.

We designed and tested the performance of a five-element objective using the ray tracing software OSLO, with a 75 mm focal length, 1" diameter plano-convex front

lens and a numerical aperture NA = 0.33 (See Fig. 3.1). This design was based off of a four-element long working distance objective design by Alt [47]. Notably, each element is commercially available (Thorlabs), and the non-conductive and non-magnetic housing was 3D printed using readily-available materials, offering an economic, in-house alternative to typically expensive custom objectives costing upwards of $100,000$ USD. The main body of the objective housing was designed to properly reference the desired positions of each of the lenses in the objective. Its inner diameter was chosen to be 1.1", slightly larger than the lens diameters, to allow for some small amount of play within the housing during the lens positioning. The walls of the housing were chosen to be thick enough to provide structural integrity, but thin enough to allow for a modified 3D printed Thorlabs 1" cage plate to fit around. Two 3D printed spacers were inserted to provide the necessary spacings between lenses 1 and 2, and lenses 3 and 4 (See Fig.3.1). The spacings between lenses 2 and 3 were set by a constriction in the inner diameter of the housing with an appropriately chosen length, such that the lenses rest upon the constriction at the proper separation. The cost to procure the objective components and assemble each objective was only 500 USD.

In order to mount the objective and properly interface it to the experimental apparatus, we designed a simple 3D printed objective "skirt" that allowed the objective to be interfaced with a suitably modified cage assembly system. The length of the skirt was chosen to provide the necessary 1 mm standoff between the glass cell window and the front objective plano-convex lens. Additionally, to provide a modest hermetic seal between the objective lenses and the glass cell, we epoxied a thin soft silicone ring around the base of the skirt with an inner diameter equal to that of the circular glass cell window.

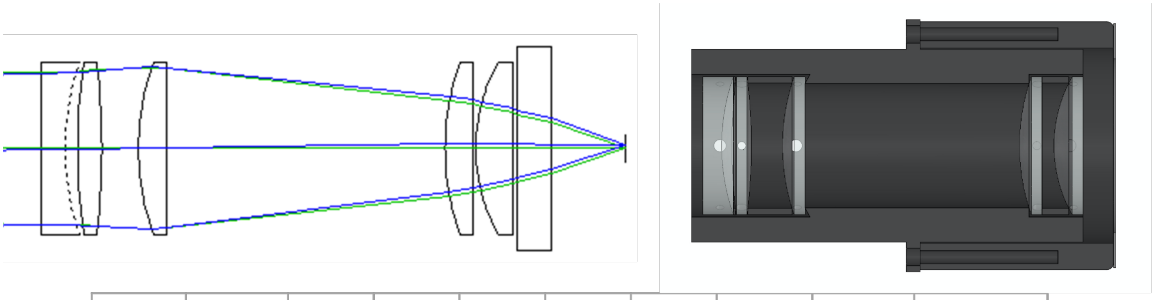

Vendor	Part #	Type	Glass	EFL	R1	R2	t_center	Diameter	Center Space
Thorlabs	LC1582-B	PCV	BK7	-75	Inf	-38.6	3.5	1"	1.4
Thorlabs	LB1676-B	BCX	BK7	100	102.4	-102.4	3.6	1"	4.37
Thorlabs	LA1608-B	PCX	BK7	75	38.6	Inf	4.1	1"	38.7
Thorlabs	LA1608-B	PCX	BK7	75	38.6	Inf	4.1	1"	.1
Thorlabs	LA1253-B	PCX	BK7	50	25.8	Inf	5.3	1"	0.88

Figure 3.1: We show the five-element objective design modelled using OSLO's ray-tracing software (top left). The top right image shows a cross-section of the objective with the 3D printed, non-conductive housing and lens-skirt attachment used for securing and mounting the objective in the experimental assembly. The lower table gives the relevant lens information.

3.1.2. Objective Assembly and Optimization

To assemble and optimize the objectives, we 3D printed the objective housing with tap holes designed for tapping 4-40 threads. For each lens in the objective, these tap holes were positioned at three equally-space distances around the circumference of the housing, and aligned to the positions of the lenses that would rest inside the housing. After threading each of these holes, we used nylon 4-40 set screws to contact the lenses inside the housing and position them appropriately. In addition to these tap holes, we included an equivalent set of slightly smaller clearance holes to be used as access points for injecting an epoxy syringe, that would be used to cement the lenses in place once positioned.

We optimized the positions of the lenses within the objective by monitoring the point spread function (PSF) on a CCD, and adjusted the positions of the lenses using the set screws on the sides of the housing. To monitor the PSF actively, we illuminanted a 10 μm pinhole with laser light generated from a source at the wavelength

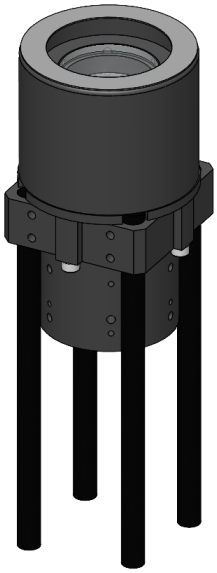

Figure 3.2: Non-conductive/magnetic objective and housing mounted in the cage assembly system, rendered using SolidWorks. The cage plate is a 3D printed modification to the Thorlabs 30 mm cageplate, with a bore diameter of 1.1" to accommodate the objective housing. The cage rods are carbon fiber and are held in place within the cage plate with set screws. The cage plate, objective housing and skirt are held together with four screws that slide through clearance holes in the cage plate and screw into threaded holes in the skirt.

of interest. The pinhole acted as a point source, which was subsequently collimated by a large focal length achromatic doublet, for the projection optical assembly. This collimated light field was large enough to uniformly illuminate the objective's front negative lens. The objective brought the beam to a focus at a distance of about 1 cm after its final plano-convex lens. Finally, we re-imaged this focal plane, and thus the objective's PSF, onto a CCD using a relay imaging system consisting of a high numerical aperture (NA) microscope objective and re-focusing tube lens. Thus, we actively monitored the objective's PSF and made adjustments to the lens positions to make the PSF as symmetric as possible. Because the lens spacings were properly set by the choice of housing and spacers, the symmetric aberrations were inherently small to begin with. Due to the possible tilt and decentrations of the lenses in the

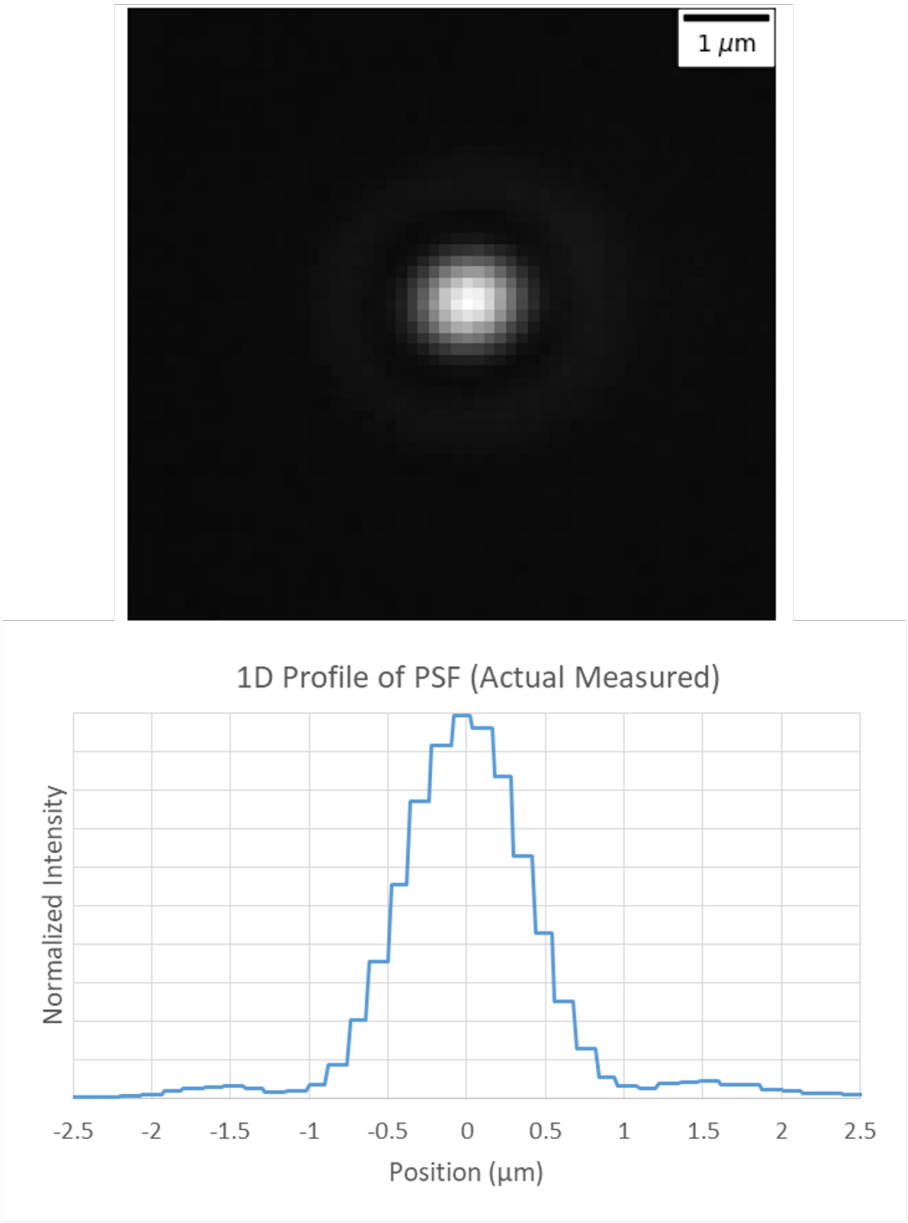

Figure 3.3: PSF of objective, optimized for 630 nm and 671 nm use. (Top) CCD-recorded image of the PSF. (Bottom) Horizontal cut of the normalized intensity profile of the above PSF. The resolution of this objective is about 1.2 μm.

housing, asymmetric aberrations dominated the PSF unless the lenses were properly positioned. When positioned properly, the PSF was highly symmetric, and corrected to a Strehl ratio of close to 1. The PSF of one of our objectives, measured on a test bench, is shown in Fig. 3.3.

Installation Process. In retrospect, the objective should have been assembled with ease-of-alignment during installation in mind, which we detail now.

While optimization on a test bench is comparatively simple, optimizing the position and orientation of the objective pair becomes substantially more complicated when installed into the main experimental apparatus. This is mainly due to the limited visual access, the tight geometric constraints (mainly set by the concentric science cell coils), and the need to simultaneously optimize the two objective positions with respect to the cell and each other. During installation, it would have been ideal to have a set of geometric references used to optimize the objective alignment. One important reference is the normal axis to the cell. This can be obtained from the back-reflection off a cell window before the objectives have been installed, and from an iris centered on a cell window, which combined give the normal axis to the cell. A second usable reference should be from the objective itself. Namely, the front planar surface of the negative lens allows a back reflection to be used as an additional reference axis. This reference axis, however, is only useful as an alignment aid if this negative lens is properly centered in the objective housing *and* the perpendicular to the normal axis to the cell.

We now outline the installation procedure assuming each objective has been constructed with the following criteria in mind:

- The objective's PSF was optimized (on the test bench) while simultaneously ensuring the objective's negative lens planar surface is parallel to the 5 mm thick fused silica window surface mimicking the cell window. This can be achieved by first finding the normal axis to the window by means of a back reflection, and then matching the back reflection off the negative lens to that axis.

- The negative lens is referenced to the exact geometric center of the objective housing. This can be achieved by mounting the objective on a cage assembly

with a pair of irises attached to it, centering the irises on the normal axis defined via the window back-reflection, and then monitoring the back reflections from both lens surfaces of the negative plano-concave lens to ensure centration on the irises.

Assuming these criteria have been met, the negative lens provides a planar surface for monitoring the back reflections of a reference beam, which by construction is referenced to the cell window normal axis, and which subsequently allows the tilt of the objective to be optimized. It also provides a geometric center to reference the objective to an iris attached to the cage assembly supporting the objective. Once the negative lens is properly positioned, it should be *fixed* while the other lens positions can be adjusted and optimized.

We install the objective into the experimental apparatus following a step-by-step procedure outlined below:

- 1) Find normal axis to the cell by sending a collimated beam down on the window and observing the back-reflection. The axis can be centered on the window by using a 3D printed cylindrical shroud with a small aperture in the center which can rest snugly around the cell window. Fix this axis with pair of sufficiently separated irises. Place another iris centered on this axis on the other side of the cell.

- 2) Carefully place the first objective over the cell. Use front lens planar surface back-reflection to align the objective tilt to the normal axis defined via 1). The throughput beam should simultaneously be centered on the downstream iris; this can be accomplished via objective translation after the tilt is fixed

- 3) Send another collimated beam the other way through the cell and installed objective, aligned with the normal axis defined in 1)

- 4) Install second objective, observing again the back-reflection off the front planar surface to ensure its tilt is correct. Simultaneously translate the objective such that the throughput beam goes through both irises aligned to the normal axis.

- 5) To ensure the objective separations are correct, first send a collimated 780 nm beam through the projection objective. Then, observe the effect of this focused beam on an atomic sample in the sheet (which is axially centered on the cell) to deduce the plane of best focus for the projection objective: Atoms will clearly be pulled to the focal point of the objective due to its high numerical aperture, when viewed from the side. Then adjust the projection objective's axial position until its focal plane coincides with the sheet. This plane should then be made to coincide with the imaging objective's plane of best focus. We do this by sending a collimated 670 nm beam through the projection objective and adjusting the position of the imaging objective until the beam emerges collimated. Due to the small chromatic focal shift in the projection objective for 670 nm light, further fine-tuning of the imaging objective's position can be made by observing the impact of the same focused resonant light on the atomic sample and adjusting until maximum atom depletion is observed. Alternatively, the imaging objective can be moved back by the same amount as the projection objective's chromatic shift between 670 nm and 780 nm (which can be measured before installation) using a calibrated micrometer stage.

We followed this installation procedure to install the pair of objectives in the experimental apparatus. To aid in the tip-tilt and translational positioning of the objective, we mounted the cage assembly supporting the objective on a tip-tilt mount, which itself was mounted onto a separate 3-axis translation stage. This mounting scheme had deficiencies in that the tip-tilt mount coupled rotational movements of

the objective to translation movements since the center of rotation was far below the glass cell. An ideal tip-tilt alignment structure would have its center of rotation in the middle of the cell (i.e. a gimbal-type mounting scheme), which is a goal of future objective mounting schemes. Nonetheless, we were able to install and position the objectives via this mounting and alignment scheme. While the performance was sufficient for the experiments details in this thesis, it was clear that a small amount of residual coma due to alignment imprecision was present. We did not have sufficient references to the optimal objective positions to make precise and informed adjustment to their positions. It is another goal of next generation objective design to have measurable references to the optimal positions and orientations.

Section 3.2

Digital Micromirror Device

In this section we will discuss how we use a digital micromirror device (DMD) to manipulate the spatial distributions of ^{6}Li atoms confined in the vertical plane of the cell.

DMDs are widely becoming to go-to for patterned optical potentials used in ultracold atoms experiments. They consist of a $\sim$ 1" rectangular megapixel array of micron-sized mirrors, each of which may be selectively toggled into either an "on" or and "off" state, which physically corresponds to the tilting of the mirror by $\pm$ 12 degrees. While a subset of mirrors on the DMD mirror array is in the "on" state, a blazed diffraction grating is formed, and light impinging on these mirrors will be diffracted into a set of orders with the pattern of the mirror subset in the "on" state projected into each. The patterns may be updated dynamically at rates exceeding 10 kHz for some DMDs, and thus sequences of patterns may be projected with each individual pattern crafted by the user. We note that when unpowered, and transiently,

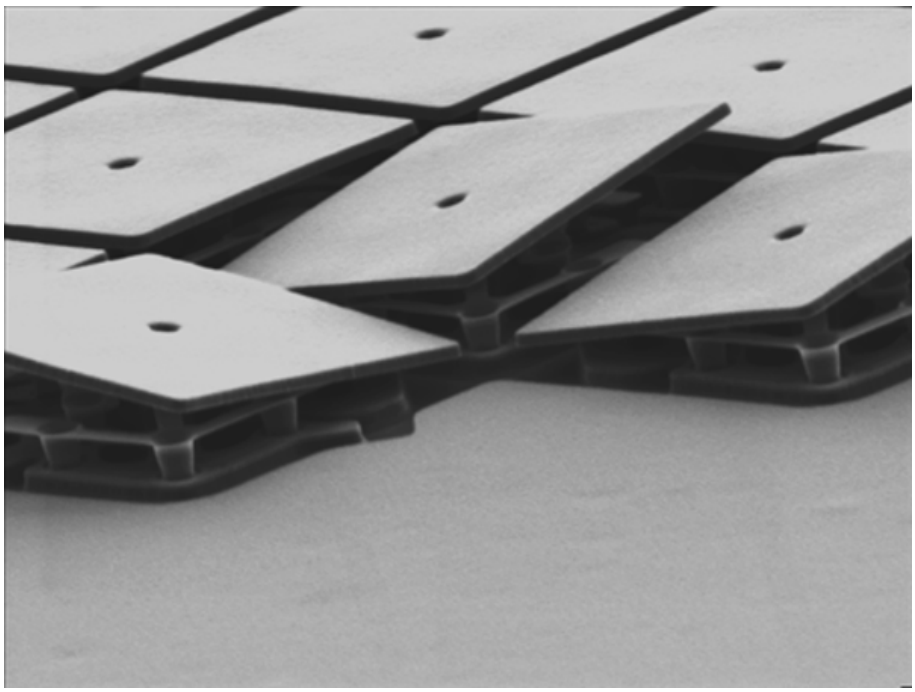

Figure 3.4: Credit: Texas Instruments. A photomicrograph showing a small number of the micron-scale mirrors on the DMD and each of their available states (on, off, and flat).

mirrors can exist in a third "flat" and untilted state.

Patterns are loaded onto the DMD as bitmap arrays of the native DMD pixel array size, each consisting of zeros and ones corresponding to inactive and active mirrors, respectively. We have written Python code to automatically generate and save commonly-used pattern bitmaps to appropriately-named file paths, which are then called during scripted experimental execution to generate desired pattern sequences.

3.2.1. Grey-Scale Projection

While incredibly versatile in the ability to produce sequences of arbitrary patterns, DMDs are binary in nature, as the micro-mirrors only operate in an on or off state. Grey-scale intensity distributions are possible to create, however, by utilizing the finite resolution of the projection optics. As long as the projection optics are unable to resolve a small block of DMD mirrors, then one can control the intensity of a region

projected from the DMD by varying the number of active mirrors within that small block. For instance, if the resolution limit of the projection optics in its focal plane corresponds to an $N \times N$ block of DMD mirrors (i.e. in the object plane), we can write

$$MN\Delta x \equiv \text{res} \tag{3.1}$$

where M is the projection optics demagnification factor and Δx is the (square) mirror pitch. Thus the projection optics will project this block of mirrors to an airy disk with radius res in the focal plane. As long as $N > 1$, then the peak intensity of this Airy disk can be controlled to a relative precision of $1/N^2$. For the parameters used in the experiment, we have $M \approx 1/10$, $\Delta x = 7.6$ μm and res $= 1.5$ μm, giving $N = 2$. Thus, by controlling the number of active mirrors in 2×2 blocks, we may create grey-scale intensity distributions with 2-bit precision.

3.2.2. Floyd-Steinberg Dithering

In order to generate and project grey-scale intensity distributions, one must selectively activate a certain number of mirrors in the resolution blocks defined in equation (3.1) in a spatially dependent manner. The most common way to accomplish this algorithmically is to use a dithering algorithm that converts an 8-bit grey-scale image into a binary image that approximates the original image when convolved with the finite resolution of the projection optics. The most commonly used dithering algorithm is the Floyd-Steinberg dithering algorithm, which in an error diffusion algorithm that shunts the binary quantization error onto neighboring pixels [48]. Essentially, by adaptively alternating between zeros and ones, depending on the desired local intensity, the dithering algorithm can achieve an approximation to the desired grey-scale image with precision determined the projection optics' resolution and demagnification.

3.2.3. Optical Potential Feedback

Oftentimes, the desired potential is smooth and flat, i.e. a smooth ring or box. Various factors, such as magnetic field curvatures, optical aberrations, and intensity variations in the DMD illumination beam, can cause the actual in-plane potential experienced by the atoms to deviate from the desired potential. Using the adaptive Floyd-Steinberg dithering algorithm, one can generate a larger set of optical potentials using the DMD that extend beyond binary intensity distributions. In particular, one can create tailored optical potentials with spatially-dependent intensities for the transverse atomic confinement. To achieve a desired potential that circumvents the issues discussed above, one may first compare the density of atoms measured in a given optical potential to the desired "target" potential. As the atomic density approximates the confining potential in certain limits, one may compute the spatially-dependent error defined as the normalized difference between the target potential and the atomic density. This error may then be fed back to the DMD pattern generation code, with some proportionality factor, to add or subtract pixels where the error is positive or negative. After several iterations, the DMD potential will begin to converge to the desired potential.

3.2.4. DMD Flicker and Clock-Thief

The DMD implemented in our experiment is a Texas Instruments DMD (DLP Lightcrafter6500). We found empirically that the measured intensity of a beam diffracted off of the DMD transiently dipped to close to zero every at regular 105 μs intervals. Atoms trapped in ring-shaped potentials generated from DMD, which experienced trap frequencies around $4 - 5$ kHz, were subject to rapid parametric heating from this roughly 10 kHz "flickering" of the DMD. This flickering in fact was a known issue relating to ^{6}Li experiments utilizing DMDs, and was discussed specifically for the Lightcrafter6500

in the review [49], who found a workaround to disable this flickering when desired.

We now give a brief description of the core functionality of our DMD and address the issue of this DMD flickering. To dynamically update the state of the DMD to display a user-defined pattern, the DMD board sends a "mirror clocking pulse" (MCP) that interacts with *every* mirror on the DMD array. This MCP then causes the mirrors to unlatch from their current position into a temporary "flat" state, and after several μs the mirrors then settle into the state described by the pattern encoded onto the static random access memory (SRAM) array beneath it. Hard-wired into the Lightcrafter6500 is a MCP that is designed to be emitted every 105 μs. This is to prevent mirrors from sticking to the landing pads on which they rest in the on or off states. For most applications, this 9.5 kHz flickering does not cause issues, but can when optical trap frequencies are roughly half this value, which is common for experiments utilizing the low-mass ^{6}Li. The workaround implemented in [49] involves augmenting the DMD circuit board with additional "clock-thief" circuitry that can selectively pull the MCP off the board when desired, and only return it to the board when the pattern is to be updated. We implemented the same version of this clock thief circuit into our DMD, with success.

Section 3.3

Loading the Ring Trap

Having discussed the custom microscope objectives and DMD, we will now give a brief general description of the loading procedure that produces degenerate ensembles of fermions in ring-shaped traps, the starting point for subsequent experiments. To aid in visualization of the following loading procedure, we show a SolidWorks rendering of the relevant components of the experimental apparatus in Figs. 3.5 and 3.6.

Hot atomic ^{6}Li is collected from an angled vapor source in the 2D MOT chamber.

The 2D MOT transversely cools the hot atoms, producing a collimated beam of ^{6}Li aimed at the 3D MOT chamber. The axial velocity of this beam is sufficient to allow a small fraction of these atoms through the small differential pumping tube connecting the 2D and 3D MOT chambers. The atoms transmitted through the differential pumping tube are then collected and cooled along all axes in the 3D MOT. The time taken to load the 3D MOT to an acceptable number is typically less than 10 seconds. After this loading time, we perform a brief grey molasses cooling on the D1 line. This cools the ensemble of about to about 50 μK. Moments before the grey molasses cooling, we ramp up power in the 1064 nm crossed optical dipole trap (XODT) generated by an IR laser (IPG YLR-50-1064-LP), which intersects the 3D MOT. After the grey molasses cooling, the MOT beams and MOT magnetic fields are extinguished, and a small fraction ($\sim$ 2%) of the atoms are captured in the 45 W XODT, whose depth is several mK. Further evaporative cooling is then performed during the hand-off from the XODT into the movable optical dipole trap (MODT) derived from the same IPG laser. This hand-off proceeds by a second-long reduction in the power to 25 W, and a simultaneous 6 second long rotation of a motorized $\lambda/2$ waveplate, which redistributes the power into the MODT beam line. The focal position of the MODT is controlled by a focus-tunable lens (Optotune EL-10-30-C-NIR-LD-MV), driven by the Gardasoft TR-CL180 lens controller. Over 5 seconds, we move the atoms trapped in the MODT from the 3D MOT chamber into the glass cell. While the transport is happening, we ramp up power in both the 1064 nm sheet beam (generated from a Koheras fiber laser) and DMD pattern beam to their maximum values. The sheet beam reaches 4 W, while the DMD beam reaches a value that is depends on the desired trapping geometry. Once transported into the cell, the MODT power is lowered to zero in one second, and the sheet is populated. At this stage, there are about 1×10^6 ^{6}Li atoms in the lowest two hyperfine states $|1\rangle$ and

$|2\rangle$. We perform the final evaporative cooling by first ramping the Feshbach fields to a value just below the 83.2 mT Feshbach resonance. Then, we lower the sheet power in an exponential fashion in about 2 seconds to some small final value. During the final moments of evaporation, weakly bound molecules form, and the DMD-generated potential is substantially occupied by cold (and typically condensed) molecules. This is now the starting point for any subsequent experiment in the cell.

We finally discuss the details of the DMD projection and imaging beam lines used in the experiment, which is also shown schematically in Fig. 3.7. A fiber launch outputs a 2 mm $1/e^2$ radius collimated 780 nm beam, which passes through a $\lambda/2$ waveplate and polarizing beam splitter (PBS) cube for polarization clean-up. This beam is directed onto the DMD, which is optimized to accept the incident beam at 24 degrees with respect to its normal. A small portion of this light is picked off via a wedged pick-off window and directed to a photodiode for intensity stabilization of the beam. The brightest diffracted order emerging from the DMD is then folded by two mirrors and impinges on a $1,000$ mm focal length plano-convex "tube" lens placed at the same distance from the DMD. This light is then directed to the lower projection objective with focal length 33 mm at a distance 1033 mm from the tube lens, ensuring the $4f$ condition is met. The $4f$ condition is crucial to maintaining object and image-space telecentricity, which ensures that the propagating DMD beam remains roughly constant in size between the tube lens and projection objective. The tube lens and objective combination results in a demagnification factor of about 1/30. Finally, the probe beam line frequency stabilized to the relevant ^{6}Li D_2 imaging transition is combined with the 780 nm beam line on a PBS cube. A subsequent $\lambda/4$ waveplate circularizes the polarity of this beam. The final PBS and $\lambda/4$ waveplate *do* affect the polarization of the 780 nm beam, but this is irrelevant to the trapping potential generated by its optical field which only depends on intensity (in the limit of not-too-

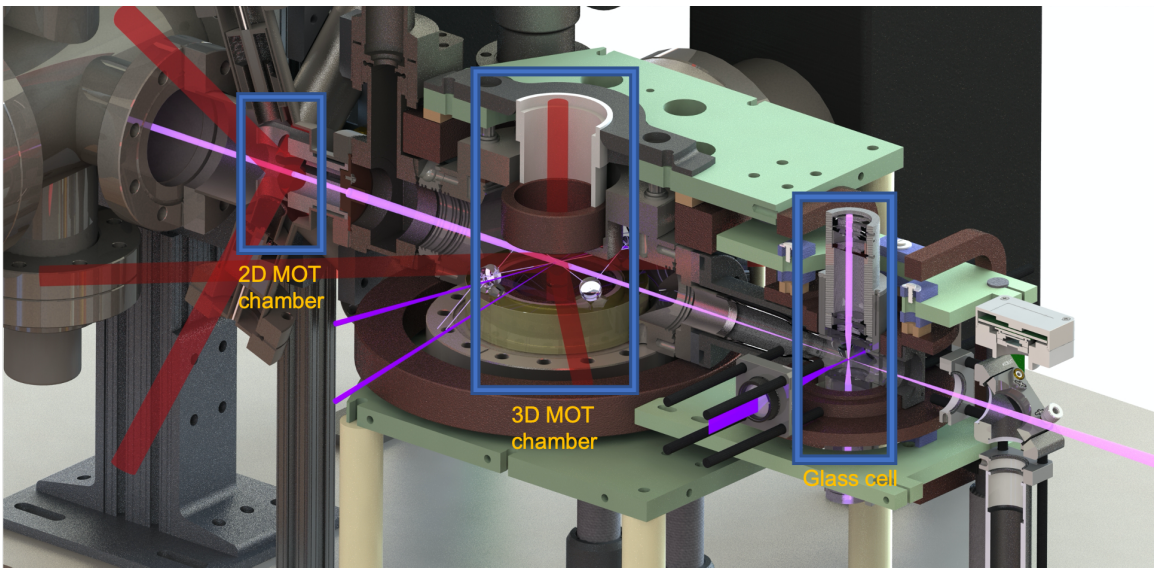

Figure 3.5: A SolidWorks rendering showing a cross-section of the main components of the experimental apparatus. The loading proceeds from the 2D MOT chamber, to the 3D MOT chamber, and ends in glass cell. The various beams represent the MOT (red) and dipole (purple/pink) beams.

large numerical aperture).

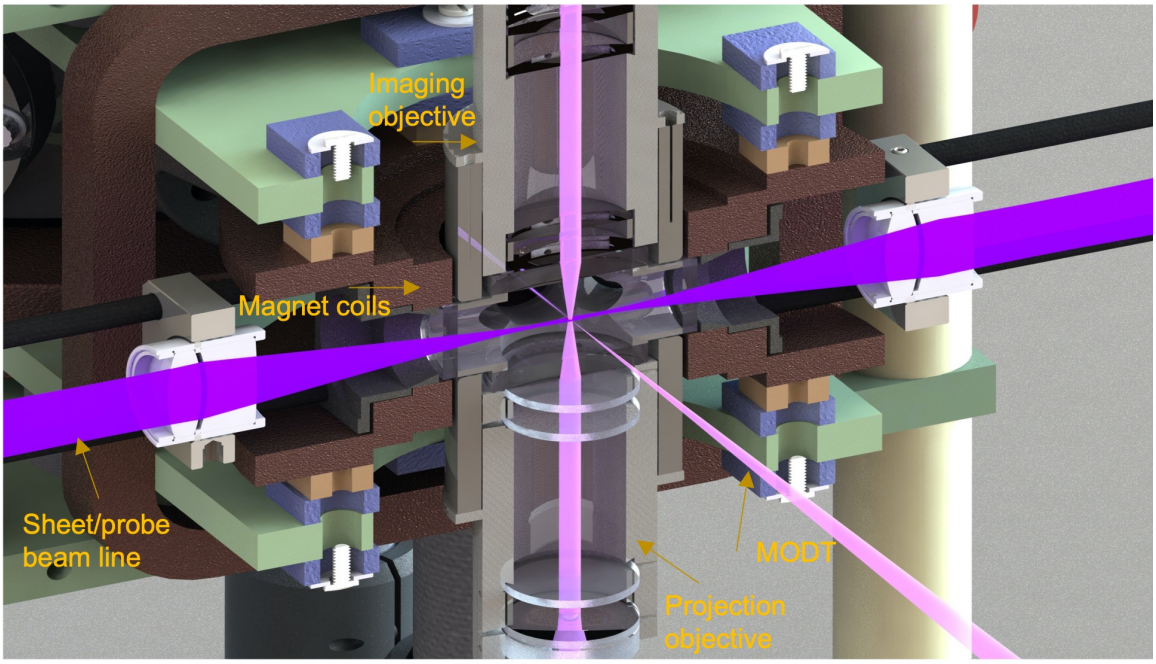

Figure 3.6: SolidWorks rendering of a cross section of the science cell and its immediate surroundings. We show the pair of NA=0.33 microscope objectives, the magnet coils surrounding the science cell, and the various beams and beamlines utilized in the experiment.

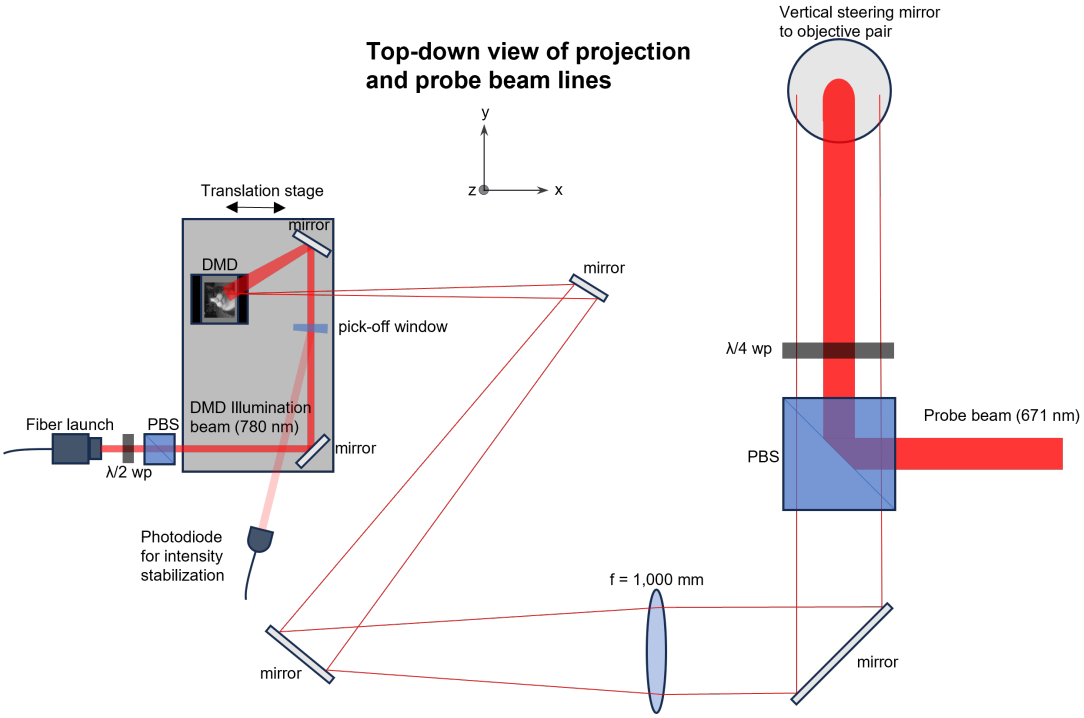

Figure 3.7: Schematic showing a top-down view of the projection and imaging beam opto-mechanical setup.

Chapter 4

Fermi Hole Heating

In this chapter, I discuss an important source of heating relevant to weakly attractive, degenerate ($T/T_F \ll 1$) fermionic systems. We demonstrate a useful technique to mitigate the detrimental effects of this heating mechanism, and compare experimental measurements of heating rates to a microscopic model of this heating process. This reduction in the heating rate played an important role in the study of spontaneous currents discussed in Chap. 7, but also opens the possibility to perform seconds-long experiments on weakly interacting BCS superfluids, where maintaining extremely low temperatures is crucial. Furthermore, this section will give important insight into the trap configuration most typical of the experiments described in this thesis, as well as our main method of in-situ thermometry involving a measurement of the local equation of state. The findings of this chapter are additionally presented in a publication from our group from 2023 [32].

Section 4.1

Introduction

Experimental studies of fermionic superfluids in the weak-pairing limit require deep quantum degeneracy. However, achieving and maintaining temperatures well below the Fermi temperature in ultracold atomic systems is experimentally challenging. Pauli-blocking reduces the efficiency of evaporative cooling in the quantum degenerate regime [50], dramatically slowing down the cooling process (For reviews, see [51, 52]). Various protocols have been proposed for circumventing this limitation, especially relying on adiabatic processes with deformations of the trapping potential [53–60]. On top of this fundamental limitation to cooling, deeply degenerate Fermi gases are especially sensitive to losses caused by collisions with background gas molecules; when atoms deep in the Fermi sea are expelled, the creation of holes substantially raises the effective temperature of the system. This "hole heating" effect was first predicted in Ref. [61] and has been previously modeled for uniform and harmonically trapped Fermi gases and Fermi-Bose mixtures [62–64]. These previous studies also investigated the possible use of a bosonic reservoir with a large heat capacity to achieve and maintain low temperatures.

In this paper, we show experimentally that for an inhomogeneous fermionic system with a deeply degenerate subsystem embedded in a large low-density reservoir, the effects of hole heating are reduced compared to the case of a similar system without the reservoir present. This result is achieved by focusing on a ring-dimple trap, a geometry advantageous to study superfluid phenomena and persistent currents, though we expect the outcome to hold for a generic trapping geometry. More specifically, we investigate the effects of fermion-hole heating for a spin-balanced pair superfluid of ^{6}Li atoms in the deep BCS limit of weak attractive interactions. Minimizing heating

rates is important for some experiments with fermion pair superfluids since the natural time scale for investigating low-energy, long-wavelength dynamics in a superfluid ring is set by the period of the lowest quantized circulation state, typically several seconds. It is even more critical for experiments in the deep BCS limit, because present methods for detecting supercurrents by matter-wave interference require an interaction ramp to the molecular BEC regime before ballistic expansion [31, 65]. Unless the initial system temperature is very low, loss of contrast makes coherent phase measurements difficult or impossible. Our most important finding is that the heating rate for fermionic atoms in a superfluid "circuit" can be substantially reduced by embedding it in a large, dilute population of atoms that acts as a heat sink and as a particle reservoir.

The paper is organized as follows: Sec. 4.2 gives a brief overview of theory pertaining to non-interacting Fermi systems, along with an outline of the optical potentials employed in the experiment. Sec. 4.3 discusses the in-situ thermometry technique we used to measure heating rates in the limit of weak attractive interactions. Sec. 4.4 gives an outline of hole-heating theory and discusses the important findings of our heating rate measurements. Finally, we conclude in Sec. 4.5 by discussing the collisions that re-establish equilibrium throughout the hole-heating process.

Section 4.2

Fermions in a Ring-Dimple Trap

A wide range of magnetic and optical trapping techniques have been used in experiments where Bose-Einstein condensates (BEC) of ultracold atoms have been confined to multiply-connected trap potentials [66–76]. Experiments with ultracold Fermi gases generally make use of magnetic Feshbach resonances and all-optical trapping techniques, and recent experiments with rings of ultracold fermions have made use of

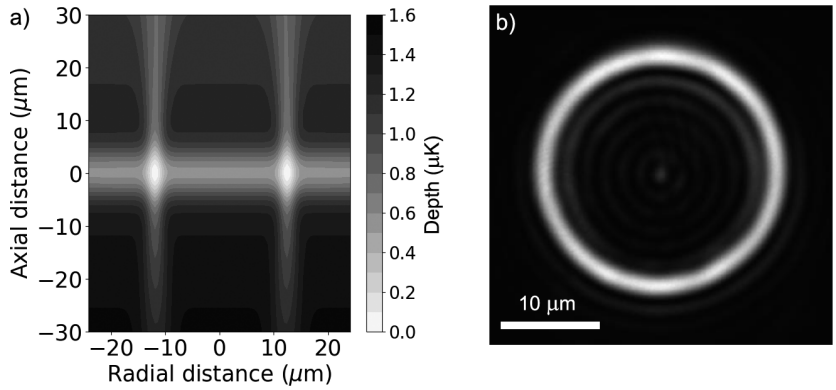

Figure 4.1: a) Side-view cross-section of a red-detuned optical trap potential used in our experiments with rings of fermionic atoms. This model includes the effects of the ring beam, the sheet beam and gravity. b) Intensity profile of the vertically propagating red-detuned ring-pattern beam modeled in (a).

both red- and blue-detuned trap configurations [31, 65]. While the conclusions of this paper about heating rates are relevant to a wide range of possible trap configurations, we will focus here on red-detuned ring traps of the type used in our first experiments with rings of ultracold fermions, which have some potentially helpful features.

Optical ring traps typically employ at least two independent laser fields, one providing mainly vertical confinement, and the other radial. In our experiments with ^{6}Li the main vertical confinement is provided by a red-detuned (1064 nm) horizontally-propagating asymmetric Gaussian beam. In most of our experiments, the radial confinement was provided by a red-detuned (780 nm) vertically propagating laser shaped into a ring-pattern beam. This overall red-detuned beam configuration is similar to those used in many previous experiments with ring-shaped Bose-Einstein condensates [72]. If the chemical potential of a quantum gas is sufficiently small compared to the depth of the ring-dimple, the atoms will be localized to the ring potential minimum and it is reasonable to treat the transverse confinement as approximately harmonic about the minimum. It is more straightforward to analytically calculate the chemical potential and other important properties of the system when this approximation is valid. For a gas of non-interacting fermionic atoms in a ring with

harmonic transverse confinement, the Fermi energy can be expressed as a function of the number of fermions N, the geometric mean of the vertical (z) and radial (r) trapping frequencies $\bar{\omega} = \sqrt{\omega_z \omega_r}$, and the characteristic angular rotation frequency $\Omega \equiv \hbar/(2mr_0^2)$, where r_0 is the ring radius.

$$\frac{E_F}{\hbar\Omega} = \left(\frac{15N}{16}\right)^{2/5} \left(\frac{\bar{\omega}}{\Omega}\right)^{4/5} \tag{4.1}$$

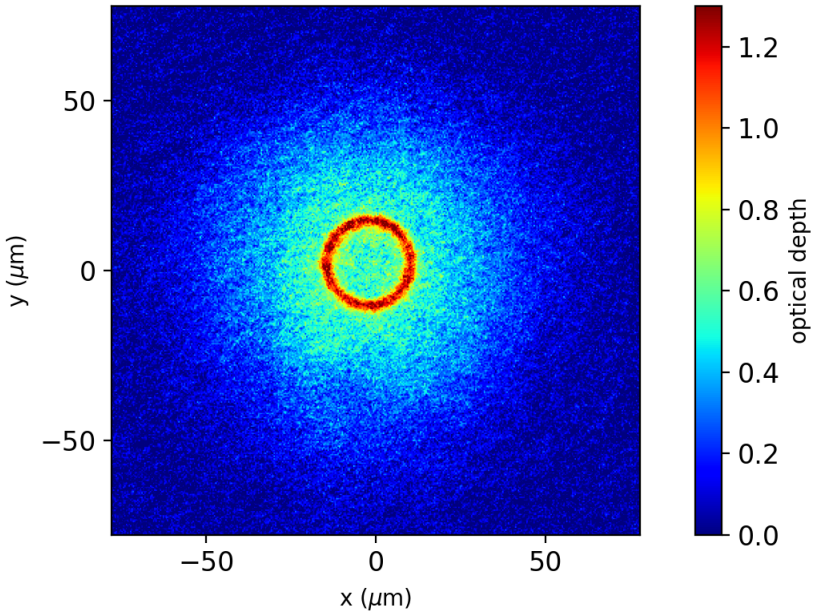

Figure 4.2: Density distribution of ^{6}Li atoms in our trap when the Fermi level is around 0.1 μK larger than the depth of the dimple created by the ring-pattern beam. The figure shows the average of 10 in-situ absorption images taken at a magnetic field of 100 mT. Both the ring-shaped region of increased density and the dilute halo are clearly visible.

We conducted our first experiments expecting to work within this approximation, but were surprised to see evidence that heating rates were higher when we evaporated until the Fermi level was smaller than the dimple depth. The atoms in the ring remained in the superfluid phase much longer when the Fermi level was higher, with many atoms spilling from the ring-dimple into the shallow extended potential created

by the sheet beam as shown in Fig. 4.2. This dilute "halo" of atoms typically contained more than two-thirds of the total atom population, and played a crucial role in the thermodynamics of the system in our experiments. The harmonic approximation is clearly not valid for this situation, so we used a numerical 3D model of the potential to estimate the relevant thermodynamic properties of our system.

To compute the Fermi energy for atoms in this extended ring-dimple potential, we used a semi-classical model to obtain the total (spin up *and* down) density of states, $g_{3D}(E)$, for a fully 3D model of the trap ($V(\mathbf{r})$) that included the sheet beam, the ring beam, and gravity:

$$g_{3D}(E) = \frac{8\pi m}{(2\pi\hbar)^3} \int_{V(\mathbf{r})\leq E} d^3r \sqrt{2m[E - V(\mathbf{r})]} \tag{4.2}$$

We then used the defining relation $N = \int_0^{E_F} g_{3D}(E)dE$ to numerically compute the Fermi energy $E_F(N)$, setting $E = 0$ at the ring potential minimum. We modeled the ring beam as having an average radius of 12.5 μm and a transverse Gaussian profile with a radial $1/e^2$ half-width of 2.2(1) μm, in the plane of the sheet beam. Vertical trapping forces from this tightly focused ring were non-negligible, and so we found the through-focus intensity profile by numerically propagating the beam using the angular spectrum method [34] to obtain its full 3D profile. We modeled the sheet beam as having an asymmetric Gaussian profile with a horizontal waist of 290 μm and a vertical waist of 7 μm.

The effect of gravity turned out to be crucial in the numerical calculation of the density of states. While gravity's effect on the exact value of the density of states at a given energy is small, the gradient due to gravity weakens the vertical confinement of atoms more substantially near the ring dimple region. This is conveniently visualized by plotting vertical cuts of the potential energy at radii near the ring radius $r_0 =$ 12.5 μm. These cuts each have a local maximum at some $z < 0$ and linearly fall away

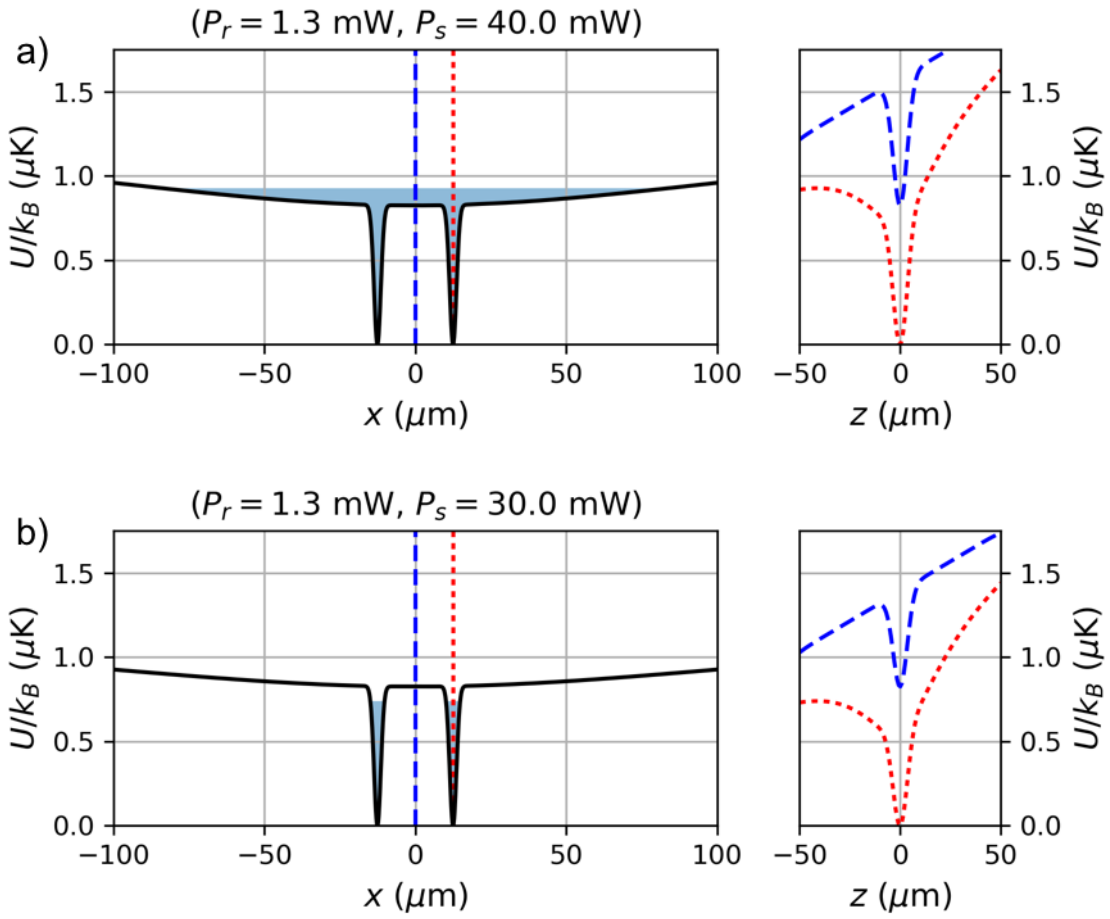

Figure 4.3: Potential energy slices of our combined trap (gravity included). a) 40 mW and b) 30 mW sheet power. Left plots show the radial trap profiles at $z = 0$ while the right plots show the vertical profiles for two different radii: The blue (dashed) line is the vertical cut along $r = 0$ and the red (dotted) line is along $r = r_0$. The shaded regions in the radial profiles (a,b) indicate where the potential energy is below the evaporation depth V_{evap}.

to $-\infty$ for $z \ll 0$ due to gravity. The smallest of these maxima lies on the cut along $r = r_0$, as shown in Fig. 4.3. Its potential energy sets the "evaporation depth" V_{evap} of the trap. Atoms with energy greater than this evaporation depth may overcome this "lip" and fall out the bottom of the trap, and thus states with $E > V_{evap}$ should carry zero weight insofar as equilibrium thermodynamic quantities are concerned. We therefore multiply equation (4.2) with the step function $\Theta(V_{evap} - E)$, which in turn

has the dramatic effect of placing upper bounds on the allowed atom number and internal energy.

As we will discuss below, there are additional subtleties in addressing the states with $E > V_{evap}$ that may remain bound to the trap via conservation laws that prevent escape through the evaporation channels near the ring dimple. The equilibrium configuration should not include these "quasi-bound" orbits, but the relaxation dynamics may depend on them.

Section 4.3

Temperature Measurement

We obtained estimates of the system temperature by fitting an appropriate theoretical model to the column density of the halo. In this region, we can approximate the potential $V(r,z) \approx V_{0,s} + m\omega_z^2 z^2/2 + V_{sheet}(r)$ where $V_{0,s}$ is the potential energy offset of the full trap at the origin and $V_{sheet}(r)$ is the cylindrically-symmetric sheet potential, with $V_{sheet}(r=0) \equiv 0$. To allow for the possibility of mixed dimensionality in our description of the density profile, we quantize the vertical motion to harmonic oscillator levels, while treating the radial motion semi-classically. This procedure is similar in spirit to the theoretical treatment of a quantum well in solid state systems [77]. In this way, we may write a hybrid description of the density of states

$$g_j(E) = \frac{s}{(2\pi\hbar)^2} \int d^2r d^2p \; \delta\left(E - \frac{p^2}{2m} - \hbar\omega_z j - V_r(r)\right) \tag{4.3}$$

which represents the density of available states in the j^{th} axial harmonic oscillator level ($j = 0, 1, ...$), for a system with s spin degrees of freedom. We have defined $V_r(r) = V_{0,s} + V_{sheet}(r) + \hbar\omega_z/2$, accounting for the zero-point energy of the axial motion. Again, we assume states with $E > V_{evap}$ do not contribute to the density of

states. Integrating over momenta and summing over j, we identify the local density of states

$$g(r;E) = s\frac{m}{2\pi\hbar^2}\left\lceil\frac{E-V_r(r)}{\hbar\omega_z}\right\rceil\Theta[E-V_r(r)]\Theta(V_{evap}-E) \tag{4.4}$$

where $\lceil x\rceil$ is the ceiling function. The column density $n_2(r)$ is found by integrating the Fermi-Dirac-weighted local density of states over energy, with the substitution $x = E/(k_BT)$, giving

$$\begin{aligned} n_2(r) &= \frac{s}{\lambda_T^2}\int_0^{\eta_c-\frac{q-q(r)}{\gamma}} dx\frac{\lceil x/\gamma\rceil}{e^{x-q(r)}+1} \\ &= \frac{s}{\lambda_T^2}\sum_{j=0}^{\infty}\Bigg\{F_0[q(r)-\gamma j] \\ &\quad - F_0\left[q(r)-\gamma j+\frac{q-q(r)}{\gamma}-\eta_c\right]\Bigg\} \end{aligned} \tag{4.5}$$

We have further defined $\lambda_T^2 \equiv 2\pi\hbar^2/(mk_BT)$, $\gamma \equiv \hbar\omega_z/(k_BT)$, $q(r) \equiv [\mu - V_r(r)]/(k_BT)$, $\eta_c = V_{evap}/(\hbar\omega_z)$ and $F_0(x) = \log(1+e^x)$ ($\sim e^x$ for $x \to -\infty$). We note, however, that typically $\eta_c \gtrsim 20$, and so the second term in the summation form of (4.5) may be neglected, and we will assume this approximation in the subsequent analysis. The integral form of (4.5) looks remarkably similar to the order 1 Fermi-Dirac integral used to describe the 3D (column) density, except for the presence of the ceiling function in the integrand, which accounts for the discrete axial energy levels. This discreteness is blurred out if either γ or $\gamma/q(r)$ is small compared to unity, which corresponds to the $3D$ limit. In this case, we can replace $\lceil x/\gamma\rceil$ with x/γ, and the resulting expression gives the proper integrated $3D$ column density

$$n_2(r) \approx \frac{s}{\gamma\lambda_T^2}F_1[q(r)]\ ; \qquad \gamma \ll 1 \text{ or } \gamma/q(r) \ll 1 \tag{4.6}$$

where $F_\nu(x)$ is the usual Fermi-Dirac integral of order ν. Conversely, if $\gamma \gg 1$ and $\gamma/q(r) \gg 1$, we approach the $2D$ limit, and we may replace $\lceil x/\gamma \rceil$ with 1, and the resulting column density gives the proper $2D$ density

$$n_2(r) \approx \frac{s}{\lambda_T^2} F_0[q(r)] \; ; \qquad \gamma \gg 1 \text{ and } \gamma/q(r) \gg 1 \tag{4.7}$$

At this point, we have not assumed a particular form for the radially symmetric sheet potential. If we do have knowledge of the sheet trap parameters, however, we may use them to eliminate a fit parameter from the fitting function. In our case, the sheet potential may be described by $V_{sheet}(r) = V_0[1 - \exp(-2r^2/w_s^2)]$ where $V_0 = m\omega_s^2 w_s^2/4$ and ω_s and w_s are the sheet radial angular trapping frequency and $1/e^2$ radius, respectively. We may therefore introduce $\eta \equiv V_0/(k_B T)$ to write $q(r) = q - \eta[1 - \exp(-2r^2/w_s^2)]$, and eliminate $\gamma = \hbar\omega_z/(k_B T) \equiv \eta/\mathcal{N}$ as a free fit parameter, assuming $\mathcal{N} = V_0/(\hbar\omega_z)$ is a known, albeit potentially uncertain, input. We rewrite the column density (4.5) as

$$n_2(r) = n_\infty + n_0 \frac{\sum_{j=0}^{j_{\max}} F_0 \left\{ q - \eta \left[1 - e^{-2\left(\frac{r-r_0}{w_s}\right)^2} + \frac{j}{\mathcal{N}} \right] \right\}}{\sum_{j=0}^{j_{\max}} F_0 \left(q - \frac{j\eta}{\mathcal{N}} \right)} \tag{4.8}$$

where we have introduced n_0 as the column density at $r = r_0$ and allowed for a non-zero density offset n_∞ and center shift r_0 in the density profile. $j_{\max}$ is the number of terms to include in the sum, and typically does not need to be very large. In total, there are five free parameters $(q, \eta, n_0, n_\infty, r_0)$ that can be extracted via a least square fitting routine. However, one should ensure that n_∞, n_0 and r_0 are as tightly bound and accurate as possible. This is achieved via careful image processing and pre-fitting analysis of the density profiles. Furthermore, the guesses for the remaining q and η should be physically reasonable. Namely, $\eta \geq 0$ and $q = (k_B T/\mu)^{-1}$ is not

too negative if dealing with a presumed near-degenerate ensemble.

We show an example radial profile of the measured density distribution obtained from the average of 10 absorption images in Fig. 4.4. The hold time used was 0.1 s. Using the hybrid fitting function, we fit the data and extract a reduced temperature and absolute temperature of 0.03 and 40 nK, respectively. The hybrid Fermi-Dirac function is only meant to fit the density profile of the halo but it does so quite well, and with sufficient precision to give reliable thermometry. Although not discussed presently, we point the reader to Appendix C which discusses a potentially useful technique to boost the accuracy of degenerate fermion thermometry.

It is also important to note that, for deeply degenerate Fermi gases, absolute temperature enters into the fit of the data only in the far dilute thermal wings of the density distribution. The use of a hybrid fitting function (4.8) was motivated by this fact, and we found that a simple 3D Fermi-Dirac function consistently overestimated the density at large radii. We found empirically that the largest source of uncertainty in the temperature estimate is from our measurement of the weak radial trap frequency of the sheet beam, f_s. Measurement noise introduces a much smaller uncertainty, and uncertainty in the axial trap frequency introduces a similarly small amount. Uncertainty in imaging beam parameters such as saturation intensity and polarization impurity will introduce systematic errors onto the temperature estimate. For the dilute halo atoms, error due to saturation effects may be neglected, and polarization purity is almost unity, so uncertainty due to it may be neglected. Finally, at large radii, the sheet becomes slightly elliptical, and this in turn causes a small systematic shift in measured temperatures to smaller values. This shift becomes more apparent in thermal ensembles where the extent of the atomic distribution into these elliptical regions is larger.

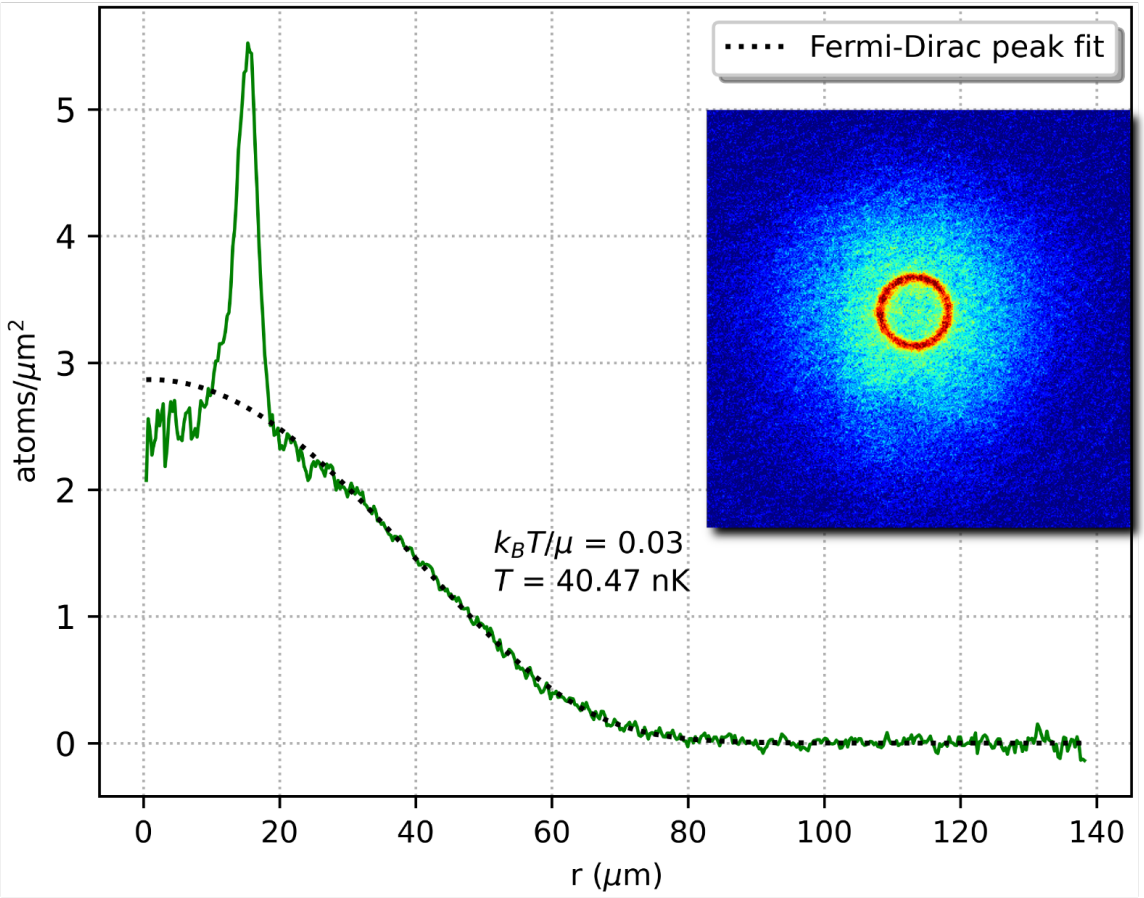

Figure 4.4: Radial profile obtained from a set of 10 in-situ measurements of the atomic density distribution after 0.1 s of holding time, and at a field of 100 mT. The profile is fit with the hybrid Fermi-Dirac function (4.8), from which we extract the reduced temperature and absolute temperature shown in the plot. The radial profile is the column density in a single spin state.

Section 4.4

Fermi hole heating

4.4.1. Theory

In the far BCS limit, the lifetime of atoms in the trap is limited by the inelastic scattering rate with background particles. In a single background scattering event, a particle in the trap is ejected from the Fermi sea, leaving a hole behind. Assuming the subsequent relaxation dynamics does not eject any additional particles, the tempera-

ture increases slightly. For uniform one-body loss with lifetime τ_L, the single-particle populations in state $|k\rangle$ and eigen-energy ϵ_k evolve according to $\dot{n}_k = -n_k/\tau_L$ (k is a set of good single-particle quantum numbers for the inhomogeneous trap). The total atom number $N = \sum_k n_k$ and internal energy $U = \sum_k n_k \epsilon_k$ subsequently evolve as $\dot{N} = -N/\tau_L$ and $\dot{U} = -U/\tau_L$, respectively, where the single-particle loss equation was used. We note that the populations n_k need not be thermally distributed. There are several equivalent methods of deriving the heating rate associated with this loss. Perhaps the most insightful method relies on the observation that the internal energy per particle $u \equiv U/N$ is a conserved quantity. Interestingly, this is true even during the elastic collisions that return the system from a non-equilibrium state to equilibrium after a hole is created. This fact implies that one can, at all times, meaningfully associate an effective temperature to the ensemble as if it were in equilibrium at the same energy and atom number. In our system, the thermodynamic variables used to describe the internal energy per particle u are atom number N, temperature T, and a set of trap parameters which we call $\mathcal{V}$. We note that the *only* thermodynamic role that $\mathcal{V}$ plays is in setting the energy scales for the single particle energy spectrum, which is fixed for the measurements performed in this paper as we are not varying the trap. The reversible mechanical work associated to trap deformations is therefore set to zero. We thus treat N, U and T as the only time-varying quantities under one-body loss, with the evolution $u(t) = u_0$ and $N(t) = N_0 e^{-t/\tau_L}$ known, and that of $T(t)$ unknown. We can study the evolution $T(t)$ in a grand canonical picture, where a time-dependent chemical potential $\mu(t)$ is introduced and whose role is to fix $N(t)$ at each instant in time. We thus solve two equations

$$\frac{U(t)}{N(t)} = u_0 = \frac{\int dE\ g(E) E f[E; \mu(t), T(t)]}{\int dE\ g(E) f[E; \mu(t), T(t)]} \tag{4.9}$$

and

$$N(t) = N_0 e^{-t/\tau_L} = \int dE\ g(E) f[E; \mu(t), T(t)] \tag{4.10}$$

for the two unknowns $T(t)$ and $\mu(t)$, where $f(E;\mu,T) = \{\exp[(E-\mu)/k_B T]+1\}^{-1}$ is the usual Fermi-Dirac distribution function and $g(E)$ the density of states. By taking a time derivative of (4.9) and utilizing (4.10), it is possible to show that the evolution is equivalent to a differential equation governing the temperature dynamics. This is easier to demonstrate, however, by simply differentiating the internal energy function $U(N,T)$ with respect to time:

$$\dot{U} = \dot{N}(\partial U/\partial N)_T + \dot{T}(\partial U/\partial T)_N \tag{4.11}$$

We then use the first law of thermodynamics $dU = TdS + \mu dN = T[dN(\partial S/\partial N)_T + dT(\partial S/\partial T)_N] + \mu dN$ to compute $(\partial U/\partial N)_T = \mu + T(\partial S/\partial N)_T$. Next, the Maxwell relation $(\partial S/\partial N)_T = -(\partial \mu/\partial T)_N$ is used to write $(\partial U/\partial N)_T = \mu - T(\partial \mu/\partial T)_N$. Finally, identifying the heat capacity at constant atom number $C_N = (\partial U/\partial T)_N$, we solve for the temperature derivative in (4.11):

$$\dot{T} = -\frac{T^2\left(\frac{\partial}{\partial T}\frac{\mu}{T}\right)_N + u_0}{\tau_L c_N} \tag{4.12}$$

with $c_N \equiv C_N/N$ and the time-dependent forms for $N(t)$ and $U(t)$ were used. This expression is in fact an extension of equation 5 in [61], which was derived using energy balance considerations, to arbitrary temperatures and inhomogeneous traps.

To quantitatively motivate the need, in certain experiments, to maintain low temperatures for long times, we briefly draw connection to the potential experiments performed in the BCS limit, which typically rely on maintaining a temperature below the critical temperature for pairing. Pairing can occur below Gor'kov's critical temperature [78], $k_B T_c \approx 0.277\mu \exp(-\pi\lambda/2)$, with $\lambda = 1/k_F|a|$ the interaction pa-

rameter. Equating this expression to $k_B T$ gives the threshold reduced temperature above which pairing cannot occur, i.e.

$$\left(\frac{k_B T}{\mu}\right)_{max} \equiv 0.277 \exp(-\pi\lambda/2) \tag{4.13}$$

Even if initially $T < T_c$, hole heating will drive the system temperature *and* the critical temperature towards each other until eventually $T = T_c$. Using Gor'kov's expression, we write $k_B T(t_c)/\mu(t_c) \equiv 0.277 \exp[-\pi\lambda(t_c)/2]$, defining the time t_c at which the BCS superfluid is completely destroyed and the temperature begins to exceed the critical temperature. We note that t_c depends on the initial interaction parameter $\lambda(t = 0) \equiv \lambda_0$, and that the critical temperature also inherits its time-dependence from the one-body loss. Furthermore, we must assume that the BCS pairing gap remains small relative to the Fermi energy to justify the use of non-interacting model of the hole-heating rate, which will inevitably break down when $\lambda_0 \to 0$.

We emphasize now the role the halo plays in maintaining low temperatures for long periods of time. First, the large density of states offered by the broad sheet helps fermions disperse external energy imparted into the system into the closely spaced energy levels. In other words, the low-density halo has a larger specific heat than the deeply-degenerate ring and can serve as an efficient heat sink, lowering the overall heating rate. Secondly, the halo acts as a particle reservoir for the ring-dimple, since the global chemical potential is only weakly dependent on the atom number when a substantial halo is present. Intuitively, any atom ejected from the ring-dimple can be "replenished" by an atom in the halo. This in turn retains large densities in the ring-dimple region for longer periods of time. Combined, these two effects help maintain a deeply degenerate Fermi gas, especially in the ring-dimple region, for times exceeding the trap lifetime.

In comparison, experiments performed in a "bare" ring, i.e without a halo present,

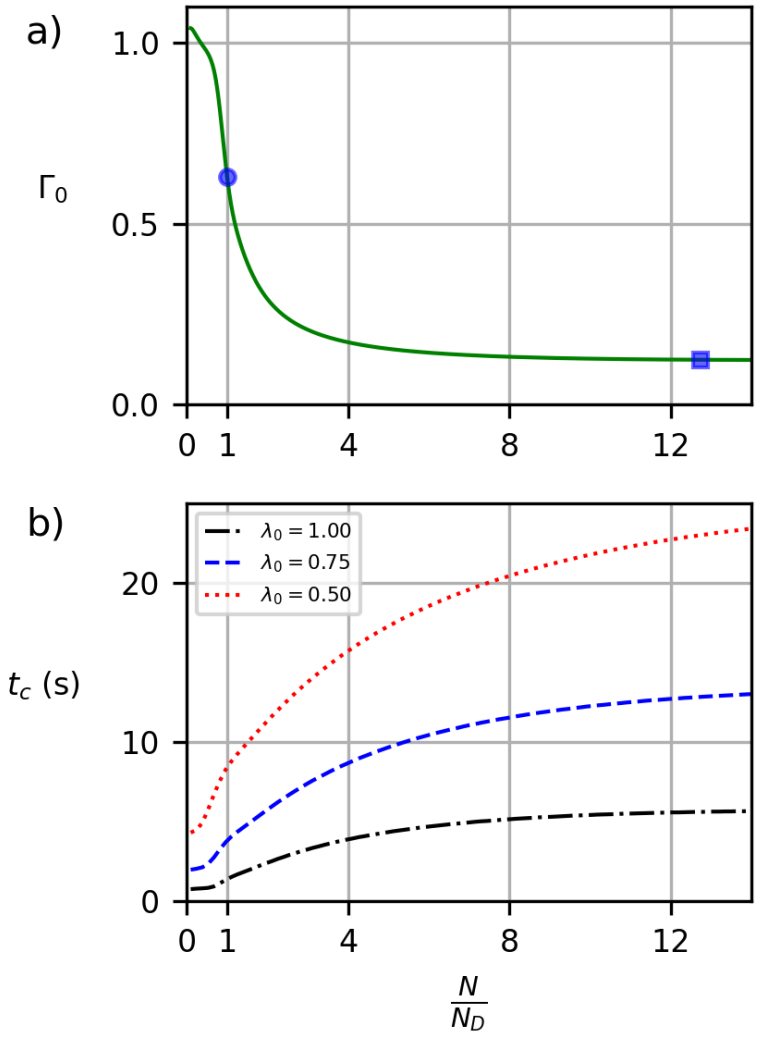

Figure 4.5: a) Predicted initial heating rate (see text) versus atom number relative to the dimple capacity. We show the point where the ring dimple is just filled (blue circle) and the conditions used in the experiment (blue square). b) Time taken to heat to the critical temperature for different initial values of the interaction parameter λ_0, and with $\tau_L = 25$ seconds. In both plots, $\frac{k_B T}{\mu}|_{t=0} = 0.03$.

are likely to suffer from unacceptable heating rates. This may become particularly apparent in experiments utilizing a blue-detuned, repulsive ring beam, where the halo population would typically be absent or separated from the superfluid population, unless the potential is carefully tailored to make this possible. Blue-detuned traps have advantageous characteristics for some experiments, but the limits imposed by

hole-heating will be a much greater problem for experiments requiring many seconds to perform.

The dependence of the heating rate on atom number is in fact strongly dependent on the distribution of the fermions in the trap. In particular, the heating rate becomes noticeably suppressed as fermions begin overfilling the ring. We demonstrate this by numerically computing the initial heating rate as a function of atom number using equation (4.12) and the 3D model of the trap density of states. To this end, it is insightful to introduce the "dimple capacity" $N_D \equiv \int_0^{V_{0,r}} g_{3D}(E)dE$, defined as the number of ideal fermion states with energy below the ring depth $V_{0,r}$. In the "bare ring" scenario, with $N \leq N_D$, the atoms are confined to the ring-shaped region of lowest potential, while for $N > N_D$, atoms spill over into the broad harmonic sheet potential and populate a dilute "halo". Fig. 4.5 shows the results of our computations. The upper plot shows the initial dimensionless heating rate $\Gamma_0 \equiv \tau_L \frac{d}{dt}\frac{k_B T}{\mu}|_{t=0}$, when $\frac{k_B T}{\mu}|_{t=0} = 0.03$, as a function of N/N_D. We see a sharp fall-off in this rate as the dimple fills up and eventually becomes overfilled, at which point the Fermi energy becomes only weakly dependent on the atom number and the halo becomes populated. For this sheet trap geometry the heating rate approaches a floor of around 0.1 when there are ten times more atoms in the halo than in the dimple, and there is negligible benefit from increasing the halo population further.

The impact of the reduced heating rate is evident in the lower plot in Fig. 4.5, which shows the time taken, t_c, for the system to heat from $k_B T/\mu = 0.03$ to the (reduced) critical temperature as a function of the same relative atom number N/N_D and a 25 second vacuum lifetime. The various curves represent different values of the interaction parameter, λ_0. The plots for $\lambda_0 > 1$ are not shown, because they already begin at $T \gtrsim T_c$. Limits imposed by hole-heating rates clearly become quite restrictive for weakly interacting systems, but can be mitigated substantially by allowing the

ring to be overfilled.

4.4.2. Experiment

Our experimental apparatus is designed to produce ultracold gases of lithium atoms in highly configurable optical dipole traps. Lithium is a natural choice for these experiments because it has a fermionic isotope (^{6}Li) with high natural abundance, a broad Feshbach resonance, and an unusually stable and long lived molecular state. After initial cooling and capture using a 2DMOT, 3DMOT, and crossed-beam optical dipole trap, we use a movable optical trap to transport 10^6 atoms to the center of a glass cell located between vertically oriented confocal objective lenses. Magnet coils surrounding the cell can generate a nearly uniform magnetic field of up to 108 mT. We prepare the ^{6}Li atoms in an equal spin mixture of the two lowest energy spin states, for which there is a broad Feshbach resonance at 83.2 mT. For more detailed information see Supplemental Material of Ref. [31]

The typical vacuum-limited lifetime of atoms in our glass cell experimental chamber is at least one minute. To ensure we could clearly distinguish the effects of hole heating from the effects of slow technical drifts in controlling the experimental conditions, we deliberately reduced the trap lifetime to 25 seconds by shutting off the ion pumps attached to the 3DMOT vacuum chamber and allowing the pressure in the cell to reach a new equilibrium, pumped only by non-evaporable getters. Under these conditions we evaporatively cooled an initial ensemble of $\sim 10^6$ atoms near the 83.2 mT Feshbach resonance to a final, spin-balanced population of $N = 3.5 \times 10^4$ total atoms. For this number of atoms, the Fermi energy is $E_F = k_B \times 1.1(1)\ \mu K$, computed from the 3D density of states of our numerically-modeled trap. The ring and sheet powers were $P_r = 1.3$ mW and $P_s = 50$ mW, respectively. The axial and radial sheet trapping frequencies were measured using a parametric heating technique, and cross-checked using our sheet beam optical model, to be $f_z = 1.6(1)$ kHz and

$f_s = 41(2)$ Hz, respectively. Furthermore, our trap model predicts $E_F/V_{evap} = 0.95$.

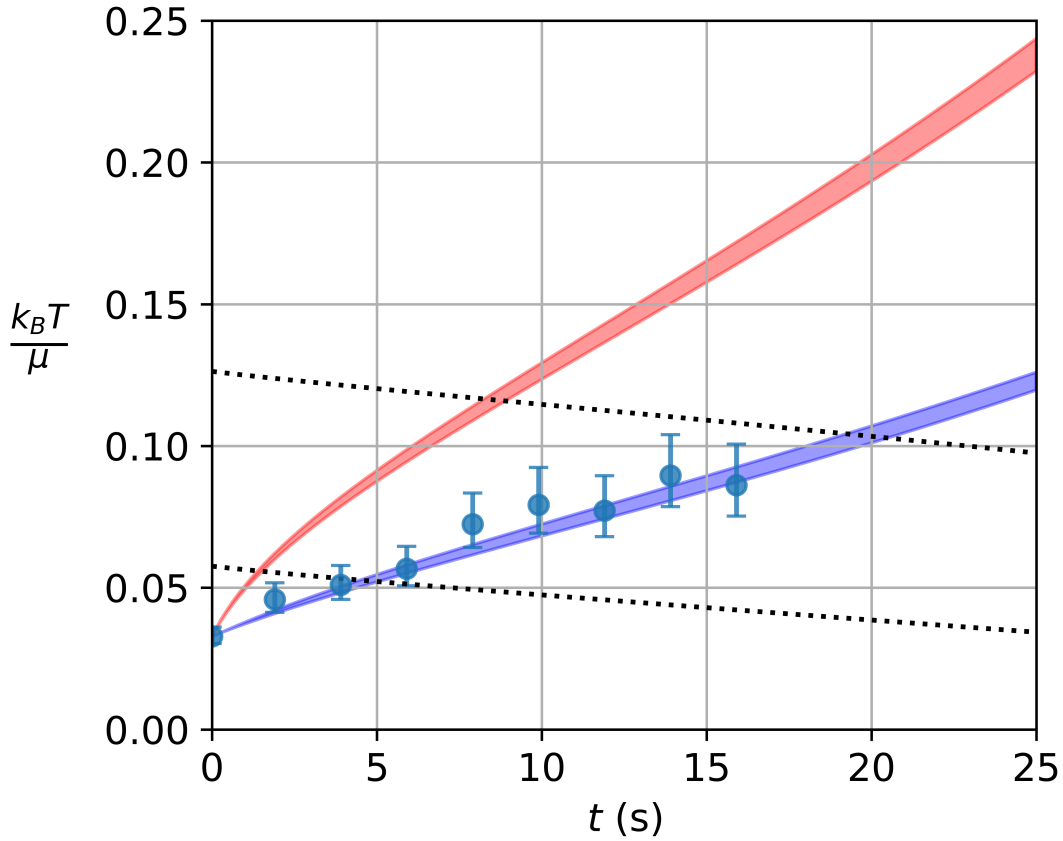

Figure 4.6: Reduced temperature versus time for an ideal Fermi gas in our trap potential. Blue circles are experimental data for an over-filled ring dimple with $N = 3.5\times10^4$ atoms at $T/T_F = 0.03$. The lower filled curve (blue online) is the temperature predicted by the model described in the text, with $\tau_L = 25$ seconds and $f_s = 60(4)$ Hz. The upper filled curve (red online) is the model's predicted temperature for $N = 2.7 \times 10^3$ atoms in the same potential, which just barely fills the ring. The black dotted lines show the threshold reduced temperatures $(k_B T/\mu)_{max}$ required for pairing when $\lambda_0 = 1.0$ (lower) and $\lambda_0 = 0.5$ (upper) in the ring.

Next, to ensure atom loss was predominantly due to one-body background collisions, and not due to rethermalizing collisions (discussed later) or parametric heating via trap vibrations, we recompressed the sheet immediately after evaporation to roughly 2.5 times the minimum sheet power. This in turn approximately halved the ratio E_F/V_{evap} and increased the sheet trap frequencies by a factor of $\sqrt{2.5}$. We sub-

sequently ramped the magnetic field adiabatically to 100 mT where the interaction parameter $1/k_F|a| \approx 1.0$. At this stage, $T/T_F \approx 0.03$. Here, we held the atoms in the trap for varying amounts of time and took a set of absorption images to be used for in-situ analysis of the local equation of state in the halo region. In particular, we extracted the global reduced temperature, k_BT/μ, using the hybrid fitting function (4.8). The use of this hybrid fit function was justified a-posteriori since the ratio $k_BT/\hbar\omega_z \lesssim 1$ for all hold times used, and dimensional crossover thus occurred in regions of the halo where $\mu(r) \sim \hbar\omega_z$.

Fig. 4.6 shows the reduced temperatures measured in this configuration, for different holding times. For comparison, we also plot the predicted temperature profile obtained by numerical integration of the heating rate equation (4.12), for the initial conditions, estimated trap parameters, and vacuum lifetime in the experiment. The theory and measurements agree to within the error shown in Fig. 4.6, which was estimated from temperature fits using the upper and lower bounds of the sheet radial trap frequency, which is the dominant source of uncertainty. The filled region in the theoretical curve is obtained using the same radial sheet frequency uncertainty, which after recompression is about 4 Hz. By comparison, this uncertainty has a much smaller effect on the theoretical heating curve than the experimental one. In Fig. 4.6 we also show the predicted temperature increase for the bare ring with $N = N_D \approx 2.7 \times 10^3$ atoms in this potential. The effects of hole-heating on the system temperature are significantly greater for a bare ring due to the reduced heat capacity per particle. In either case, hole heating also sets a practical limit on the lowest achievable T/T_F, due to both the finite state preparation time used in the experiment and the balance between the thermalization rate and hole-heating rate. This window of preparation time is narrower in the bare-ring configuration however, since the heating rate is roughly twice that of the ring-dimple for all hold times shown in Fig. 4.6.

Additionally, we plot the time-dependent threshold reduced temperatures, given by the R.H.S. of equation (4.13), in Fig. 4.6 for $\lambda_0 = 1.0$ and $\lambda_0 = 0.5$. t_c can be identified as the time at which the threshold reduced temperature intersects the reduced temperature curve. Clearly, a ring-dimple configuration can offer a substantially larger (more than twice as large) window of time to perform BCS-limit experiments compared to a bare-ring configuration. This could be especially important in an experimental apparatus with limited vacuum lifetime, or for experiments attempting to probe increasing $1/k_F|a|$ limits.

Because our temperature measurement method involves a fit to the halo atoms, whose broad extent into the harmonic sheet potential makes in-situ thermometry convenient, we did not obtain measurements of the temperature of atoms in a bare ring, as some other method of thermometry would be required to obtain data on the heating rate in that configuration. One alternative we may eventually employ is to adiabatically deform the trap into a harmonic potential, then relate temperature measurements in that configuration to the temperature of the bare ring by conservation of entropy (see, for example, Refs. [79, 80]). This technique is substantially more complex and involves more potential sources of error than extracting the temperature from a fit to the halo, however. The utility that a halo offers for temperature measurements in these kinds of fermionic systems should not be overlooked.

Section 4.5

Thermalization and Loss

In the idealized scenario described above, the equilibrium state after the ejection of an atom by a background collision is still a mostly-filled Fermi sea, and subsequent elastic collisions within the system will tend to repopulate the empty state. In the simplest case, this occurs when two atoms at the Fermi level scatter (Pauli blocking

suppresses scattering in the Fermi sea), one drops in energy to fill the empty state and the other is promoted to an energy $\epsilon \geq E_F$, in something like an Auger process. If $\epsilon \geq V_{evap}$, the excited atom can escape from the trap, and the new equilibrium is a filled Fermi sea with $N-2$ atoms. This loss of an additional atom always occurs (at $T=0$) for $V_{evap} = E_F$, and the probability decreases to zero when $V_{evap} = 2E_F$, since the maximum scattering energy is $2E_F$.

More generally, the additional loss above the background rate will depend on other quantities that may include the ratio E_F/V_{evap}, the elastic collision rate, temperature, and conserved quantities pertaining to the trap potential. Experimentally we observed that the initial loss rate was three times the background rate when we did not increase the sheet depth after evaporation. This can occur if fermions scattered via the Auger process (with energy up to $2E_F$) scatter off another fermion and in turn excite another fermion to an energy above the Fermi level (up to $1.5E_F$), which can also escape if its energy is above V_{evap}. This process can repeat if one or both of these atoms remain in the trap long enough. Thus, a single background collision in our ring-dimple trap may seed a cascade of energy from a single highly excited "Auger" fermion to a state of many weakly excited fermions above the Fermi level, some of which may escape the trap. A non-trivial trap geometry can make the re-equilibration dynamics quite complicated, but qualitatively we would expect modifications to the loss and heating rates especially for $E_F \approx V_{evap}$. In this case the system would typically experience increased initial loss, with high energy atoms being lost from the trap, keeping the temperature low but causing the Fermi energy to drop rapidly. The loss rate would also become time dependent, and asymptotically approach the vacuum-limited loss rate as the Fermi energy drops well below the evaporation depth. These re-equilibration dynamics in ring-shaped systems are interesting in their own right, and further experimental and theoretical investigation is warranted.

Section 4.6

Adiabatic Cooling/Heating

Adiabatically ramping the scattering strength from the BCS limit to the weakly interacting BEC limit causes the system temperature to increase. This is a consequence of entropy and atom number being constant for such a ramp. If expressions are known for the entropy in both regimes, one may in theory enforce entropy conservation to extract a heating/cooling factor attained during the ramp. In the spirit of [60], we compute the entropy as a function of temperature, numerically, for a fixed atom number in both regimes, and invert the resulting entropy-conservation equation to find the heating factor.

The entropy may be universally computed as

$$S(N,T) = \log \mathcal{Z}(\mu,T) + \frac{U(\mu,T) - \mu N}{k_B T} \tag{4.14}$$

with $\mu = \mu(N,T)$, $\mathcal{Z}$ the grand canonical partition function and U the internal energy. We assume the trap parameters, which define the extensive thermodynamic volume and intensive trap depths and aspect ratios, are fixed. The quantities $\mathcal{Z}$ and U may each be calculated with knowledge of the density of states, while μ is computed by equation of state for the atom number. It therefore is a matter of computing the appropriate density of states in each regime.

The 3D DoS for ideal fermions is given by

$$g_F(E) = 2 \times \frac{4\pi m}{(2\pi\hbar)^3} \int_{V(\mathbf{r})\leq E} d^3r \sqrt{2m[E - V(\mathbf{r})]} \tag{4.15}$$

which one may have to compute numerically if $V(\mathbf{r})$ is complicated. In our case, the optical potential is formed by the intersection of a vertically propagating ring-

shaped beam and a broad horizontally propagating sheet beam. The full potential $V(\mathbf{r})$ includes gravity as well. The DoS for a weakly interacting BEC is slightly less straightforward. One begins with the Bogoliubov dispersion relation in the local-density approximation [60]

$$\epsilon_b(\mathbf{r},p) = \begin{cases} \sqrt{\frac{p^2}{2m_{mol}}\left\{\frac{p^2}{2m_{mol}} + 2[\mu - V(\mathbf{r})]\right\}} \\ \frac{p^2}{2m_{mol}} + V(\mathbf{r}) - \mu \end{cases} \tag{4.16}$$

where we have used the Thomas-Fermi approximation to express the condensate density as $gn_{cond}(\mathbf{r}) = \mu - V(\mathbf{r}) \equiv \mu(\mathbf{r})$. This dispersion may be inserted into the density of states integral

$$g_B(E) = \frac{1}{(2\pi\hbar)^3}\iint d^3r d^3p\ \delta\left[E - \epsilon_b(\mathbf{r},p)\right] \tag{4.17}$$

which is then broken into two pieces, corresponding to the Thomas-Fermi region and its exterior. Carrying out the integrations explicitly gives

$$\begin{aligned}\frac{(2\pi\hbar)^3}{4\pi m\sqrt{2m}}g_B(E) = E\int_{\mu(\mathbf{r})\geq 0} d^3r \sqrt{\frac{\sqrt{\mu(\mathbf{r})^2+E^2}-\mu(\mathbf{r})}{\mu(\mathbf{r})^2+E^2}} \\ + \int_{0<-\mu(\mathbf{r})\leq E} d^3r\sqrt{E+\mu(\mathbf{r})}\end{aligned}$$

It is important to note that here the energy E is measured above the chemical potential, as the Bogoliubov dispersion relation was obtained by diagonalizing $\hat{H} - \mu\hat{N}$. The density of states is sufficient to compute the relevant thermodynamic quantities in the weakly interacting BEC limit. Importantly, one may compute the BEC entropy and equate it to the BCS entropy to obtain the adiabatic heating factor during a ramp from the BCS to BEC limit. This heating factor sets practical limitations on the detecting superfluid coherence on the mBEC side of resonance.

For completeness we give the relevant thermodynamic formulae:

$$\log \mathcal{Z}_F = -\int_0^\infty dE\ g_F(E) \log\left[1 + e^{-(E-\mu)/k_B T}\right] \tag{4.18}$$

$$N_F = \int_0^\infty dE\ g_F(E) \frac{1}{e^{(E-\mu)/k_B T} + 1} \tag{4.19}$$

$$U_F = \int_0^\infty dE\ g_F(E) \frac{E}{e^{(E-\mu)/k_B T} + 1} \tag{4.20}$$

$$\log \mathcal{Z}_B = \int_0^\infty dE\ g_B(E,\mu) \log\left(1 - e^{-E/k_B T}\right) \tag{4.21}$$

$$N_B = \int_0^\infty dE\ g_B(E,\mu) \frac{1}{e^{E/k_B T} - 1} + N_{cond} \tag{4.22}$$

$$U_B = \int_0^\infty dE\ g_B(E,\mu) \frac{E}{e^{E/k_B T} - 1} \tag{4.23}$$

Then, from equation (4.14) we may, equation the fermionic and molecular bosonic entropies

$$S_B(N, T_{mBEC}) = S_F(N, T_{BCS}), \tag{4.24}$$

which describes the adiabatic connection for a ramp from the BCS to BEC limit. One may solve for T_{mBEC}, the final temperature in the mBEC limit, as a function of the initial T_{BCS}, the initial BCS temperature. We plot the entropies in the mBEC and BCS limits in figure 4.7 for a system of $20,000$ atoms in the trap described above. Due to the flatness of the fermionic entropy (red dashed line) above 250 nK, the final mBEC temperature is roughly constant as long as the atom number is fixed. Due to the hole-induced loss and heating, however, the shape of these entropy plots changes

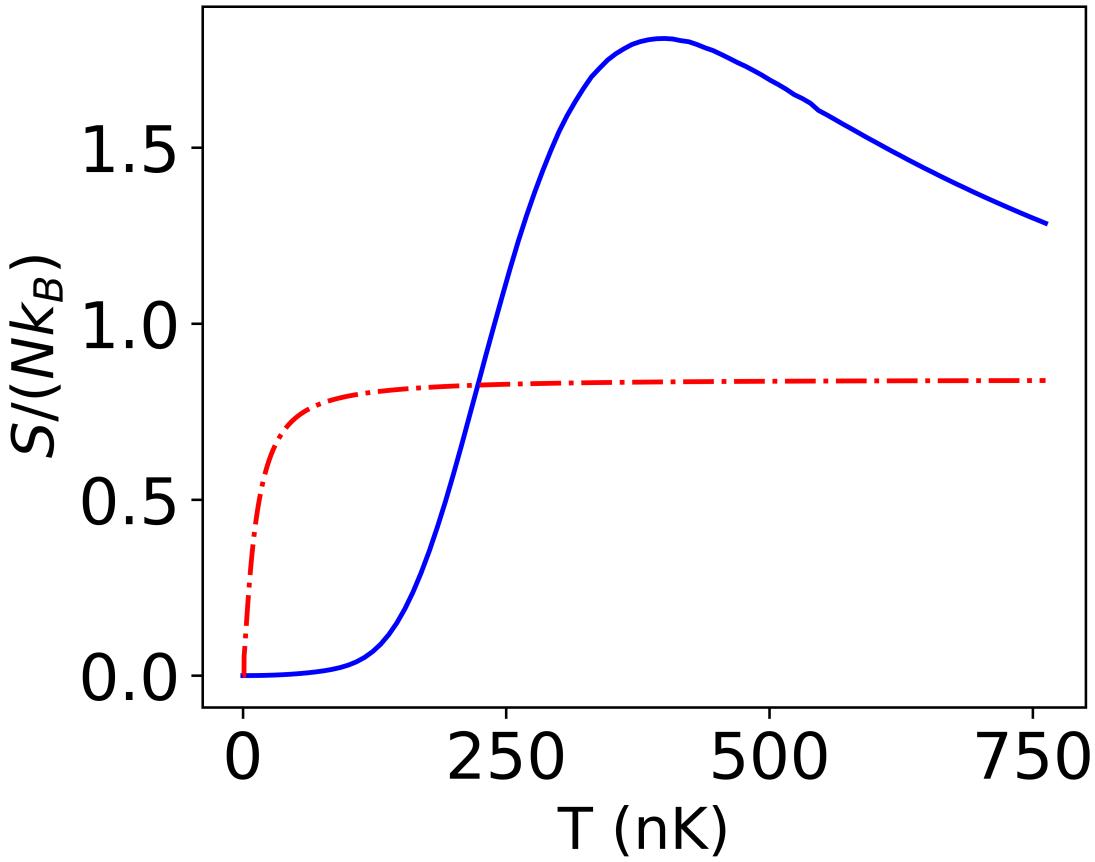

Figure 4.7: Entropy per particle as a function of temperature for the BEC (blue-solid line) and BCS (red-dashed line) regimes, with fixed $N = 20,000$.

over time, and we will discuss the impacts below.

In addition to the above thermodynamic relations, we may also consider the condensed fraction of molecules present in the mBEC regime. Since the local condensate density n_{cond} is defined by the Thomas-Fermi relation $gn_{\text{cond}}(\mathbf{r}) = \mu - V(\mathbf{r})$, we can define the condensed molecular number within some region Ω of space $N_{\text{cond}}(\Omega) = \int_\Omega d^3r\ n_{\text{cond}}(\mathbf{r})$. The condensed fraction of molecules is then $f_{\text{cond}}(\Omega) = N_{\text{cond}}(\Omega)/N_{\text{total}}(\Omega)$.

It is important to notice that, for the sake of interferometric detection, the condensate fraction f_{cond} before ballistic expansion should be sufficiently non-zero, at

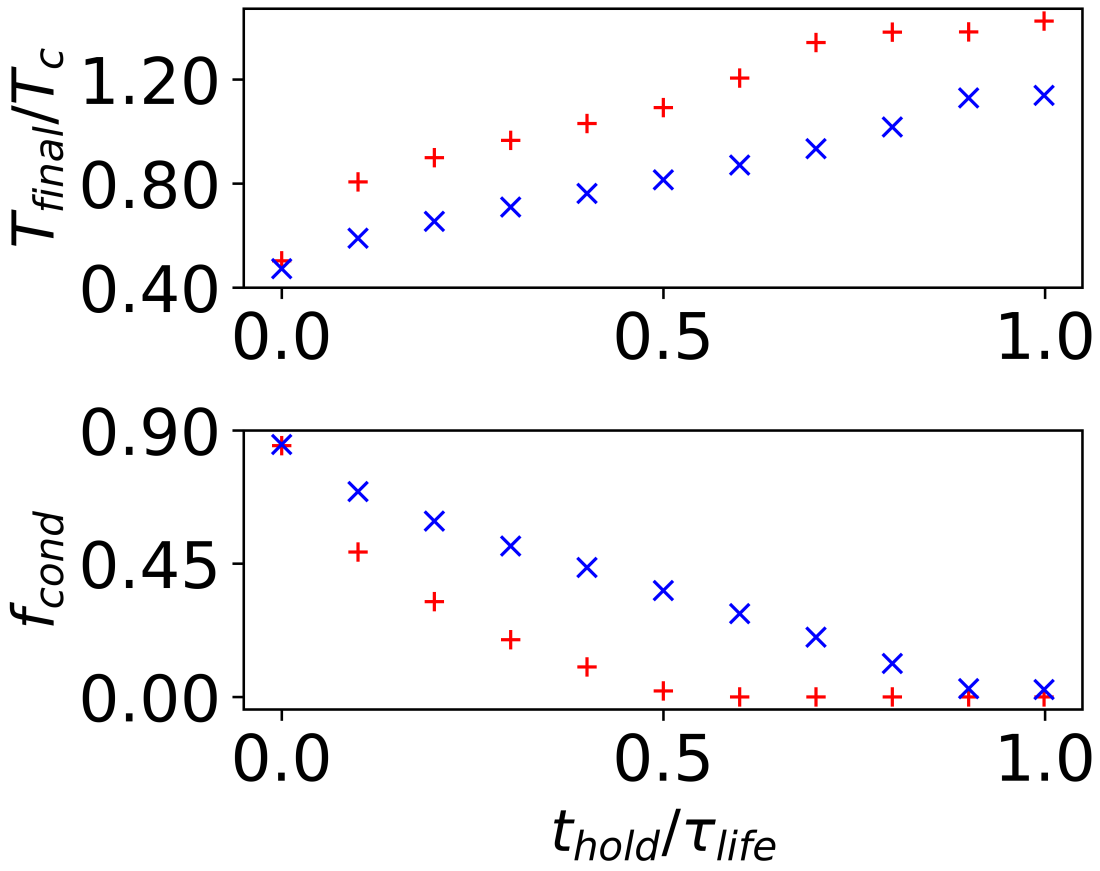

Figure 4.8: Top: Final relative temperature, T_{final}/T_c, after holding for a given time in the BCS limit and adiabatically ramping back to the mBEC limit. Bottom: Final molecular condensate fraction, f_{cond}, after the same process. The initial BCS temperature is 10 nK and hole-heating drives this temperature up over the holding time. Blue x markers corresponds to an initial population of 20000 atoms, while red + markers corresponds to 1500.

least in the regions of the trap of interest (i.e. the ring dimple region). In some of the early experiments performed in this thesis and in that of [31] and [65], signatures of BCS superfluidity are detected interferometrically in time-of-flight (ToF) expansion after an adiabatic ramp to the mBEC side of resonance. Due to Fermi hole heating, there is a finite amount of time one has to perform BCS-side experiments before the adiabatic BCS-to-mBEC ramp heating depletes, or substantially reduces, the molecular condensate. To predict the upper limits on BCS-side experiment time, we

combine the predictions for the time-dependent BCS heating rate (4.12) with the adiabatic heating factor modelled using the BCS and mBEC entropies. Namely, we solve (4.24) for the final mBEC temperatures as a function of the initial time-dependent BCS temperature and atom number obatined from the hole-heating equations. We plot in figure 4.8 the final temperatures and condensate fractions in the ring-shaped region of highest density after an adiabatic ramp to the mBEC side of resonance, as a function of the BCS hold time. Furthermore, we distinguish the cases of a ring-dimple and a bare ring by studying the adabatic heating for a initial populations of $N = 20,000$ and $1,500$ atoms, respectively. We see that the condensate fraction for the ring-dimple system is still substantial even for hold times $t_{hold} \sim \tau_L/2$, while that of the bare-ring is practically zero at this time. This demonstrates numerically the capability of our system to perform bosonic interferometric detection after seconds-long experiments in the BCS limit, as long as one operates in the ring-dimple configration. One may still have to worry about decreased phase coherence as atom loss drives the system to lower dimensions and phase fluctuations become more prominent, which is an interesting topic for several reasons, but not discussed presently.

Section 4.7

Conclusion

We have demonstrated that one-body loss in a ring-shaped ensemble of ultracold fermions causes heating. We predicted the rate of temperature rise using a model that accounted for hole-induced heating, and have argued that this heating can be reduced by a particular choice of trap configuration. In particular, maintaining a large, dilute atomic background in contact with the ring helps to dissipate energy imparted into the ensemble via background collisions, which in turn keeps the temperature low for longer periods of time. A high quality vacuum is still essential to ensure that timescales

for heating are long enough to permit low-energy long-wavelength experiments on superfluids with low critical temperatures, but there are clear advantages to consider forgoing the simplicity of a bare-ring configuration in favor of the more complex but useful ring-dimple configuration.

Chapter 5

Detection of Persistent Currents

The experiment performed in Chap. 7 hinged on the ability to properly measure both the sign and magnitude of spontaneous persistent currents formed after quenching an degenerate ensemble of fermions into a superfluid state. This chapter gives important theoretical and experimental background for describing how the in-trap momentum distribution can be mapped in various ways onto observable density distributions. In particular, we will describe how the winding number -the observable quantifying the degree of quantized circulation of a persistent current around some closed path- can be measured using several different techniques. This chapter also presents the methods used to reliably perform such measurements, and discusses complications to their successful implementation for the given experimental configuration.

Section 5.1

Mapping Momentum onto Density

Experiments probing the signatures of superfluidity in ultracold gases very typically rely on obtaining information about the superfluid's flow properties. In multiply connected geometries such as the ones employed in this work, superfluidity can manifest itself in metastable states of quantized circulation. We are typically interested

in obtaining measurements of not just the total amount of flow around some closed path (i.e. global flow properties/winding numbers), but also local variations in the superfluid velocity field due to, for instance, thermal phase fluctuations or a locally introduced density perturbation. As flow properties are typically difficult to observe by taking in-situ measurements, time-of-flight (ToF) techniques are often employed as a means of mapping momentum distributions into observable density variations. We note however that Bragg or Raman techniques may be used to obtain information about the momentum distribution and correlation functions, although we do not discuss those techniques here [81–83]. In standard ToF, information about the initial momentum distribution of the ensemble is obtained after some amount of mostly-free ballistic expansion. For sufficiently long time of flight t_{ToF}, and in the non-interacting limit, the initial in-situ momentum distribution $n_0(k)$ becomes proportional to the instantaneous density distribution $\rho(x, t_{\mathrm{ToF}})$; The two are related by $n_0(k) \sim \rho(x = \hbar k t_{\mathrm{ToF}}/m)$. Furthermore, the momentum distribution is related to the density distribution through a Fourier transform. Thus, in this limit, there is a direct connection between the observable density and the desired momentum distribution in the trap. For shorter times of flight, there is still important information that can be extracted from the density profile after ToF, as we will discuss later in this chapter. However, the density distribution will not directly reflect the in-trap momentum distribution as it does in the long-time limit.

Section 5.2

Techniques for Detecting Persistent Currents

There are two main techniques used to detect persistent currents: The vortex core-size measurement, and the interferometric detection method. Both typically rely on a stage of ballistic expansion in the weakly interacting molecular BEC (mBEC) limit,

although one may still have sufficient signal to perform the latter technique on weakly interacting Cooper pairs in the BCS limit. We focus on mBEC ballistic expansion here.

Vortex core size measurement. With the vortex core-size measurement, the magnitude of a persistent current is obtained from the size of the vortex core after some amount of ballistic ToF [84]. In the far-field expansion limit, the density distribution is related to the in-situ momentum distribution by a simple Fourier transform. A persistent current state in a smooth, narrow ring of radius R and width $w \ll R$, is represented in polar coordinates as $\psi_\ell(r,\theta) = f_\ell(\frac{r-R}{w})\exp(i\ell\theta)$ where the z coordinate has been neglected for simplicity. Although technically the amplitude function f_ℓ generally depends on ℓ, its dependence is typically very weak for small values of ℓ. The Fourier transform of ψ_ℓ is related to $J_\ell(x)$, the cylindrical Bessel function of order ℓ:

$$\phi(k,\theta_k) = e^{i\ell\theta_k}\int_0^\infty drrf_\ell\left(\frac{r-R}{w}\right)J_\ell(kr) \overset{w\ll R}{\sim} e^{i\ell\theta_k}J_\ell(kR) \tag{5.1}$$

The complex square of this expression give the in-situ momentum distribution of the persistent current. In ToF, a non-zero winding number ℓ will reveal itself as density depletion in the vortex core around $r = 0$. For some fixed ToF $t_{\text{ToF}} \gtrsim mR^2/\hbar$, the size of this core will grow with increasing ℓ, as characterized by the ToF density distribution $\rho(r, t_{\text{ToF}}) \sim J_\ell^2[mrR/(\hbar t_{\text{ToF}})]$, and the core size $r_{\text{core}} \sim \hbar t_{\text{ToF}}\ell/(mR)$. Measuring this core size at some specific t_{ToF} and comparing to a pre-determined reference core size for an $\ell = 1$ persistent current at the same time allows the magnitude of the winding number $|\ell|$ to be obtained. It is important to note that no sign information about the persistent flow can be obtained from measurements of this nature. Additionally, only the global features of the flow (i.e. winding number) can be extracted from the vortex core size measurement.

5.2.1. Interferometric Detection

We now discuss in detail the interferometric detection technique, which was utilized extensively in the study of spontaneous current formation. While the magnitude of a persistent current may be revealed by the size of the vortex core after sufficiently long time of flight, extracting the sign of the current requires an alternative approach. A phase-sensitive measurement, i.e. one that extracts the complete phase information of the ensemble, is a commonly used technique for probing the flow of a persistent current state. Specifically, these techniques utilize the phase coherence between the superfluid ring and a suitably chosen reference superfluid to convert their respective local phase differences into a physically observable density profiles [65, 85–87]. This configuration can be engineered experimentally using the DMD, where either a target-shaped trap or a double ring is projected onto the atoms, with one sub-trap serving as the reference. The reference should be made to have as fixed and unchanging a phase as possible, regardless of the experiment being performed.

When released into ballistic expansion, the superfluids expanding from each of the sub-traps will begin to overlap and interfere coherently. The superfluid density n_{tot} can in general be written as

$$n_{\mathrm{tot}} = |\psi + \psi_{\mathrm{ref}}|^2 \tag{5.2}$$

$$= n + n_{\mathrm{ref}} + 2\sqrt{n n_{\mathrm{ref}}} \cos \Delta\phi \tag{5.3}$$

where ψ, n are respectively the wavefunction and density of the "experiment" sub-system, ψ_{ref} and n_{ref} are respectively the reference wavefunction and density, and $\Delta\phi$ is the phase difference between the two ensembles. The self-interference terms can be difficult to interpret, and do not give straightforward insight into the phase profile of the respective ensemble. The interference term, proportional to $\cos \Delta\phi$,

contains the relevant information about the phase profile of the experimental sub-trap of interest, insofar as the phase difference $\Delta\phi$ of the overlapping superfluids can be straightforwardly mapped back onto the phase difference in the trap.

To extract meaningful information about the phase profile of one of the sub-ensembles, there is an optimal time of ballistic expansion to perform the absorption image. This time should be chosen long enough such that the sub-ensembles can interfere substantially with each other, but short enough such that a given sub-ensemble doesn't self-interfere substantially. Additionally, the far-field expansion limit should be avoided as the density distribution becomes isotropic and phase differences between the sub-ensembles become too small to detect.

We can study the specific case of the double ring geometry used extensively in the spontaneous currents experiment. In this scenario, we have two concentric rings of inner radii r_1 and r_2 and equal widths $w_1 = w_2 \equiv w$ (with $r_2 > r_1 + w$). The ring widths roughly set the velocity scale at which the superfluid expands ballistically in the radial direction: $v_r \approx \hbar/(2mw)$ (The factor of 2 accounts for the molecular pair mass). The sub-ensembles begin to interfere substantially at time t_{ToF} when $v_r t_{\mathrm{ToF}} \approx (r_2 - r_1)/2 \equiv \Delta r/2$. This defines the optimal time scale $t_{\mathrm{ToF}} = mw\Delta r/\hbar$ at which phase differences can be meaningfully extracted interferometrically. Self-interference becomes substantial at time $t \approx mw\bar{r}/\hbar$, where $\bar{r} = (r_1 + r_2)/2$. For the double ring configuration typically employed in our experiment, $r_1 = 6$ μm, $r_2 = 11$ μm, and $w = 3$ μm. This gives $t_{\mathrm{ToF}} = 1.4$ ms. This is roughly the same as the time of flight typically used in the spontaneous current experiments to perform interferometric detection of the winding number.

In a cylindrically-symmetric (not necessrily ring-shaped) trap, the expectation value of the order parameter representing a low-lying metastable persistent current state or vortex state with winding ℓ may be generally written as $\psi_\ell(\mathbf{r}) =$

$\sqrt{n_{0,\ell}(r,z)}e^{i\ell\theta}$, with density $n_{0,\ell}$ being a function of only the transverse degrees of freedom. In the target or double ring trap configuration, we have additionally an azimuthally-symmetric reference wavefunction, $\psi_{ref}(\mathbf{r}) = \sqrt{n_{0,ref}(r,z)}$. When the trap and interactions are suddenly switched off, the atomic ensemble is projected onto free particle eigenstates which propagate according to the corresponding free-particle propagator. Due to angular momentum conservation, the time-evolved persistent current wavefunction retains the same angular phase dependence, and can be written $\Psi_l(\mathbf{r},t) = [\sqrt{n_\ell(r,z,t)}e^{i\phi_\ell(r,z,t)}]e^{i\ell\theta}$ for some time-dependent density n_ℓ and phase ϕ_ℓ. This wavefunction will interfere with the time-evolved reference wavefunction, $\Psi_{ref}(\mathbf{r},t) = \sqrt{n_{ref}(r,z,t)}e^{i\phi_{ref}(r,z,t)}$, whose angular phase profile is flat but whose radial phase profile is in general not. The total density profile after time of flight t is

$$\begin{aligned} n_\ell^{\text{tot}}(\mathbf{r},t) &= |\Psi_\ell(\mathbf{r},t) + \Psi_{ref}(\mathbf{r},t)|^2 \\ &= n_\ell(r,z,t) + n_{ref}(r,z,t) + ... \\ &\quad 2\sqrt{n_\ell(r,z,t)n_{ref}(r,z,t)}\cos\left[\phi_\ell(r,z,t) - \phi_{ref}(r,z,t) + \ell\theta\right] \end{aligned} \tag{5.4}$$

Thus, the interference results in a periodic modulation of the azimuthal density profile. There are exactly ℓ maxima (or minima) present in the angular density profile for fixed r. Sign information is revealed whenever there is a radial velocity mismatch between the persistent current state and the reference state for non-zero ℓ. This can be seen by examining curves of maximum or minimum density, $r_c(\theta)$, defined by $\frac{\partial n_\ell^{\text{tot}}}{\partial\theta}|_{r=r_c(\theta)} = 0$. This condition implies $\phi_\ell(r_c(\theta),z,t) - \phi_{ref}(r_c(\theta),z,t) + \ell\theta = m\pi$, with m an integer. Even m describe the density maxima, while odd m the minima. Assuming a linear *radial* phase difference between the persistent current and reference state (valid in the near-to-mid field limit), a series of spiral arms emerge in the density profile, with polar profile $r_c(\theta) = r_0(l\theta + 2m\pi)$ for some constant r_0. Tracing a single spiral arm

(labelled by integer m) around a full 2π revolution, a (signed) radial displacement $\Delta r = 2\pi r_0 \ell$ is observed. The radial distance between successive spirals (m and $m+1$) is $\delta r = 2\pi r_0$. Thus, the ratio of these two quantities, rounded to the nearest integer, is the winding number ℓ, with both magnitude and sign.

We can further isolate the interference (third) term in equation (5.4) by multiplying by $e^{-im\theta}$ (with $m \neq 0$) and integrating from 0 to 2π. As the first two terms in (5.4) are θ-independent, they integrate to 0. Meanwhile, the integration picks out only terms with $|m| = |\ell|$. Explicitly, with $\Delta\phi_\ell \equiv \phi_\ell - \phi_{ref}$, we find

$$c_{\ell,m} \equiv \frac{1}{2\pi}\int_0^{2\pi} n_\ell^{\mathrm{tot}}(\mathbf{r},t)e^{-im\theta}d\theta = \sqrt{n_\ell n_{ref}}\left(\delta_{m,\ell}e^{i\Delta\phi_\ell} + \delta_{m,-\ell}e^{-i\Delta\phi_\ell}\right) \tag{5.5}$$

which is zero for any $|m| \neq |l|$. Furthermore, when $m = l$, if we take $m > 0$ WLOG, then the phase difference $\Delta\phi_l(r,z,t) = \arg c_{l,l}(r,z,t)$ can be extracted. The sense of the persistent current is also extractable via $\Delta\phi_l(r,z,t)$; Since the phase difference is approximately linear in the near-to-mid field limit, and $\Delta\phi_l = \Delta\phi_{-l}$, then by fitting a line to this phase profile, we identify the sign of the winding number with the sign of the fit-extracted slope. The $m = 0$ case should be treated separately, since we would have the additional non-interfering terms entering into the analysis. If $\ell \neq 0$, then an azimuthal average of the density profile will eliminate the interference term, whereas if $\ell = 0$ this term will remain unaffected, and the density profile is equal to its azimuthal average. This azimuthally averaged comparison allows one to check for an $\ell = 0$ non-circulating state.

We can further model the expansion dynamics in the molecular BEC (mBEC) limit by assuming an initial Thomas-Fermi distribution in each ring and assuming the expansion occurs ballistically [88]. Then, the time-evolved wavefunction can be obtained from the free-particle propagator acting on the initial wavefunction, which essentially amount to performing a Fourier and inverse Fourier transform. Namely,

if the initial wavefunction in sub-ring j and its momentum-space representation are given by $\psi_0^{(j)}(\mathbf{r})$ and $\phi_0^{(j)}(\mathbf{k}) = \mathcal{F}[\psi_0^{(j)}](\mathbf{k})$, respectively, then the time evolution is obtained via

$$\Psi^{(j)}(\mathbf{r},t) = \int d\mathbf{k}\phi_0^{(j)}(\mathbf{k})e^{-i\hbar k^2 t/2m + i\mathbf{k}\cdot\mathbf{r}} = \mathcal{F}^{-1}\{\mathcal{F}[\psi_0^{(j)}](\mathbf{k})e^{-i\hbar k^2 t/2m}\}(\mathbf{r}) \tag{5.6}$$

In the Thomas-Fermi limit, the initial wavefunction within each sub-ring can be written as $\psi_0^{(j)}(\mathbf{r}) \sim \sqrt{1 - V(\mathbf{r})/\mu_j}\exp(i\ell_j\theta)$, where where V is the ring potential, typically of the form $V(\mathbf{r}) \sim 1 - \exp[-2(r - r_j)^2/w^2]$, μ_j is the chemical potential and ℓ_j the winding number for sub-ring j. From earlier analysis, we have approximately $\phi_0^{(j)}(k,\theta_k) \sim \exp(i\ell_j\theta_k)J_{\ell_j}(kr_j)$.

For long ToF $t \gg mw^2/\hbar$, a stationary phase analysis of the integral (5.6) with rapidly oscillating phase function $f(\mathbf{k}) = \hbar k^2 t/(2m) + \mathbf{k}\cdot\mathbf{r}$ reveals the asymptotic behavior

$$\Psi^{(j)}(\mathbf{r},t) \sim \frac{1}{t^{3/2}}\phi_0^{(j)}\left(\frac{m\mathbf{r}}{\hbar t}\right)e^{imr^2/(2\hbar t)}. \tag{5.7}$$

Due to the common radial phase factor between the two subrings, there is no radial velocity mismatch between the expanding condensates at long ToF. Therefore, signatures of persistent currents in this limit show up only as azimuthal density modulations with frequency $|\ell_1 - \ell_2|$, superimposed upon vortex cores of size $r_{\text{core}} \sim t\min(|\ell_1|,|\ell_2|)$. Importantly, interferometric techniques do not reveal sign information in this limit, but only magnitude. Additionally, the signal strength falls as $t^{-3/2}$, which makes detection even more difficult in this limit.

The appearance of spiral arms occurs in the near-to-mid field expansion regime. If $t_0 \equiv \frac{mw^2}{\hbar} \sim 1.5$ ms sets the expansion time scale for a ring of width $w \sim 2$ μm, then we expect to see spirals when $0 < t \lesssim t_0$. The fringe visibility and spacing is also a function of the reference ensemble population and geometry. A tightly confined

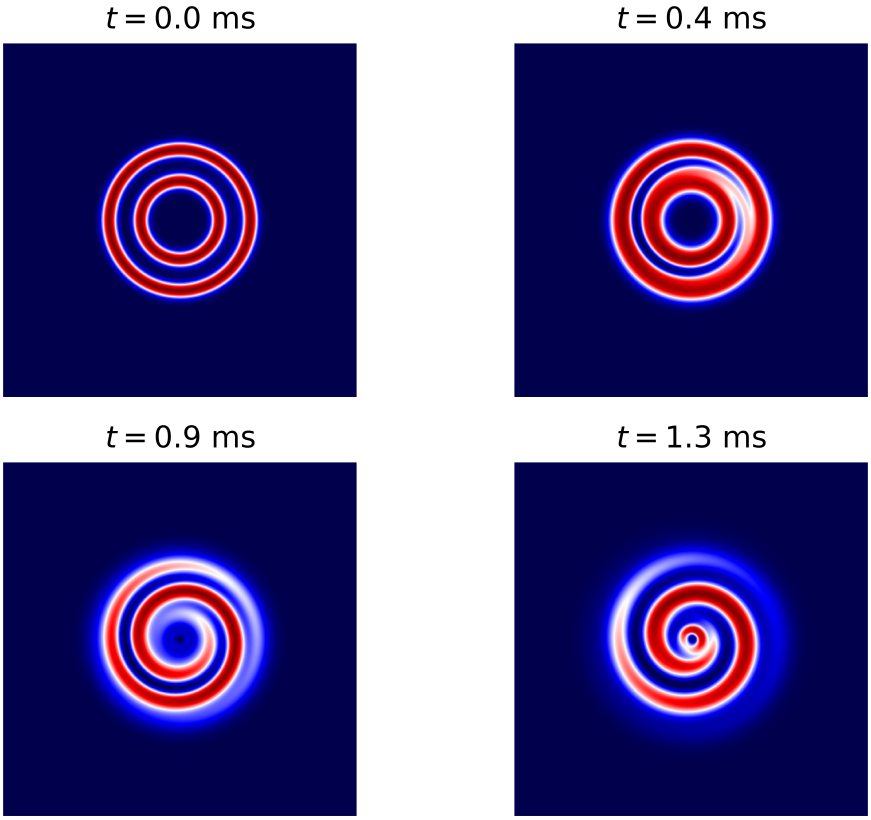

Figure 5.1: Simulation of a typical $\ell = 1$ spiral interferogram showing expansion from two concentric annuli at various times of flight. The outer (reference) ring has $\ell = 0$ while the inner ring has $\ell = 1$. Spirals start to become visible after about 0.5 ms ToF, and the vortex core can also be seen in the two latter-most images.

reference ensemble will expand more rapidly than a weakly confined one, producing spirals that are initially closely spaced together as the rapidly moving molecules expand, but grow apart during the expansion into the far field. Furthermore, the density of molecules in the overlap region should be made to be as equal as possible amongst the persistent current and reference ones, to ensure maximum spiral contrast. This can be achieved by ensuring an equal population of molecules in each sub-ring before expansion. Additionally, closely spaced spirals will be blurred by the imaging objective PSF (see figure 5.1 for a numerical simulation). While local phase information can be measured in the near-field, variations in the position of the fringes may be

difficult to detect if they occur on length scales at or beneath the imaging resolution.

Phase Fluctuations. Due to the possibility of phase fluctuations in tightly confined rings with small atom number (below the limit for the phase-fluctuating condensate regime), the contrast and/or connectivity of spirals may be noticeably reduced. We can model phase fluctuations around the ring by assuming, when in this regime, that the phase of the order parameter is a fluctuating quantity. That is, at each point on the circumference of the ring, the phase field is decomposed as $\phi_\ell(\theta) = \ell\theta + \delta\phi(\theta)$. The smooth non-fluctuating component encodes the phase winding ℓ of the superfluid. The fluctuating component $\delta\phi$ of the phase field is represented as a stochastic Gaussian variable satisfying $\langle\delta\phi(\theta)\rangle = 0$. Following the theory in [89–91], we can expand the fluctuating phase field in terms of the small-amplitude phononic excitations of the superfluid. In the long-wavelength limit, and in 1D for simplicity, we can model phase fluctuations as

$$\delta\phi(\theta) = \frac{1}{\pi}\sqrt{\frac{C}{l_\phi}}\sum_{m=1}^{\infty}\frac{1}{m}\xi_m e^{im\theta} + \text{c.c} \tag{5.8}$$

where the phonon creation/annihilation operators were replaced with Gaussian variables with variance N_m, the Bose-Einstein distributed occupancy of mode m. The long-wavelength behavior $N_m \sim 1/E_m$, with the phononic dispersion $E_m \sim |m|$. l_ϕ is the so-called thermal correlation length, quantifying the extent over which phase fluctuations are correlated, and C the ring circumference. Finally, the ξ_m are standard i.i.d. random variables. Due to the built-in single-valuedness of the expansion (5.8), the phase fluctuations do not contribute to the winding number, which is set only by the smooth non-fluctuating part $\langle\phi(\theta)\rangle$. For larger amplitude superfluid excitations, we may expect phase-slips events to occur randomly due to these fluctuations, but they do not appear in the linear phononic model.

We show the results of simulating the phase fluctuating regime on the interferometric detection of a persistent current in Fig. 5.2. While it is also possible that density fluctuations can impact the interferometric of a persistent current, we assume that the condensate is robust enough that density fluctuations are heavily suppressed, and that structure in the spiral fringes is predominantly due to phase fluctuations.

It is a goal of future experiment to measure these phase fluctuations, and in particular their onset, by utilizing the interferometric detection scheme. With a perfectly flat and non-fluctuating phase reference, phase fluctuations in the "experiment" ring appears as ripples in the spiral arms. These ripples thus encode important information about the strength of phase fluctuations, and the distances over which those fluctuations are correlated.

5.2.2. Experimental protocols for interferometric detection

Both the vortex core-size measurement and the interferometric detection technique rely on a stage of (mostly) free ballistic expansion so that the momentum distribution is minimally altered during flight. To accomplish this, one may chose to either adiabatically ramp the scattering length in ~ 100 ms from a potentially large initial value to the weakly attractive mBEC limit before release, or to utilize a magnetic field "jump" to rapidly reduce the scattering length over ~ 10 μs time scales before release. The field jump technique preserves the pair momentum distribution, which adjusts on much longer time scales compared to the two-body collisional time scale [40, 92]. We discuss now the two approaches.

Adiabatic Ramp Technique. The adiabatic ramp technique, while most straight forward to implement technically, is prone to complications. Three-body losses for weakly interacting molecules set upper limits on the ramp times one may use before release: One must be sure to ramp slow enough for the dynamics to remain adiabatic,

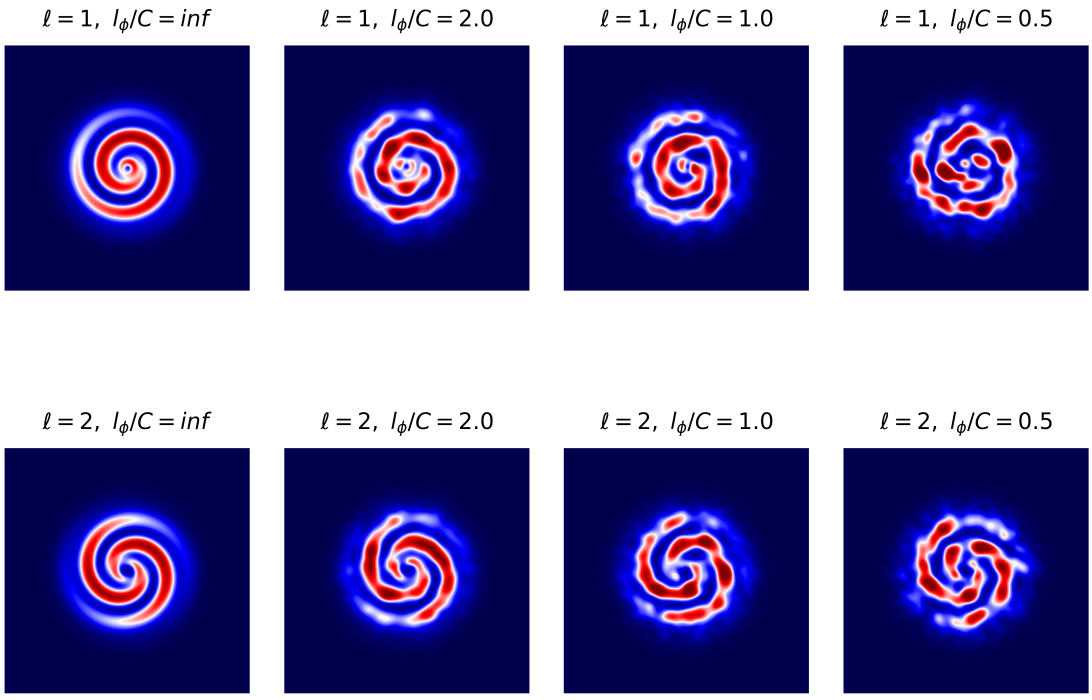

Figure 5.2: 1.3 ms time evolution of the same in-situ double ring configuration as in Fig. 5.1, but with phase fluctuations included, simulating the phase-fluctuating regime. The interferograms have been convolved with a 1.5 μm point-spread function to simulate the finite resolution of our imaging objective. The top row shows persistent currents with winding number 1, and the bottom row with winding number 2. We can see how thermal phase fluctuations, quantified by their correlation length l_ϕ, can play a very important role in the subsequent ToF dynamics, and can greatly diminish the signatures of the persistent current in the initial state. These fluctuations, however, do not cause phase slips, and the winding number is still preserved despite the ripples and breaks in the interference fringes. In this simulation, both the inner and outer ring are fluctuating, although experimentally measuring the fluctuations may require engineering the reference ensemble to be as smooth as possible.

while fast enough to avoid loss on the ramp time-scales. Losses are accelerated by the fact that, for round-bottomed ring traps, the molecular condensate density can become quite large, especially when the scattering length becomes small. This can

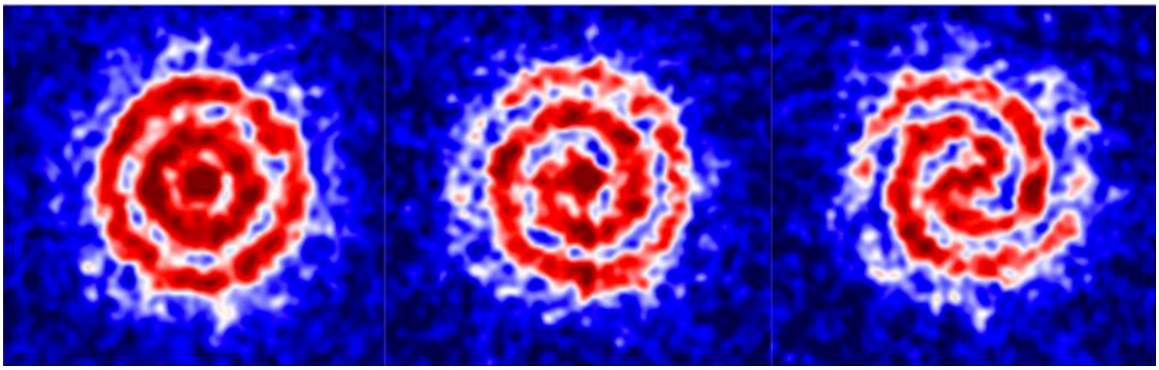

Figure 5.3: Example measured interferograms obtained after ballistic expansion for 1.2 ms from a double ring configuration, and using the rapid ramp technique. From left to right, the winding numbers are 0, 1, and 2. The ripples in the fringe patterns are indicative of phase fluctuations in the in-situ phase profile of the superfluid, although they do not destroy the topological properties of the persistent current.

be mitigated somewhat by using a wider, flatter ring to limit the density. On the other hand, slightly faster ramps, which are still adiabatic with respect to the *local* many-body thermodynamics, may not be adiabatic with respect to motion of bound pairs or atoms within the trap. This is especially true with atoms present in the halo, which may experience radial trap frequencies of only a few tens of hertz. Clearly ramps on the order of a few tens of milliseconds are not sufficient for halo atoms or molecules to wick into the ring dimple region and equilibrate. As a result, the pre-release distribution won't be in global thermodynamic equilibrium, and so care should be taken when interpreting results from ballistic expansion. Additionally, we found that adiabatic ramps to the mBEC limit affected the stability of persistent currents, and often times the wicking of normal-component atoms or pairs into the ring dimple during the ramp caused supercurrent phase slip events. This complicated initial efforts to measure the statistics of spontaneous current formation.

We discovered that even for mBEC ramps that are adiabatic with respect to motion in the broad sheet, the rotational state of the halo can significantly impact the persistent current state in the ring after the ramp. This is because the chemical

potential decreases as molecules bind more tightly together, which causes these pairs to wick into the ring region during the ramp. As angular momentum is conserved in this process, and the moment of inertia is substantially reduced by the end of the ramp, the average angular momentum per particle in the ring is greatly increased. This is turn enhances the likelihood of a phase slip causing a vortex, or vortices, to penetrate into the ring. Thus, if a persistent current is prepared in a well-defined state near the Feshbach resonance, it may wind up to a larger rotational state after a slow ramp to the mBEC limit if there is even a small amount of angular momentum in the halo.

Rapid Ramp Technique. The rapid field jump technique mitigates many of the above issues, and we will now discuss some of the important criteria for its successful implementation. The rapid ramp technique relies on a separation of important time scales in the system. Namely, the jump must be adiabatic with respect to two-body time scales, but fast enough to project the many-body momentum distribution onto a state of weakly interacting pairs which can expand freely. The two body-scale is typically set by the inverse energy gap between the bound Feshbach molecular state and the zero-energy free two-particle state at the Feshbach resonance. A Landau-Zener analysis reveals that transitions between this molecular state and an unbound pair are suppressed when the combination $An/\dot{B} \gg 1$, where n is the density and A depends on the details of the Feshbach coupling [40]. The key point is that molecules are preserved when the density is high, reflecting the enhanced likelihood for two free atoms to pair up, or when the magnetic field sweep rate $\dot{B}$ is small. The requirement that we preserve the pair momentum distribution, however, means that the time taken to leave the strongly interacting regime, approximately $\Delta B/\dot{B}$, should be small compared to the inverse scattering rate of pairs in the trap, which scales as $(E_F/h)^{-1}$ near the Feshbach resonance. We found empirically that, for field jumps rates of 10

G/μs, the pair conversion efficiencies were about 80% for typical densities of around 1 atom/μm^3 (See Appendix A). Due to such high efficiencies, we utilized the rapid ramp technique in most experiments requiring ToF analysis of the momentum distribution, and in interferometric detection of the winding number.

Several difficulties, however, presented themselves when optimizing the rapid ramp technique for our system, which we will discuss now. The first difficulty was related to the technical implementation of a rapid field jump. The field jump is accomplished by connecting sub-coils in the science cell coil assembly to dedicated power supplies and switching circuitry. This enabled one or both of the sub-coils to be switched off independently, and the magnetic field to be jumped quickly. Large transiently induced currents in the sub-coils from the rapid switching of the so-called "jump coil", however, caused oscillations in the magnetic field that only decayed on tens-of-millisecond time scales. To circumvent this issue, we performed coil switching "acrobatics", using the IGBT based switches on each sub-coil, as follows:

- 1) Simultaneously switch off both the jump-coil and main science cell coil to allow current and transients to rapidly decay.
- 2) Some small amount of time t_{so} later switch back on the main science cell coil to allow current back through this sub-coil

If timed properly, we found we could stabilize the current in the science cell coil after the jump coil had been switched off after only 100 μs, as opposed to several ms. The optimal switch-on time t_{so} for the science cell coils was empirically determined to follow a linear trend in the jump-coil current:

$$t_{\mathrm{so}} = 9.1\ \mu\mathrm{s} + 2.28\ \frac{\mu\mathrm{s}}{\mathrm{amp}} I_{\mathrm{JC}} \tag{5.9}$$

where I_{JC} is the jump-coil current before switch-off. The currents in each sub-coil

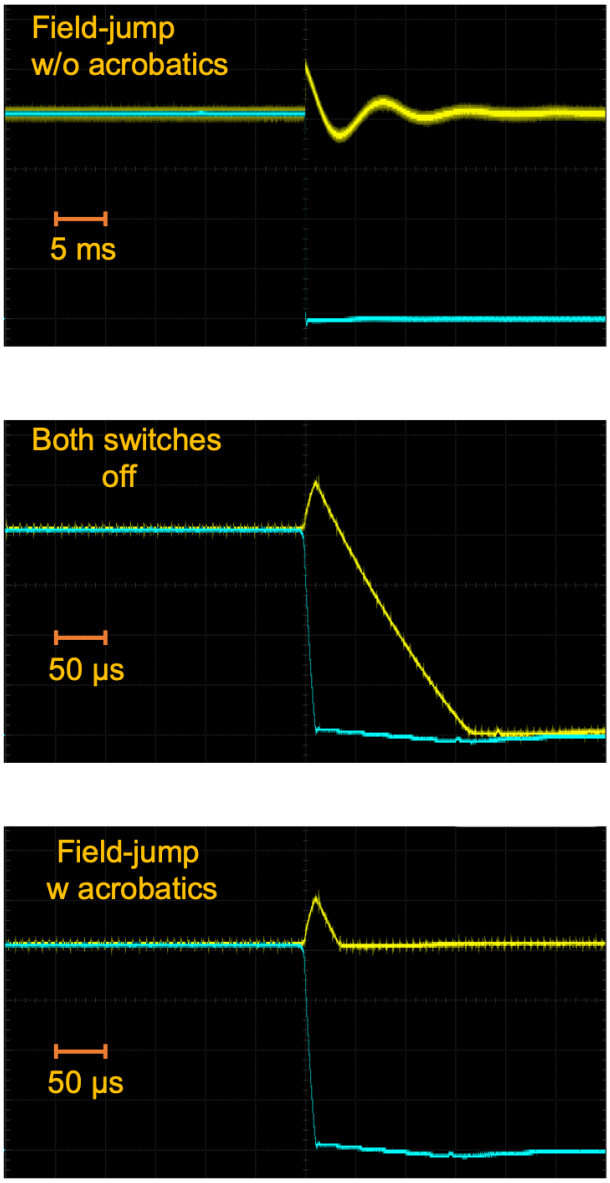

Figure 5.4: Oscilloscope traces showing the currents in the science cell (yellow trace) and jump (blue trace) coils for various switching methods. (Top) A simple switch-off of the jump-coil causes transients in the science cell coil that decay in about 20 ms, which is far too long for a successful rapid field ramp. (Middle) Both switches are shut off and the current in each coil decays rapidly. (Bottom) Using the field-jump acrobatics described in the text, we can null out the induced transients in the science cell coil after only 50 μs and in the jump-coil after only a few hundred μs.

were monitored using hall current sensors, which aided in determining the proper timings to switch the science cell coils back on.

The second difficulty was due to the slight misalignment of the magnetic field centers of each sub-coil; The field center when run at the same current together was different to the field center of a singly operated sub-coil. This in turn caused a shift in the magnetic field center during the field jump. As a result, the atoms and molecules would drift towards the new field center during ballistic expansion. Since the magnetic field gradient experience by the molecules was roughly constant, the relative motion of the molecules was preserved during time of flight, and only the center of mass position varied. This meant that the in-situ momentum distribution could still be faithfully measured in ToF, despite a shift in the center of mass position of the molecular cloud.

In its present configuration, the magnet coils only allow for jumps between fields separated by about 200 G. For jumps starting from fields below the Feshbach resonance, the final field ends up being small enough ($\lesssim 600$ G) such that the molecules begin to bind very tightly together and shift out of resonance of the imaging beam. Jumps from at or slightly above the Feshbach resonance, however, conveniently place the final field at around 650 G which is typically used for mBEC ballistic expansion. This was indeed the configuration used in the experiment detailed in the next chapter, which utilized a jump from around 850 G to 650 G to initiate free ballistic expansion.

Interferometric detection, in conjunction with the rapid field jump technique, allows one to access the instantaneous phase profile of the order parameter over the entire BEC-BCS crossover. This is particularly enticing for experiments intending to probe the dynamics of fluctuating phase-coherent quantities, such as the cooper pairing field near the BCS transition. Sign information of persistent currents also opens to door to performing experiments on spontaneous current formation, where the statistics of the corresponding winding numbers shed light onto dynamical universality. In particular, the interferometric detection scheme was crucial for probing

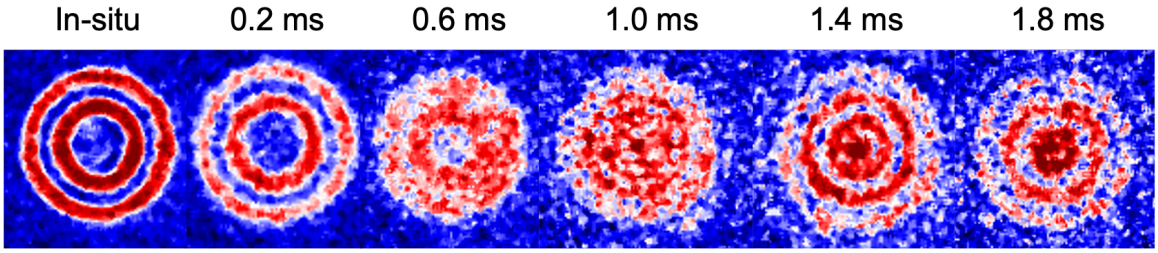

Figure 5.5: Time evolution of an $\ell = 0$ current state undergoing ballistic expansion. The expansion was initiated after a rapid field jump from the Feshbach resonance at 83 mT to a final field of 65 mT, which preserve the initial momentum distribution of the pairs at unitarity. Detectable interference features emerge after roughly 1 ms of ToF, and clear resolvable fringes at around 1.4 ms. Each image is a single realization, although with sufficient phase stability between the two sub-traps, one may build up averages of many interferograms to assess the phase profile encoded by the fringes more precisely.

biases in the winding number statistics due to, for instance, a non-zero rotation in the normal fluid above the BCS transition.

Chapter 6

The Kibble-Zurek Mechanism

The Kibble-Zurek Mechanism (KZM) is a paradigmatic model of non-equilibrium phase transitions. It predicts a scaling law for the density of defects nucleated during a quench across a second-order phase transition. The theory originated from efforts by T. Kibble to describe large-scale cosmological structures that were purported to have been created after a rapid cooling phase following the big bang [7]. Building upon Kibble's insights, W. Zurek then attempted to bridge a connection between Kibble's predictions in a cosmological setting to experiments performed on superfluid Helium [8]. The notion of universality -that microscopically distinct system can behave strikingly similarly close to a second-order phase transition- provides such a bridge. The key prediction of the KZM is that the density of defects formed as a system is dynamically quenched through its critical point is governed by a set of universal properties pertaining to the static (equilibrium) phase transition. We will discuss how defects are created by invoking a simple adiabatic-impulse-adiabatic approximation, and how these defects may subsequently "fuse" into topologically protected metastable states with observable and measurable properties. While heavy focus will be placed on ring-shaped geometries here, which support topologically protected states of quantized flow called persistent currents, more generally we hope to

understand how dynamically quenching from a disordered state into an ordered state create spontaneous superfluid excitations, whose properties meaningfully connect to the properties encoding the description of the corresponding phase transition. To this end we study a model of spontaneously-formed persistent currents based off of a stochastic Landau-Ginzburg model, with the goal of understanding how variable-rate quenches affects the statistics of winding number formation in superfluid rings.

Section 6.1

Homogeneous KZM

6.1.1. Correlation Functions

To understand the Kibble-Zurek mechanism, the notion of a correlation function, and its associated correlation length, is needed. The correlation length -the quantity that sets the average extent of an internally-correlated domain during the quench- is a single length scale associated to the two-point equilibrium correlation function. In KZ theory, the order parameter is assumed to take on a fixed an well-defined value within the correlation region.

In a uniform and isotropic system, this correlation function is given by

$$G(r) = \langle \delta\psi(r)\delta\psi(0)\rangle - \langle \delta\psi(0)\rangle^2 \tag{6.1}$$

where $\delta\psi(r) \equiv \psi(r) - \langle\psi(r)\rangle$ measures deviations from the expected value of the order parameter ψ, r is distance, and angle brackets denote thermal averaging. Near a second order phase transition, the correlation function has an asymptotic scaling form

$$G(r) \sim r^{-s} e^{-r/\xi} \tag{6.2}$$

with some exponent s that depends on the system dimension and length scale ξ, known

as the correlation length. Although we do not derive this result here, it is a well-known consequence of the fluctuation-dissipation theorem that relates statistical fluctuations in some thermodynamic quantity to its response to small external perturbations [93]. The correlation length ξ sets the length scale over which fluctuations are correlated, and depends on the distance to the transition, $\epsilon \equiv 1 - T/T_c$. It scales as

$$\xi \sim |\epsilon|^{-\nu}(1 + c|\epsilon|^{\nu'} + ...) \tag{6.3}$$

which is the scaling hypothesis for the correlation length with leading-order critical exponent ν. Non-universal higher-order corrections to this scaling hypothesis are captured by the additional terms in the series.

In a non-equilibrium setting, the correlation functions become time-dependent, and should in general be written as

$$G(r; t, t') = \langle \delta\psi(r, t)\delta\psi(0, t')\rangle - \langle \delta\psi(r, t)\rangle\langle \delta\psi(0, t')\rangle \tag{6.4}$$

for potentially distinct times t and t'. Here, angle brackets in general do not denote equilibrium ensemble averaging but rather averaging over the stochastic realizations of the order parameter ψ. The equal-time correlation function ($t = t'$) need not have the same spatial scaling form as (6.2), as we will see in subsequent sections. However, in an infinite and uniform system, we can typically write an equal-time correlation function with scaling form

$$G(r; t, t) \equiv f(r/\xi, t/\tau) \tag{6.5}$$

with length and time scales ξ and τ, respectively. Near the transition, the two are typically related by $\tau \sim \xi^z$, defining the dynamical exponent z. This relation is

rooted in causality arguments, which say that the correlations require a finite and non-zero amount of time to be established. Equivalently, there is a maximal velocity at which fluctuations can propagate (typically determined by the sound speed) and communication of these fluctuations can only happen within the sonic horizon set by the corresponding speed of sound [8, 94].

6.1.2. KZM Basics

A second order phase transition, which occurs at a critical temperature T_c, is characterized by a diverging correlation length, ξ and relaxation time τ as the reduced temperature $\epsilon \equiv 1 - T/T_c$ approaches zero. For a homogeneous system, the reduced temperature may be uniformly swept across the transition in a linear fashion, $\epsilon(t) = t/t_q$ with t_q the quench time. This may be done by varying the temperature, the critical temperature, or both, in some linear fashion. The details of experimentally implementing such a linear quench are discussed in a subsequent section. Near the transition, the correlation length is hypothesized to diverge at leading order as

$$\xi(\epsilon) = \xi_0 |\epsilon|^{-\nu} \tag{6.6}$$

with some microscopic length-scale ξ_0 and critical exponent ν, while the relaxation time is likewise hypothesized to diverge as

$$\tau(\epsilon) = \tau_0 |\epsilon|^{-\nu z} = \tau_0 \left(\frac{\xi}{\xi_0} \right)^z \tag{6.7}$$

with microscopic time-scale τ_0 and dynamical exponent z. Equations (6.6) and (6.7) implicitly assume the thermodynamic limit has been taken, but in a real experiment, neither of these quantities possess such singular behavior; Finite-size effects smooth out the transition, and complicate the interpretation of such simple scaling laws. Fur-

thermore, the correlation and response functions from which the correlation length and relaxation time are derived can be in general quite complex, perhaps even possessing many more relevant scales. We simply neglect finite-size effects for the time being, but revisit their effects in the subsequent sections.

The correlation length and relaxation time inherit a time-dependence through the externally imposed changes to the reduced temperature $\epsilon(t)$. The fluctuating order parameter, i.e. the coherent bosonic field associated to the Landau-Ginzburg action [95, 96], can only respond to changes in $\epsilon(t)$ if it can relax to equilibrium on a sufficiently fast timescale; The order parameter follows the quench adiabatically only when $\tau[\epsilon(t)] \lesssim |\epsilon/\dot{\epsilon}| = t$ (for a linear quench). The reverse inequality defines a region near the transition, called the impulse region, where the dynamics of the order parameter cannot follow changes in the reduced temperature, and fluctuations in the order parameter are effectively frozen-out. The length-scale over which these fluctuations are correlated is then set by the correlation length at the moment, $t = \hat{t}_{KZ}$, of freeze-out when $\tau[\epsilon(\hat{t}_{KZ})] \equiv \hat{t}_{KZ}$, from which we compute $\hat{\xi}_{KZ} \equiv \xi[\epsilon(\hat{t}_{KZ})]$. For $|t| \gtrsim \hat{t}_{KZ}$, the order parameter can adiabatically follow the quench, however a robust condensate may only form below the transition where $T < T_c$. Since the freezing-out of the fluctuations creates uncorrelated domains of size $\sim \hat{\xi}_{KZ}$, within which the phase is roughly uniform, the subsequent condensate growth allows these domains to fuse and stochastically choose a topological order guided by free energy minimization. In a ring geometry, such defects fuse into spontaneously-formed topologically-protected persistent currents. A depiction of the KZM in a ring-shaped geometry is shown in Fig. 6.1, within the so-called adiabatic-impulse-adiabatic approximation described above.

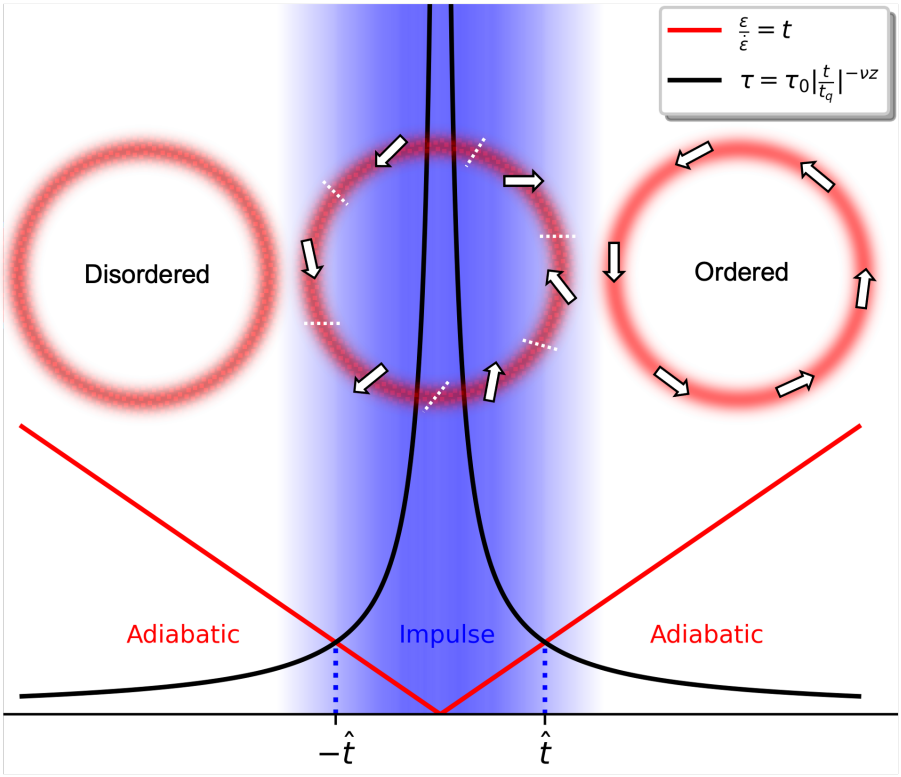

Figure 6.1: A graphic showing the idea of the KZM within the adiabatic-impulse-adiabatic approximation. The order parameter can follow the linear quench adiabatically only when its relaxation time is short compared to the time until the transition. The impulse regime defines the interval during which the order parameter cannot follow the quench adiabatically, and its fluctuations are effectively frozen. In a ring-shaped system, the independent domains of size $\sim \hat{\xi}_{KZ}$ that are frozen in during the crossing of the transition eventually merge in to a smooth phase profile once the order parameter can respond to the quench again and the condensate grows. The merging domains stochastically choose a topological order (winding number) that is guided by free energy minimization.

6.1.3. Computing the KZ Scaling Laws

The freeze-out time, where the dynamics of the order parameter cease to follow the quench adiabatically, occurs at time $t \equiv -\hat{t}_{KZ}$ when

$$\tau[\epsilon(\hat{t}_{KZ})] = \hat{t}_{KZ} \tag{6.8}$$

Using the scaling relation (6.7) and $\epsilon(t) = t/t_q$ we solve for $\hat{t}$ as a function of the quench time t_q:

$$\hat{t}_{KZ} = \tau_0 \left(\frac{t_q}{\tau_0}\right)^{\frac{\nu z}{1+\nu z}} \sim t_q^{\frac{\nu z}{1+\nu z}} \tag{6.9}$$

The corresponding reduced temperature at the freeze-out time is

$$\hat{\epsilon}_{KZ} \equiv \epsilon(\hat{t}_{KZ}) = \left(\frac{\tau_0}{t_q}\right)^{\frac{1}{1+\nu z}} \tag{6.10}$$

With this, we solve for the correlation length at the freeze-out time using (6.10) and (6.6) and find

$$\hat{\xi}_{KZ} \equiv \xi(\hat{\epsilon}_{KZ}) = \xi_0 \left(\frac{t_q}{\tau_0}\right)^{\frac{\nu}{1+\nu z}} \sim t_q^{\frac{\nu}{1+\nu z}} \tag{6.11}$$

Additionally, the relaxation time at freeze-out is given by

$$\hat{\tau}_{KZ} \equiv \tau(\hat{\epsilon}_{KZ}) = \tau_0 \left(\frac{t_q}{\tau_0}\right)^{\frac{\nu z}{1+\nu z}} \sim t_q^{\frac{\nu z}{1+\nu z}} \tag{6.12}$$

In the thermodynamic limit, the frozen-out properties of the system as it traverses the critical point should carry relevant information pertaining to the universality class of the phase transition. Namely, the combination $\hat{\xi}_{KZ}$ and $\hat{\tau}_{KZ}$, or i.e. $\hat{\xi}_{KZ}$ and $\hat{v}_{KZ} \equiv \hat{\xi}_{KZ}/\hat{\tau}_{KZ}$, scale with the controllable t_q with different combinations of critical exponents ν and z describing to the transition. One of the goals of the Kibble-Zurek mechanism is to describe a means of extracting these exponents, or at least a particular combination $a(\nu, z)$, using readily observable and measurable quantities. Such quantities depend highly on the geometry and dimensionality of the confinement. For instance, in a annular geometries, the observable is typically the winding number of spontaneous currents formed after the quench, although the exact statistics depend on properties such as the ring circumference and thickness [97]. In uniform or harmonically-trapped systems, the observable is frequently the number of

vortices nucleated, and in this framework dimensionality plays a critical role in how these topological defects form [98]. Additionally, finite size effects are known to play a crucial role in the scaling behavior [99, 100]. In this work, we focus on narrow ring geometries, the setting originally envisaged by W. Zurek in his attempts to explain topologically protected states of circulation in quenched superfluid ^{3}He [8].

KZM in a Ring. For a thin one-dimensional ring of circumference C and width w, i.e. with $\hat{\xi}_{KZ} \ll w$ such that transverse excitations are frozen out, the number of uncorrelated domains formed at the freeze-out point is

$$N_d \approx \frac{C}{f\hat{\xi}_{KZ}} \tag{6.13}$$

The scaling reflects the fact that the notion "domain" is not a well-defined concept, and depends on how the correlation length is defined, which can vary from system to system. The fudge factor $f \sim \mathcal{O}(1-10)$ is introduced to account for this ambiguity, but is system-dependent. While the statistics of spontaneous current formation for arbitrary rings depend on N_d in somewhat complicated ways, the scenario originally envisaged by W. Zurek in [8] predicts a scaling of the winding number $\langle |w| \rangle \sim N_d^{1/2}$, in accordance with a large-N_d random walk amongst the phase domains. In the opposite limit of small N_d, various arguments, based off of a gaussian random velocity field or the distribution of vortex-antivortex pairs bounding a small ring, have predicted a doubling of the winding number exponent ([10, 100]). For small N_d, the winding number formation will become dependent on the exact phase profile within each domain, and on the periodic boundary conditions, since in general N_d as defined in (6.13) is not an integer and will have some potentially non-negligible remainder [101]. Furthermore, meaningfully defining a correlation length that approaches, and perhaps exceeds, the ring circumference is challenging, which makes the notion of a

domain an even blurrier concept. While the domain picture is simplistic and accurate in the large N_d limit, a complete description of the relation between spontaneous current formation and the quench dynamics is desirable, especially one that accurately describes the intermediate to slow quench regimes.

Section 6.2

Landau-Ginzburg Theory

To motivate following discussion of spontaneous current formation, it is necessary to first discuss the Landau-Ginzburg (LG) model, a paradigmatic model used to describe the order parameter in the vicinity of a generic second-order phase transition [5]. An extension of the LG model to a dynamical setting will then allow us to study the behavior of spontaneous persistent currents formed during variable-rate quenches across the critical point.

The LG model is an equilibrium, mean-field description of the order parameter for values of the reduced temperature $|\epsilon| \equiv |T_c - T|/T \ll 1$. Since in all second-order phase transitions, such as a BCS transition, the order parameter ψ is small when $T \approx T_c$, a Taylor expansion of the relevant free-energy functional for small ψ can be made.

Landau-Ginzburg free energy. The phenomenological Landau-Ginzburg theory is defined via the Landau-Ginzburg (equilibrium) free energy functional

$$F[\psi, \nabla\psi] \equiv \int d\mathbf{r} \left[\frac{\hbar^2}{2m} |\nabla\psi(\mathbf{r})|^2 + a|\psi(\mathbf{r})|^2 + \frac{b}{2}|\psi(\mathbf{r})|^4 \right] \tag{6.14}$$

Here $|\psi|^2$ is assumed to be small, justifying the expansion to second order. The constants a and b are assumed to be analytic across the transition, and their Taylor expansions for small ϵ and $|\psi|$ are given by $a \equiv a_0\epsilon$ and $b \equiv b_0 \geq 0$. Here, a_0 and b_0

are independent of ϵ. b_0 is chosen to be positive to ensure thermodynamic stability. The exact values of these constants can in theory be derived from the corresponding microscopic Hamiltonian [78, 102]. We also note that the equation (6.14) holds for *any* system (obeying the same generic symmetries as the one described here) near its second order phase transition, and is exact; The description is universal, apart from the microscopic details of the constants a_0 and b_0. In order to utilize equation (6.14), however, one typically makes a so-called saddle point approximation, where the equilibrium order parameter chooses a value that extremizes the Landau-Ginzburg free energy functional. Varying $\psi^*(\mathbf{r})$ in (6.14) then gives

$$-\frac{\hbar^2}{2m}\nabla^2\psi + a\psi + b|\psi|^2\psi = 0 \tag{6.15}$$

which is the differential equation governing the mean-field spatial distribution of the order parameter. It has the exact same form as the Gross-Pitaevski formula describing weakly interacting bosons [103, 104].

Static Configurations. Although the differential equation (6.15) describes a static configuration, it is still insightful to study generic features in this setting. Taking a uniform system first, we see the equilibrium order parameter satisfies

$$a\psi_{\text{eq}} + b|\psi_{\text{eq}}|^2\psi_{\text{eq}} = 0 \tag{6.16}$$

The minimum free-energy configuration depends on the value of ϵ. Namely, above the transition $\epsilon > 0$, and

$$\psi_{\text{eq}}^{+} = 0 \tag{6.17}$$

which describes the disordered state. Below the transition point, where $\epsilon < 0$, the order parameter assumes a non-zero value given by

$$|\psi_{\text{eq}}|^2 = -\frac{a}{b} \sim |\epsilon| \tag{6.18}$$

In the context of universality classes, we can identify the critical exponent β associated to the order parameter, which scales as $\psi \sim |\epsilon|^{\beta}$. From (6.18) we find $\beta = 1/2$ for the mean-field LG model.

In a non-uniform configuration and for $T < T_c$, we can recast equation (6.15) into an equivalent form by dividing by $a|\psi_{\text{eq}}|$, and defining $\tilde{\psi} = \psi/|\psi_{\text{eq}}|$:

$$-\frac{\hbar^2}{2ma}\nabla^2\tilde{\psi} + \tilde{\psi} + |\tilde{\psi}|^2\tilde{\psi} = 0 \tag{6.19}$$

There is a free-energy cost associated to spatial variations in the order parameter. This cost is substantial for variations that occur over the length scale defined by

$$\xi \equiv \sqrt{\frac{\hbar^2}{2ma}} \sim |\epsilon|^{-1/2} \tag{6.20}$$

This quantity is referred to as the healing or coherence length of the order parameter. It is the length scale over which the order parameter can heal from a value of 0 to its bulk value in a locally homogeneous medium, $|\psi_{\text{eq}}|$. By defining $\tilde{\mathbf{r}} = \mathbf{r}/\xi$, we can write the LG equation in non-dimensional form as

$$-\tilde{\nabla}^2\tilde{\psi} + \tilde{\psi} + |\tilde{\psi}|^2\tilde{\psi} = 0 \tag{6.21}$$

where $\tilde{\nabla}^2$ is the Laplacian operator in $\tilde{\mathbf{r}}$ space. Clearly, this form of the LG equation makes no reference to microscopic parameters in the model; It is completely universal.

In the immediate vicinity of the transition, the non-linear interaction can be ne-

glected, and we may approximate

$$-\frac{\hbar^2}{2m}\nabla^2\psi + a\psi \approx 0 \tag{6.22}$$

The Green's function for this equation describes correlations between fluctuations of the order parameter (in a thermodynamic sense) at two distinct points separated by some distance $r = |\mathbf{r} - \mathbf{r}'|$. This can be seen by studying these fluctuations within the context of linear response theory, although this is more generally a consequence of the fluctuation-dissipation theorem. The correlation (Green's) function $G(\mathbf{r}, \mathbf{r}')$ for the LG equation therefore obeys

$$-\frac{\hbar^2}{2m}\nabla^2 G(r) + aG(r) = \delta(\mathbf{r} - \mathbf{r}') \tag{6.23}$$

In Fourier space, the solution is given by

$$\tilde{G}(k) = \frac{1}{a + \frac{\hbar^2 k^2}{2m}} = \frac{1/a}{1 + \xi^2 k^2} \tag{6.24}$$

which can be inverted to find the real space behavior for $r \gtrsim \xi$

$$G(r) \sim f(r)e^{-r/\xi} \tag{6.25}$$

with some dimension-dependent algebraic function $f(r)$. This establishes a connection between the healing length as defined in (6.20) and the correlation length of statistical fluctuations in the order parameter about its mean value. Namely, we find the scaling relation for the correlation length to be the same as that of the healing length, and this defines the critical exponent

$$\xi \sim |\epsilon|^{-\nu} \tag{6.26}$$

with $\nu = 1/2$ for this mean-field model.

Time-Dependent LG Theory. In a dynamical setting, one can allow the order parameter to be perturbed a small amount away from equilibrium. In this case, the order parameter will attempt to recover to its instantaneous equilibrium value, and does so at a rate proportional to how strongly it was driven out of equilibrium. Mathematically, we can account for this by setting the L.H.S of equation (6.15) equal to a damping term, which gives the time-dependent Landau-Ginzburg equation

$$-\frac{\hbar^2}{2m}\nabla^2\psi + a(t)\psi + b(t)|\psi|^2\psi = -\frac{1}{\Gamma}\frac{\partial\psi}{\partial t} \tag{6.27}$$

The constant Γ is a relaxation coefficient that sets the rate scale for which the order parameter can relax to equilibrium. The equation (6.27) is a fairly generic equation describing the dynamics of the order parameter near a second order phase transition. It effectively captures the dynamics of the long-wavelength, low frequency dynamics of the order parameter. Note that we have now allowed for the parameters a and b to carry explicit time-dependence.

We can analyze the dynamics in the immediate vicinity of the transition, where the non-linear term can be safely neglected. The linearized equation of motion can then be written in Fourier space as

$$\left(\frac{\hbar^2 k^2}{2m} + a\right)\phi = -\frac{1}{\Gamma}\frac{\partial\phi}{\partial t} \tag{6.28}$$

where $\phi(\mathbf{k}, t) = \mathcal{F}[\psi(\mathbf{r}, t)](\mathbf{k})$. This equation has an exponentially decaying solution for each value of $\mathbf{k}$, with time constant

$$\tau_k^{-1} = \Gamma\left(a + \frac{\hbar^2 k^2}{2m}\right) \tag{6.29}$$

In particular, the slowest decay occurs for the uniform component, $k = 0$, with time constant

$$\tau_{k=0} = \frac{1}{\Gamma a} \sim |\epsilon|^{-1} \tag{6.30}$$

which sets the time-scale over which the order parameter can respond to sudden perturbations. The scaling of this relaxation time scale $\tau_{k=0}$ defines the dynamical critical exponent z. It is conventionally defined such that $\tau_{k=0} \sim \xi^z$. Using the critical exponent $\nu = 1/2$ for the correlation length, we find $z = 2$ for the mean-field Landau-Ginzburg model.

Adding Thermal Noise. It is important to realize that, as defined, $\psi \equiv \langle\hat{\psi}\rangle$, i.e. it is the expectation value of the coherent bosonic field associated to the microscopic action, obtained from tracing out any fermionic degrees of freedom (via i.e. the Hubbard-Stratonovich transformation). In many scenarios, one would like to describe the stochastic dynamics associated to the order parameter as it interacts incoherently with the surrounding heat bath. In essence, one models the evolution of the order parameter *in a given realization* as a Langevin equation driven by a random forcing term describing the system-bath interactions. Mathematically, we may augment (6.27) with such a noise term and write

$$-\frac{\hbar^2}{2m}\nabla^2\psi + a(t)\psi + b(t)|\psi|^2\psi = -\frac{1}{\Gamma}\frac{\partial\psi}{\partial t} + \zeta \tag{6.31}$$

where the stochastic driving force $\zeta(\mathbf{r}, t)$ is a zero-mean complex Gaussian variable with white-noise correlations, $\langle\zeta(\mathbf{r}, t)^*\zeta(\mathbf{r}', t')\rangle \sim k_B T\delta(\mathbf{r}-\mathbf{r}')\delta(t-t')$. Angle brackets here refer to ensemble averaging over the i.i.d. normal distributions from which the ζ are pulled from. One can interpret equation (6.31) as follows: As the order parameter is driven away from equilibrium, it will attempt to recover its equilibrium value at a rate set by Γ, but interactions with the heat bath will kick the order parameter along

a random trajectory through the complex plane on its return. This Langevin form of the dynamics is essential to study the stochastic formation of spontaneous persistent currents, as will be discussed in Chap. 7. It is the random kicks supplied by the noise term that continually drive phase slips -discontinuous jumps in the winding number of the order parameter- near the transition, and this in turn is responsible for the stochastic nature of spontaneous current formation.

Section 6.3

Phenomenological Theory of Spontaneous Currents

The purpose of this section is to derive analytical expressions for the probability distributions and related properties of spontaneous currents formed after a quench through a second order phase transition. The results of this analysis are then compared to the correlation functions that pertain to the KZ theory of defect formation. The subsequent theory was developed from initial attempts to explain certain observations made by Yanping Cai in his studies of fermionic persistent currents in the BEC-BCS crossover [31]. In particular, the question arose as to what role a finite, non-zero rotational velocity of the system had on the final distribution of *spontaneous* currents obtained on return to a superfluid state from the fully normal state above the transition. This physical setting has a direct analogy to superconducting rings pierced by a uniform magnetic field, which plays the role of the rotating normal-fluid "bias", and was studied in [99, 105]. While the analysis performed in this section focuses on the *non-rotating* scenario -the setting for the spontaneous current measurements performed in Chap. 7- we point the reader to Chap. 8 for further analysis of the effects of this "rotational bias" on the statistics of spontaneous current formation.

We will now provide a theoretical framework, based off of a stochastic Laundau-

Ginzburg model, for reproducing and interpolating between the fast quench and slow quench limits. This model treats the Fourier components of the fluctuating order parameter as Gaussian variables evolving according to a damped, stochastically-driven Landau-Ginzburg model introduced in Sec. 6.2. We argue that the linearized version of this model is sufficient to reproduce the key predictions in both the large t_q and small t_q limits, and provides a reasonable, although non-universal, interpolation between the two limits.

6.3.1. A stochastic model for spontaneous currents

In a ring-shaped trap, the KZM offers a means to predict the statistics of winding number formation for variable-rate ramps across a second-order phase transition. In the BCS limit where the relevant experiment performed in this work takes place, these spontaneous current are incredibly stable against decay via thermal fluctuations due to the low compressibility and high heat capacity of the mostly-filled Fermi sea; The order parameter must locally fluctuate to zero at some point on the ring for the phase to unwind [106]. Thus, the observed probability for a given winding number w is typically set by the stochastic dynamics within the narrow "impulse" region of the ramp near the local critical temperature at the ring minimum.

In particular, we are interested in the limit where the interaction parameter $k_F|a| \to 0$ and $T \to 0$, with $T/T_c(n, k_F|a|) \sim 1$. The critical temperature T_c depends on both the fermion density n and the interaction parameter. In this limit, the isothermal compressibility $\kappa_T \to 0$, and thus density fluctuations become negligible. Temperature fluctuations similarly become negligible. As the order parameter ψ (i.e. the superfluid pairing field) depends on the local fermion density and temperature via T/T_c, its fluctuations are effectively frozen out except in the immediate vicinity of the transition point where $|\psi| \approx 0$. Furthermore, the spontaneous persistent currents are incredibly robust once formed, and survive for timescales on the

order of the vacuum-limited lifetime. Near the transition point is therefore where we choose to focus attention with respect to analytic considerations. We therefore base calculations of the order parameter and fluctuations off of a linearized stochastic time-dependent Landau-Ginzburg equation, motivated by numerical studies of quenched Bose and Fermi systems, and in field-theoretical models [99, 107–109], and discussed previously in Sec. 6.2.

In a smooth one-dimensional ring of radius R, the time-dependent stochastic Landau-Ginzburg equation (SLGE) describing the evolution of the order parameter can be written in non-dimensional units as

$$\frac{\partial \psi}{\partial t} = \left[\alpha(t) + \frac{\partial^2}{\partial \theta^2} + \beta|\psi|^2\right]\psi + \zeta(\theta, t) \tag{6.32}$$

which is expected to approximate the dynamics at the mean-field level. Here, we measure time in units of γ/Ω_0, where γ is the dimensionless relaxation rate and $\Omega_0 = \hbar/(2mR^2)$ is the frequency associated to quantized circulation around the ring. $\alpha(t) = (R/\xi_{\rm BCS})^2\epsilon(t)$ is the dimensionless Landau-Ginzburg chemical potential, written in terms of the BCS coherence length $\xi_{\rm BCS}$, and β is the non-linear interaction strength. In the limit $k_F|a| \to 0$, $\xi_{\rm BCS} = \hbar v_F/(\pi\Delta_0)$, with v_F the Fermi velocity and Δ_0 the zero-temperature Cooper pairing gap [40]. $\zeta(\theta, t)$ is a zero-mean complex Gaussian white noise field, satisfying $\langle\zeta(\theta, t)\rangle = 0$ and $\langle\zeta^*(\theta, t)\zeta(\theta', t')\rangle = D\delta(\theta-\theta')\delta(t-t')$, with $D \sim k_B T$ a phenomenological "diffusion" constant proportional to the temperature T, in accordance with the fluctuation-dissipation theorem. Angle brackets denote ensemble averaging over the i.i.d complex, zero-mean Gaussian distributions with variance D at each time t and angle θ).

To study quench dynamics, we vary the reduced temperature linearly as $\epsilon(t) = t/t_{q,0}$, and we can write $\alpha(t) \equiv t/t_q$, for some effective quench time $t_q \equiv (\xi_{\rm BCS}/R)^2 t_{q,0}$. Close to the transition, where fluctuations in the order parameter are expected to

become frozen in according the KZM, we may neglect the non-linear term and write a linearized Fourier space representation of (6.33):

$$\dot{c_\ell} = \left(\frac{t}{t_q} - \ell^2\right) c_\ell + \zeta_\ell \tag{6.33}$$

where the order parameter and noise term were expanded as

$$\psi(\theta, t) = \sum_{\ell=-\infty}^{\infty} c_\ell(t) e^{i\ell\theta} \tag{6.34}$$

and

$$\zeta(\theta, t) = \sum_{\ell=-\infty}^{\infty} \zeta_\ell(t) e^{i\ell\theta} \tag{6.35}$$

respectively. We can find a formal solution to the stochastic differential equation (6.33) by integration:

$$c_\ell(t) = \int_{-\infty}^{t} dt' \zeta_l(t') e^{-\ell^2(t-t') + \frac{t^2 - t'^2}{2t_q}} \tag{6.36}$$

Then, we find an exact expression for the mean-square fluctuations of each Fourier component by complex squaring and averaging (6.36)

$$\langle |c_\ell(t)|^2 \rangle \equiv \sigma_\ell^2(t) = \sqrt{\pi} D\hat{t}\ F\left(\frac{t}{\hat{t}} - \hat{t}\ell^2\right) \tag{6.37}$$

where $\hat{t} \equiv \sqrt{t_q}$. The dimensionless function $F(x) \equiv \frac{1}{2}e^{x^2}[1 + \mathrm{erf}(x)] = \mathrm{erfcx}(-x)/2$ where erfcx is the complimentary scaled error function. Importantly, for $x \to -\infty$, $F(x) \sim 1/(2\sqrt{\pi}x)$ while for $x \gtrsim 1$, $F(x) \sim \exp(x^2)$. We plot this function and its asymptotic approximations in Fig. 6.2. The meaning of $\hat{t}$ will become clear shortly.

For any time t, $\sigma_\ell^2(t)$ is maximal at $\ell = 0$. Additionally, the growth dynamics of

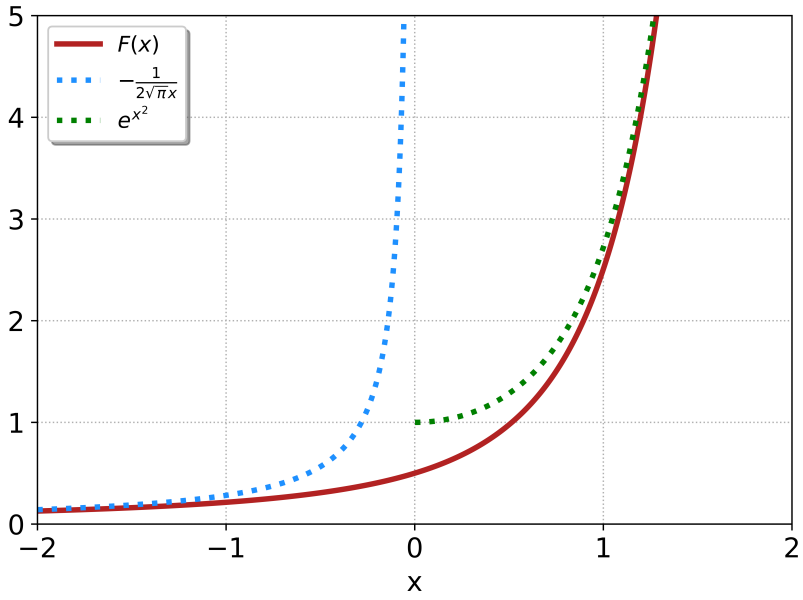

Figure 6.2: The function $F(x)$ and its asymptotic approximations.

the σ_ℓ^2 depend only on the variable

$$x_\ell(t) \equiv \frac{t}{\hat{t}} - \hat{t}\ell^2 \tag{6.38}$$

Due to the exponential nature of $F(x)$ near $x = 1$, the fluctuations in mode $\ell = 0$ experience a brief period of rapid growth, before any other mode, following the transition at times when $x_{\ell=0}(t) \approx 1$. This condition defines the "blow-up" time

$$t^* \equiv \hat{t} \tag{6.39}$$

after which non-linear effects kick in and the condensate begins to relax toward its instantaneous, non-zero equilibrium value value [108]. Thus, in some short interval of time following t^*, the condensate becomes robust with respect to fluctuations large enough to cause any persistent current to decay; The winding number becomes a topologically protected quantity at times $t \geq t_{\text{eval}} \equiv ft^*$. Here f is an $\mathcal{O}(1)$ "fudge"

factor that scales the blow-up time to the so-called evaluation time where the winding number is stabilized [110]. We note that although f is non-universal, it depends only logarithmically on the microscopic parameters and quench details and is thus roughly constant across many decades of quench times.

While the definition of $\hat{t}$ is suggestive of the "freezing" and "unfreezing" time associated to the Kibble-Zurek mechanism, it is not immediately clear why this would be the case. We will see in subsequent discussion of the relevant correlation functions that the two are indeed the same, in the limit of sufficiently fast quenches.

6.3.2. Estimating the Winding Number Distribution

With the mathematical machinery needed to calculate the winding number from a set of Fourier coefficients (see Sec. 2.3), we now turn our attention to the physical scenario introduced above. The goal is to calculate the probability of observing a given winding number w given the set of time-dependent Fourier coefficients expressed in (8.2). To motivate following analysis, we begin by assuming crudely that the order parameter can be written as a two-mode linear combination of the form $\psi(\theta) = c_0 + c_1 \exp(i\theta)$, i.e. that there are only two relevant modes pertaining to the quench dynamics, and that the winding number $w = 0$ or 1. As linear combinations of Gaussian variables are themselves Gaussian variables, the c_ℓ are Gaussian variables. The winding number is thus set by the relative strength of the two modes, $|c_0/c_1|$, according to (2.49). One may construct a so-called complex ratio distribution $P_R(Z)$ defined as the distribution of the ratio Z of two complex Gaussian random variables X and Y. The corresponding probability density function may be written, assuming X and Y uncorrelated, as

$$f(z = x/y) = \frac{\sigma_x^2}{\pi\sigma_y^2} \frac{1}{(|z|^2 + \sigma_x^2/\sigma_y^2)^2} \tag{6.40}$$

Here, $\sigma_{x,y}$ are the standard deviations of the corresponding complex random variables x and y. With the substitutions $x = c_0$, $y = c_1$, $\sigma_x^2 = \sigma_0^2$, and $\sigma_y^2 = \sigma_1^2$, we find

$$\langle w(t) \rangle = \text{Prob}(|c_0/c_1|(t) < 1) \tag{6.41}$$

$$= 2\pi \int_0^1 d|z||z| f(|z|) \tag{6.42}$$

$$= \frac{\sigma_1^2(t)}{\sigma_0^2(t) + \sigma_1^2(t)} \tag{6.43}$$

Here, we used the mean-square fluctuations defined in (6.37). Evaluating this expression at the evaluation time t_{eval} gives the approximate winding number expectation value $\langle w \rangle$ after the quench, since as noted earlier the winding number is effectively frozen in at this time.

In order to go beyond the simple two-mode model described above, one would have to determine the winding number from the Fourier components and find the proper multidimensional complex distribution function that describes those coefficients. This becomes very challenging for three or more modes, although we note there is a field of mathematics devoted to the study of roots of random polynomials,and therefore random winding numbers (see i.e. [111, 112]). Instead, one could claim that the probability to observe a particular winding number w is proportional to the probability that $|c_{\ell=w}| > \{|c_{\ell \neq w}|\}$. This claim is not true in a general realization, as the winding number also depends on the magnitudes and phases of each of the Fourier coefficients in a complicated way. However, this is the least restrictive criterion to observe a given winding number that incorporates many modes in a simple manner. Furthermore, given that a winding number w can still be observed even if the above condition does *not* hold, we can expect some mitigation of the error due to this simplification. One then analytically models the probability P_w of a given winding w as

an infinite product of factors of the form (6.41):

$$\begin{aligned} P_w &\approx \text{Prob}(|c_w| > |c_0| \cap |c_w| > |c_1| \cap ...)/Z \\ &= \frac{1}{Z}\prod_\ell \frac{\sigma_w^2}{\sigma_w^2 + \sigma_\ell^2} \end{aligned} \tag{6.44}$$

where Z ensures proper probability normalization, $\sum_w P_w = 1$.

Alternatively, we may numerically simulate the winding number distribution by sampling the $c_\ell(t)$ from the complex Gaussian distribution $\mathcal{CN}(0, \sigma_\ell^2(t))$. The variances $\sigma_\ell(t)$ are given by (6.37). Recapping the discussion from Sec. 2.3, the winding number w is given by

$$w = \mathcal{N} - \ell_c \tag{6.45}$$

with $\mathcal{N}$ the number of roots of $\psi(z) = \sum_{\ell=0}^{2\ell_c} c_{\ell-\ell_c} z^\ell$ lying within the complex unit disk $|z| < 1$ and ℓ_c the mode cutoff. This Fourier-space method of computing the winding number circumvents issues with phase ambiguities and undersampling errors associated with the real-space computation of w. For a single randomly-chosen set $\{c_\ell(t)\}$, the roots of $\psi(z)$ are found numerically and w is then computed via (6.45).

When evaluated at t_{eval}, the probability distribution depends only on the combination $\hat{t} \sim \sqrt{t_q}/R^2$. Also notably the phenomenological diffusion constant D drops out of the equation as long as the winding number assumes its final value at the blow-up time and non-linear effects can be neglected. Small values of $\hat{t}$ correspond to either rapid quenches, *or* temperatures well above the initial critical temperature of the ramp, *or* large ring radii. The latter-most corresponds to the thermodynamic (infinite size) limit, but in each case, it describes the regime initially envisioned by Zurek (many small, uncorrelated domains with uniform phase locked within). Conversely, large values of $\hat{t}$ (slow quenches and small temperatures) or small radius rings give rise to sharper distributions of persistent currents, centered at winding number $\ell = 0$.

Importantly, the phase coherence extends across the circumference of the ring, and the details of the phase profile along the circumference, as well as periodic boundary conditions, become important. Thus, there is always a small but finite probability to generate persistent currents even when $N \leq 2$ domains are formed. For intermediate values of $\hat{t}$, equation (6.44) gives an interpolation between the two regimes discussed previously, where standard treatments of spontaneous current formation become inaccurate, and simple scaling laws describing the rate of defect formation break down. It is still unclear, however, exactly what role microscopic, non-universal details play in this intermediate regime.

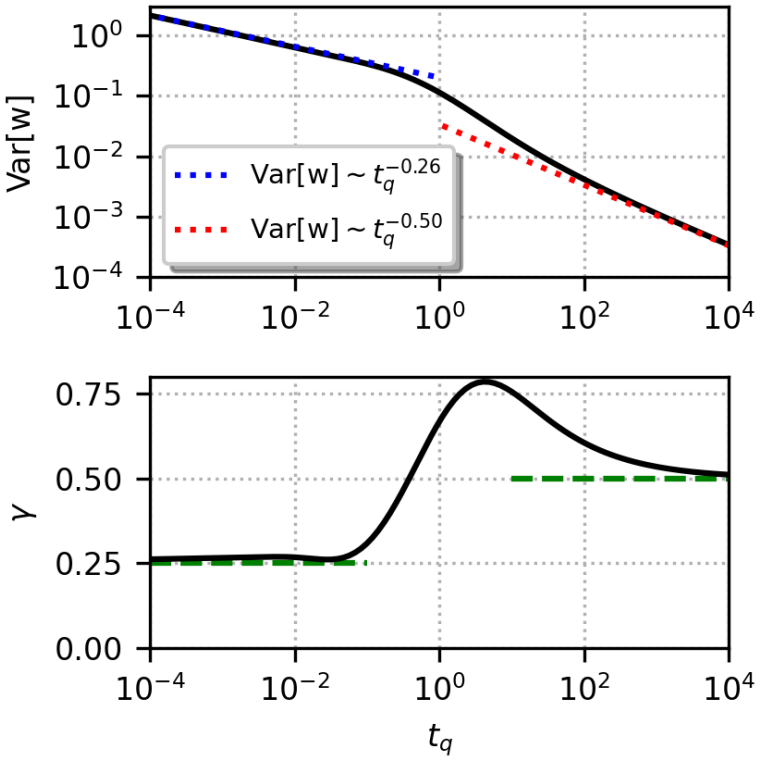

Figure 6.3: (Top) Plot of variance in the winding number as a function of the quench time using the analytical model, and evaluated at time $t_{\text{eval}} = \hat{t}$. We fit the data at slow and fast quenches with a power-law of the form $\text{Var}[w] \sim t_q^{-\sigma}$. (Bottom) Slope of upper line-shape as a function of quench time: $\gamma = d \log \text{Var}[w] / d \log(t_q)$. Horizontal dashed green lines show the two regimes where the scaling is a simple power-law.

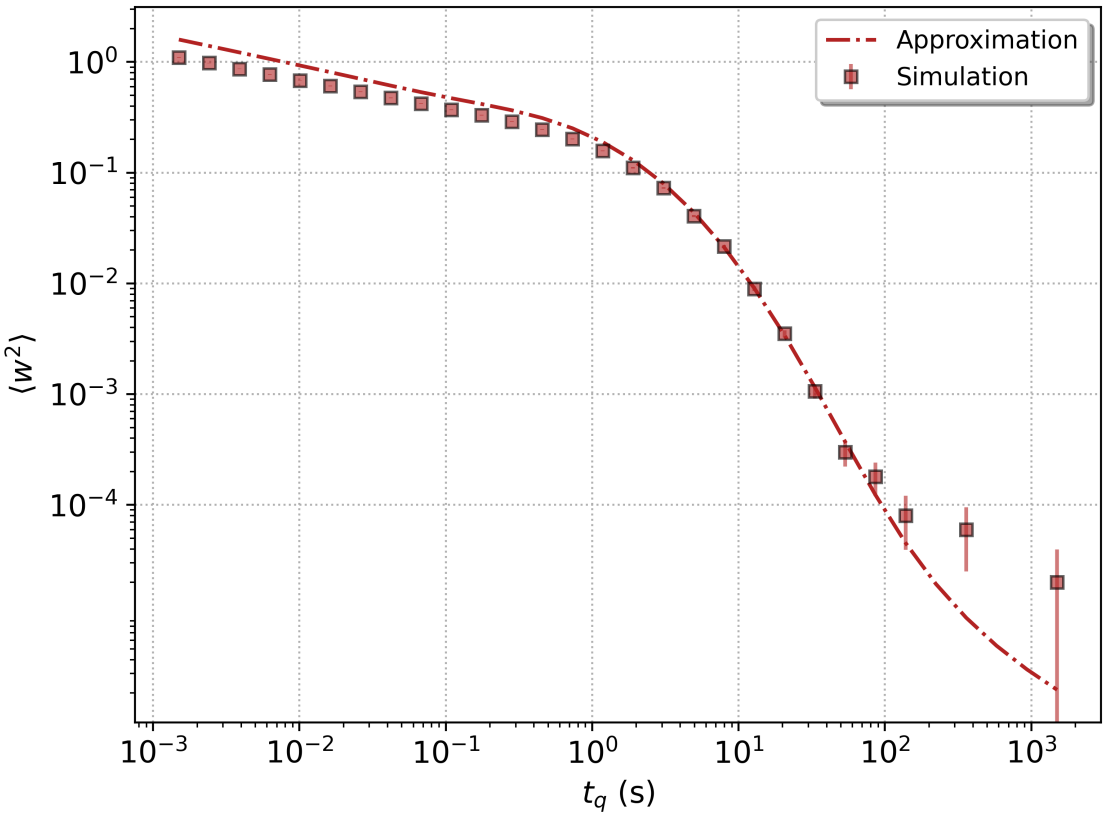

Figure 6.4: Mean-square winding numbers computed from the analytical approximation to the winding number distribution (red dashed-dotted line) and the simulation (red squares) as a function of the quench time. The distribution is evaluated at $t = 3\hat{t}$.

Analyzing the Distribution. With the probability distribution, one may readily compute the various relevant moments of the distribution as functions of $\hat{t}$, which we show in Fig. 6.3 using the analytical approximation to the probability distribution (6.44). For simplicity, we take $t_{\text{eval}} = \hat{t}$. As the Kibble-Zurek mechanism predicts the scaling of the defect density, and thus the variance of the winding number distribution, with the quench rate, it is informative to define the quench-rate-dependent scaling exponent $\gamma \approx -\frac{d \log \text{var}[w]}{d \log t_q}$, which we also plot in Fig. 6.3. The plot of the scaling exponent highlights three main regimes of stochastic persistent formation. The small $\hat{t}$ regime is the KZ regime of Gaussian probabilities. For large $\hat{t}$, the scaling exponent is seen to double. This doubling has been suggested to be a result of Gaussianity

in the winding number *density*, or due to geometric considerations pertaining to the distribution of vortex-antivortex pairs in small rings [100, 105]. This scaling is likely difficult to observe experimentally with great precision, as the probability to generate non-zero persistent currents becomes incredibly small for large $\hat{t}$. For intermediate values of $\hat{t}$, the winding number statistics become non-universal and as indicated in Fig. 6.3. Furthermore, the functional dependence of the variance on the quench time becomes dependent on the blow-up time in a way that depends on the non-linear interaction term that was neglected. However, it should still be possible to define the notion of a "defect", given that the correlation length is still smaller that the ring circumference at intermediate quench times.

We also show the variances obtained from numerically simulating the winding number distribution using the procedure described earlier. The result is shown in Fig. 6.4. In this plot, we evaluate the distribution at time $t_{\text{eval}} = 3\hat{t}$. We also show the analytical approximation evaluated at the same time. We see fairly good agreement between the two models across many decades of quench times. For fast quenches, the analytic approximation tends to overestimate the simulated variance, although the approximate scaling exponent $\sigma = 1/4$ is still roughly maintained. For the slowest quenches, where the probability of measuring a non-zero winding number becomes incredibly small, the simulated variance starts departs from the analytical approximation. We see the best agreement between the simulation and the analytical model in the intermediate regime.

The KZ Regime. We now show that the approximate probability distribution (6.44) successfully reproduces the KZ scaling laws for rapid quenches. In this regime, $\hat{t}$ is small, and we can approximate the scaling function in (6.37) at $t = \hat{t}$ as

$$F(1 - \hat{t}\ell^2) \sim \exp\bigl(-2\hat{t}\ell^2\bigr) \tag{6.46}$$

where the term in the exponential of $\mathcal{O}(\hat{t}^2)$ was neglected. Then from (6.44) we have

$$\begin{aligned}\log P_w &\sim -\sum_{\ell} \log\left(1 + z_w e^{-2\hat{t}\ell^2}\right) \\ &\sim -\frac{1}{\sqrt{\hat{t}}}\int_{-\infty}^{\infty} dx \log\left(1 + z_w e^{-x^2}\right) \\ &\sim -\frac{1}{\sqrt{\hat{t}}}\mathrm{Li}_{3/2}(-z_w)\end{aligned} \tag{6.47}$$

where $z_w \equiv \exp\left(-2\hat{t}w^2\right)$ and the sum was approximated by an integral. A small $\hat{t}$ expansion of the polylogarithm $\mathrm{Li}_{3/2}$ about $z_w = 1$ then yields

$$P_w \sim \hat{t}^{-1/4} \exp\left(-\sqrt{\frac{\hat{t}}{\hat{t}_0}} w^2\right) \tag{6.48}$$

where $\hat{t}_0$ is a number. Since $\hat{t}$ is small, the distribution P_w is very broad, and its discrete nature is blurred out. w is then approximately a continuous variable. Then, we compute the lowest order cumulants

$$\mathrm{E}[w] \approx \int_{-\infty}^{\infty} dw w P_w = 0 \tag{6.49}$$

and

$$\mathrm{Var}[w] \approx \int_{-\infty}^{\infty} dw w^2 P_w \sim \hat{t}^{-1/2} \sim t_q^{-1/4} \tag{6.50}$$

the result predicted by the KZ argument.

6.3.3. Connection to the KZM: Correlation functions

We conclude this chapter by making connection between the phenomenological spontaneous current theory outlined previously with the the core predictions of the KZ scaling hypothesis. As the KZM relies on the concept of a diverging correlation length and relaxation time, it is the goal of the remainder of this section to study the relevant

correlation function from the microscopic theory.

The normalized correlation function in an azimuthally symmetric, 1-D ring is defined as

$$g(\theta, t) = \frac{\langle \psi^*(\theta, t)\psi(0, t)\rangle}{\langle \psi^*(0, t)\psi(0, t)\rangle} \tag{6.51}$$

where translation invariance was used to set the reference position to $\theta = 0$, and the normalization is set by the maximum of $\langle \psi^*(\theta, t)\psi(0, t)\rangle$, which also occurrs at $\theta = 0$. As the order parameter $\psi(\theta, t)$ is single-valued, in can be Fourier-decomposed as

$$\psi(\theta, t) = \sum_\ell c_\ell(t) e^{i\ell\theta} \tag{6.52}$$

with the c_ℓ the same as those appearing in Eq. (6.36). By inserting (6.52) into (6.51) and using $\langle c_\ell^* c_{\ell'}\rangle(t) = \delta_{\ell,\ell'}\sigma_\ell^2(t)$, we find

$$g(\theta, t) = \frac{\sum_\ell \sigma_\ell^2(t) e^{i\ell\theta}}{\sum_\ell \sigma_\ell^2(t)} \tag{6.53}$$

with $\sigma_\ell^2(t)$ defined in (6.37). By symmetry arguments, the distribution of the c_ℓ will be peaked around $\ell = 0$. Due to the inherent periodicity of the correlation function, care must be taken in meaningfully defining a correlation length, since finite size effects are expected to play a role when the correlations can extend around the circumference of the ring. We expect however that for fast quenches, the correlation function should quickly decay, and the notion of a "domain" can be formulated. Using the scaling arguments presented earlier, and defining $\hat{\sigma}_\ell^2 = \sigma_\ell^2(\hat{t})$, we have

$$\hat{\sigma}_\ell^2 \sim e^{-2\hat{t}\ell^2} \tag{6.54}$$

Inserting this expression into (6.53) and replacing the sum with an integral, valid in

the $\hat{t} \to 0$ limit, we find

$$\hat{g}(\theta) \equiv g(\theta, \hat{t}) = e^{-(R\theta)^2/8\hat{t}R^2} \tag{6.55}$$

from which we can identify the correlation length at the unfreezing time

$$\hat{\xi}_\infty \equiv 4R\sqrt{\hat{t}} \sim t_q^{1/4} \tag{6.56}$$

since $\hat{t} \sim \sqrt{t_q}/R^2$. Finite-size effects, captured by the dependence of the correlation length on the system size $2\pi R$, vanish in this limit. The exponent $1/4$ matches that predicted from the KZ scaling arguments, $\nu/(1+\nu z)$, using the mean-field exponents $\nu_{MF} = 1/2$ and $z_{MF} = 2$. The approximation (6.55) should be valid for $0 \ll |\theta| \lesssim \pi$. This is because the slow roll-off of the correlation function at large distances is captured by the low-frequency components of the order parameter (6.54). On the contrary, the short-range behavior for $|\theta| \approx 0$ (where the correlation function varies most rapidly) is captured by the asymptotic behavior of the c_ℓ ($\sim 1/\ell^2$ for $|\ell| \to \infty$). Typically the correlation length is defined via the asymptotic behavior of the correlation function, and so (6.56) should be a good indicator of the scaling behavior for short quench times. We derive the more rigorous asymptotic behavior in Appendix B, however. We note too that the correlation length cannot be defined by the curvature of the correlation function at $\theta = 0$, as would be possible if the correlation function had Gaussian character everywhere. This is because the algebraic $1/\ell^2$ decay of the fluctuation spectrum gives rise to discontinuities in all derivatives of the correlation function at $\theta = 0$.

It is interesting to note that the variances σ_ℓ^2 defined in (6.37) depend only on the variable $t/\hat{t} - \hat{t}\ell^2$. We could have anticipated the scaling relation of the correlation length from the prefactor of the ℓ^2 term, i.e., that the relevant length scale should

go as $\hat{t}^{1/2} \sim t_q^{1/4}$. This scaling relation would be expected to hold for $\hat{t} \to 0$, when the sum (6.53) can be replaced by an integral with small error estimatable by the Euler-Maclaurin formula. In fact, insofar as the replacement of this sum with an integral is justified, then the *single* relevant length scale in the correlation function is $\hat{t}^{1/2}$. It is in this limit that the original Kibble-Zurek argument is expected to hold, and that deviations occur when additional length scales enter into the problem due to the discreteness effects of periodicity and/or finite size. The combination of variables present in (6.37) additionally implies that the relevant time scale $\hat{\tau}$ for unstable long-wavelength fluctuations to grow should be set by $\hat{t} \sim t_q^{1/2}$. Both of these observations are in line with the predicted KZM scaling laws for the correlation length and the relaxation time. Finally, we can identify the relevant velocity scale at which fluctuations propagate near the unfreezing time, which is determined from the condition $t/\hat{t} - \theta(t)^2/\hat{t} = 0$. This implies that, at the unfreezing point, fluctuations propagate with a speed limit set by

$$\hat{v} \lesssim \dot{\theta}(t)|_{\hat{t}} \sim \hat{t}^{-1/2} \sim t_q^{-1/4} \tag{6.57}$$

This scaling relation will be important for discussions about the imhomogeneous Kibble Zurek mechanism Chap. 8.

As the quench time is increases, the correlation length defined in (6.56) becomes comparable to the ring circumference, at which point correlations extend around the ring (See Fig. 6.5). We choose to define the generalized correlation length as twice the distance at which the correlation function (6.51) falls to a value of $1/\sqrt{e}$, in accordance with the Gaussian definition of the correlation length. By using the exact expressions for the σ_ℓ^2, Eq.(6.37), we compute the t_q dependence of the correlation length at time $t = \hat{t}$ according to the above criterion. This is shown in Fig. 6.6. We fit a power law to the points at the shortest quench times to confirm the scaling law $\hat{\xi} \sim t_q^{1/4}$,

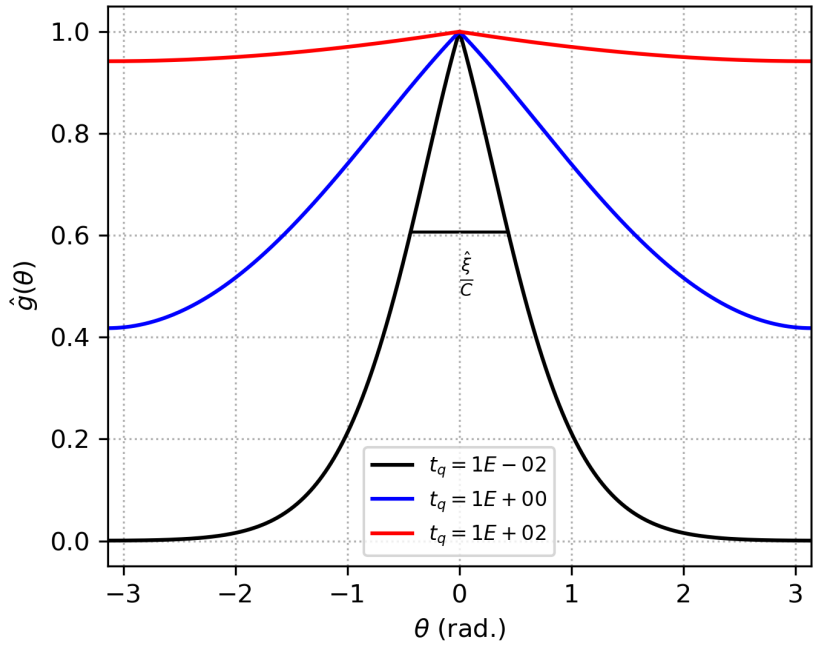

Figure 6.5: Example correlation functions for various quench times, each evaluated at $t = \hat{t}$. The correlation length $\hat{\xi}$ is computed at twice the $1/\sqrt{e}$ distance. For $\hat{\xi} \geq C$, we take the ring circumference C to be the correlation length instead, as correlations can fully extend around the ring.

but see deviations at longer quenches when correlations begin to extend around the ring. Eventually, the correlation length equals the ring circumference, at which point the ring becomes completely correlated according to the above definition. We note, however, that this does *not* imply that spontaneous current formation is completely suppressed; The usual arguments of the KZM break down at this point, and the details of the order parameter phase profile play a significant role in determining the winding number statistics.

We can find an approximate expression for the slow-quench correlation function by noting that $F(x) \sim 1/(2\sqrt{\pi}x)$ for $x \to -\infty$. As $\hat{t} \to \infty$ in this case, all terms in

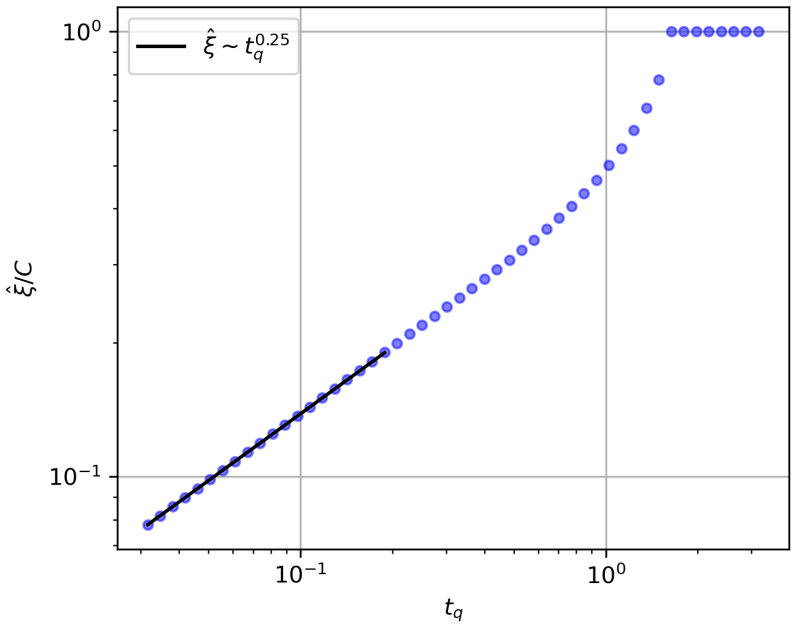

Figure 6.6: Correlation length $\hat{\xi}$ at time $t = \hat{t}$, defined via the $1/\sqrt{e}$ criterion, as a function of the quench time. For the fastest quenches we observe a power law scaling with exponent 0.25, which matches the mean-field prediction. For slower quenches, the correlations start to extend around the ring, and modified scaling occurs until eventually $\hat{\xi} = C$, and the ring is completely correlated.

the sum (6.53) with $\ell \neq 0$ can be replaced by their asymptotic expression. We find

$$\hat{g}(\theta) \approx \frac{1 + \frac{2\pi^{3/2}}{F(1)\hat{t}} B_2\left(\frac{|\theta|}{2\pi}\right)}{1 + \frac{2\pi^{3/2}}{6F(1)\hat{t}}} \tag{6.58}$$

where $B_2(x) = x^2 - x + 1/6$ is the Bernoulli polynomial of order $n = 2$ and a remarkable property of the polylogarithm was used, $\mathrm{Li}_n[\exp(2\pi i x)] + (-1)^n \mathrm{Li}_n[\exp(-2\pi i x)] = -(2\pi i)^n B_n(x)/n!$. Notably, the expression (6.58) lacks an obvious length scale, other than the (dimensionless) ring circumference 2π, demonstrating that finite-size effects tend to ruin the Kibble-Zurek argument in its original form. Any connection to the critical behavior should therefore be discerned from the order parameter itself, rather than its correlations, for slow quenches where finite size effects dominate.

We show two examples of correlation functions for fast and slow quenches, and

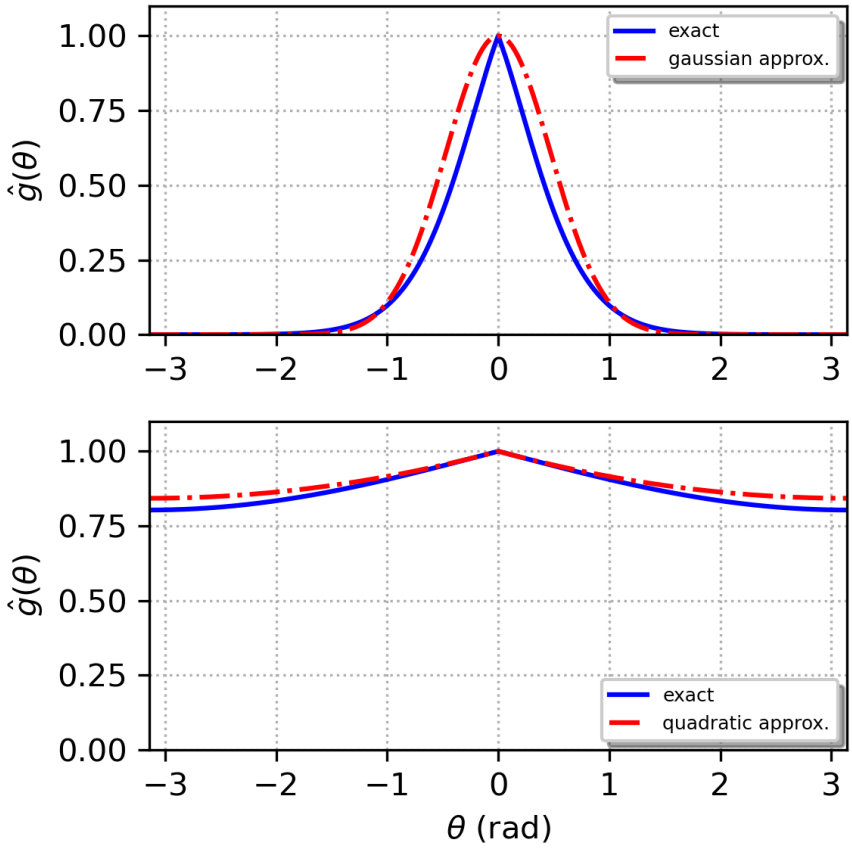

Figure 6.7: (Top) Exact correlation function corresponding to a fast quench, with its gaussian approximation shown for comparison. (Bottom) Exact correlation function corresponding to a slow quench, and the quadratic Bernoulli approximation shown for comparison.

their corresponding predicted asymptotic behaviors given by (6.55) and (6.58), respectively, in Fig. 6.7. For fast quenches (upper plot) the Gaussian captures the average size of the true correlation function quite well, although fails to capture its exact functional form at all length scales; The Gaussian is a course-grained approximation to the true correlation function. This is hardly a matter for the KZ argument, which only predicts the average domain size created during a rapid quench through the transition. We can obtain a better approximation to the true fast-quench correlation function with more sophisticated analysis, but we divert that calculation

to Appendix B. On the other hand, for slow quenches, the quadratic Bernoulli approximation successfully captures the short and long distance behavior of the true correlation function, although in this limit we lose a well-defined notion of a length scale meaningful to describe the average domain size during the quench.

We may combine the analytical analysis describing the distribution of spontaneous currents with the correlation function analysis to connect the variance in the winding number with average domain size. For faster quenches where a domain can be defined by a correlation length $\hat{\xi} \lesssim C$, we can define in the spirit of the KZ argument the number of domains $N_d = C/\hat{\xi} \gtrsim 1$. Clearly there can be issues with non-integer or fractional numbers of domains, but we ignore that complication for now. From the approximate probability distribution (6.44), we compute both $\langle w^2 \rangle$ and $\langle |w| \rangle$ as functions of the quench time t_q and evaluated at $t_{\text{eval}} = \hat{t}$. We then compute the number of domains N_d from the correlation function (6.53) using the $1/\sqrt{e}$ criterion for the same range of quench times. We plot both mean square and mean absolute value of the winding numbers $\langle w^2 \rangle$ and $\langle |w| \rangle$ as a function of N_d, which is shown in Fig. 6.8. As the Zurek argument predicts a scaling of the mean-square winding number $\langle w^2 \rangle \sim N_d$ in accordance to a random walk, we fit a power law to the points with $N_d \geq 3$ and recover an exponent of 1.09. The true random walk regime is accessed only when the mean absolute winding number $\langle |w| \rangle \sim N_d^{1/2}$, which does not occur until $N_d \gtrsim 10$. Our experiment, and the experiment in [86], occurs in the region $N_d \lesssim 10$, which does not access the random walk regime. Nonetheless, the mean-square winding number still roughly follows a linear scaling in the defect density for $N_d \gtrsim 3$, which allows it to be conveniently tied back to the critical exponents relating to the correlation length.

To conclude this subsection, we would like to draw a meaningful connection between the Kibble-Zurek freeze-out and unfreezing time, $\hat{t}_{KZ}$, and the blow-up time

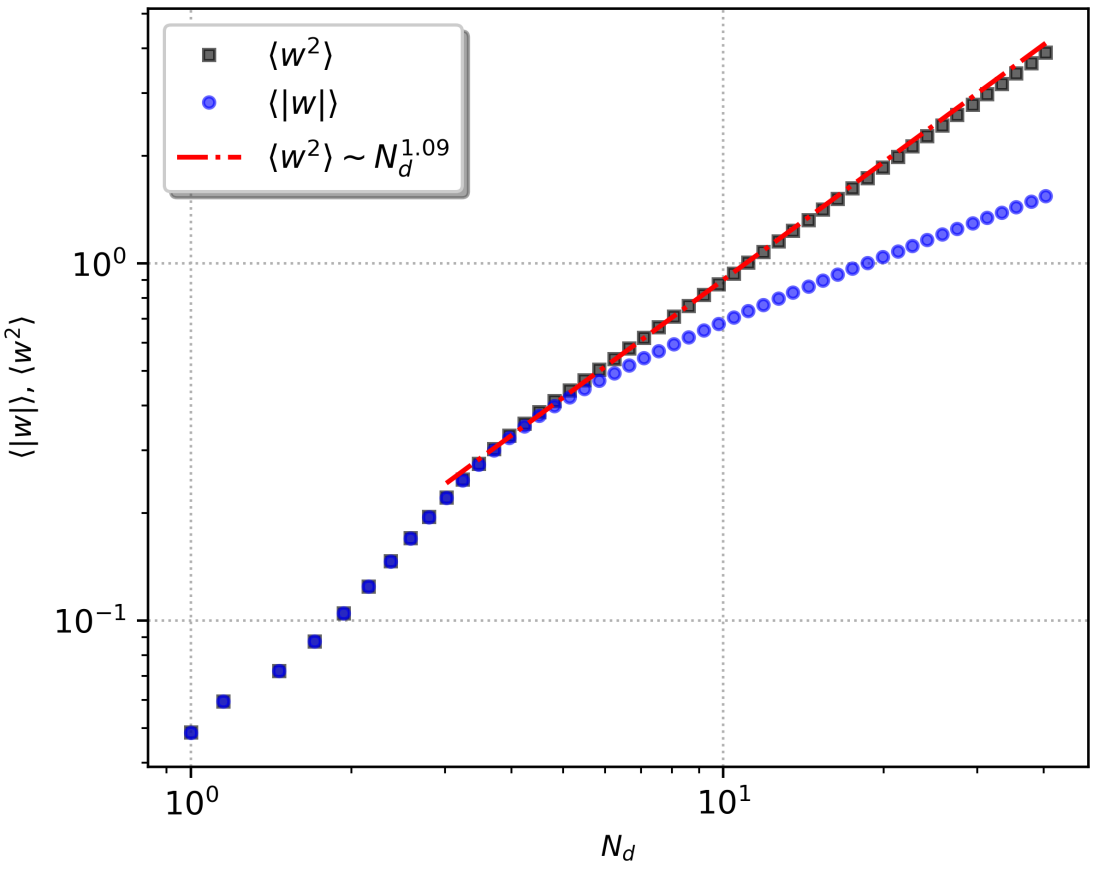

Figure 6.8: Log-log plot of mean absolute value and square of the winding number computed from the LSLG model. The scaling law $\langle w^2 \rangle \sim N_d$ is robust for defect numbers $N_d \gtrsim 3$, where $\langle |w| \rangle \gtrsim 0.25$. Incidentally, a fit to $\langle |w| \rangle$ for $3 \leq N_d \leq 10$ yields and exponent 0.85, which agrees with the result of the simple model in [86], although it is clear that this regime does not obey a power law.

$\hat{t}$ defined in our microscopic theory. The former is the approximate moment during the quench when the time until the transition is crossed becomes equal to the order parameter's equilibrium relaxation time. For fast quenches, the dynamics of the order parameter can adiabatically follow the quench protocol except for a brief period of time about the transition, where the relaxation dynamics slows down. Since this non-adiabatic regime is traversed rapidly for fast quenches, the phase transition occurs rapidly and the correlation length is effectively frozen in at the value it assumes at $t = -\hat{t}_{KZ}$, with no chance of adjusting its value as the transition occurs. Only when

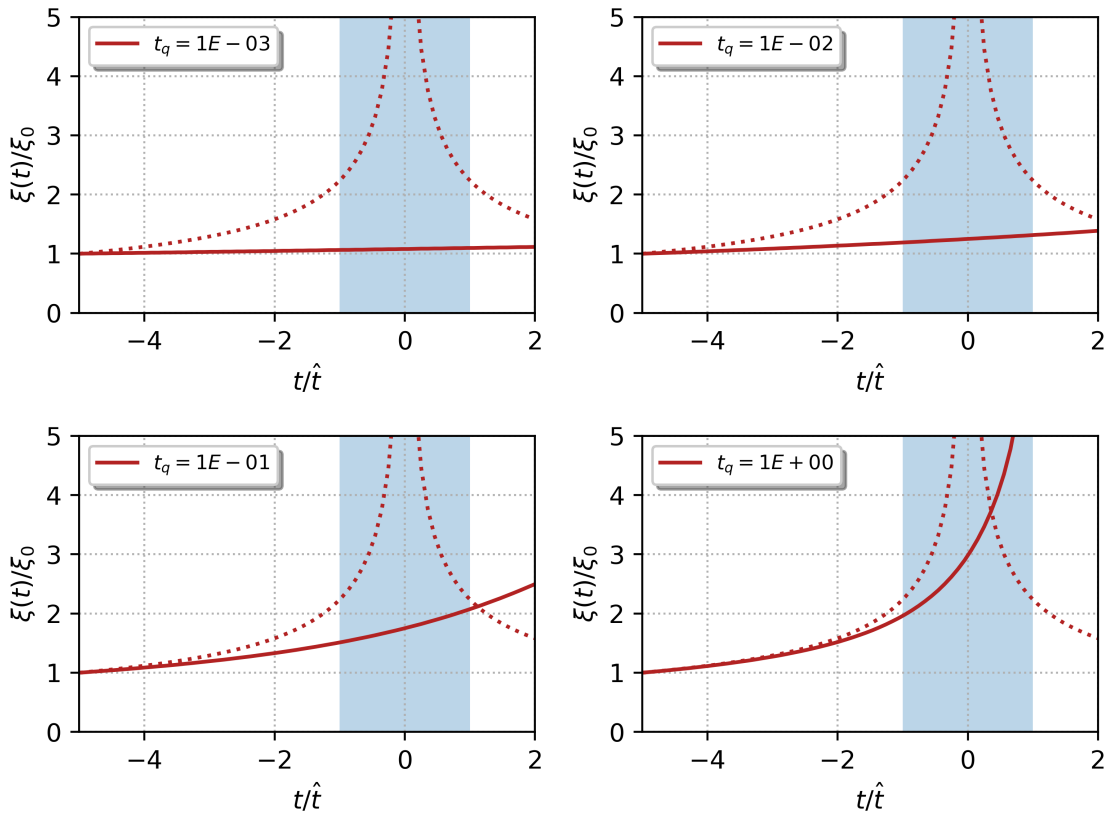

Figure 6.9: Dependence of the instantaneous correlation length (normalized to to its initial value) versus time in the interval $[-5\hat{t}, 2\hat{t}]$ for various quench times. The red solid lines indicate the instantaneous correlation length derived from the exact correlation function (6.53), while the dotted red lines indicate the mean-field (instantaneous) equilibrium prediction, $\xi \sim |\epsilon(t)|^{-1/2}$. The shaded blue region indicates the freeze-out region.

the unfreezing time occurs at $t = \hat{t}_{KZ}$ can the correlation length resume adiabatically following the quench, but at this stage, a sufficiently robust persistent current will have formed from the merging phase domains whose size were set by $\hat{\xi}_{KZ}$, the correlation length at the freeze-out time. We explicitly demonstrate the evolution of the correlation length within the non-adiabatic regime from the time-dependent correlation function (6.53). In Fig. 6.9 we plot the time-dependent correlation length normalized to its initial value ξ_0 as a function of $t/\hat{t}$ for four different quench times. For comparison, we show the equilibrium prediction for the correlation length $\xi \sim |\epsilon(t)|^{-1/2}$ using

the mean-field critical exponent $\nu = 1/2$. For the three fastest quenches, the relative variation of the correlation length within the non-adiabatic regime is under 50%, while for the slowest quench the variation is substantial. This behavior suggests a breakdown of the simple adiabatic-impulse-adiabatic cartoon picture for slower quenches. Furthermore, only for the slowest quenches does the instantaneous correlation length faithfully track the equilibrium prediction for times $t \lesssim \hat{t}$. Despite being "frozen" out for the fastest quenches, there is a significant mismatch in the actual and equilibrium correlation lengths at the freeze-out point. This is the motivation for incorporating a "fudge" factor into the KZM-predicted freeze-out correlation length that describes the domain size. Evidently in this case the fudge factor $f \sim 2$.

Chapter 7

Spontaneous currents in a Ring of Ultracold Fermionic Atoms

In this chapter, I will discuss the experimental details and results of exploring the Kibble-Zurek mechanism (KZM) in a fermionic ring of ^{6}Li. In particular, I will discuss the necessary steps to prepare an ensemble of cold fermions above the BCS superfluid transition, how the cold ensemble is quenched across this BCS transition into a superfluid state, and the statistics of spontaneous persistent current formation resulting from such quenches. Next, I will highlight several distinct and key advantages to performing KZ-type studies in the configuration that we employed in this experiment. Finally, I will discuss several key discoveries and open questions pertaining to the results.

Section 7.1

Introduction

The Kibble-Zurek mechanism (KZM) predicts the scaling of the density of defects nucleated as a system is quenched at variable rates across a second order phase transition [7, 8]. While simplistic in its argument, the KZM hinges on the thermodynamic

limit and uniformity. Neither of these conditions are ever met in reality, and various modifications to the KZM have been made to explain scaling laws observed in experiments. Since one of the goals of the KZM is to relate the quench scaling exponents to the adiabatic critical exponents ν and z respectively pertaining to the correlation length and relaxation time, one must be confident that these measured scaling exponents can be accurately tied back to the adiabatic ones.

To date, experimental studies of the KZM using ultracold atoms have utilized thermal quenches of bosons in harmonic, uniform box, and ring potentials, or of fermions in a harmonic or uniform box potentials[86, 113–117]. In the case of a harmonic trap, the KZ scaling exponents are modified, as causality restricts the trap region in which the KZM can proceed as usual [118]. In harmonic and uniform box traps, post-quench dynamics of the spontaneously nucleated vortices lead to non-universal saturation of the defect density for fast quenches. These two observations can complicate interpretation of the KZ scaling laws in those settings. KZM studies in ring-shaped traps have some advantages for mitigating these effects: The ring is homogeneous azimuthally and the spontaneous excitations (persistent currents) are long lived and topologically protected. This work is the first exploration of KZM for fermionic atoms in a ring potential, and the first to simultaneously utilize interaction quenches as well as thermal quenches. However, finite-size effects can still be important, and for technical reasons ring traps tend to be smaller than the broad harmonic traps. In all experiments of these types, there is the additional complicating factor that the universality class describing the transition may be mean-field or beyond mean-field in nature, and may depend on both the quench details and the microscopic physics [113].

For a homogeneous system, the reduced temperature may be uniformly swept across the transition in a linear fashion, $\epsilon(t) = t/t_q$ with t_q the quench time. The KZM predicts the density of defects nucleated while crossing the transition, which

is related to the equilibrium correlation length at the moment the order parameter ceases to follow the quench adiabatically due to critical slowing down:

$$\hat{\xi}_{KZ} \sim t_q^{\frac{\nu}{1+\nu z}} \tag{7.1}$$

For a thin one-dimensional ring of circumference C with $\hat{\xi}_{KZ} \ll C$ the number of uncorrelated domains formed at the freeze-out point is

$$N_d \sim \frac{C}{\hat{\xi}_{KZ}} \tag{7.2}$$

This is the scenario originally envisaged by W. Zurek [8], who further predicted a scaling of the mean absolute winding number $\langle |w| \rangle \sim N_d^{1/2}$, in accordance with a large-N_d random walk amongst the phase domains. Experiments have attempted to probe this regime but have hit limits on maximum quench rates due to prohibitively long thermalization times. For slower quenches, $\hat{\xi}_{KZ} \to C$, and the notion of a single well-defined correlation length starts to lose its meaning as correlations begin to extend around the ring. Various theories have predicted both a doubling of the scaling exponent and an exponential damping of the winding number in the slow quench regime [10, 99, 100]. Importantly, finite-size effects and periodic boundary conditions will become important, and the winding number statistics will become dependent on the exact phase profile within each domain.

Section 7.2

Experimental Details

To probe the statistics of spontaneous persistent current formation during a quench through the BCS transition, it is necessary to first discuss how we experimentally enact changes to the reduced temperature $\epsilon = 1 - T/T_c$ which drives the transition.

Clearly, one can vary ϵ by changing either the system temperature T, the critical temperature T_c, or both. The former is typically controlled via evaporative cooling, where the height of the confining potential is lowered and hot atoms can escape, lowering the system temperature while causing atom loss. While simple in its approach, changes enacted to the confining potential during evaporation will also cause the density profile to change, which in turn may complicate the quench dynamics. Furthermore, evaporative quenches are unidirectional in the sense that they are always associated with irreversible atomic loss. The latter can be controlled, in ^{6}Li, using a broad Feshbach resonance to tune the scattering length, which in turn affects T_c through its dependence on the combination $k_F a$. There are several notable advantages to using an interaction-based quench compared to an evaporative quench. Firstly, the scattering length a, and therefore the critical temperature T_c, responds to changes in magnetic field on very short timescales (typically ~ 100 ns) set by the two-body scattering timescales. In comparison, a temperature quench must be slow enough such that (local) thermodynamic equilibrium is maintained at each instant in the quench. This is only true if the elastic scattering rate, which depends on both two-body *and* many-body properties, is large enough compared to the instantaneous rate of change of the confining potential. As a result, interaction quenches are limited primarily by the rate at which the magnetic field can be slewed, independently of the state of the system. Secondly, the critical temperature in the BCS limit depends exponentially on the interaction parameter, i.e. $T_c \sim \exp[-\pi/(2k_F|a|)]$, and thus it can be swept rapidly across the transition with relatively little change in a. Finally because the chemical potential is only weakly dependent on $k_F|a|$ for $1/(k_F a) < 0$, the density profile does not change significantly during interaction quenches that remain on the attractive side of the Feshbach resonance. One may choose to additionally employ a "hybrid" quench protocol, where both the temperature and the critical temperature

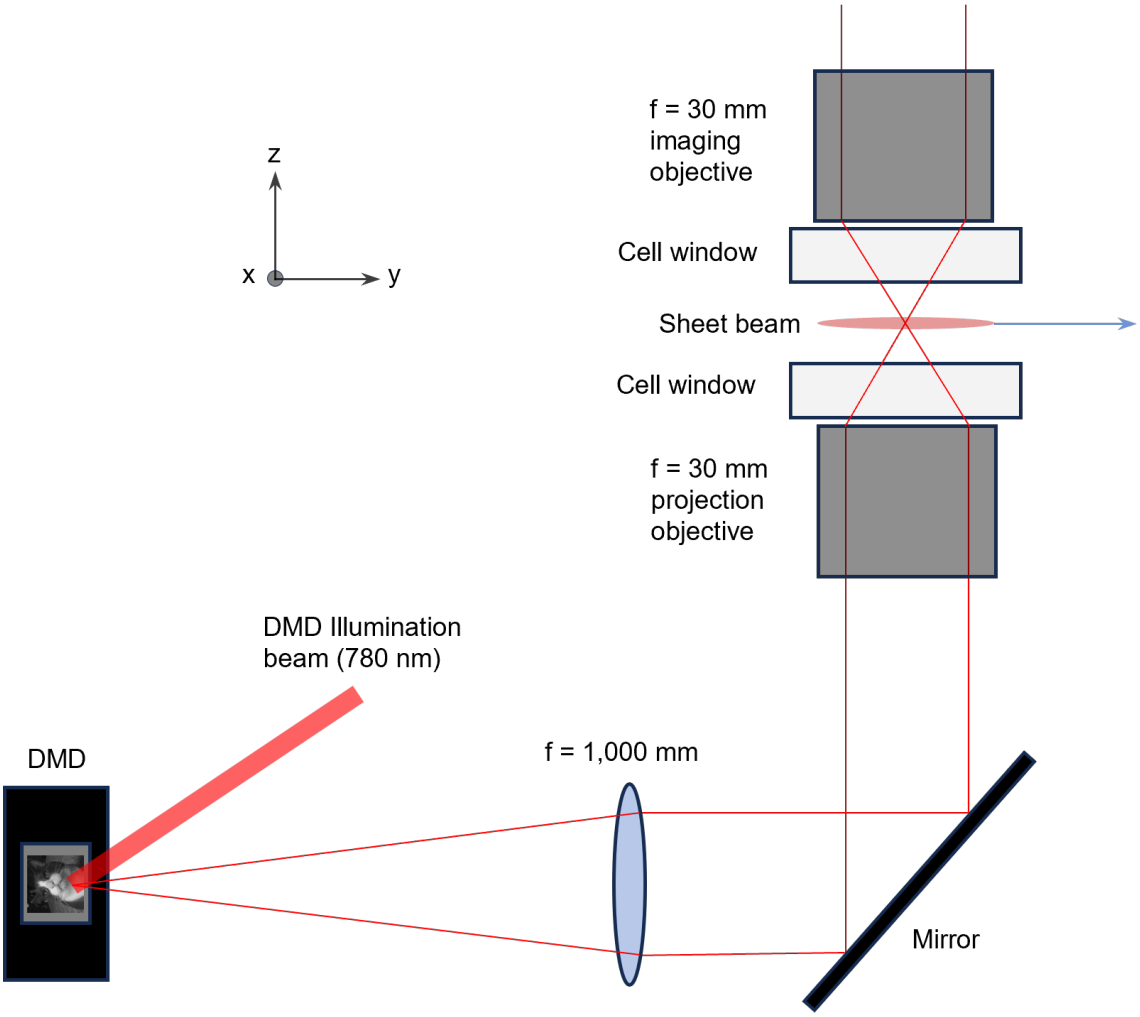

Figure 7.1: Simplified schematic showing a side-view of the DMD projection system (not to scale). An arbitrary pattern generated on the DMD is directly imaged in a 4-f configuration onto the middle of the cell, piercing the flat horizontally propagating sheet beam and allowing for arbitrary transverse confinement potentials.

are ramped simultaneously. This has the effect of boosting the effective quench rate for a given ramp time, while accomplishing the quench using a less extreme range of control parameters. It is also worth noting that interaction-based quenches are completely reversible, making prospects of performing repeated quenches possible. This could pave the way to experimentally realizing a spontaneous current "pump," where a superfluid can be wound up into a high state of circulation using repeated quenches across the transition.

In the BCS limit, where the experiment takes place, $1/(k_F a) \lesssim 0$, and the critical temperature for the superfluid transition can be expressed by Gorkov's expression

$$\frac{T_c}{T_F} = \alpha \exp\left(-\frac{\pi}{2k_F|a|}\right) \tag{7.3}$$

with the constant $\alpha = \left(\frac{2}{e}\right)^{7/3} \frac{e^\gamma}{\pi} \approx 0.277$. For a given temperature T/T_F, the transition occurs when $1 = T/T_c = T/T_F \times T_F/T_c$, which can be inverted to find

$$\lambda_c \equiv \frac{1}{k_F|a_c|} = \frac{2\log\left(\frac{\alpha T_F}{T}\right)}{\pi} \tag{7.4}$$

This critical interaction parameter at which the transition occurs acquires a position dependence via the local density approximation, in which $\mu(\mathbf{r}, T, a) \equiv \mu(T, a) - V(\mathbf{r}) \approx \mu_0[n(\mathbf{r}), T, a]$ where μ is the global chemical potential in the trap and $\mu_0(n, T, a)$ is the chemical potential in the homogeneous system of density n, temperature T and scattering length a. The local critical interaction parameter attains a maximum at the potential minimum, which in a ring-dimple trap occurs in the ring-shaped region of highest density. During a quench, the transition occurs simultaneously at all angles around the ring minimum (in a perfectly smooth ring), but occurs at different later times for radii excluding the ring radius. Thus, the quench dynamics are mixed-dimensional. However, as long as causality is obeyed in the radial and axial directions, transverse excitations are supressed and the dynamics of the order parameter can be approximated as one-dimensional [118].

The experiment utilizes a fully red-detuned trapping geometry consisting of a 1064 nm horizontally-propagating sheet, and a 780 nm vertically propagating pattern beam, typically shaped via the DMD and subsequently directly imaged onto the sheet. We show a simplified schematic of the DMD projection optics in Fig. 7.1. In the experiment detailed in this chapter, a double ring geometry was utilized, which was

found empirically to produce interferometric spiral fringes with the largest contrast (See Chap. 5).

We begin with a roughly equal mixture of 10^6 ^{6}Li atoms in the two lowest energy hyperfine states at a field of 81.7 mT, just beneath the 83.2 mT Feshbach resonance. With the double ring beam at full power, we evaporatively cool the ensemble by lowering the sheet power from an initial value of 3 W to a final value of around 400 mW, which is slightly above the point at which the loosely bound molecules begin to condense. The sheet power is ramped according to an exponential profile, with total time $t_{\mathrm{evap}} = 2$ seconds and time constant 0.3 s, giving an initially rapid evaporation with a smooth tail near the end of the ramp. By the end of the evaporation the double ring shaped region is modestly populated, although the majority of the atoms/molecules still reside in a broad halo in the sheet. Next, we keep the sheet power fixed and adiabatically ramp in $t_{\mathrm{ramp}} = 100$ ms the magnetic field above the Feshbach resonance to around 98 mT. At this point, the interaction parameter $1/(k_F|a|) \approx 0.7$, which was determined from a numerical model of the full trapping potential [31, 32]. Here a is the tunable s-wave scattering length and k_F is the Fermi wave-vector. The reduced temperature T/T_F is large enough such that $T > T_c$ and the system is in the normal state above the transition. We confirm this by performing in-situ thermometry (see Sec.4.3 and [32, 79]) on the atoms in the halo and find that $(T/T_F)_{\mathrm{initial}} \approx 0.25$. From Gor'kov's critical temperature prediction $T_c/T_F = 0.277\exp[-\pi/(2k_F|a|)]$ [78], we subsequently find $(T/T_c)_{\mathrm{initial}} \approx 3$. We show the radial profile of the density distribution and the corresponding fit using the equation of state in Fig. 7.2. Values of various relevant thermodynamic quantities extracted from the fit are shown in the plot at well.

To reliably initialize a static, non-rotating state before the quench, we keep narrow barriers in both the inner and outer rings during the state preparation. This is

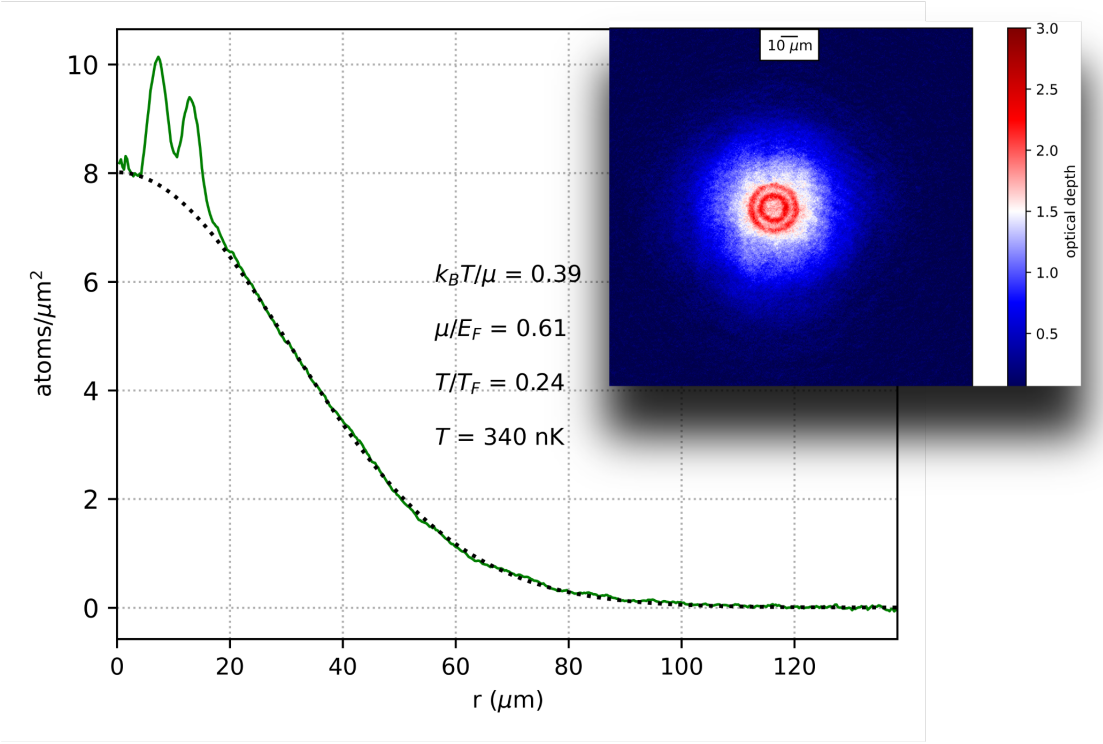

Figure 7.2: Radial density profile in a particular spin state (green solid line) and corresponding fit (black dashed line) to the in-situ density distribution of atoms at 97.6 mT (See Chap. 4.4. From the fit to the broad, dilute halo of atoms we extract the reduced temperature, chemical potential, and absolute temperature. The Fermi energy is obtained from a model of the full trapping potential described in Chap. 4.4. We additionally show the column density obtained from an average of 20 in-situ images from which the radial profile is obtained. The full field of view of the imaging system is shown and the halo is clearly visible.

achieved by dynamically updating a digital micromirror device (DMD, Texas Instruments DLP Lightcrafter6500) to display patterns that have barriers of controllable depth. The barriers themselves, which break rotational symmetry, act to halt flow in both rings before the quench. Since the inner ring was inherently smoother and less aberrated than the outer ring, we chose to the inner ring to be the "experiment" ring, and the outer to be the reference ring for interferometric detection. Thus, just before the quench, we remove the barrier in the inner ring while keeping the barrier in the outer ring up to prevent spontaneous currents from forming in it during the quench. To enhance the probability of forming spontaneous currents, we employ a

hybrid quench protocol, where both the temperature *and* the critical temperature are changed and various rates. The former is controlled by linearly reducing the sheet power, causing evaporation that lowers the temperature in an approximately linear fashion. The latter is controlled by tuning the scattering length via Feshbach resonances, which in turn affects the critical temperature according to the Gor'kov relation [78]. A distinct advantage of such a quench is that one can get an enhancement of the quench rate using a less extreme range of control parameters. In particular, the exponential suppression of the critical temperature with interaction strength, coupled with the relatively small sensitivity of the chemical potential to the interaction parameter for $1/(k_F a) < 0$, means that one can enact a fairly rapid quench while minimally disturbing the density profile of the ensemble. Additionally, the evaporative cooling that has been frequently employed to perform thermal quenches can be driven over a smaller range, again with the motivation of disturbing the atomic density as little as possible, and to reduce atomic losses during evaporation as much as possible.

To perform this hybrid quench discussed above experimentally, we simultaneously ramp the magnetic field and the sheet power to the final values 85 mT and 40 mW, respectively, over times ranging from 50 ms to 4.4 s. We show the in-situ density profiles of the ring-dimple trap before and after the hybrid quench in Fig. 7.4. Due to the blow-up of the scattering length near the Feshbach resonance, the transition is crossed in the middle of the quench but close to unitarity, at a value of $1/(k_F a) \approx -0.3$. At the end of the quench, we adiabatically remove the barrier in the outer ring over 100 ms and then snap off the current in the jump coil while simultaneously extinguishing the power in the dipole beams. This initiates free ballistic expansion of tightly bound molecules at around 65 mT, owing to the efficient molecule conversion during the rapid field jump. After 1.3 ms of time-of-flight, we take an absorption image on the D_2 high-field σ^- cycling transition and extract the winding number

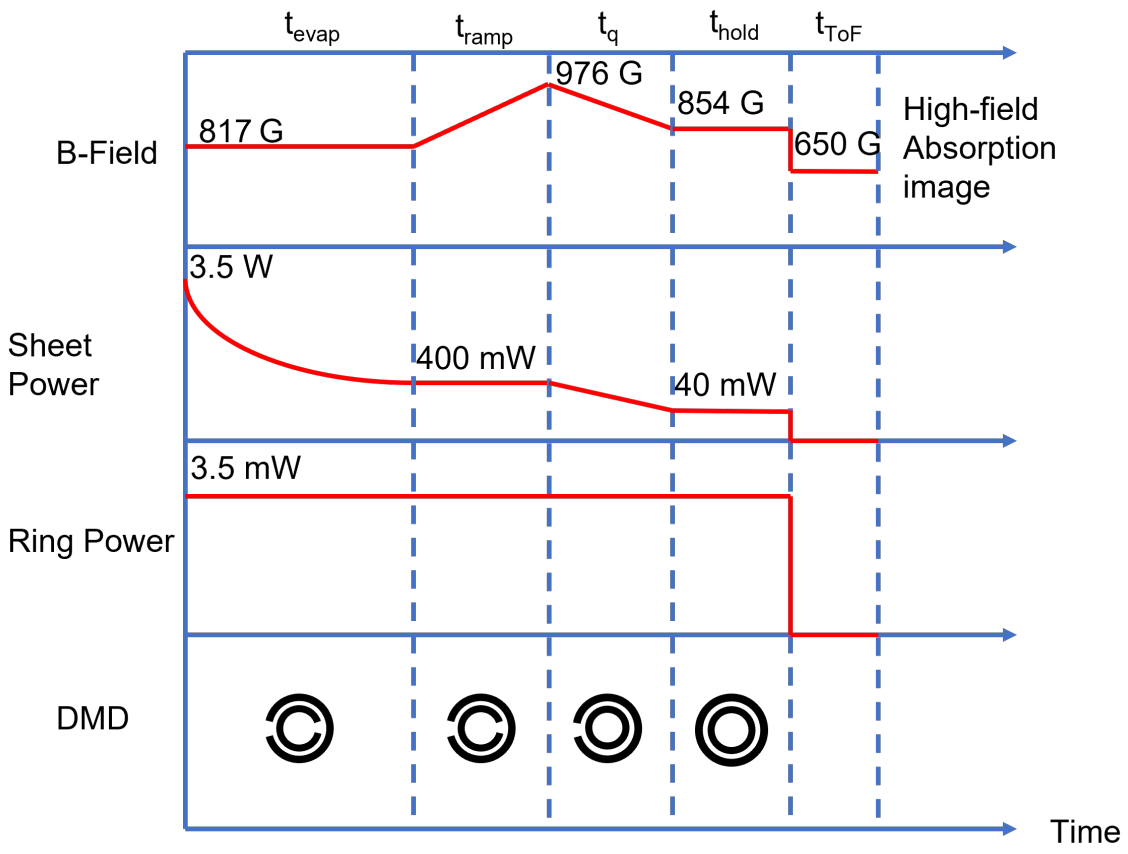

Figure 7.3: Schematic detailing the preparation and hybrid quench procedure. Neither the vertical axes nor the time axis is to scale with respect to the actual experimental values. The quench occurs over a variable interval t_q, while all of the other time intervals are fixed, and have self-explanatory labels. The state preparation phase terminates at the end of t_{ramp}, at which point the hybrid quench proceeds. DMD patterns are shown in inverse for visual clarity (dark regions are intensity maxima).

of the persistent current formed at the end of the quench inteferometrically. The is repeated at least 40 times for each quench time, and statistics of the spontaneous current formation process are measured. Example interferograms, showing winding numbers $w = 0$, $w = -1$ and $w = 2$ are shown in Fig. 7.4. The clear spiral arms the interferograms allow for unambiguous measurements of the winding numbers.

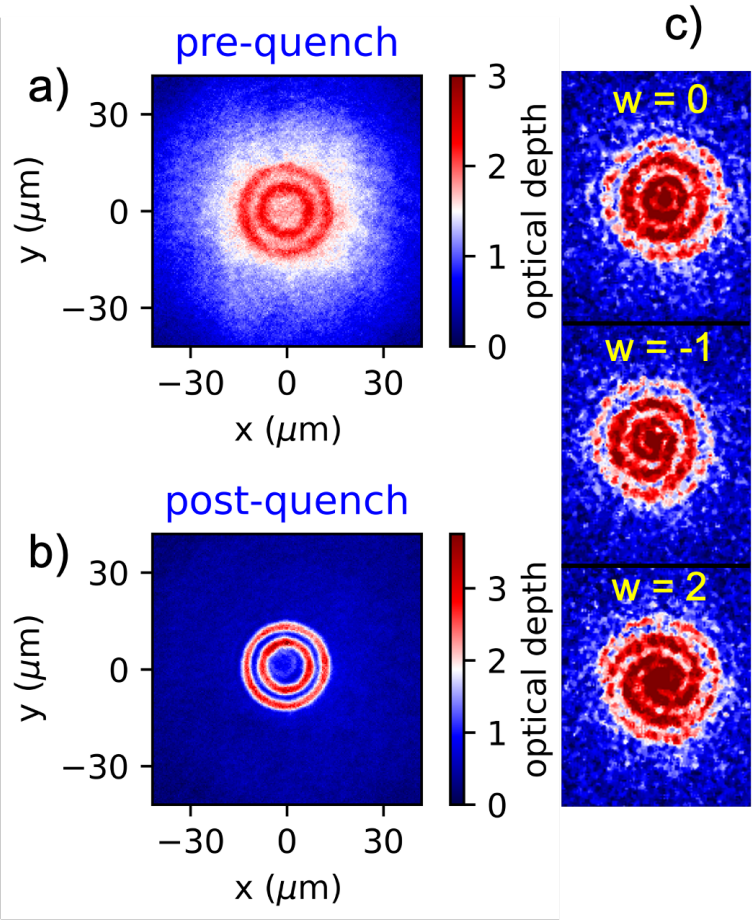

Figure 7.4: a) We start with an equal mixture of $N = 9.6 \times 10^4$ total atoms at a field of 976 G. We don't include barriers in the DMD potential here. b) After a 50 ms hybrid quench discussed in the main text, we end up with $N = 6.5 \times 10^4$ total atoms. The broad, dilute halo can be seen in both images, and is responsible for limiting the deleterious effects of heating due to various collisions, and for maintaining a roughly constant peak density in the ring dimple region during the quench. c) Example interferograms after ballistic expansion for 1.3 ms.

Section 7.3

Results and Discussion

The distribution of measured spontaneous currents is peaked around $w = 0$ for all quench times. Although the degree of symmetry of the distribution varies between quench times, the average of measured winding numbers for all quench times is con-

sistent with a zero-mean and symmetric distribution. We show several example histograms of measured winding numbers in Fig. 7.5.

It is important to additionally rule out the possibility of post-quench persistent current decay due to thermally activated phase slips or vortex annihilation events causing systematic effects on the winding number distribution. To confirm this, we prepared with $\approx 100\%$ fidelity an $\ell = 2$ persistent current state using a 2-axis acousto-optic deflector and a blue-detuned "stirring" beam [31], and observed no decay of the winding number even for hold times exceeding 5 s. As mentioned earlier, the lack of destructive post-quench dynamics is a unique benefit to performing KZM studies in ring-shaped traps.

We show in Fig. 7.6 the winding number variance of spontaneous currents formed after a quench across the BCS transition at various rates, spanning several decades. Each data point represents at least 40 realizations, and the error bars are obtained from a bootstrapping technique [119]. We also show the numerically simulated mean-square winding number evaluated at $t_{\text{eval}} = 3\hat{t}$ (See Sec. 6.3). We now highlight several additional important features of Fig. 7.6.

For the fastest quenches, we see an approximate power law scaling of the form $\langle w^2 \rangle \sim t_q^{-\sigma}$. Fitting the first nine data points to this power law function gives a scaling exponent $\sigma = 0.24(2)$. This exponent can be compared to the KZM prediction,

$$\sigma_{KZ} = \frac{\nu}{1 + \nu z} \tag{7.5}$$

with the usual equilibrium exponents ν and z describing the correlation length and relaxation time, respectively. For the mean-field predictions $\nu_{MF} = 1/2$ and $z_{MF} = 2$, giving $\sigma_{KZ} = 1/4$, which is in line with our measured σ. The F-model exponents describing the 3D BEC transition, $\nu_F = 2/3$ and $z_F = 3/2$ give $\sigma_{KZ} = 1/3$, larger than that observed. The slightly lower observed exponent may be significant if one

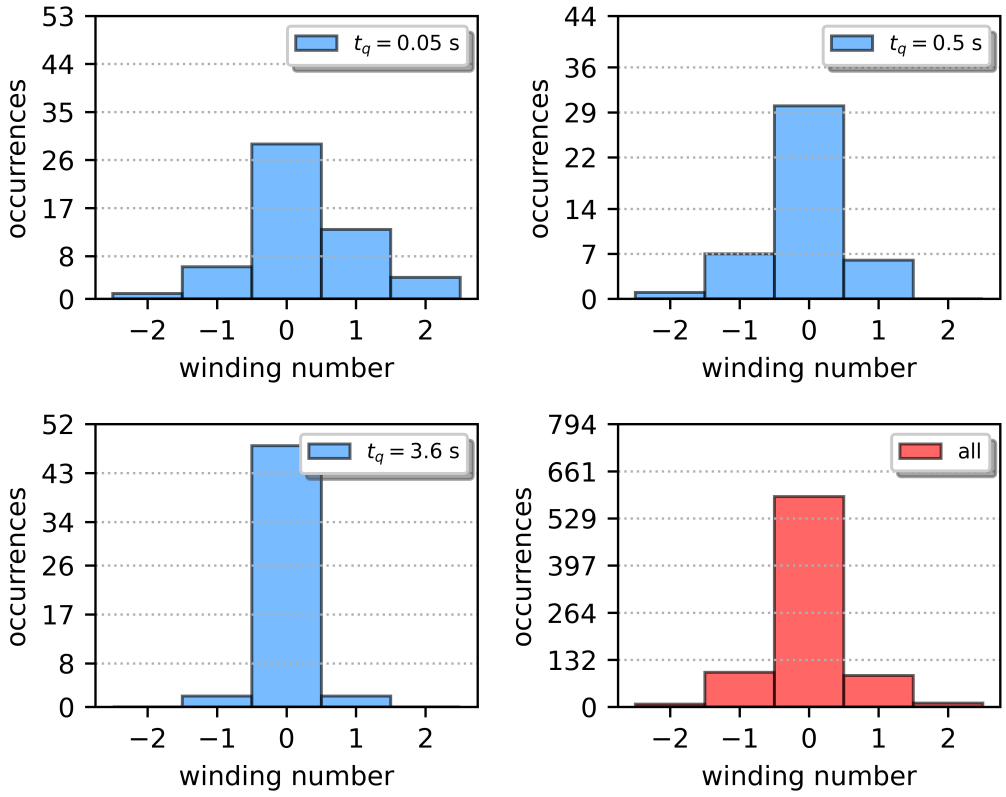

Figure 7.5: Observed occurrences of winding numbers for various quench times (blue histograms). Each histogram contains at least 40 samples. The number of samples for each displayed histogram is given by the largest number on the y-axis. We also show a histogram of winding numbers for all quenches (red histogram). The global average of all winding number measurements $\langle w \rangle_{\text{all}} = 0.004$, indicating that there are no biases to the winding number distribution and the spontaneous current formation is a stochastic process with zero mean.

accounts for the modified interactions with the large fermionic reservoir [120]. In particular, if one accounts for energy damping collisions with the reservoir, substantial multiplicative noise may be introduced onto the order parameter during its evolution, affecting the rate at which it may relax to its equilibrium value. This in turn has been observed to increase the value of the dynamical exponent by a factor of about 2, while preserving the correlation length exponent. This leads to a prediction of $\sigma \approx 0.19$, which is also in line with our measured value. The mean-field scaling is expected to hold when the reduced temperature at the point of freeze-out, $\hat{\epsilon}$, is large

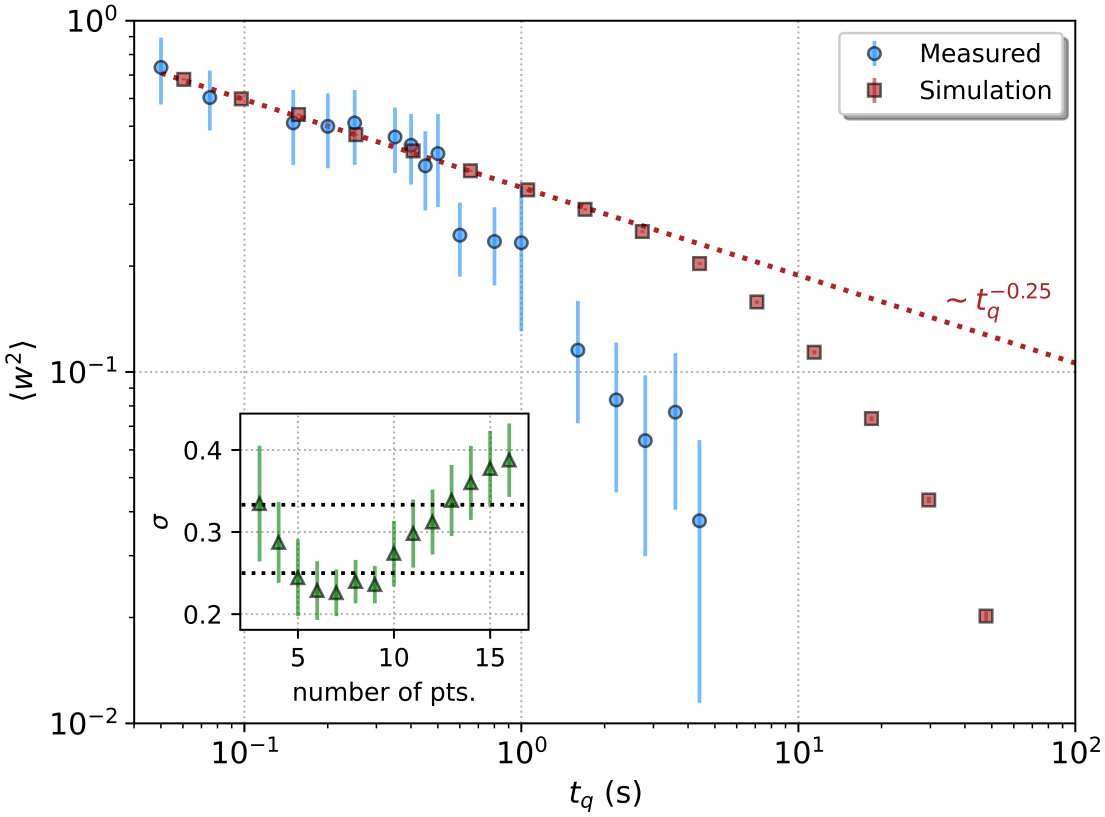

Figure 7.6: Plot of measured winding number variance versus quench time (blue circles). A power-law fit to the measured data for the nine fastest quenches reveals a scaling exponent $\sigma = 0.24(2)$. We also show the variances obtained from the simulated winding number distribution obtained using the 1D LSLG model (red squares). The simulated distribution is evaluated at a time $t = 3\hat{t}$ (See text for details). The straight red dotted line shows a power law with exponent 0.25. The inset shows the power law fit-extracted exponents σ obtained from fits to various numbers of fastest-quench data points. The dotted lines show the mean-field and F-model predictions $\sigma = 1/4$ and $\sigma = 1/3$, respectively.

compared to the Ginzburg number Gi, which is the reduced temperature below which Gaussian fluctuations of the order parameter dominate over its mean [121, 122]. In the BCS limit, Gi $\sim (T_c/T_F)^4 \lesssim (0.277)^4 \approx 0.006$, where Gor'kov's critical temperature $T_c/T_F = 0.277 \exp[-\pi/(2k_F|a|)]$ was used. On the other hand, winding numbers observed in the experiment are consistent with the average number of domains $N_d \approx C/\hat{\xi}_{KZ} \lesssim 10$ [86]. Using the mean-field scaling relationship $\hat{\xi}_{KZ} \approx \xi_{\mathrm{BCS}} \hat{\epsilon}^{-1/2}$

with the BCS coherence length $\xi_{\mathrm{BCS}} \approx 0.5\ \mu$m, we estimate $\hat{\epsilon} \lesssim 0.01$. As $\hat{\epsilon} \gtrsim$ Gi for the faster quenches, we expect a mean-field scaling law to roughly hold. Unambiguous distinction between mean-field and F-model scaling has been elusive due to the precision required to probe the relatively small scaling exponents.

We note that by varying the number of points used in the fit, we obtain a set of scaling exponents, which is shown in the inset of Fig. 7.6 (Errorbars are obtained from the fit covariance matrix). Using the first 5 to 9 points, however, gives a roughly constant exponent near 0.24, although each exponent is systematically lower than the mean-field result 0.25. The slightly lower observed exponent may be significant if one accounts for the modified interactions with the large fermionic reservoir [120]. In particular, if one accounts for energy damping collisions with the reservoir, substantial multiplicative noise may be introduced onto the order parameter during its evolution, affecting the rate at which it may relax to its equilibrium value. This in turn has been observed to increase the value of the dynamical exponent by a factor of about 2, while preserving the correlation length exponent. This leads to a prediction of $\sigma \approx 0.19$, which is below our measured value slightly, but still potentially relevant.

For the slower quenches, we observe a clear transition from the KZ regime of fast quenches into the intermediate-quench regime where the variance falls more rapidly with the quench time. This scaling laws in this intermediate regime are non-universal, and depend on the microscopic details of the system as well as system geometry and finite-size effects. While several theories have been put forth to explain observed scaling laws in small rings [10, 99, 100], experimental findings are somewhat contradictory, especially in the transition region following the KZ regime. While the data points to an exponential fall-off in the variance for intermediate quenches, in line with the predictions from [99] and from our linearized stochastic Landau-Ginzburg model, importantly we show that the KZ regime is distinct for a significant range of quench

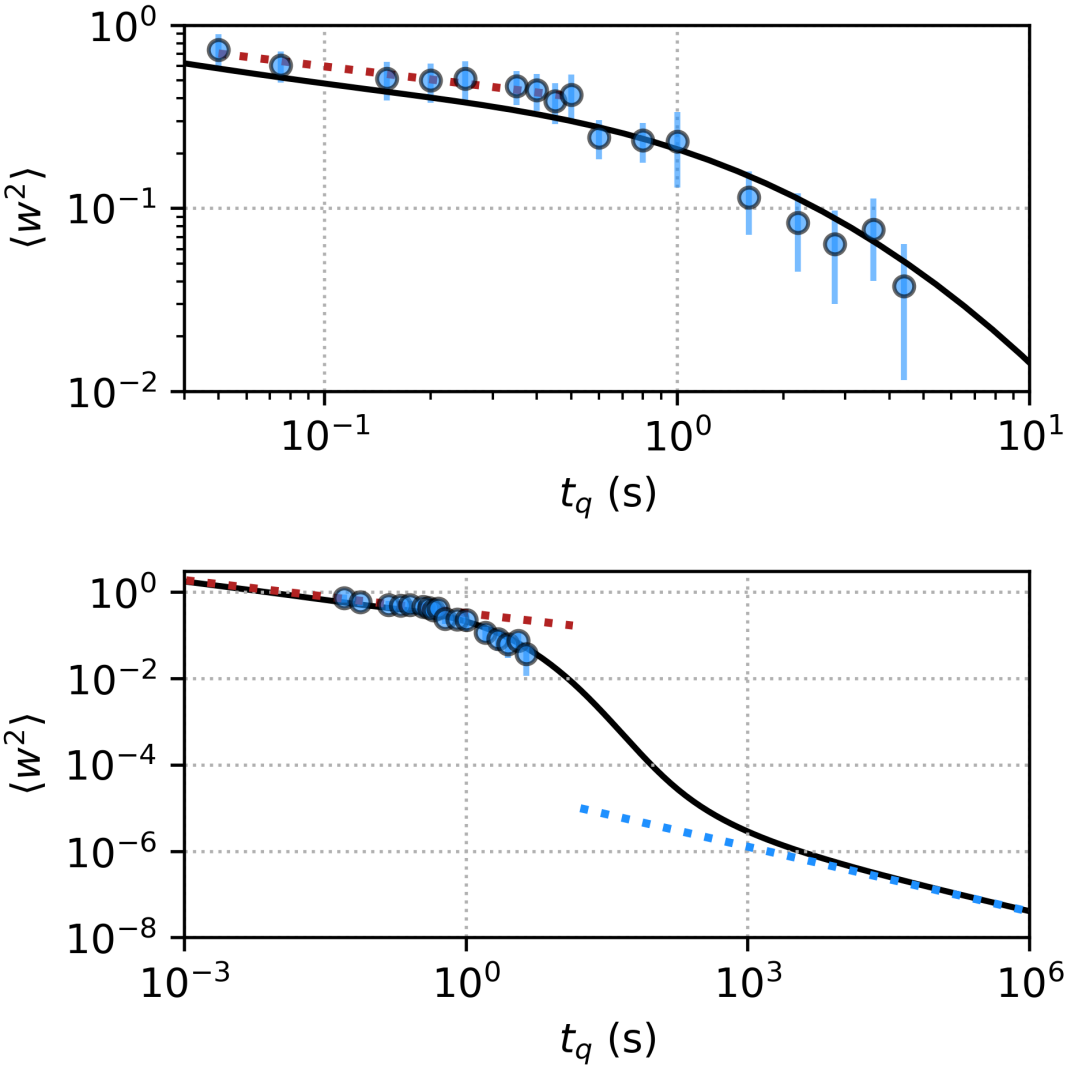

Figure 7.7: (Left) Plot of measured winding number variance versus quench time (blue circles). We show the theoretical variance (black dotted line) obtained from the LSLG model, evaluated at time $t = 3\hat{t}$. We also show a power-law fit to the fastest nine quenches, which shows a scaling exponent $\sigma = 0.24(2)$ in line with the mean-field KZ prediction $\sigma_{MF} = 1/4$. (Right) Theoretical prediction from the same LSLG model showing an expanded range of quench times. We fit a power law function to the fastest and slowest quenches, which reveals scaling exponents of 1/4 and 1/2, respectively. The highlighted patch of the curve is where our experiment is believed to take place, and encloses both the KZ regime and the intermediate crossover regime, which is of exponential character.

times used in our experiment. While a scaling exponent *doubling* has been predicted to occur for the slowest quenches, we note that the onset of this scaling regime of extremely rare occurrences may depend on microscopic properties and finite size effects within the system. Our data does not appear to capture this regime; Fitting a power law to the slowest quench data gives an exponent of around unity, although we do not have the precision to assess whether this is a universal or an non-universal quench regime with a single well-defined scaling exponent. We show the same measured mean-square winding numbers in Fig. 7.7, but this time using the analytical approximation to the winding number distribution described in Sec. 6.3. This plot highlights the fact that this slow quench regime may exist, but lies within a range of prohibitively difficult-to-access experimental conditions.

We see good agreement in the measured and simulated data for the fastest quenches, bolstering Zurek's original theoretical argument for winding number scaling in 1D rings. Additionally, we see a more rapid fall-off for slower quenches, although our simulated values do not match the measured values in this regime. This can potentially be explained by the effects of dimensionality on spontaneous current formation, as was observed in numerical simulations in [99]. The sharper fall-off in the measured data for slow quenches may point to an enhanced role of 2D or 3D effects, and further investigation into the effects of dimensionality in an experimental setting is warranted, i.e. by performing quenches into rings of variable widths.

In the fast-quench limit, the critical exponents describing the transition are directly related to the quench time scaling exponent σ in a straightforward and *physically transparent* way; The variance of the winding number is set by the large number of uncorrelated phase domains according to a random walk description, and finite-size effects are negligible. To connect the measured scaling laws in this regime to the adiabatic critical exponents, however, requires more information. In particular,

a measurement of the mean-square winding number scaling in the KZ regime reveals only the combination given in (7.5). Additional measurements probing some different scaling exponent, that is itself a different combination of the critical exponents ν and z, would be required to extract simultaneously ν and z. In the absence of such measurements, one can only relate the observed KZ exponent to predictions for what the critical exponents should be. On the other hand, if one is confident in the value of one of the critical exponents, then the other may be estimated from the measured scaling exponent in the KZ regime. For instance, in both the mean-field and F-model predictions, the combination $\nu z = 1$. This implies that $\nu = 2\sigma_{KZ}$ and $z = 1/(2\sigma_{KZ})$ for both models. Insofar as a measured exponent σ can be associated with the KZ exponent σ_{KZ} and the above condition $\nu z = 1$ holds, ν and z can be independently estimated.

The findings of this experiment, and the results from [120], raise questions as to how reservoir interactions can affect the critical exponents of the phase transition. However, the robust scaling behavior for the fast-quench regime points to a a scaling regime in line with the Zurek scaling argument. While the measurements in this experiment were taking in a ring-dimple configuration, where a large background bath of normal fluid was present during the quench, we note that reservoir interactions are *always* present in real systems. The exact details of the reservoir, which vary from system to system, seem to limit the range of applicability of universal descriptions of phase transitions. It would be very insightful to study the same scaling laws in a blue-detuned double ring trap, where the halo atoms could be isolated and the reservoir is contained entirely in the ring.

An additional relevant point of discussion regards the role of pairing and pseudogap physics in quenches of Fermi gases [123, 124]. It is well-known that there is a separation between the temperatures at which pairs form, T^*, and the criti-

cal temperature marking the onset of condensation T_c, with $T_c < T^*$. In the BCS limit $(k_F a)^{-1} \to -\infty$ the two temperatures coincide, but for large negative and finite $(k_F a)^{-1}$, a narrow band of temperature exists for which $T_c < T < T^*$ and $(T^* - T_c)/T_c \ll 1$. For quenches in the BCS limit, the correlation length of fluctuations in the Cooper pairing field is essentially zero for all $T(t) > T^*$, as Cooper pairs hardly exist then. Only in the narrow temperature band $T_c < T(t) < T^*$ can correlations in fluctuations of the Cooper pair field be established, and the correlations will attempt to equilibrate with a length scale $\xi_{\rm eq} \sim (T^* - T_c)^{-\nu}$. This length scale can potentially be extremely large, but the fluctuations have not been able to grow on such a short time scale. We can posit that the correlation length will grow linearly from zero following the time t^* in the quench when $T(t = t^*) \equiv T^*$, on a time scale set by the instantaneous relaxation time $\tau(t^*) \sim |(T^* - T_c)/T_c|^{-\nu z} \equiv |\epsilon^*|^{-\nu z}$:

$$\xi(t) \sim \frac{t - t^*}{\tau(t^*)}. \tag{7.6}$$

with $|\epsilon^*| \ll 1$. The correlations grow until the unfreezing time $+\hat{t} \sim t_q^{\nu z/(1+\nu z)}$ is reached on the other side of the transition and rapid condensate growth can occur. At this point, the correlation length will have grown to about

$$\xi(t = +\hat{t}) \sim \frac{\hat{t} - t^*}{\tau(t^*)} \sim |\epsilon^*|^{\nu z} \left(t_q^{\frac{\nu z}{1+\nu z}} - c \right) \tag{7.7}$$

where $c \sim |\epsilon^*|$ is some small constant. Therefore to leading order in $|\epsilon|^*$, the correlation length at the unfreezing time scales with the quench time with an exponent $\nu z/(1+\nu z)$, which is z times that of the usual KZ scaling exponent. The Cooper pairing field experiences a brief and sudden "whack" as the pairing critical temperature T^* is crossed, and the small correlation length of these fluctuations can give rise to an enhancement in the rate of defect formation with an enhanced scaling exponent.

Importantly, the correlation length setting the domain size should, in the deep BCS limit, be determined by its growth within the impulse period of the quench below the transition, $t \in [0, +\hat{t}]$, as opposed to its value at the moment when the order parameter fluctuations are first frozen out as described within the adiabatic-impulse-adiabatic approximation. In our experiment, as was stated earlier, the transition is crossed closer to unitarity at $(k_F a)^{-1} \approx -0.3$, and where $T^*/T_c \sim 2$. Thus, the role of pairing in the quench dynamics likely does not play a central role in the outcome of spontaneous current formation, but it is still a potentially very relevant detail for quenches taking place in the BCS limit, and a possible direction for future experiments probing different scaling laws with a different combination of adiabatic critical exponents.

Finally, in order to further distinguish the crossover from the slow-quench to the fast-quench scaling regimes, we plot the measured mean-square winding number $\langle w^2 \rangle$ versus the mean absolute winding number $\langle |w| \rangle$ in Fig. 7.8. This so-called dispersion law is indicative of the underlying probability distribution describing the spontaneous current formation, and takes different forms depending on the quench regime. For slow quenches, by far the most probable winding numbers are $w = 0$ and $|w| = 1$, implying that $\langle w^2 \rangle \approx \langle |w| \rangle$. The prediction of W. Zurek in [100] points to a *doubling* of the scaling exponent for the mean-square winding numbers in this limit, relative to that of the fast-quench limit. However, it appears from Figs. 7.8 and 7.7 that the condition $\langle w^2 \rangle = \langle |w| \rangle$ is not sufficient to definitively claim the scaling exponent should be doubled. A further condition, such as $\langle |w| \rangle \lll 1$ should perhaps be appended to describe this universal regime of slowest quenches. It should be noted that this limit is incredibly difficult to access (experimentally and numerically), given both the extreme rarity in measuring non-zero winding numbers, *and* to the enhanced sensitivity to experimental imperfection in i.e. the trapping potential. The

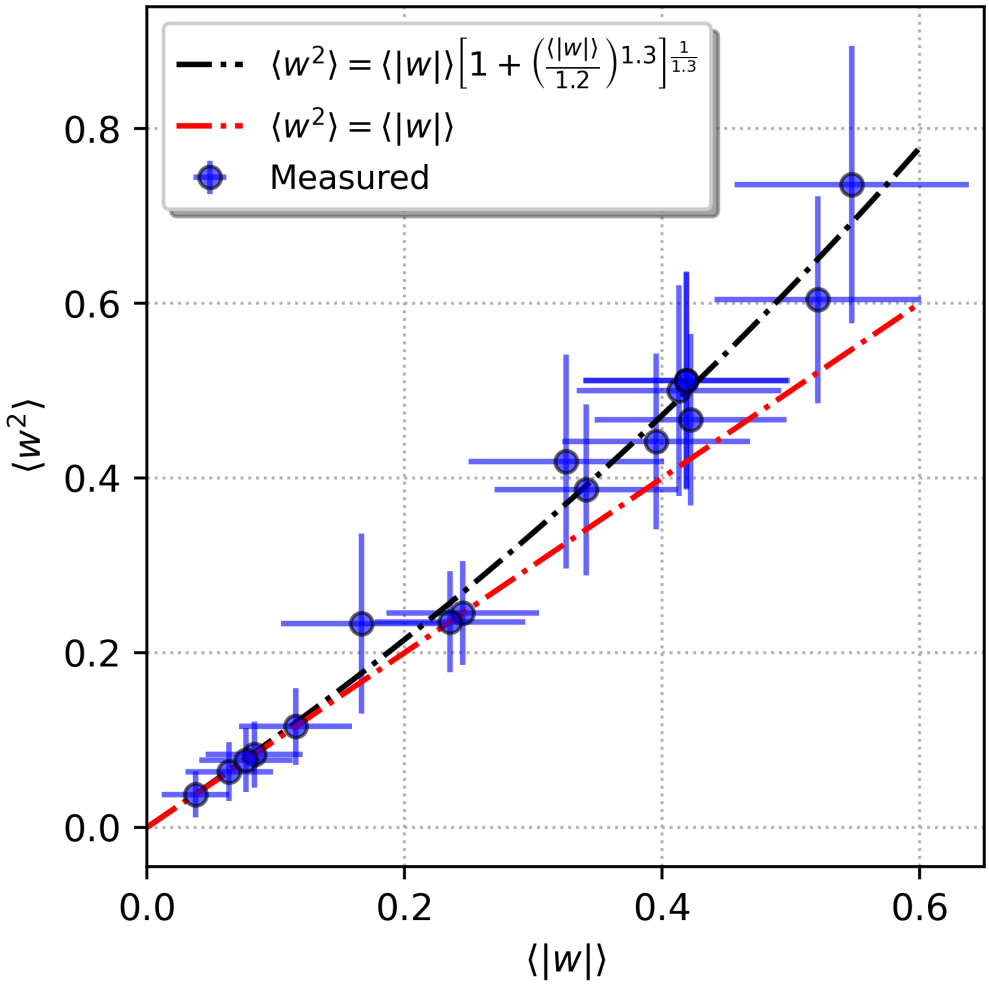

Figure 7.8: Measured winding number dispersion relation, $\langle w^2\rangle = f(\langle|w|\rangle)$. The black solid line is a fit to the function $f(x) = x[1+(x/x_0)^a]^{1/a}$ while the red dashed-dotted line is a linear function $f(x) = x$. The random walk regime is accessed when the scaling becomes quadratic while the slow-quench regime occurs in the linear portion. Error-bars on the measured data are computed using a bootstrapping approach.

slow-quench asymptotic prediction from our linearized stochastic model provides an indication that this regime may in fact exist, but further confirmation is needed. In the opposite limit of fast quenches, the winding number distribution is approximately Gaussian, implying that $\langle w^2\rangle \sim \langle|w|\rangle^2$. This is suggestive of a random-walk scaling behavior. In this regime, the critical exponents pertaining to the phase transition

enter into the scaling law in a straightforward manner, and the frozen-out correlation length has an obvious physical meaning.

To interpolate between these two limiting regimes, we fit the measured dispersion law to the functional form $f(x) = x[1+(x/x_0)^a]^{1/a}$, where x_0 and a are fit parameters. This function reduces to the discussed scaling laws in the $x \ll x_0$ and $x \gg x_0$ limits. The fit parameter $x_0 \approx 1.2$, suggesting that the crossover into the random-walk regime occurs for even faster quenches with $\langle|w|\rangle \gtrsim 1.2$, which are likely inaccessible to our, and many other, current experimental capabilities due to the weak scaling exponent $\sigma = 1/4$. Namely, a doubling of $\langle|w|\rangle$ would require roughly a factor of 16 enhancement in the fastest available quench rate. However, when looking at the robust scaling law for the fast-quench regime shown in Fig. 7.7, which is clearly distinct from the intermediate-to-slow quench regime, it appears as though the KZ scaling argument may still hold for the data obtained in this experiment, insofar as the mean-square winding number behaves like the sum of Gaussian random variables. Certainly, the measured mean-square scaling exponent $\sigma = 0.24(2)$ agrees with the mean-field prediction $\sigma_{MF} = 1/4$. This realization implies that the mean-square winding number scaling exponent can be reliably tied back into the adiabatic critical exponents via the relation (7.5) even if the true random-walk regime cannot be accessed.

7.3.1. Conclusion

We have studied the statistics of spontaneous current formation in a thermally-quenched ring of ultracold fermions. We observe a fast-quench regime with a measured scaling law in line with predictions from mean-field KZ theory, and a slow-quench regime governed by an exponential suppression of spontaneous currents. It is important to mention, however, that our data may not be sufficient enough to discern the underlying critical exponents and their association to the mean-field or F-model predictions. Including several additional points into our fit to the fastest quenches,

we obtain a scaling exponent closer to the F-model prediction $\sigma_F = 1/3$. The goal of future experiments would be to probe the fast-quench limit in finer detail, and over a greater range, by boosting the effective quench rate. With improvements to the slew rates of our magnet coils, this regime can be better explored, and the scaling exponents measured with a higher degree of confidence.

Chapter 8

Future Experiments

Section 8.1

Spontaneous Currents with a Rotational Bias

In this section we extend the phenomenological spontaneous current theory discussed in Sec.6.3 to scenarios where a non-zero rotation of the normal fluid component is present. We show that this rotational "bias" preserves some essential predictions of the KZ argument in certain limits, but also opens the possibility to utilize a known bias to make predictions about the underlying static critical exponents pertaining to the phase transition. In particular, the finite kinetic energy of the normal component causes a potentially measurable shift in the critical temperature, and onset of rapid condensate growth, associated to the transition, in accordance to the Little-Parks effect.

The linearized stochastic LG equation can be modified to include a rotational bias by introducing a uniform rotational "gauge" field that couples to the single particle angular momentum operator $i\hbar d/d\theta$. In particular in Fourier space, we make the replacement $\ell \to \ell - \ell_\Omega$ in equation (6.33) and write the dynamical evolution of the

Fourier components as

$$\dot{c_\ell} = \left[\frac{t}{t_q} - (\ell - \ell_\Omega)^2\right] c_\ell + \zeta_\ell \tag{8.1}$$

Here $\ell_\Omega \equiv \Omega/\Omega_0$ ($\Omega_0 = \hbar/2mR^2$) is the important additional gauge term used to account for the finite rotation of the normal (background) fluid, which acts as an angular momentum "reservoir". Technically, Ω is the Lagrange multiplier that fixes the average (conserved) angular momentum $\langle L_z \rangle$ of the system. In a narrow ring-shaped trap, the normal component rotates as a rigid body with $\Omega = \langle L_z \rangle/(mNR^2)$. Here R the ring radius, m the atomic mass and N is the total atom number.

Formally integrating (8.1), we have

$$c_\ell(t) = \int_{-\infty}^{t} dt' \zeta_l(t') e^{-(\ell-\ell_\Omega)^2(t-t') + \frac{t^2 - t'^2}{2t_q}} \tag{8.2}$$

We find an exact expression for the mean-square fluctuations of each Fourier component by complex squaring and averaging (8.2)

$$\langle |c_\ell(t)|^2 \rangle \equiv \sigma_\ell^2(t) = \sqrt{\pi} D\hat{t}\ F\left(\frac{t - \Delta t(\ell - \ell_\Omega)^2}{\hat{t}}\right) \tag{8.3}$$

where $\hat{t} \equiv \sqrt{t_q}$ and $\Delta t \equiv \hat{t}^2 = t_q$. The dimensionless function $F(x) \equiv \frac{1}{2} e^{x^2}[1+\mathrm{erf}(x)] = \mathrm{erfcx}(-x)/2$ where erfcx is the complimentary scaled error function. Importantly, for $x \to -\infty$, $F(x) \sim 1/(2\sqrt{\pi}x)$ while for $x \gtrsim 1$, $F(x) \sim \exp(x^2)$. The meanings of $\hat{t}$ and Δt will become clear shortly.

For any time t, $\sigma_\ell^2(t)$ is maximal at $\ell = \mathrm{round}(\ell_\Omega) \equiv \ell^*$. Additionally, the growth dynamics of the σ_ℓ^2 depend only on the variable

$$x_\ell(t) \equiv \frac{t - \Delta t(\ell - \ell_\Omega)^2}{\hat{t}} \tag{8.4}$$

Due to the exponentially-increasing nature of $F(x)$ near $x = 1$, the fluctuations in

mode ℓ^* experience a brief period of rapid growth, before any other mode, following the transition at times when $x_{\ell^*}(t) \approx 1$. This condition defines the "blow-up" time for the biased quench

$$t^* \equiv \hat{t} + \Delta t(\ell^* - \ell_\Omega)^2, \tag{8.5}$$

after which non-linear effects kick in and the condensate begins to relax toward its instantaneous, non-zero equilibrium value value [108]. Thus, in some short interval of time following t^*, the condensate becomes robust with respect to fluctuations large enough to cause any persistent current to decay; The winding number becomes a topologically protected quantity at times $t \geq t_{\text{eval}} \equiv ft^*$. Here f is an $\mathcal{O}(1)$ "fudge" factor that scales the blow-up time to the so-called evaluation time where the winding number is stabilized [110]. We note that although f is non-universal, it depends only logarithmically on the microscopic parameters and quench details and is thus roughly constant across many decades of quench times.

The non-rotating $\ell_\Omega = 0$ case was discussed in detail in Sec. 6.3, and in that case $t^* = \hat{t}$. For the case of $\ell_\Omega \notin \mathbb{Z}$, expression (8.5) shows that the condensate growth is delayed by an amount proportional to Δt. This makes sense when considering the pairing gap relative to (twice) the atomic kinetic energy, which is non-zero in the presence of a normal-component flow and can cause pairs to fragment. We can also interpret this delay in condensate growth as being due to a reduction in the critical temperature due to the bias flow. This is the essence of the Little-Parks effect applied to a system quenched through its critical point [125, 126].

It is potentially an interesting feature of the quench dynamics that the condensate growth is delayed by an amount given by $t_{\text{delay}} \equiv \Delta t(\ell^* - \ell_\Omega)^2$. If a known bias flow ℓ_Ω is introduced, this delay, if measurable, can give insight into Δt, which itself is predicted to depend on the combination of critical exponents $b \equiv \nu z/(1 + \nu z)$. By measuring t_{delay} for various ℓ_Ω, Δt and therefore b can perhaps be measured, in

addition to the usual KZ scaling exponent $\sigma = \nu/(1+\nu z)$.

8.1.1. Estimating the Winding Number Distribution

To make progress analytically, we employ the same approximation to the probability distribution as discussed in Sec. 6.3. Namely, we take the probability distribution to be described by the infinite product

$$\begin{aligned} P_w &\approx \text{Prob}(|c_w| > |c_0| \cap |c_w| > |c_1| \cap ...)/Z \\ &= \frac{1}{Z}\prod_{\ell} \frac{\sigma_w^2}{\sigma_w^2 + \sigma_\ell^2} \end{aligned} \tag{8.6}$$

When evaluated at t_{eval}, the probability distribution depends only on the parameters $\hat{t} \sim \sqrt{t_q}/R^2$ and ℓ_Ω. Notably the phenomenological diffusion constant D drops out of the equation as long as the winding number assumes its final value at the blow-up time and non-linear effects can be neglected. Small values of $\hat{t}$ correspond to either rapid quenches *or* large ring radii. The latter corresponds to the thermodynamic (infinite size) limit, but in either case, it describes the regime initially envisioned by Kibble and Zurek (many small, uncorrelated domains with uniform phase locked within). Conversely, large values of $\hat{t}$ (slow quenches and small temperatures) or small radius rings give rise to sharper distributions of persistent currents, centered at winding number l^*, which agrees with the predictions of Hess and Fairbank in their studies of superfluid Helium [127]. Importantly, the phase coherence extends across the circumference of the ring, and the details of the phase profile along the circumference, as well as periodic boundary conditions, become important. Thus, there is always a small but finite probability to generate persistent currents even when $N_d \leq 2$ domains are formed. For intermediate values of $\hat{t}$, equation (8.6) gives an interpolation between the two regimes discussed previously, where standard treatments of spontaneous current formation become inaccurate, and simple scaling

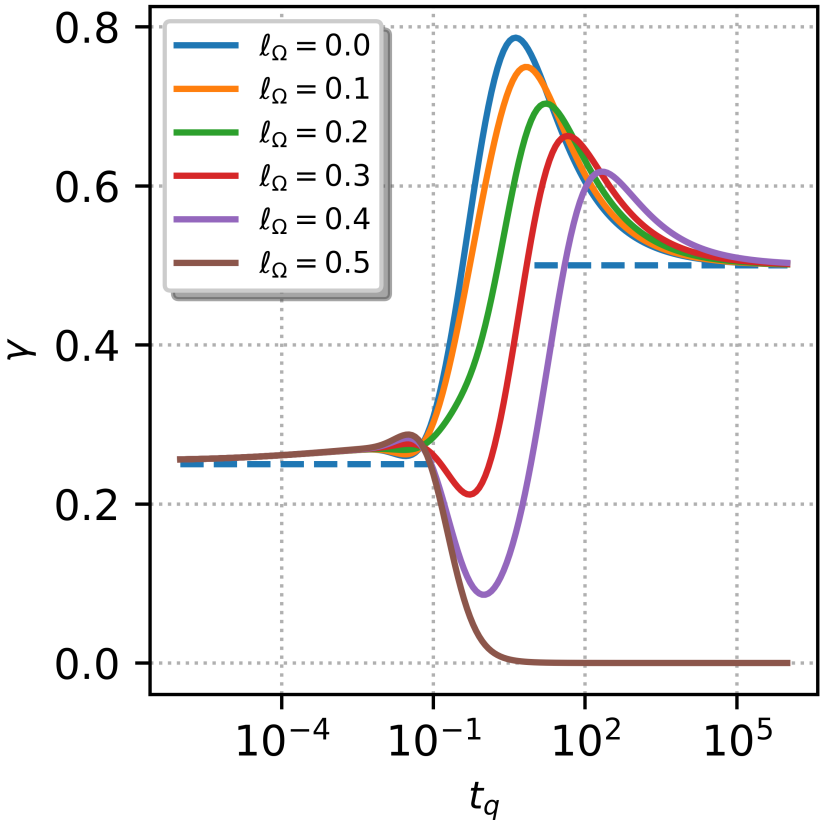

Figure 8.1: Plot of the scaling exponent $\gamma \equiv -\frac{d \log \mathrm{var}[w]}{d \log t_q}$ versus quench time for several values of the bias flow parameter ℓ_Ω. The two horizontal blue dashed lines at $\gamma = 1/4$ and $\gamma = 1/2$ show the mean-field KZ scaling exponent and slow-quench scaling exponent, respectively. At the frustration point $\ell_\Omega = 1/2$, there is no preference to choosing a winding number $w = 0$ or $w = 1$ for slow quenches, although for rapid quenches the KZ argument seems to hold for all bias values.

laws describing the rate of defect formation break down. This is the first time that we know of that an approximate analytic treatment of the intermediate quench rate regime has been put forth, although it is still unclear exactly what role microscopic, non-universal details play.

Analyzing the Distribution. With the probability distribution, one may readily compute the various relevant moments of the distribution as functions of $\hat{t}$ and ℓ_Ω,

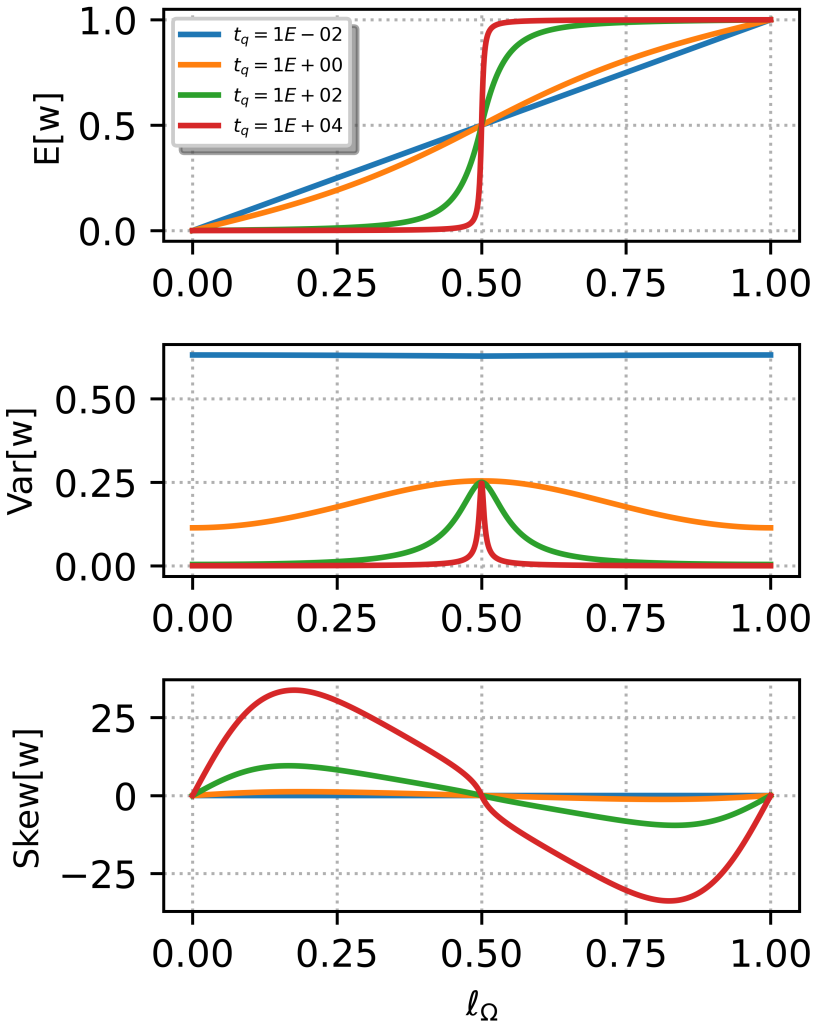

Figure 8.2: Various moments of the winding number distribution, computed from (8.6), as a function of the bias flow ℓ_Ω and several different quench times t_q. The skewness $\mathrm{Skew}[w] \equiv \mathrm{E}[(w-\mathrm{E}[w])^3]/\mathrm{Var}[w]^{3/2}$ describes the asymmetry in the winding distribution about the mean.

which we show in Fig. 8.2. For simplicity, we take $t_{\mathrm{eval}} = t^*$. As the Kibble-Zurek mechanism predicts the scaling of the defect density, and thus the variance of the winding number distribution, with the quench rate, it is informative to define the quench-rate-dependent scaling exponent $\gamma \approx -\frac{d \log \mathrm{var}[w]}{d \log t_q}$, which we plot in Fig. 8.1. The plot of the scaling exponent highlights three main regimes of stochastic persistent formation. The small $\hat{t}$ regime is the KZ regime of Gaussian probabilities.

Notably, the scaling becomes independent of ℓ_Ω, the background flow. For large $\hat{t}$, the scaling exponent is seen to double. This doubling has been suggested to be a result of Gaussianity in the winding number *density*. Furthermore, the scaling is again independent of ℓ_Ω as long as $\ell_\Omega \neq 1/2$. This scaling is likely difficult to observe experimentally with great precision, as the probability to generate non-zero persistent currents becomes quite small for large $\hat{t}$. However, it is clear from the variance plot in figure 8.2 that tuning the background flow near (but not on) the "frustration point" $\ell_\Omega = 1/2$ should boost the variance substantially, perhaps enough to observe this universal scaling behavior. For intermediate values of $\hat{t}$, the winding number statistics become non-universal and ℓ_Ω-dependent as indicated in figure 8.1. Furthermore, the functional dependence of the variance on the quench time becomes dependent on the blow-up time in a way that depends on the non-linear interaction term that was neglected. However, it should still be possible to define the notion of a "defect", given that the correlation length is still smaller that the ring circumference at intermediate quench times.

It is interesting to note that an exact expression for the expected winding number $\langle w \rangle$ exists, and is due to a result from the study of roots of random polynomials [128]. The expected density of roots of a random polynomial of the form $\psi(z) = \sum_{\ell=0}^{2\ell_c} c_{\ell-\ell_c} z^\ell$ is given simply by

$$\rho(z) = \frac{1}{\pi} \frac{\partial^2}{\partial z \partial z^*} \log \langle \psi(z) \psi(z^*) \rangle \tag{8.7}$$

where angle brackets denote averaging over the random polynomials $\psi(z)$. As the c_ℓ are drawn from the complex Gaussian random distribution $\mathcal{CN}(0, \sigma_\ell)$, on can readily show that (8.7) can be written as

$$\rho(s) = \frac{1}{\pi} \frac{d}{ds} \left(s \frac{d}{ds} \log \sum_{\ell=0}^{2\ell_c} \sigma^2_{\ell-\ell_c} s^\ell \right) \tag{8.8}$$

where $s = |z|^2$. As the winding number w is related to the number of roots of $\psi(z)$ lying within the complex unit disk (see Sec. 2.3), we find $\langle w \rangle$ by integrating the root density (8.8) over the region $|z| < 1$:

$$\begin{aligned} \langle w \rangle &= \int_0^1 \rho(s) ds - \ell_c \\ &= \left(\frac{d}{ds} \log \sum_{\ell=-\ell_c}^{\ell_c} \sigma_\ell^2 s^\ell \right) \Big|_{s=1} \\ &= \frac{\sum_{\ell=-\ell_c}^{\ell_c} \ell \sigma_\ell^2}{\sum_{\ell=-\ell_c}^{\ell_c} \sigma_\ell^2} \end{aligned} \tag{8.9}$$

which has a nice intuitive form. Since $\langle w \rangle = \sum_w w P_w$, it is tempting to associate with the winding number distribution $P_w = \sigma_w^2 / \sum_{\ell=-\ell_c}^{\ell_c} \sigma_\ell^2$. This cannot be true, however, as the algebraic decay $1/\ell^2$ decay of the σ_ℓ^2 for large $|\ell|$ would result in diverging higher-order moments. While there exist formulae for describing higher order correlation functions between the random roots of $\psi(z)$, which in turn can be used to find expressions for the higher order moments of the winding number distribution, they are very unwieldy and approximations or numerics become necessary.

It is also interesting to note the connection between the normalized correlation function as defined in Sec. 6.3.3

$$g(\theta) \equiv \frac{\sum_\ell \sigma_\ell^2 e^{i\ell\theta}}{\sum_\ell \sigma_\ell^2} \tag{8.10}$$

and the average winding number (8.9). On inspection, we find several equivalent relations:

$$\langle w \rangle = -i g'(0) = \mathrm{Im}[g'(0)] = -i \frac{d}{d\theta} \log g(\theta)|_{\theta=0}. \tag{8.11}$$

These relations are reminiscent of the optical theorem in scattering theory.

The KZ Regime. We now show that the probability distribution (8.6) successfully reproduces the KZ scaling laws for rapid quenches, but also sheds light onto the scaling laws in the biased $\ell_\Omega \neq 0$ case. In this regime, $\hat{t}$ is small, and we can approximate the scaling function in (8.3) at $t = t^*$ as

$$F\{1 - \hat{t}[(\ell - \ell_\Omega)^2 - (\ell^* - \ell_\Omega)^2]\} \sim \exp\left[-2\hat{t}(\ell - \ell_\Omega)^2\right] \tag{8.12}$$

where the term in the exponential of $\mathcal{O}(\hat{t}^2)$ was neglected. Then from (8.6) we have

$$\begin{aligned} \log P_w &\sim -\sum_\ell \log\left[1 + z_w e^{-2\hat{t}(\ell-\ell_\Omega)^2}\right] \\ &\sim -\frac{1}{\sqrt{\hat{t}}}\int_{-\infty}^{\infty} dx \log\left(1 + z_w e^{-x^2}\right) \\ &\sim -\frac{1}{\sqrt{\hat{t}}}\mathrm{Li}_{3/2}(-z_w) \end{aligned} \tag{8.13}$$

where $z_w \equiv \exp\left[-2\hat{t}(w - \ell_\Omega)^2\right]$ and the sum was approximated by an integral. A small $\hat{t}$ expansion of the polylogarithm $\mathrm{Li}_{3/2}$ about $z_w = 1$ then yields

$$P_w \sim \hat{t}^{-1/4} \exp\left[-\sqrt{\frac{\hat{t}}{\hat{t}_0}}(w - \ell_\Omega)^2\right] \tag{8.14}$$

where $\hat{t}_0$ is a number. Since $\hat{t}$ is small, the distribution P_w is very broad, and its discrete nature is blurred out. w is then approximately a continuous variable. Then, we compute the lowest order cumulants

$$\mathrm{E}[w] \approx \int_{-\infty}^{\infty} dw w P_w = \ell_\Omega \tag{8.15}$$

and

$$\mathrm{Var}[w] \approx \int_{-\infty}^{\infty} dw (w - \ell_\Omega)^2 P_w \sim \hat{t}^{-1/2} \sim t_q^{-1/4} \tag{8.16}$$

the result predicted by the KZ argument. This variance scaling is independent of the bias flow ℓ_Ω and retains the same scaling exponent $\sigma = 1/4$, suggesting that the KZ argument can be extended to a larger class that includes rotating/biased systems.

Section 8.2

KZM in a Spatially-Modulated Ring

The speed at which fluctuations in the superfluid propagate, relative to the speed at which the phase transitional front propagates during the quench, determines the region in which causally disconnected domains may form during the quench [118]. It is interesting to study this inhomogeneous scenario in a ring-shaped geometry. In particular, we expect a suppression of spontaneous current formation when fluctuations are allowed to propagate the circumference of the ring by the time the entire ring crosses the phase transition. In certain limits, the rate at which fluctuations propagate obeys a simple scaling relation, with a different combination of exponents ν and z governing the size of correlated patches in the usual Kibble-Zurek scenario. In theory, if one can measure the scaling governing this propagation velocity, in addition to that governing the defect density after a quench, one may be able to simultaneously extract *both* critical exponents pertaining to the KZM. This is in constrast to the usual homogeneous KZ scenario, where typically only the combination $a(\nu, z) = \nu/(1 + \nu z)$ is measurable. We now propose an experiment to extract the exponent, $b(\nu, z)$, relating to the propagation speed at the freeze-out time, by utilizing a known inhomogeneity around a ring shaped optical potential.

We focus on a particular form of azimuthal inhomogeneity, namely a triangular modulation described by $V(\theta) = V_0|\theta|/\pi$, with $\theta \in [-\pi, \pi)$ (see Fig. 8.3). While this potential can be engineered in multiple ways, we simply project this optical potential using the DMD. The potential has a minimum at $\theta = 0$, where the phase transition

is first crossed during the quench, and a maximum at $\theta = \pi$. In the limit that the potential amplitude V_0 is small, the local critical temperature can be linearized as $T_c(\theta) = T_c[V(\theta)] \approx T_c(0)+V_0T_c'(0)|\theta|/\pi \equiv T_c(0)(1-\delta|\theta|)$, where $\delta = |V_0T_c'(0)/[\pi T_c(0)]|$ is a small dimensionless number characterizing the relative variation in the critical temperature around the ring. We note that in the BCS limit, $\delta \sim V_0/E_F$, with E_F the Fermi energy at the peak density point. Assuming the reduced temperature, at $\theta = 0$, is quenched linearly (at least within some small window about the transition) as $\epsilon(\theta = 0, t) \equiv t/t_q$, then the local reduced temperature can be written as

$$\epsilon(\theta, t) = 1 - \frac{T(t)}{T_c(\theta, t)} \equiv \frac{t - t_F(\theta)}{t_q(\theta)} \tag{8.17}$$

where we have defined $t_F(\theta) = t_q\delta|\theta|$ and $t_q(\theta) = t_q(1 - \delta|\theta|)$

In this approximation, the local quench time $t_q(\theta)$ varies in a triangular fashion around the ring. Causality arguments discussed above suggest defects can only nucleate locally when the condensation front velocity $v_F(\theta)$ exceeds the speed at which fluctuations in the order parameter can propagate, approximated as $\hat{v}(\theta) = \hat{\xi}(\theta)/\hat{\tau}(\theta)$. We find $v_F(\theta)$ by differentiating the condition $t \equiv t_F(\theta_F(t), t)$, defining the condensation front $\epsilon[\theta_F(t), t] = 0$, with respect to time. Using $t_F(\theta) = t_q\delta|\theta|$, we find

$$|v_F| = \frac{R}{t_q\delta} \tag{8.18}$$

with $v_F = Rd\theta_F/dt$. Next, the fluctuation propagation speed $\hat{v}(\theta)$ can be found using the (local) scaling laws discussed previously:

$$\hat{v}(\theta) = \frac{\xi_0}{\tau_0}\left[\frac{t_q(\theta)}{\tau_0}\right]^{-\frac{\nu(z-1)}{1+\nu z}} \tag{8.19}$$

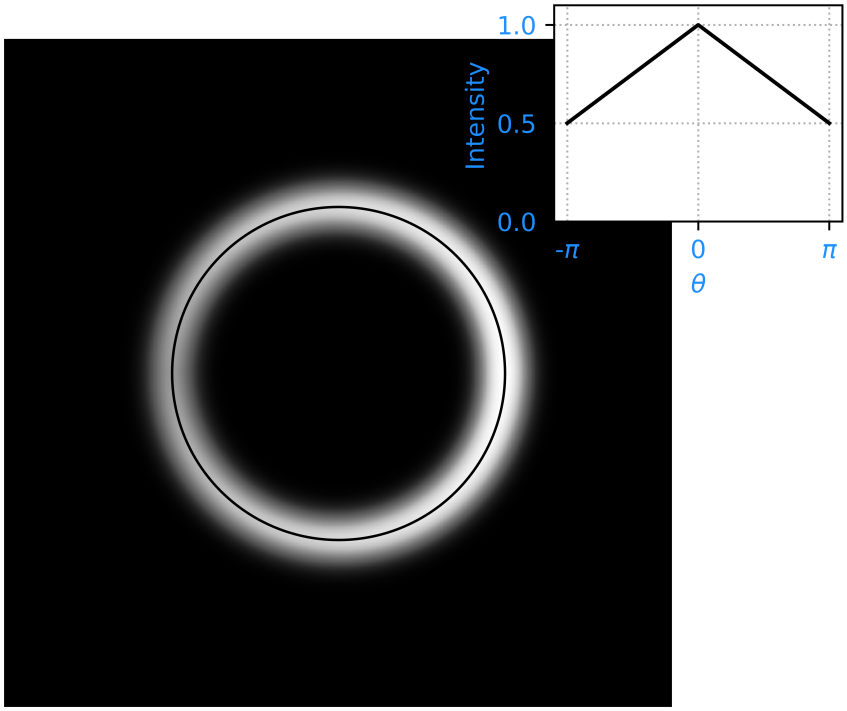

Figure 8.3: Optical potential for a triangular-wave modulated ring. The modulation depth shown here is 50% between the minimum and maximum intensity points. This is a potential setting for probing the speed at which fluctuations can propagate in a quenched ultracold atomic superfluid. The inset shows the normalized azimuthal intensity profile measured along the ring radius R.

Then, the condition for local defect nucleation becomes

$$\frac{\xi_0}{\tau_0}\left\{\frac{t_q(1-\delta|\theta|)}{\tau_0}\right\}^{-\frac{\nu(z-1)}{1+\nu z}} \approx \frac{\xi_0}{\tau_0}\left(\frac{t_q}{\tau_0}\right)^{-\frac{\nu(z-1)}{1+\nu z}} \lesssim \frac{R}{t_q\delta} \tag{8.20}$$

to lowest non-vanishing order in δ. Globally, i.e. across the ring, domains of internally well-defined but separately uncorrelated phase form when the inequality (8.20) is obeyed. If we imagine increasing the quench time t_q from some small initial value, where (8.20) holds globally and the Kibble-Zurek mechanism proceeds as usual, even-

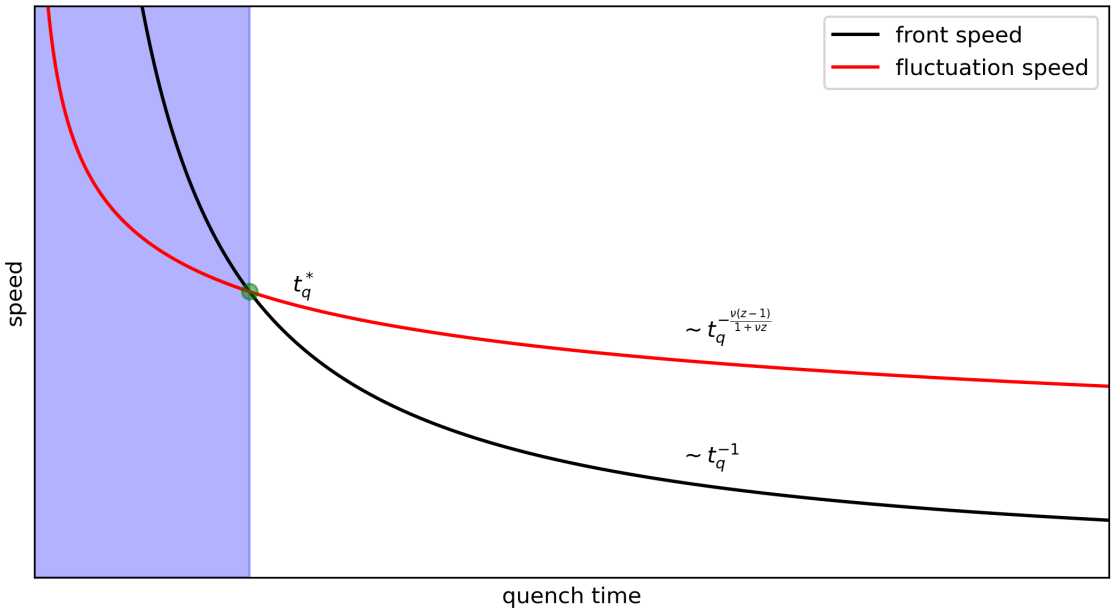

Figure 8.4: Qualitative plot showing the two velocity scales v_F and $\hat{v}$. The blue shaded region corresponds to the causally disconnected regime, within which the KZM proceeds as usual. For quench times large than t_q^* (green circle), the tilted ring becomes causally connected and spontaneous current formation is suppressed

tually there will be some critical quench time t_q^* such that equality of (8.20) is met. For quench times larger than t_q^*, the ring becomes causally connected within the two regions around $\theta = 0$. As a result, the defect formation rate should fall abruptly after this point, as existing condensate has time to communicate its phase to neighboring points as they cross the transition. A qualitative picture of this effect is shown in Fig. 8.4

We can solve for equality in (8.20) to find

$$t_q^* \approx \tau_0 \left(\frac{R}{\xi_0 \delta} \right)^{\frac{1+\nu z}{1+\nu}} \sim \delta^{-\frac{1+\nu z}{1+\nu}} \tag{8.21}$$

suggesting a measurable scaling of the critical quench time, marking the onset of causal connectedness in the ring, with the (small) modulation amplitude. The combination of critical exponents $b \equiv (1+\nu z)/(1+\nu)$ in (8.21) is different than the

one governing the homogeneous defect extent predicted by Kibble-Zurek scaling arguments, $a \equiv \nu/(1+\nu z)$. Introducing a known inhomogeneity and observing the scaling in (8.21), in addition to the known techniques used to measure the usual KZM exponent a, would allow one to extract simultaneously the two fundamental exponents ν and z that distinguish the second order transition. While the goal of such an experiment would be to measure ν and z directly, assuming the mean-field values $\nu_{MF} = 1/2$ and $z_{MF} = 2$, we can estimate $a_{MF} = 1/4$ and $b_{MF} = 4/3$. Such super-linear scaling in the causality exponent b_{MF} suggests that this scaling (8.20) should be detectable, even if δ is limited to small values. Furthermore, we found that the winding numbers were still easily recorded for the case of quenching in tilted rings, without modification to the optical potential at the end of the quench.

To extract the scaling of the critical quench time t_q^* with the tilt amplitude δ, one would repeat the full set of measurements for various tilts, and from the log-log plot of $\langle|w|\rangle$ vs t_q, identify a knee in the data where $\langle|w|\rangle$ drops noticeably. This point corresponds to the point at which the ring becomes causally connected on either side of $\theta = 0$ and defect formation is suppressed.

Chapter 9

Conclusion and Outlook

In this thesis, we studied ensembles of fermionic ^{6}Li confined in ring-shaped traps. More specifically, we highlighted findings from two distinct, yet related, experiments. We first gained insight into the effects of hole-induced heating on degenerate fermion samples due to collisions with background particles, and found a means of mitigating this heating by preserving a large, dilute halo of non-degenerate fermions in contact with the ring-shaped degenerate component. The long system lifetime, coupled with the ability to maintain low temperatures for long periods of time due to the halo, opens the possibility to perform seconds-long experiments on weakly interacting BCS superfluids that require low temperatures due to the fragility of pairing in this limit. More than just a technical result, we hope to utilize this feature in future experiments where extreme low-temperature conditions are required for extended periods of time. For instance, efforts to find signatures of uncoventionally-paired superfluids in spin-polarized samples, such as the elusive FFLO state [2, 3], will most certainly require achieving and maintaining extremely low temperatures, which further motivates the use of our heat mitigation technique.

The second main experimental result revolved around the investigation of spontaneous currents formed following a quench through a BCS phase transition. By

exploiting the long lifetimes and heat-mitigation features offered by our choice of trapping potential, we were able to measure a KZ-like scaling law for fast quenches and showed that this regime was distinct from the slow-quench regime characterized by a rapid suppression in spontaneous current formation. The findings of this experiment were supported by a theoretical model of spontaneous current formation and correlation functions. This model operated entirely in a linear regime, but a more complete picture of the quench dynamics should be obtained by including non-linear corrections to the numerics, as well as specific microscopic parameters associated to the sample. This experimental investigation was not exhaustive; Further probing of the fast-quench limit is still desired, and with technical improvements to the magnetic coil switching speeds should be possible. With these modifications, one could imagine gathering enough statistics with sufficient precision to be able to distinguish clearly between mean-field and F-model predictions, and perhaps engineer a configuration that allows one to transition from one model to another.

While the all red-detuned traps used in these experiments had distinct advantages, transitioning to blue-detuned ring traps for KZM studies may help isolate any effects the halo may have on the quench statistics. In a blue-detuned ring, in particular, atoms are entirely confined to the ring region and can be completely isolated from the background halo of non-degenerate atoms. While the quench quality will perhaps be degraded due to the enhanced loss of atoms from a bare ring, the decoupling from the halo may aid in studies within the fast-quench limit. Certainly, blue-detuned ring traps have other advantages when it comes to manipulating the state of the system in the ring. For the biased KZM experiment discussed in the previous chapter, having the ability to stir up the normal component to a controlled and well-characterized rotational state without unwanted impact from the halo is desirable. As of 2023, we again have the ability to perform stirring using a blue-detuned 2-axis acousto-optic

deflector. Combined with a blue-detuned ring, the biased KZM scenario should be readily studied.

As with the experiments performed in this work, there are likely to be unexpected observations and complications in future experiments that may deviate strongly from initial expectations. This was certainly true for the KZM studies performed in this work. While incredibly elegant, the KZM can in some cases be an oversimplification of the rich physics surrounding the phase transition, and system-dependent and non-universal details will always play a profound and non-negligible role in the experimental dynamics.

Our experimental apparatus in its current state has the capability of allowing explorations of a vast number of interesting and relevant experiments. While KZM studies were at the fore-front of the work in this thesis, leveraging our experimental capabilities utilizing ring-shaped traps, we hope to someday explore topics that include but are certainly not limited to

- Superfluids with exotic pairing mechanisms/spin-imbalanced Fermi gases
- Quasi-1D superfluids
- Josephson junction and barrier physics, SQUIDS, and atomtronic circuits
- Normal fluid dynamics and Normal-Superfluid interactions
- Ring lattice physics

The degree of control of our system can allow for further variations on and additional investigations into experiments that have been performed prior on i.e. Bose gases or condensed matter and real materials systems. This is certainly an exciting time for our lab, and with time, effort and a bit of luck, the doors of novel and exciting experiments on ultracold quantum systems can be opened further.

Appendix A

Tables of Important Values

Section A.1

Typical Experimental Trap Parameters

Ring beam	Radius r_0	$1/e^2$ Half-Width w_r	Ring beam power P_{ring}
	12 μm	2.2 μm	2 mW
Sheet beam	Vertical width w_z	Horizontal width w_s	Sheet power P_{sheet}
	7 μm	290 μm	50 mW

Related quantities derivable from the trap parameters include the trap frequencies $\omega_j = \sqrt{4V_j/(mw_j^2)}$ and quantum harmonic oscillator length $a_j = \sqrt{\hbar/(m\omega_j)}$ where $j \in \{r, z, s\}$ refers to the trap component of interest and V_j are the trap depths.

Section A.2

2D and 3D Density

We show the typical column densities $n_2(x, y) = \int dz n_3(x, y, z)$ in the ring-dimple region and halo, which can be related to the measurable optical depth. Although not directly measurable itself, the 3D density at $z = 0$, $n_3(x, y, 0)$ can be related to $n_2(x, y)$ by assuming a harmonic vertical confinement and using the local density

approximation to estimate the vertical distribution of the density distribution (See Chap. 2). The result is $n_3(x,y,0) \approx \left(\frac{512}{81\pi^5}\right)^{1/4} \left[\frac{n_2(x,y)}{a_z^2}\right]^{3/4}$.

Density Scales		
Density (2D/3D)	Ring	Halo
2D (Column): n_2	15 μm^{-2}	5 μm^{-2}
3D: n_3	3 μm^{-3}	1 μm^{-3}

Section A.3

Length and Energy Scales

We show typical values of important length and energy scales at the 100 mT B-fields utilized typically in this work. The zero temperature pairing gap $\Delta_0 = \pi e^{-\gamma} k_B T_c$ with γ the Euler-Mascheroni constant. The typical critical temperature $T_c \sim \mathcal{O}(T_F/20)$. The BCS coherence length is $\xi_{\mathrm{BCS}} = \hbar v_F/(\pi\Delta_0)$ with $v_F = \sqrt{2E_F/m}$ the Fermi velocity. The Fermi wavelength $\lambda_F = 2\pi\hbar/\sqrt{2mE_F} = 2\pi/k_F$. Finally the elastic collision rate can be upper bounded in the BCS limit by $\Gamma_0 = 4\pi n_3 v_F a^2/[1+(k_F a)^2]$. Pauli blocking suppresses this rate somewhat at this magnetic field, however.

Local length Scales at $B = 100$ mT		
Length	Ring	Halo
Interparticle spacing: $n_3^{-1/3}$	0.7 μm	1 μm
Fermi wavelength: λ_F	1.5 μm	1.9 μm
BCS coherence length: ξ_{BCS}	1.7 μm	3.8 μm
s-wave scattering length: a	0.2 μm	0.2 μm
Halo extent: R_{halo}	N/A	100 μm

Local energy and rate scales at $B = 100$ mT		
Energy/Rate	Ring	Halo
Fermi energy: E_F/h	15 kHz	9 kHz
Zero-temperature gap: Δ_0/h	1.3 kHz	0.5 kHz
Elastic Collision rate: Γ_0	40 kHz	16 kHz

Appendix B

Asymptotic Analysis of Correlation Functions

Section B.1

Small $\hat{t}$ Expansion

In the limit of rapid quenches, the correlation function can be written as an integral

$$\begin{aligned} g(\theta,t) &= \int_{-\infty}^{\infty} dk F\left(\frac{t}{\hat{t}} - \hat{t}k^2\right) e^{ik\theta} \\ &= \frac{1}{\sqrt{\hat{t}}} \int_{-\infty}^{\infty} dx F\left(\frac{t}{\hat{t}} - x^2\right) e^{ix\theta/\sqrt{\hat{t}}} \\ &\equiv \frac{1}{\sqrt{\hat{t}}} I(\tau, z) \end{aligned} \tag{B.1}$$

where the substitutions $z \equiv \theta/\sqrt{\hat{t}}$ and $\tau = t/\hat{t}$ have been made, and

$$I(\tau, z) \equiv \int_{-\infty}^{\infty} dx F\left(\tau - x^2\right) e^{ixz} \tag{B.2}$$

The asymptotic behavior of the correlation function for $|\theta| \gg \sqrt{\hat{t}}$ can be therefore be determined by studying the $|z| \to \infty$ limit of $I(z, \tau)$.

Using the properties $\frac{\partial}{\partial\tau}F(\tau-x^2) = 2(\tau-x^2)F(\tau-x^2)+1/\sqrt{\pi}$ and $\frac{\partial}{\partial x}F(\tau-x^2) = -2x[2(\tau-x^2)F(\tau-x^2)+1/\sqrt{\pi}]$ we can integrate (B.2) by parts to obtain

$$\begin{aligned} I(\tau,z) &= \frac{2}{iz}\int_{-\infty}^{\infty} dx x[2(\tau-x^2)F(\tau-x^2)+1/\sqrt{\pi}]e^{ixz} \\ &= -\frac{2}{z}\int_{-\infty}^{\infty} dx \frac{\partial}{\partial\tau}[F(\tau-x^2)]\frac{\partial}{\partial z}e^{ixz} \\ &= -\frac{2}{z}\frac{\partial^2 I}{\partial\tau\partial z} \end{aligned} \tag{B.3}$$

Thus, $I(\tau,z)$ obeys a simple second order partial differential equation, which we can use to examine the asymptotic behavior. Using separation of variables we define $I_s(\tau,z) = T(\tau)Z(z)$, from which we derive the ordinary differential equations

$$\frac{dT}{d\tau} = \frac{T}{\alpha} \rightarrow T(\tau) \propto e^{\tau/\alpha} \tag{B.4}$$

and

$$\frac{dZ}{dz} = -\frac{\alpha}{2}zZ \rightarrow Z(z) \propto e^{-\alpha z^2/4} \tag{B.5}$$

where $\alpha > 0$ is the separation constant, chosen such that the solution decays to zero as $\tau \rightarrow -\infty$. Thus, we have

$$I_s(\tau,z) \propto e^{\tau/\alpha}e^{-\alpha z^2/4} \tag{B.6}$$

We find the general solution as a linear combination of the separable solutions:

$$I(\tau,z) = I_0\int_0^{\infty} d\alpha A(\alpha)e^{\tau/\alpha}e^{-\alpha z^2/4} \tag{B.7}$$

We can determine the amplitude $A(\alpha)$ via the initial condition

$$I(0,z) = \int_{-\infty}^{\infty} dx F(-x^2)e^{ixz} = I_0\int_0^{\infty} d\alpha A(\alpha)e^{-\alpha z^2/4} \tag{B.8}$$

Using the Fourier representation of the gaussian function,

$$e^{-\alpha z^2/4} \propto \frac{1}{\sqrt{\alpha}} \int_{-\infty}^{\infty} dx e^{ixz} e^{-x^2/\alpha} \tag{B.9}$$

we can identify

$$\begin{aligned} F(-x) &= \int_0^{\infty} d\alpha \frac{1}{\sqrt{\alpha}} A(\alpha) e^{-x/\alpha} \\ &= \int_0^{\infty} du \frac{1}{u^{3/2}} A(1/u) e^{-ux} \\ &= \mathcal{L}\left[\frac{A(1/u)}{u^{3/2}}\right](x) \end{aligned} \tag{B.10}$$

where the substitution $u = 1/\alpha$ was made. We now use the Laplace transform of $\mathrm{erf}(u/2)$:

$$\begin{aligned} \mathcal{L}[\mathrm{erf}(u/2)](x) \equiv \int_0^{\infty} du\, \mathrm{erf}(u/2) e^{-ux} &= \frac{2}{x} e^{x^2}[1 - \mathrm{erf}(x)] \\ &= \frac{1}{x} F(-x) \end{aligned} \tag{B.11}$$

Combining (B.10) and (B.11), we can write

$$\begin{aligned} F(-x) &= \mathcal{L}\left[\frac{A(1/u)}{u^{3/2}}\right](x) \\ &= x\mathcal{L}[\mathrm{erf}(u/2)](x) \\ &= \mathcal{L}[\delta'(u)](x)\mathcal{L}[\mathrm{erf}(u/2)](x) \\ &= \mathcal{L}[\delta'(u) \circledast \mathrm{erf}(u/2)](x) \end{aligned} \tag{B.12}$$

where the convolution theorem for Laplace transforms was used. We can then identify

$$\frac{A(1/u)}{u^{3/2}} = \delta'(u) \circledast \mathrm{erf}(u/2) = \frac{1}{\sqrt{\pi}} e^{-u^2/4} \tag{B.13}$$

from which we finally find

$$A(u) \propto \frac{1}{u^{3/2}} e^{-\frac{1}{4u^2}} \tag{B.14}$$

Substituting this expression into the definition of $I(\tau, z)$ gives

$$\begin{aligned} I(\tau, z) &= I_0 \int_0^\infty d\alpha \frac{1}{\alpha^{3/2}} e^{-\frac{1}{4\alpha^2} + \frac{\tau}{\alpha} - \frac{\alpha z^2}{4}} \\ &= I_0 \int_0^\infty du \frac{1}{\sqrt{u}} e^{-\frac{u^2}{4} + \tau u - \frac{z^2}{4u}} \end{aligned} \tag{B.15}$$

One may check that this solution indeed satisfies the original partial differential equation (B.3). Additionally, the numerical prefactor I_0 can be determined by normalizing the correlation function to unity at $z = 0$. For the case $\tau = 1$, this prefactor $I_0 \approx 0.132$.

B.1.1. $|z| \to \infty$ limit

We are now in a position to study the $|z| \to \infty$ limit via Laplace's asymptotic method. For $\tau = 1$ we find, to leading order in $1/|z|$,

$$I(\tau = 1, z) \sim \frac{0.3}{|z|^{1/3}} e^{-\frac{3}{4}\left(\frac{z^2}{2}\right)^{2/3} + \left(\frac{z^2}{2}\right)^{1/3}} \tag{B.16}$$

where the numerical prefactor combines I_0 and the prefactors associated to the Laplace asymptotic expansion. The corresponding correlation function, at distances $|\theta| \gtrsim \sqrt{\hat{t}}$, therefore behaves as

$$g(\theta, \hat{t}) \sim \frac{0.3}{|\theta|^{1/3}} e^{-\frac{3}{4}\left(\frac{\theta^2}{2\hat{t}}\right)^{2/3} + \left(\frac{\theta^2}{2\hat{t}}\right)^{1/3}} \tag{B.17}$$

which preserves the same scaling of the correlation length as the simple Gaussian approximation, but has quite a different functional form. This example highlights the ambiguity in choosing the "correct" correlation length to describe the uncorrelated

phase domains; There are many different, yet equally valid ways, of associating a single length scale to the correlations.

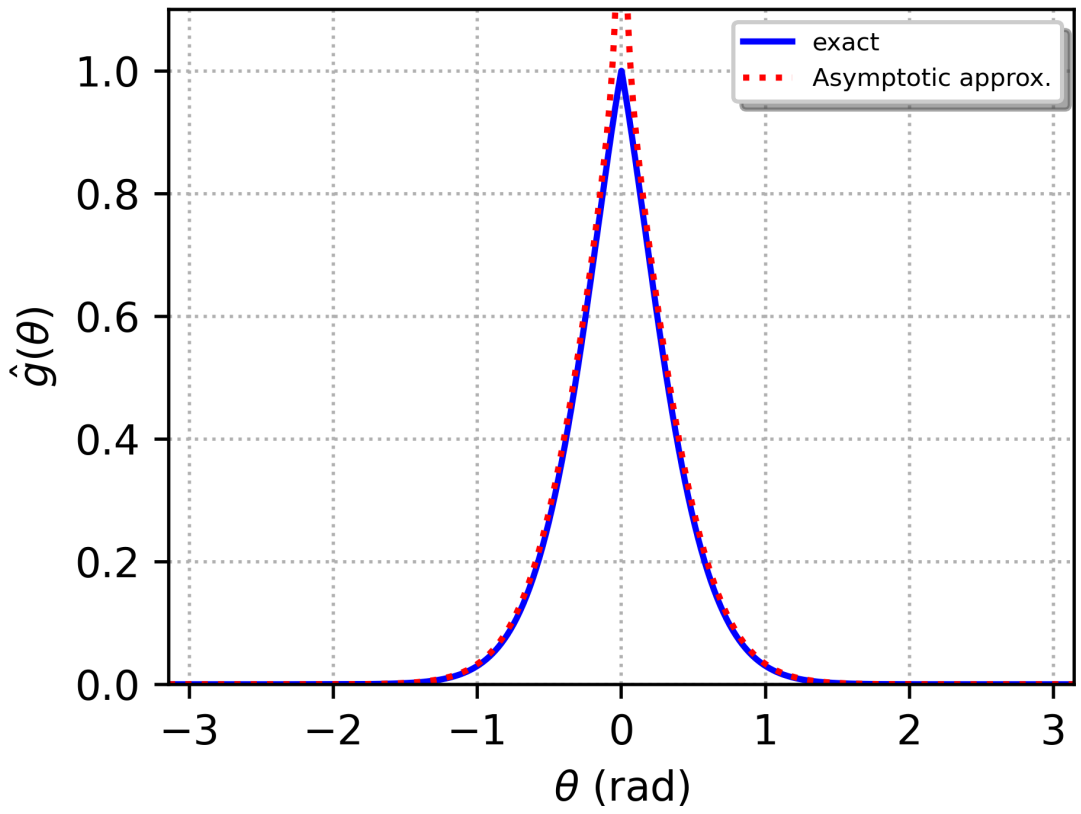

Figure B.1: Exact asymptotic behavior of the correlation function for a rapid quench. The functional form is quite different from the simple Gaussian approximation to the correlation function, and even captures intermediate range behavior quite well.

Appendix C

Zero-Noise Extrapolation of Temperature

We outline and give results from a potentially novel procedure to increase the accuracy of in-situ thermometry on degenerate Fermi gases. This technique was stumbled upon when I decided to study the effects of adding random noise to the measured in-situ density profiles of degenerate Fermi gases. We note that zero-noise extrapolation (ZNE) techniques are commonly used for quantum error-mitigation [129], but in this subsection we demonstrate its potential use in improving the accuracy of degenerate fermion thermometry.

To account for temperature estimation errors due to low SNR at large radii, one may perform a "zero-noise extrapolation" by linearly fitting temperatures extracted from in-situ density profile fits with varying amounts of added simulated random noise, and extrapolating to the zero-noise limit. We found empirically that the effect of added simulated noise is to increase the apparent temperature of the system by an amount proportional to the noise amplitude. To outline the procedure algorithmically:

- Obtain a base noise amplitude A_0 from unperturbed data as the mean of the absolute value of the fit residuals at each radius

- Add random noise to data with some small fixed amplitude A_1, perform fit to data to extract temperature, and repeat at least 10 times. Average these temperatures and store value T_1
- Repeat above step N times for different noise amplitudes A_i to obtain temperatures T_i, $i = 2, 3, ..., N$
- Fit $(\{A_i + A_0\},\ \{T_i\})_{i=1,2,...,N}$ to straight line, extract noise-free temperature T_{NF} as the y-intercept.

We found empirically that the largest source of temperature estimation uncertainty is uncertainty in the weak radial trap frequency of the sheet beam. This uncertainty puts about 3 nK of uncertainty onto the temperature. Measurement noise introduces a much smaller uncertainty, and uncertainty in the axial trap frequency introduces a similar amount. Uncertainty in imaging beam parameters such as saturation intensity and polarization impurity will introduce systematic errors onto the temperature estimate. For the dilute halo atoms, error due to saturation effects may be neglected. Finally, we empirically determined that the uncertainty in background offset of the atomic density profile contributed sub-nK uncertainty to the temperature.

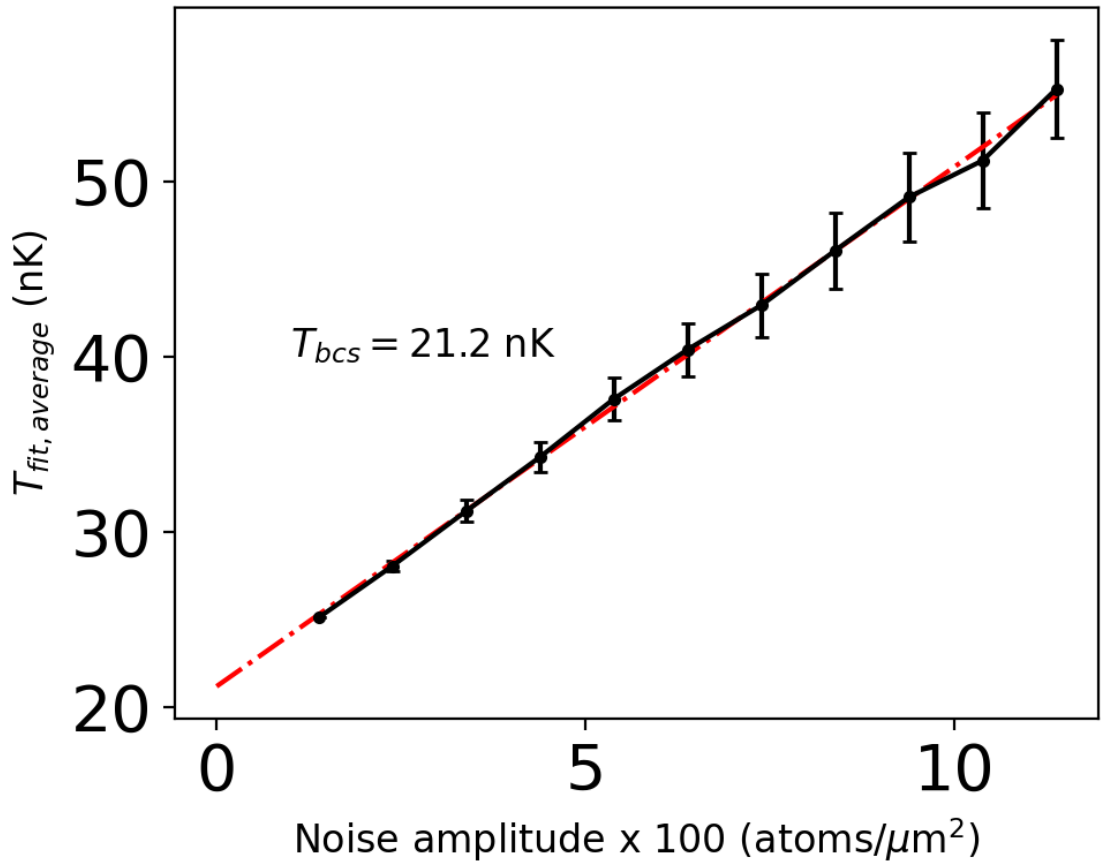

Figure C.1: Extrapolation of noise-augmented, fit-extracted temperatures to the zero-noise limit, using the algorithm defined above. Each black point is the average of 100 fits at fixed noise amplitude, while the red dash-dotted line is the linear fit, which extrapolates the measured $T_{BCS} = 25$ nK to the noise free limit $T_{NF} = 21.2(5)$ nK. Uncertainty is estimated as half the difference in y-intercepts between the extremal fits to the data, assuming measurement noise is the main source of error. We empirically find that the largest contribution to the error in temperature is uncertainty in the weak radial trap frequency. This alone introduces several nK of uncertainty into T_{BCS}.

Bibliography

[1] F. Steglich, J. Aarts, C. D. Bredl, W. Lieke, D. Meschede, W. Franz, and H. Schäfer, "Superconductivity in the Presence of Strong Pauli Paramagnetism: $CeCu_2Si_2$", Phys. Rev. Lett. **43**, 1892–1896 (1979) (page 1).

[2] P. Fulde and R. A. Ferrell, "Superconductivity in a strong spin-exchange field", Physical Review **135**, A550 (1964) (pages 1, 174).

[3] A. Larkin, "Inhomogeneous state of superconductors", Sov. Phys. JETP **20**, 762 (1965) (pages 1, 174).

[4] J. Bardeen, L. N. Cooper, and J. R. Schrieffer, "Theory of Superconductivity", Phys. Rev. **108**, 1175–1204 (1957) (pages 1, 29).

[5] V. L. Ginzburg and L. D. Landau, "On the theory of superconductivity", in *On superconductivity and superfluidity: a scientific autobiography* (Springer Berlin Heidelberg, Berlin, Heidelberg, 2009), pp. 113–137 (pages 2, 109).

[6] L. P. Kadanoff, "Scaling laws for Ising models near T_c", Physics Physique Fizika **2**, 263–272 (1966) (page 2).

[7] T. W. B. Kibble, "Topology of cosmic domains and strings", Journal of Physics A: Mathematical and General **9**, 1387 (1976) (pages 2–4, 101, 137).

[8] W. H. Zurek, "Cosmological experiments in superfluid helium?", Nature **317**, 505–508 (1985) (pages 2, 4, 101, 104, 108, 137, 139).

[9] Y. B. Zel'Dovich, I. Y. Kobzarev, and L. B. Okun', "Cosmological consequences of a spontaneous breakdown of a discrete symmetry", Soviet Journal of Experimental and Theoretical Physics **40**, 1 (1975) (page 3).

[10] R. Monaco, J. Mygind, R. J. Rivers, and V. P. Koshelets, "Spontaneous fluxoid formation in superconducting loops", Phys. Rev. B **80**, 180501 (2009) (pages 3, 108, 139, 151).

[11] S. Deutschländer, P. Dillmann, G. Maret, and P. Keim, "Kibble–Zurek mechanism in colloidal monolayers", Proceedings of the National Academy of Sciences **112**, 6925–6930 (2015) (page 3).

[12] C. Bäuerle, Y. M. Bunkov, S. Fisher, H. Godfrin, and G. Pickett, "Laboratory simulation of cosmic string formation in the early Universe using superfluid ^{3}He", Nature **382**, 332–334 (1996) (page 3).

[13] V. Ruutu, V. Eltsov, A. Gill, T. Kibble, M. Krusius, Y. G. Makhlin, B. Placais, G. Volovik, and W. Xu, "Vortex formation in neutron-irradiated superfluid ^{3}He as an analogue of cosmological defect formation", Nature **382**, 334–336 (1996) (page 3).

[14] S. Ducci, P. L. Ramazza, W. González-Viñas, and F. Arecchi, "Order parameter fragmentation after a symmetry-breaking transition", Physical Review Letters **83**, 5210 (1999) (page 3).

[15] R. Carmi and E. Polturak, "Search for spontaneous nucleation of magnetic flux during rapid cooling of YBa 2 Cu 3 O 7- δ films through T_c", Physical Review B **60**, 7595 (1999) (page 3).

[16] J. Kirtley, C. Tsuei, and F. Tafuri, "Thermally activated spontaneous fluxoid formation in superconducting thin film rings", Physical review letters **90**, 257001 (2003) (page 3).

[17] L. Sadler, J. Higbie, S. Leslie, M. Vengalattore, and D. Stamper-Kurn, "Spontaneous symmetry breaking in a quenched ferromagnetic spinor Bose-Einstein condensate", Nature **443**, 312–315 (2006) (page 3).

[18] S. Chae, N. Lee, Y. Horibe, M. Tanimura, S. Mori, B. Gao, S. Carr, and S.-W. Cheong, "Direct observation of the proliferation of ferroelectric loop domains and vortex-antivortex pairs", Physical review letters **108**, 167603 (2012) (page 3).

[19] A. Keesling, A. Omran, H. Levine, H. Bernien, H. Pichler, S. Choi, R. Samajdar, S. Schwartz, P. Silvi, S. Sachdev, et al., "Quantum Kibble-Zurek mechanism and critical dynamics on a programmable Rydberg simulator", Nature **568**, 207–211 (2019) (page 3).

[20] M. Anquez, B. A. Robbins, H. M. Bharath, M. Boguslawski, T. M. Hoang, and M. S. Chapman, "Quantum Kibble-Zurek Mechanism in a Spin-1 Bose-Einstein Condensate", Phys. Rev. Lett. **116**, 155301 (2016) (page 3).

[21] D. Chen, M. White, C. Borries, and B. DeMarco, "Quantum quench of an atomic Mott insulator", Physical Review Letters **106**, 235304 (2011) (page 3).

[22] S. Braun, M. Friesdorf, S. S. Hodgman, M. Schreiber, J. P. Ronzheimer, A. Riera, M. Del Rey, I. Bloch, J. Eisert, and U. Schneider, "Emergence of coherence and the dynamics of quantum phase transitions", Proceedings of the National Academy of Sciences **112**, 3641–3646 (2015) (page 3).

[23] I. Bloch, J. Dalibard, and S. Nascimbene, "Quantum simulations with ultracold quantum gases", Nature Physics **8**, 267–276 (2012) (page 3).

[24] L. Amico, M. Boshier, G. Birkl, A. Minguzzi, C. Miniatura, L.-C. Kwek, D. Aghamalyan, V. Ahufinger, D. Anderson, N. Andrei, et al., "Roadmap on

Atomtronics: State of the art and perspective", AVS Quantum Science **3** (2021) (pages 3, 30).

[25] R. Grimm, M. Weidemüller, and Y. B. Ovchinnikov, in *Advances in atomic, molecular, and optical physics*, Vol. 42 (Elsevier, 2000), pp. 95–170 (page 7).

[26] G. Gauthier, I. Lenton, N. M. Parry, M. Baker, M. Davis, H. Rubinsztein-Dunlop, and T. Neely, "Direct imaging of a digital-micromirror device for configurable microscopic optical potentials", Optica **3**, 1136–1143 (2016) (page 7).

[27] D. A. Butts and D. S. Rokhsar, "Trapped Fermi gases", Phys. Rev. A **55**, 4346–4350 (1997) (page 10).

[28] R. Dingle, "The Fermi-Dirac integrals", Applied Scientific Research, Section B **6**, 225–239 (1957) (page 12).

[29] W. Ketterle, D. S. Durfee, and D. M. Stamper-Kurn, *Making, probing and understanding Bose-Einstein condensates*, 1999 (page 13).

[30] N. Abel, "Auflösung einer mechanischen Aufgabe.", ger, Journal für die reine und angewandte Mathematik **1**, 153–157 (1826) (page 13).

[31] Y. Cai, D. G. Allman, P. Sabharwal, and K. C. Wright, "Persistent Currents in Rings of Ultracold Fermionic Atoms", Phys. Rev. Lett. **128**, 150401 (2022) (pages 18, 56, 57, 71, 80, 115, 143, 148).

[32] D. G. Allman, P. Sabharwal, and K. C. Wright, "Mitigating heating of degenerate fermions in a ring-dimple atomic trap", Physical Review A **107**, 043322 (2023) (pages 18, 54, 143).

[33] K. Matsushima, H. Schimmel, and F. Wyrowski, "Fast calculation method for optical diffraction on tilted planes by use of the angular spectrum of plane waves", JOSA A **20**, 1755–1762 (2003) (page 21).

[34] J. W. Goodman, *Introduction to Fourier Optics*, Third (Roberts New York, 2016) (pages 21, 59).

[35] H. Feshbach, "Unified theory of nuclear reactions", Annals of Physics **5**, 357–390 (1958) (page 24).

[36] P. Courteille, R. Freeland, D. J. Heinzen, F. Van Abeelen, and B. Verhaar, "Observation of a Feshbach resonance in cold atom scattering", Physical review letters **81**, 69 (1998) (page 24).

[37] S. Inouye, M. Andrews, J. Stenger, H.-J. Miesner, D. M. Stamper-Kurn, and W. Ketterle, "Observation of Feshbach resonances in a Bose-Einstein condensate", Nature **392**, 151–154 (1998) (page 24).

[38] K. O'hara, S. Hemmer, M. Gehm, S. Granade, and J. Thomas, "Observation of a strongly interacting degenerate Fermi gas of atoms", Science **298**, 2179–2182 (2002) (page 24).

[39] T. Bourdel, J. Cubizolles, L. Khaykovich, K. Magalhaes, S. Kokkelmans, G. V. Shlyapnikov, and C. Salomon, "Measurement of the Interaction Energy near a Feshbach Resonance in a ^{6}Li Fermi Gas", Physical review letters **91**, 020402 (2003) (page 24).

[40] W. Ketterle and M. W. Zwierlein, "Making, probing and understanding ultracold Fermi gases", La Rivista del Nuovo Cimento **31**, 247–422 (2008) (pages 25, 93, 96, 117).

[41] M. E. Gehm, "Properties of ^{6}Li", Jetlab, (2003) (page 26).

[42] G. Zürn, T. Lompe, A. N. Wenz, S. Jochim, P. Julienne, and J. Hutson, "Precise characterization of Li 6 Feshbach resonances using trap-sideband-resolved RF spectroscopy of weakly bound molecules", Physical review letters **110**, 135301 (2013) (page 26).

[43] O. Penrose and L. Onsager, "Bose-Einstein Condensation and Liquid Helium", Phys. Rev. **104**, 576–584 (1956) (page 27).

[44] A. J. Leggett, in *Modern trends in the theory of condensed matter: proceedings of the xvi karpacz winter school of theoretical physics, february 19–march 3, 1979 karpacz, poland* (Springer, 2008), pp. 13–27 (pages 27, 28).

[45] T. Bland, Q. Marolleau, P. Comaron, B. A. Malomed, and N. P. Proukakis, "Persistent current formation in double-ring geometries", Journal of Physics B: Atomic, Molecular and Optical Physics **53**, 115301 (2020) (page 30).

[46] W. S. Bakr, J. I. Gillen, A. Peng, S. Fölling, and M. Greiner, "A quantum gas microscope for detecting single atoms in a Hubbard-regime optical lattice", Nature **462**, 74–77 (2009) (page 36).

[47] W. Alt, "An objective lens for efficient fluorescence detection of single atoms", Optik **113**, 142–144 (2002) (page 37).

[48] R. W. Floyd, "An adaptive algorithm for spatial gray-scale", in Proc. soc. inf. disp. Vol. 17 (1976), pp. 75–77 (page 46).

[49] K. Hueck, A. Mazurenko, N. Luick, T. Lompe, and H. Moritz, "Note: Suppression of kHz-frequency switching noise in digital micro-mirror devices", Review of Scientific Instruments **88** (2017) (page 48).

[50] M. J. Holland, B. DeMarco, and D. S. Jin, "Evaporative cooling of a two-component degenerate Fermi gas", Phys. Rev. A **61**, 053610 (2000) (page 55).

[51] D. C. McKay and B. DeMarco, "Cooling in strongly correlated optical lattices: prospects and challenges", Reports on Progress in Physics **74**, 054401 (2011) (page 55).

[52] R. Onofrio, "Physics of our Days: Cooling and thermometry of atomic Fermi gases", Physics-Uspekhi **59**, 1129 (2016) (page 55).

[53] D. M. Stamper-Kurn, H.-J. Miesner, A. P. Chikkatur, S. Inouye, J. Stenger, and W. Ketterle, "Reversible Formation of a Bose-Einstein Condensate", Phys. Rev. Lett. **81**, 2194–2197 (1998) (page 55).

[54] L. Viverit, S. Giorgini, L. P. Pitaevskii, and S. Stringari, "Adiabatic compression of a trapped Fermi gas", Phys. Rev. A **63**, 033603 (2001) (page 55).

[55] P. Schuck and X. Viñas, "Suppression of Superfluidity upon Overflow of Trapped Fermions: Quantal and Thomas-Fermi Studies", Phys. Rev. Lett. **107**, 205301 (2011) (page 55).

[56] G. Zürn, "Few-fermion systems in one dimension", PhD thesis (University of Heidelberg, 2012) (page 55).

[57] S. Stellmer, B. Pasquiou, R. Grimm, and F. Schreck, "Laser Cooling to Quantum Degeneracy", Phys. Rev. Lett. **110**, 263003 (2013) (page 55).

[58] P. M. Duarte, R. A. Hart, T.-L. Yang, X. Liu, T. Paiva, E. Khatami, R. T. Scalettar, N. Trivedi, and R. G. Hulet, "Compressibility of a Fermionic Mott Insulator of Ultracold Atoms", Phys. Rev. Lett. **114**, 070403 (2015) (page 55).

[59] A. Guttridge, "A quantum degenerate gas of cs", in *Photoassociation of ultracold csyb molecules and determination of interspecies scattering lengths* (Springer International Publishing, Cham, 2019), pp. 91–111 (page 55).

[60] L. D. Carr, G. V. Shlyapnikov, and Y. Castin, "Achieving a BCS transition in an atomic Fermi gas", Phys. Rev. Lett. **92**, 150404 (2004) (pages 55, 76, 77).

[61] E. Timmermans, "Degenerate Fermion Gas Heating by Hole Creation", Phys. Rev. Lett. **87**, 240403 (2001) (pages 55, 67).

[62] L. D. Carr, T. Bourdel, and Y. Castin, "Limits of sympathetic cooling of fermions by zero-temperature bosons due to particle losses", Phys. Rev. A **69**, 033603 (2004) (page 55).

[63] R. Côté, R. Onofrio, and E. Timmermans, "Sympathetic cooling route to Bose-Einstein condensate and Fermi-liquid mixtures", Phys. Rev. A **72**, 041605 (2005) (page 55).

[64] Z. Idziaszek, L. Santos, and M. Lewenstein, "Sympathetic cooling of trapped fermions by bosons in the presence of particle losses", Europhysics Letters **70**, 572 (2005) (page 55).

[65] G. Del Pace, K. Xhani, A. M. Falconi, M. Fedrizzi, N. Grani, D. H. Rajkov, M. Inguscio, F. Scazza, W. J. Kwon, and G. Roati, *Imprinting persistent currents in tunable fermionic rings*, 2022 (pages 56, 57, 80, 86).

[66] S. Gupta, K. W. Murch, K. L. Moore, T. P. Purdy, and D. M. Stamper-Kurn, "Bose-Einstein Condensation in a Circular Waveguide", Phys. Rev. Lett. **95**, 143201 (2005) (page 56).

[67] A. S. Arnold, C. S. Garvie, and E. Riis, "Large magnetic storage ring for Bose-Einstein condensates", Phys. Rev. A **73**, 041606 (2006) (page 56).

[68] C. Ryu, M. F. Andersen, P. Cladé, V. Natarajan, K. Helmerson, and W. D. Phillips, "Observation of Persistent Flow of a Bose-Einstein Condensate in a Toroidal Trap", Phys. Rev. Lett. **99**, 260401 (2007) (page 56).

[69] K. Henderson, C. Ryu, C. MacCormick, and M. G. Boshier, "Experimental demonstration of painting arbitrary and dynamic potentials for Bose-Einstein condensates", New J. Phys. **11**, 43030 (2009) (page 56).

[70] G. D. Bruce, J. Mayoh, G. Smirne, L. Torralbo-Campo, and D. Cassettari, "A smooth, holographically generated ring trap for the investigation of superfluidity in ultracold atoms", Phys. Scr. **T143**, 014008 (2011) (page 56).

[71] B. E. Sherlock, M. Gildemeister, E. Owen, E. Nugent, and C. J. Foot, "Time-averaged adiabatic ring potential for ultracold atoms", Phys. Rev. A **83**, 043408 (2011) (page 56).

[72] A. Ramanathan, K. C. Wright, S. R. Muniz, M. Zelan, W. T. Hill, C. J. Lobb, K. Helmerson, W. D. Phillips, and G. K. Campbell, "Superflow in a Toroidal Bose-Einstein Condensate: An Atom Circuit with a Tunable Weak Link", Phys. Rev. Lett. **106**, 130401 (2011) (pages 56, 57).

[73] S. Beattie, S. Moulder, R. J. Fletcher, and Z. Hadzibabic, "Persistent Currents in Spinor Condensates", Phys. Rev. Lett. **110**, 025301 (2013) (page 56).

[74] T. W. Neely, A. S. Bradley, E. C. Samson, S. J. Rooney, E. M. Wright, K. J. H. Law, R. Carretero-González, P. G. Kevrekidis, M. J. Davis, and B. P. Anderson, "Characteristics of Two-Dimensional Quantum Turbulence in a Compressible Superfluid", Phys. Rev. Lett **111**, 235301 (2013) (page 56).

[75] P. Navez, S. Pandey, H. Mas, K. Poulios, T. Fernholz, and W. von Klitzing, "Matter-wave interferometers using TAAP rings", New J. Phys. **18**, 075014 (2016) (page 56).

[76] M. de Goër de Herve, Y. Guo, C. De Rossi, A. Kumar, T. Badr, R. Dubessy, L. Longchambon, and H. Perrin, "A versatile ring trap for quantum gases", J. Phys. B **54**, 125302 (2021) (page 56).

[77] S. Shi, G. Jin, and D. W. Prather, "Electromagnetic simulation of quantum well structures", Opt. Express **14**, 2459–2472 (2006) (page 61).

[78] L. P. Gor'kov and T. K. Melik-Barkhudarov, "Contribution to the Theory of Superfluidity in an Imperfect Fermi Gas", Sov. Phys. JETP **13**, 1018 (1961) (pages 67, 110, 143, 145).

[79] C. De Daniloff, M. Tharrault, C. Enesa, C. Salomon, F. Chevy, T. Reimann, and J. Struck, "In Situ Thermometry of Fermionic Cold-Atom Quantum Wires", Phys. Rev. Lett. **127**, 113602 (2021) (pages 74, 143).

[80] D. Baillie, P. B. Blakie, and A. S. Bradley, "Geometric scale invariance as a route to macroscopic degeneracy: Loading a toroidal trap with a Bose or Fermi gas", Phys. Rev. A **82**, 013626 (2010) (page 74).

[81] J. Stenger, S. Inouye, A. P. Chikkatur, D. M. Stamper-Kurn, D. E. Pritchard, and W. Ketterle, "Bragg Spectroscopy of a Bose-Einstein Condensate", Phys. Rev. Lett. **82**, 4569–4573 (1999) (page 84).

[82] B. Deh, C. Marzok, S. Slama, C. Zimmermann, and P. W. Courteille, "Bragg spectroscopy and Ramsey interferometry with an ultracold Fermi gas", Applied Physics B **97**, 387–396 (2009) (page 84).

[83] C. Shkedrov, G. Ness, Y. Florshaim, and Y. Sagi, "In situ momentum-distribution measurement of a quantum degenerate Fermi gas using Raman spectroscopy", Phys. Rev. A **101**, 013609 (2020) (page 84).

[84] K. C. Wright, R. B. Blakestad, C. J. Lobb, W. D. Phillips, and G. K. Campbell, "Driving Phase Slips in a Superfluid Atom Circuit with a Rotating Weak Link", Phys. Rev. Lett. **110**, 025302 (2013) (page 85).

[85] S. Eckel, F. Jendrzejewski, A. Kumar, C. J. Lobb, and G. K. Campbell, "Interferometric Measurement of the Current-Phase Relationship of a Superfluid Weak Link", Phys. Rev. X **4**, 031052 (2014) (page 86).

[86] L. Corman, L. Chomaz, T. Bienaimé, R. Desbuquois, C. Weitenberg, S. Nascimbène, J. Dalibard, and J. Beugnon, "Quench-Induced Supercurrents in an Annular Bose Gas", Phys. Rev. Lett. **113**, 135302 (2014) (pages 86, 133, 134, 138, 150).

[87] M. Aidelsburger, J. L. Ville, R. Saint-Jalm, S. Nascimbène, J. Dalibard, and J. Beugnon, "Relaxation Dynamics in the Merging of N Independent Condensates", Phys. Rev. Lett **119**, 190403 (2017) (page 86).

[88] P. Schuck and X. Viñas, "Thomas-Fermi approximation for Bose-Einstein condensates in traps", Phys. Rev. A **61**, 043603 (2000) (page 89).

[89] L. Mathey, A. Ramanathan, K. C. Wright, S. R. Muniz, W. D. Phillips, and C. W. Clark, "Phase fluctuations in anisotropic Bose-Einstein condensates: From cigars to rings", Phys. Rev. A **82**, 033607 (2010) (page 92).

[90] D. S. Petrov, G. V. Shlyapnikov, and J. T. M. Walraven, "Phase-Fluctuating 3D Bose-Einstein Condensates in Elongated Traps", Phys. Rev. Lett. **87**, 050404 (2001) (page 92).

[91] S. Dettmer, D. Hellweg, P. Ryytty, J. J. Arlt, W. Ertmer, K. Sengstock, D. S. Petrov, G. V. Shlyapnikov, H. Kreutzmann, L. Santos, and M. Lewenstein, "Observation of Phase Fluctuations in Elongated Bose-Einstein Condensates", Phys. Rev. Lett. **87**, 160406 (2001) (page 92).

[92] C. A. Regal, M. Greiner, and D. S. Jin, "Observation of Resonance Condensation of Fermionic Atom Pairs", Phys. Rev. Lett. **92**, 040403 (2004) (page 93).

[93] R. Kubo, "The fluctuation-dissipation theorem", Reports on progress in physics **29**, 255 (1966) (page 103).

[94] P. C. Hohenberg and B. I. Halperin, "Theory of dynamic critical phenomena", Rev. Mod. Phys. **49**, 435–479 (1977) (page 104).

[95] J. Hubbard, "Calculation of Partition Functions", Phys. Rev. Lett. **3**, 77–78 (1959) (page 105).

[96] R. Stratonovich, "On a method of calculating quantum distribution functions", in Soviet physics doklady, Vol. 2 (1957), p. 416 (page 105).

[97] A. Del Campo and W. H. Zurek, "Universality of phase transition dynamics: Topological defects from symmetry breaking", International Journal of Modern Physics A **29**, 1430018 (2014) (page 107).

[98] A. Jelić and L. F. Cugliandolo, "Quench dynamics of the 2d XY model", Journal of Statistical Mechanics: Theory and Experiment **2011**, P02032 (2011) (page 108).

[99] D. J. Weir, R. Monaco, V. P. Koshelets, J. Mygind, and R. J. Rivers, "Gaussianity revisited: exploring the Kibble–Zurek mechanism with superconducting rings", Journal of Physics: Condensed Matter **25**, 404207 (2013) (pages 108, 115, 117, 139, 151, 153).

[100] W. H. Zurek, "Topological relics of symmetry breaking: winding numbers and scaling tilts from random vortex–antivortex pairs", Journal of Physics: Condensed Matter **25**, 404209 (2013) (pages 108, 125, 139, 151, 156).

[101] C.-Y. Xia and H.-B. Zeng, "Winding up a finite size holographic superconducting ring beyond Kibble-Zurek mechanism", Physical Review D **102**, 126005 (2020) (page 108).

[102] M. Houbiers and H. T. C. Stoof, "Cooper-pair formation in trapped atomic Fermi gases", Phys. Rev. A **59**, 1556–1561 (1999) (page 110).

[103] E. P. Gross, "Structure of a quantized vortex in boson systems", Il Nuovo Cimento (1955-1965) **20**, 454–477 (1961) (page 110).

[104] L. P. Pitaevskii, "Vortex lines in an imperfect Bose gas", Sov. Phys. JETP **13**, 451–454 (1961) (page 110).

[105] R. Monaco, M. Aaroe, J. Mygind, R. J. Rivers, and V. P. Koshelets, "Spontaneous fluxon production in annular Josephson tunnel junctions in the presence of a magnetic field", Phys. Rev. B **77**, 054509 (2008) (pages 115, 125).

[106] W. A. Little, "Decay of Persistent Currents in Small Superconductors", Phys. Rev. **156**, 396–403 (1967) (page 116).

[107] A. Das, J. Sabbatini, and W. H. Zurek, "Winding up superfluid in a torus via Bose Einstein condensation.", Sci. Rep. **2**, 352 (2012) (page 117).

[108] I.-K. Liu, J. Dziarmaga, S.-C. Gou, F. Dalfovo, and N. P. Proukakis, "Kibble-zurek dynamics in a trapped ultracold bose gas", Phys. Rev. Res. **2**, 033183 (2020) (pages 117, 119, 162).

[109] P. Laguna and W. H. Zurek, "Density of Kinks after a Quench: When Symmetry Breaks, How Big are the Pieces?", Phys. Rev. Lett. **78**, 2519–2522 (1997) (page 117).

[110] P. M. Chesler, A. M. Garcıa-Garcıa, and H. Liu, "Defect Formation beyond Kibble-Zurek Mechanism and Holography", Phys. Rev. X **5**, 021015 (2015) (pages 120, 162).

[111] E. Bogomolny, O. Bohigas, and P. Leboeuf, "Distribution of roots of random polynomials", Phys. Rev. Lett. **68**, 2726–2729 (1992) (page 121).

[112] L. A. Shepp and R. J. Vanderbei, "The complex zeros of random polynomials", Transactions of the American Mathematical Society, 4365–4384 (1995) (page 121).

[113] N. Navon, A. L. Gaunt, R. P. Smith, and Z. Hadzibabic, "Critical dynamics of spontaneous symmetry breaking in a homogeneous Bose gas", Science **347**, 167–170 (2015) (page 138).

[114] S. Donadello, S. Serafini, T. Bienaimé, F. Dalfovo, G. Lamporesi, and G. Ferrari, "Creation and counting of defects in a temperature-quenched Bose-Einstein condensate", Phys. Rev. A **94**, 023628 (2016) (page 138).

[115] J. Beugnon and N. Navon, "Exploring the Kibble–Zurek mechanism with homogeneous Bose gases", Journal of Physics B: Atomic, Molecular and Optical Physics **50**, 022002 (2017) (page 138).

[116] B. Ko, J. W. Park, and Y. Shin, "Kibble–Zurek universality in a strongly interacting Fermi superfluid", Nat. Phys. **15**, 1227–1231 (2019) (page 138).

[117] J. Goo, Y. Lee, Y. Lim, D. Bae, T. Rabga, and Y. Shin, "Universal Early Coarsening of Quenched Bose Gases", Phys. Rev. Lett. **128**, 135701 (2022) (page 138).

[118] A. del Campo, A. Retzker, and M. B. Plenio, "The inhomogeneous Kibble–Zurek mechanism: vortex nucleation during Bose–Einstein condensation", New Journal of Physics **13**, 083022 (2011) (pages 138, 142, 169).

[119] R. W. Johnson, "An introduction to the bootstrap", Teaching statistics **23**, 49–54 (2001) (page 148).

[120] R. G. McDonald and A. S. Bradley, "Reservoir interactions during Bose-Einstein condensation: Modified critical scaling in the Kibble-Zurek mechanism of defect formation", Phys. Rev. A **92**, 033616 (2015) (pages 149, 151, 154).

[121] A. Larkin and A. Varlamov, *Theory of fluctuations in superconductors*, Vol. 127 (OUP Oxford, 2005) (page 150).

[122] C. A. R. Sá de Melo, M. Randeria, and J. R. Engelbrecht, "Crossover from BCS to Bose superconductivity: Transition temperature and time-dependent Ginzburg-Landau theory", Phys. Rev. Lett. **71**, 3202–3205 (1993) (page 150).

[123] X.-P. Liu, X.-C. Yao, Y. Deng, Y.-X. Wang, X.-Q. Wang, X. Li, Q. Chen, Y.-A. Chen, and J.-W. Pan, "Dynamic formation of quasicondensate and sponta-

neous vortices in a strongly interacting Fermi gas", Phys. Rev. Res. **3**, 043115 (2021) (page 154).

[124] P. Dyke, A. Hogan, I. Herrera, C. C. N. Kuhn, S. Hoinka, and C. J. Vale, "Dynamics of a Fermi Gas Quenched to Unitarity", Phys. Rev. Lett. **127**, 100405 (2021) (page 154).

[125] W. A. Little and R. D. Parks, "Observation of quantum periodicity in the transition temperature of a superconducting cylinder", Phys. Rev. Lett. **9**, 9–12 (1962) (page 162).

[126] Z.-H. Li and H.-Q. Zhang, "Periodicities in a multiply connected geometry from quenched dynamics", Phys. Rev. Res. **4**, 023201 (2022) (page 162).

[127] G. B. Hess and W. M. Fairbank, "Measurements of Angular Momentum in Superfluid Helium", Phys. Rev. Lett. **19**, 216–218 (1967) (page 163).

[128] P. J. Forrester and G. Honner, "Exact statistical properties of the zeros of complex random polynomials", Journal of Physics A: Mathematical and General **32**, 2961 (1999) (page 166).

[129] V. R. Pascuzzi, A. He, C. W. Bauer, W. A. de Jong, and B. Nachman, "Computationally efficient zero-noise extrapolation for quantum-gate-error mitigation", Phys. Rev. A **105**, 042406 (2022) (page 185).